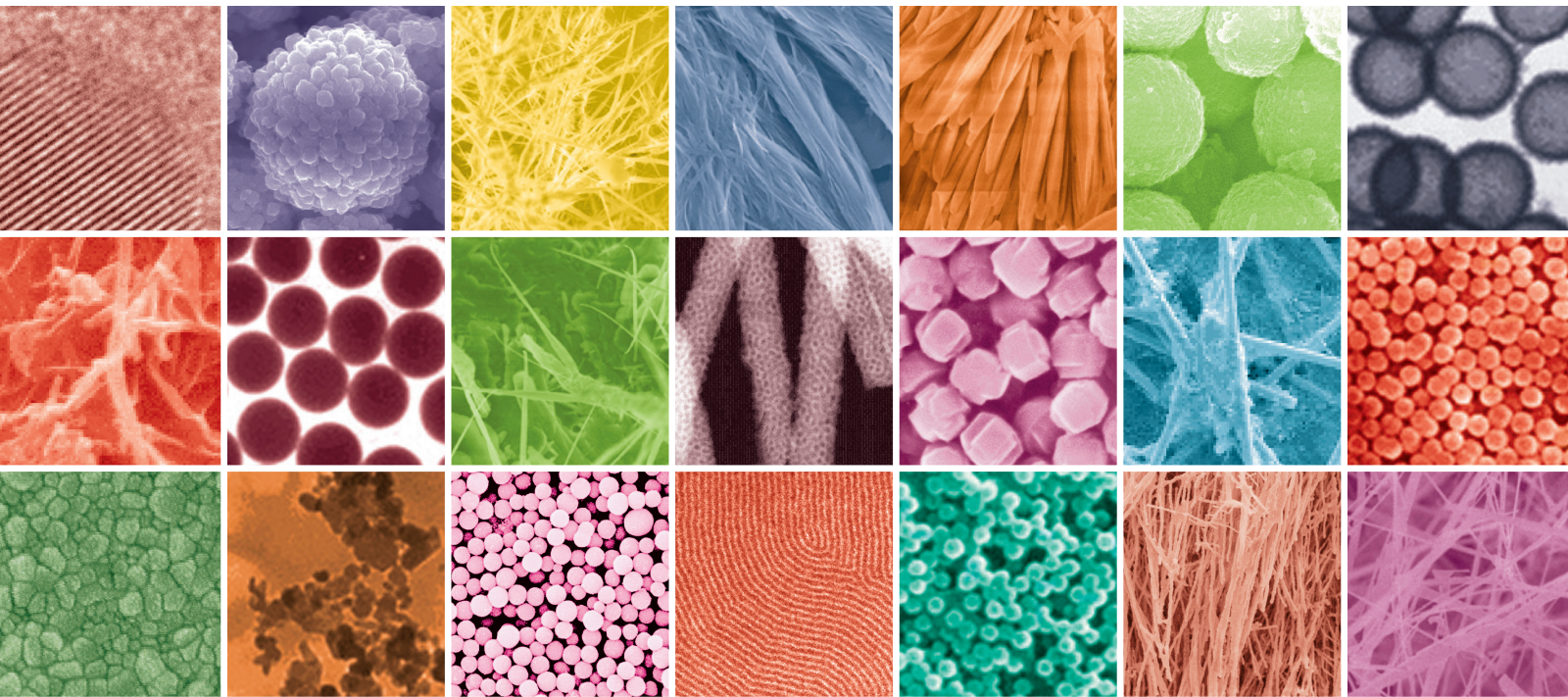


Advanced Nanomaterials for Catalysis: Synthesis, Characterization, and Application

Guest Editors: Xianwen Zhang, Xin Zhang, Baojuan Xi,
and Maofeng Zhang





Advanced Nanomaterials for Catalysis: Synthesis, Characterization, and Application

Journal of Nanomaterials

Advanced Nanomaterials for Catalysis: Synthesis, Characterization, and Application

Guest Editors: Xianwen Zhang, Xin Zhang, Baojuan Xi,
and Maofeng Zhang



Copyright © 2015 Hindawi Publishing Corporation. All rights reserved.

This is a special issue published in "Journal of Nanomaterials." All articles are open access articles distributed under the Creative Commons Attribution License, which permits unrestricted use, distribution, and reproduction in any medium, provided the original work is properly cited.

Editorial Board

Domenico Acierno, Italy
Katerina Aifantis, USA
Sheikh Akbar, USA
Nageh K. Allam, USA
Margarida Amaral, Portugal
Martin Andersson, Sweden
Raul Arenal, Spain
Ilaria Armentano, Italy
Vincenzo Baglio, Italy
Lavinia Balan, France
Thierry Baron, France
Andrew R. Barron, USA
Reza Bayati, USA
Hongbin Bei, USA
Daniel Bellet, France
Stefano Bellucci, Italy
Enrico Bergamaschi, Italy
Samuel Bernard, France
D. Bhattacharyya, New Zealand
Sergio Bietti, Italy
Giovanni Bongiovanni, Italy
Theodorian Borca-Tasciuc, USA
Mohamed Bououdina, Bahrain
Torsten Brezesinski, Germany
C. Jeffrey Brinker, USA
Christian Brosseau, France
Philippe Caroff, Australia
Victor M. Castaño, Mexico
Albano Cavaleiro, Portugal
Bhanu P. S. Chauhan, USA
Shafiq Chowdhury, USA
Jin-Ho Choy, Korea
Kwang-Leong Choy, UK
Yu-Lun Chueh, Taiwan
Elisabetta Comini, Italy
Giuseppe Compagnini, Italy
David Cornu, France
Miguel A. Correa-Duarte, Spain
P. Davide Cozzoli, Italy
Shadi A. Dayeh, USA
Luca Deseri, USA
Yong Ding, USA
Philippe Dubois, Belgium
Alain Dufresne, France
Zehra Durmus, Turkey
Joydeep Dutta, Oman
Ali Eftekhari, USA
Jeffrey Elam, USA
Samy El-Shall, USA
Ovidiu Ersen, France
Claude Estournès, France
Andrea Falqui, KSA
Matteo Ferroni, Italy
E. Johan Foster, USA
Ilaria Fratoddi, Italy
Wolfgang Fritzsche, Germany
Alan Fuchs, USA
Miguel A. Garcia, Spain
Siddhartha Ghosh, Singapore
P. K. Giri, India
Russell E. Gorga, USA
Jihua Gou, USA
Jean M. Greneche, France
Smrati Gupta, Germany
Kimberly Hamad-Schifferli, USA
Simo-Pekka Hannula, Finland
Michael Harris, USA
Yasuhiko Hayashi, Japan
F. Hernandez-Ramirez, Spain
Michael Z. Hu, USA
Nay Ming Huang, Malaysia
Shaoming Huang, China
David Hui, USA
Zafar Iqbal, USA
Balachandran Jeyadevan, Japan
Xin Jiang, Germany
Rakesh Joshi, Australia
Jeong-won Kang, Korea
Hassan Karimi-Maleh, Iran
Antonios Kelarakis, UK
Alireza Khataee, Iran
Ali Khorsand Zak, Iran
Philippe Knauth, France
Ralph Krupke, Germany
Christian Kübel, Germany
Prashant Kumar, UK
Michele Laus, Italy
Eric Le Bourhis, France
Burtrand Lee, USA
Jun Li, Singapore
Meiyong Liao, Japan
Shijun Liao, China
Silvia Licocchia, Italy
Wei Lin, USA
Jun Liu, USA
Zainovia Lockman, Malaysia
Nico Lovergine, Italy
Jim Low, Australia
Jue Lu, USA
Songwei Lu, USA
Ed Ma, USA
Laura M. Maestro, Spain
Gaurav Mago, USA
Muhamamd A. Malik, UK
Devanesan Mangalaraj, India
Sanjay R. Mathur, Germany
Tony McNally, UK
Yogendra Mishra, Germany
Paulo Cesar Morais, Brazil
Paul Munroe, Australia
Jae-Min Myoung, Korea
Rajesh R. Naik, USA
Albert Nasibulin, Russia
Toshiaki Natsuki, Japan
Koichi Niihara, Japan
Natalia Noginova, USA
Sherine Obare, USA
Won-Chun Oh, Republic of Korea
Atsuto Okamoto, Japan
Abdelwahab Omri, Canada
Ungyu Paik, Republic of Korea
Piersandro Pallavicini, Italy
Edward A. Payzant, USA
Alessandro Pegoretti, Italy
Ton Peijs, UK
Oscar Perales-Pérez, Puerto Rico
Jorge Pérez-Juste, Spain
Alexey P. Popov, Finland
Philip D. Rack, USA
Peter Reiss, France
Orlando Rojas, USA
Marco Rossi, Italy
Ilker S. Bayer, Italy
Cengiz S. Ozkan, USA
Sudipta Seal, USA



Shu Seki, Japan
Vladimir Šepelák, Germany
Huaiyu Shao, Japan
Prashant Sharma, USA
Donglu Shi, USA
Bhanu P. Singh, India
Surinder Singh, USA
Vladimir Sivakov, Germany
Ashok Sood, USA
Adolfo Speghini, Italy
Marinella Striccoli, Italy
Xuping Sun, KSA
Ashok K. Sundramoorthy, USA
Angelo Taglietti, Italy

Bo Tan, Canada
Leander Tapfer, Italy
Valeri P. Tolstoy, Russia
Muhammet S. Toprak, Sweden
Ramon Torrecillas, Spain
Takuya Tsuzuki, Australia
Tamer Uyar, Turkey
Bala Vaidhyanathan, UK
Luca Valentini, Italy
Rajender S. Varma, USA
Ester Vazquez, Spain
Antonio Villaverde, Spain
Ajayan Vinu, Australia
Ruibing Wang, Macau

Shiren Wang, USA
Yong Wang, USA
Magnus Willander, Sweden
Ping Xiao, UK
Zhi Li Xiao, USA
Yangchuan Xing, USA
Doron Yadlovker, Israel
Yoke K. Yap, USA
Kui Yu, Canada
William W. Yu, USA
Michele Zappalorto, Italy
Renyun Zhang, Sweden

Contents

Advanced Nanomaterials for Catalysis: Synthesis, Characterization, and Application, Xianwen Zhang, Xin Zhang, Baojuan Xi, and Maofeng Zhang
Volume 2015, Article ID 541801, 1 page

Core-Shell Nanocatalysts Obtained in Reverse Micelles: Structural and Kinetic Aspects, Concha Tojo, David Buceta, and M. Arturo López-Quintela
Volume 2015, Article ID 601617, 10 pages

Microwave-Assisted Synthesis of Porous ZnO/SnS₂ Heterojunction and Its Enhanced Photoactivity for Water Purification, A. B. Makama, A. Salmiaton, E. B. Saion, T. S. Y. Choong, and N. Abdullah
Volume 2015, Article ID 108297, 13 pages

Electrochemical Glucose Oxidation Using Glassy Carbon Electrodes Modified with Au-Ag Nanoparticles: Influence of Ag Content, Nancy Gabriela García-Morales, Luis Alfonso García-Cerda, Bertha Alicia Puente-Urbina, Leonor María Blanco-Jerez, René Antaño-López, and Federico Castañeda-Zaldivar
Volume 2015, Article ID 295314, 12 pages

Recent Developments in Environmental Photocatalytic Degradation of Organic Pollutants: The Case of Titanium Dioxide Nanoparticles—A Review, Mphilisi M. Mahlambi, Catherine J. Ngila, and Bhekie B. Mamba
Volume 2015, Article ID 790173, 29 pages

Three-Dimensional Graphene-Based Nanomaterials as Electrocatalysts for Oxygen Reduction Reaction, Xuan Ji, Xin Zhang, and Xianwen Zhang
Volume 2015, Article ID 357196, 9 pages

Rice Husk Supported Catalysts for Degradation of Chlorobenzenes in Capillary Microreactor, Abdulelah Thabet, Chanbasha Basheer, Than Htun Maung, Hasan Ali Al-Muallem, and Abdul Nasar Kalanthoden
Volume 2015, Article ID 912036, 9 pages

Editorial

Advanced Nanomaterials for Catalysis: Synthesis, Characterization, and Application

Xianwen Zhang,^{1,2} Xin Zhang,³ Baojuan Xi,⁴ and Maofeng Zhang⁵

¹*Institute of Advanced Energy Technology and Equipment, Hefei University of Technology, Hefei 230009, China*

²*Texas Tech University, Lubbock, TX 79409, USA*

³*Pacific Northwest National Laboratory, Richland, WA 99352, USA*

⁴*National University of Singapore, Singapore 119077*

⁵*Chinese Academy of Sciences, Hefei 230031, China*

Correspondence should be addressed to Xianwen Zhang; xianwen.zhang@ttu.edu

Received 8 October 2015; Accepted 8 October 2015

Copyright © 2015 Xianwen Zhang et al. This is an open access article distributed under the Creative Commons Attribution License, which permits unrestricted use, distribution, and reproduction in any medium, provided the original work is properly cited.

A great attention is being paid to catalysts which act to enhance the rate or yield of the reaction without being consumed by the reaction itself. Catalysis has become a key strategy in solving many of today's challenges. Up to now, almost all industrial processes employ catalyst in multiple forms to increase economic viability, from batteries to refineries. Meanwhile, increased concerns about environmental pollution have led to the development of novel catalysts, which can catalyze desirable chemical reactions. Catalysis is rather prevalent everywhere as a key enabling technology in energy conversion, fuel production, production of chemicals, and environmental mitigation. On the other hand, nanotechnology has become an indispensable tool of material engineering for catalysis related applications. Nanoparticles with controlled morphology and structure have a higher surface area, which provide the best platform to catalyze desirable chemical transformations and lead to the increased catalytic activity. The current barrier for widespread industrial and environmental use is ascribed to the controlled synthesis of nanocrystals with high-energy surfaces and the understanding of synthesis-structure-performance relationships. Multidisciplinary advances from chemistry, physics, and materials science have played a major role in catalyst synthesis, structural and compositional modification, and mechanistic understanding with molecular and atomic-level precision by advanced characterization techniques and modeling.

Last year, we invited investigators to contribute original research as well as review articles that address the field of advanced nanocatalysts. We encourage manuscripts that will concern new progress in controlled synthesis, thorough understanding of the reaction mechanism and cutting-edge characterization techniques. Today, we are very happy to publish this special issue of this journal.

In this issue, original research and review articles are accepted. The research papers focused on nanocatalysts with novel structure produced by innovative synthetic technologies and detailed kinetic mechanism through experiments and promising application.

Acknowledgment

We would like to thank all authors who submitted their work to this special issue.

*Xianwen Zhang
Xin Zhang
Baojuan Xi
Maofeng Zhang*

Review Article

Core-Shell Nanocatalysts Obtained in Reverse Micelles: Structural and Kinetic Aspects

Concha Tojo,¹ David Buceta,² and M. Arturo López-Quintela²

¹Physical Chemistry Department, University of Vigo, 36310 Vigo, Spain

²Laboratory of Magnetism and Nanotechnology, University of Santiago de Compostela, 15782 Santiago de Compostela, Spain

Correspondence should be addressed to Concha Tojo; ctojo@uvigo.es

Received 15 May 2015; Accepted 15 September 2015

Academic Editor: Xianwen Zhang

Copyright © 2015 Concha Tojo et al. This is an open access article distributed under the Creative Commons Attribution License, which permits unrestricted use, distribution, and reproduction in any medium, provided the original work is properly cited.

Ability to control the metal arrangement in bimetallic nanocatalysts is the key to improving their catalytic activity. To investigate how metal distribution in nanostructures can be modified, we developed a computer simulation model on the synthesis of bimetallic nanoparticles obtained in microemulsions by a one-pot method. The calculations allow predicting the metal arrangement in nanoparticle under different experimental conditions. We present results for two couples of metals, Au/Pt ($\Delta\varepsilon = 0.26$ V) and Au/Ag ($\Delta\varepsilon = 0.19$ V), but conclusions can be generalized to other bimetallic pairs with similar difference in standard reduction potentials. It was proved that both surface and interior compositions can be controlled at nanometer resolution easily by changing the initial reactant concentration inside micelles. Kinetic analysis demonstrates that the confinement of reactants inside micelles has a strong effect on the reaction rates of the metal precursors. As a result, the final nanocatalyst shows a more mixed core and a better defined shell as concentration is higher.

1. Introduction

The development of new improved nanocatalysts has attracted extensive research due to scientific and technological interest [1–3]. Special attention was paid to core-shell bimetallic nanoparticles. The presence of an additional metal in bimetallic nanoparticles leads to different properties from monometallic ones. Such particles not only maximize the catalytic surface due to a high surface-to-volume ratio, but also enhance catalytic properties in comparison to monometallic nanoparticles even at lower temperatures [4, 5]. Specifically, the catalytic behaviour of monolayers of one metal on another metal was shown to be definitely different compared to those of the parent metals [6]. It was shown that the formation of a bond between two different metals on a surface induces an electronic transfer towards the metal with more empty states in the valence band. This implies that the heteronuclear metal-metal bond depends on the geometry of the bimetallic particle [7], which in turn strongly affects catalytic activity. As an example, the catalytic activity of Au/Pt particles was shown to be directly related to

surface composition [8]. Therefore, the ability to control the metal arrangement in bimetallic nanoparticles is the key to improving the catalytic activity.

In spite of existing several successful strategies to obtain core-shell bimetallic nanoparticles, the control of the metals arrangement is still an open question [8–11]. Moreover, the metal distribution in a bimetallic nanoparticle depends not only on the particular couple of metals but also on the preparation method [12, 13]. So we will focus our attention on one particular route to prepare bimetallic nanoparticles, the precipitation of nanoparticles inside the droplets of a microemulsion [9, 10, 14, 15]. A water in oil (w/o) microemulsion consists of water droplets dispersed in the oil phase and stabilized interfacially by a surfactant monolayer [16, 17]. Reactants (metal precursors and reducing agent) are solved inside the water droplets. Mixing of two or more microemulsions (each containing one of the reactants) can result in the formation of monodisperse metal particles inside these aqueous nanoreactors. The reacting species are believed to be exchanged between water droplets during interdroplet collision, which can be able to open a channel for mass

transfer [14, 18]. Microemulsion micelles are ideal templates because each droplet can isolate a particle from those in neighboring droplets. In this way, particle aggregation is prevented, so this method allows a precise control over the composition and size of the final nanoparticles. In the case of bimetallic nanoparticles, the reacting species are two different metal precursors and a reducing agent, initially located in different microemulsion droplets. Due to collisions and material interdroplet exchange, both chemical reductions can take place inside the same water pool, resulting in a bimetallic nanoparticle which remains confined in the micelle. Nanoparticles composed of different couples of metals have been prepared by this method [19–22]. Nevertheless, even using microemulsions, there are a high number of variables controlling the final arrangement of the two metals in the nanoparticle. In order to optimize the metal distribution in a bimetallic nanocatalyst, a deeper understanding of the mechanism of nanoparticle formation in microemulsions is needed. We have developed a Monte Carlo simulation model, which predicts the metal distribution in the bimetallic particle and allowed us to study nanoparticle formation from a kinetic point of view. The validity of the model predictions was proved by comparison between experimental and simulation results [23]. The metal arrangement of Au/Pt nanoparticles prepared in a 75% isooctane/20% tergitol/5% water microemulsion was studied by HR-STEM (scanning transmission electron microscopy) and cross section with EDX analysis was performed to get their nanostructure. Theoretical STEM profiles were calculated from the structures predicted by simulation, using the same synthesis conditions compared to those of experimental studies. A successful concordance between simulated and experimental STEM profiles supports the validity of the simulation model.

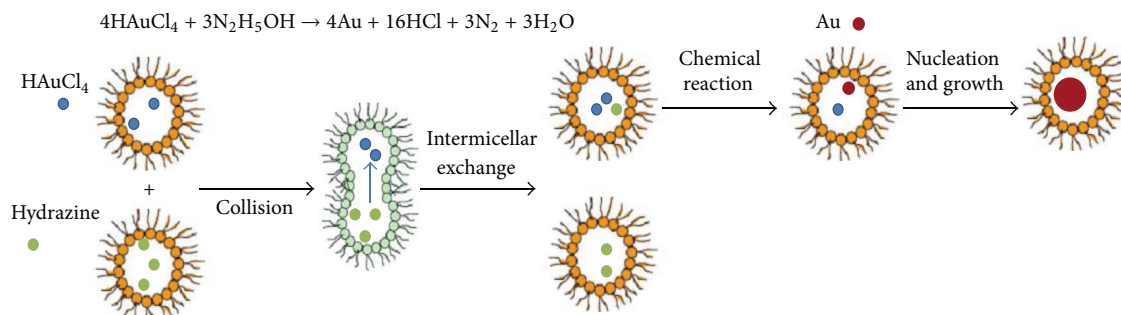
For a better understanding of the metals arrangement in a bimetallic nanocatalyst, one must take into account that a nanoparticle is formed from a nucleus, which can grow by building up new layers as new atoms are deposited on the previous ones. If there are two different metal atoms in the reaction medium, the metal distribution in final particle will be defined by the sequence of deposition of the two metals. The long term objective of the present study is implementing the know-how in the preparation of bimetallic nanoparticles in microemulsions. Such a challenge aim can only be reached if the factors affecting the sequence of metals are analyzed.

First, it is well-known that this sequence is conditioned by the rates of chemical reduction of the two metal ions. If ions of two different metals are very close to each other (as inside a water pool), and one metal reduces faster than the other, the sequence of deposition will be first the faster metal and then the slower one. So the resulting distribution will be a core-shell structure. On the contrary, a mix of metals is expected when both ions are reduced simultaneously. Therefore, at first, the key factor to decide what structure should be (core-shell or mix) is the difference in reduction potentials of both metals [1, 24–26]. Nevertheless, it is not the only factor, because core-shell geometries have been obtained from metals with quite similar reduction potential, such as Pt/Ag [27, 28], Pd/Au [29], and Pt/Pd [19, 20, 30–32].

Second, the order of metals deposition is also affected by the nucleation rate of each metal [33, 34]. This is based on the fact that clustering used to take a longer time than reduction [35], so the chemical reduction is usually considered as instantaneous. In this case, the subsequent nucleation process would be the major factor to determine the order of metals. Consequently, the majority of seeds from which nanoparticles are formed will be composed of the metal with the fastest nucleation. The growth of these seeds will lead to a monometallic core. The slower metal would be deposited on the core forming the surrounding shell. This argument was used to explain Pd-Pt bimetallic nanocluster structures [20, 21, 36].

Also relevant to the discussion is the observation that the last two factors, reduction rate and nucleation rate, are characteristics of the particular couple of metals. That is, if one wants to prepare a bimetallic nanoparticle composed of two specific metals, the reduction potentials and the critical nucleus sizes cannot be modified. However, both processes (reduction and nucleation) can be altered by changing the values of reactants concentration. Therefore, a third factor affecting the sequence of metals can be concentration, which is easily modified.

Finally, one must keep in mind that micelles are demonstrated to be a reaction medium that does not always obey classical assumptions. As an example, it was proved that the usual definition of pH cannot be employed inside micelles [37]. So chemical kinetics in micelles must take into account the compartmentalization of the reaction media [38]. Although the fact that reactants are trapped into micelles plays a key role in metal arrangement in bimetallic nanoparticles, studies in this direction are limited. In the research at hand, a comprehensive analysis of the resulting nanostructures is performed, based on the hypothesis that metal arrangement is due to the particular combination of three main factors: the difference in reduction rate of both metals (characteristic of the pair of metals), the intermicellar exchange rate (determined by microemulsion composition), and the amount of metal precursors inside micelles. All together give rise to a particular order of metals deposition, which in turn determines the metal distribution in final nanoparticle. To investigate how metal distribution in the nanostructure can be easily modified by changing reactant concentration, two couples of metals were chosen, and microemulsion composition was kept unvariable. Because of their high catalytic activity the nanocatalysts chosen for the study were Au/Pt [12, 13, 39–42] and Au/Ag [43–46]. The couple of the metals was characterized by the ratio between the reduction rates of the fast and the slow metal. The structure of Au/Pt nanoparticles (difference in standard reduction potentials $\Delta\varepsilon = 0.26$ V) was shown to be successfully reproduced by simulation by means of reduction rates ratio $v_{\text{Au}}/v_{\text{Pt}} \approx 10$ [23]. By means of the Volmer equation, a smaller difference in standard reduction potentials such as Au/Ag system ($\Delta\varepsilon \approx 0.19$ V) can be simulated by a reduction rate ratio $v_{\text{Au}}/v_{\text{Ag}} \approx 5$. Because the reduction rate ratio is the simulation parameter used to characterize the nature of the metals, all results can be generalized to other bimetallic systems whose difference in standard reduction potentials is about this range.



SCHEME 1: Scheme of nanoparticle formation inside microemulsion droplets.

2. Simulation Model

The kinetic course of the reaction is simulated as follows (see [47] for details): the microemulsion is described as a set of micelles, which move and collide with each other. Initially, each kind of reactant is located in one microemulsion. The reactants are the metal salts (HAuCl_4 and H_2PtCl_6 to prepare Au/Pt, or HAuCl_4 and AgNO_3 to prepare Au/Ag) and the reductor agent hydrazine. The concentration of reactants can be modified by varying the concentration of the water phase for each microemulsion. To study the influence of concentration we present results using different average values of the number of reactants inside the droplets, keeping a 1:1 proportion: $\langle c_{\text{Au salt}} \rangle = \langle c_{\text{Pt or Ag salt}} \rangle = 4, 32, 64,$ and 128 metal ions in a droplet, which corresponds to 0.02 M, 0.16 M, 0.40 M, and 0.64 M, respectively. Then microemulsions, each one containing one reactant, are mixed.

The diffusion of micelles is assumed to be governed by Brownian motion. Upon collision micelles can establish a water channel forming a transient dimer, exchanging their contents (reactants, products, and/or growing particles). In each step, 10% of micelles are randomly chosen to collide, fuse, and redisperse, allowing material exchange (see Scheme 1). One Monte Carlo step (mcs) is completed when the composition of colliding droplets is revised after collision according to the criteria described below.

The intermicellar exchange protocol of free units (reactants and nonaggregated metal atoms) consists in their redistribution between two colliding droplets in accordance with the concentration gradient principle: reactants and free metal atoms are transferred from the more to the less occupied droplet. The exchange parameter (k_{ex}) quantifies the maximum amount of reactants (metal precursors and/or reductor agent) and metallic atoms which can be transferred during a collision. When collision takes place between two micelles containing different kind of reactants, redistribution of material can lead to one metal precursor and the reductor being located inside the same micelle. At this stage, chemical reduction can take place. Model assumes that chemical reduction of Au precursor is instantaneous (100% of HAuCl_4 inside the same micelle is reduced); that is, reaction is completed, and only Au atoms and excess of reactants (either Au salt and/or hydrazine) are to be distributed in daughter micelles. This implies that reactants Au salt and hydrazine will

not exist together in a micelle. To take into account different reductions rates, the probability that reactants are trapped together in the same micelle which reduce to metal atoms can be diminished. To simulate the Au/Pt synthesis only 10% of H_2PtCl_6 is reduced in each collision ($v_{\text{Au}}/v_{\text{Pt}} = 10$). In the case of Au/Ag, 20% of the pairs AgNO_3 and hydrazine available in the micelle produce Ag atoms ($v_{\text{Au}}/v_{\text{Ag}} = 5$). The rest of metal salt and reducing agent remain in the micelle and will be exchanged or will react in a posterior collision. All atoms produced in each micelle are considered to be aggregated forming a growing nanoparticle. As the synthesis advances, more micelles carry reactants and particles simultaneously. If one colliding droplet is carrying a particle, the reaction always proceeds on it, acting as nucleation point. When both colliding micelles contain particles, reaction takes place in the micelle containing the larger one, which has a larger surface, increasing the probability of playing as catalyst.

The intermicellar exchange protocol of growing particles is limited by the size of the channel through which colliding micelles exchange their content, which is determined by the flexibility of the surfactant film. The flexibility parameter (f) specifies the maximum particle size for transfer between micelles. The exchange criteria of particles are also dictated by Ostwald ripening, which assumes that the largest particles will grow by condensation of material, coming from the smallest particles that solubilise more readily than larger ones. Therefore, if both colliding micelles contain particle, the smaller one is transferred to the micelle carrying the larger one, whenever the channel size would be large enough.

Despite their simplicity, material intermicellar exchange protocols allow us to simulate the surfactant film flexibility. At first, the requirements for material intermicellar exchange to take place are that colliding micelles must remain long enough together, and the size of the channel connecting both micelles must be large enough. It can be assumed that the main factor determining the exchange of isolated species (reactants and free metals) is the dimer stability, because they traverse the intermicellar channel one by one. That is, more species can be exchanged when the two micelles stay together longer (higher dimer stability), and channel size would not be relevant. Based on this, k_{ex} is related to the dimer stability. On the contrary, the channel size becomes decisive when the transferred material is a particle constituted by aggregation of metal atoms, which have to be exchanged as a whole. As a

consequence, this kind of material exchange will be restricted by the intermicellar channel size (f parameter). From this picture, the flexibility of the surfactant film is included in the simulation model by means of k_{ex} (dimer stability) and f (intermicellar channel size) parameters [48]. Good agreement between simulation and experimental results was obtained when a rigid film, such as AOT (dioctyl sodium sulfosuccinate)/n-heptane/water microemulsion, was related to a channel size $f = 5$, associated with $k_{\text{ex}} = 1$ free atom exchanged during a collision [49]. In case of flexible film, both factors have to rise together. In this study we present results obtained using a more flexible microemulsion, such as isooctane/tergitol/water, which was successful compared to simulation data using $f = 30$, $k_{\text{ex}} = 5$ [23].

Each simulation run ends when the contents of each micelle remain invariable; that is, all metal salts were reduced and no material intermicellar exchange is taking place. It results in a set of micelles, each one of which can contain one particle. The metal distribution in the final particle is defined by the order with which the two metals are deposited on particle surface. Therefore, in order to study the particle composition, the sequence of the two metals in each micelle is monitored as a function on time.

The metals in each nanoparticle are assumed to take a spherical arrangement. Each nanoparticle sequence is divided in ten concentric layers, and the dispersity and averaged composition (% Au) are calculated layer by layer. Finally results are averaged over 1000 runs. The composition (% Au) of each layer is showed by a colour grading: the degradation goes from blue (0%–10% of fast metal Au) to red (90%–100% Au). Grey means a 50% of each metal. A lighter colour indicates a higher proportion of pure metal in the layer. The resulting structures are represented as histograms, in which the number of particles with a given % Au is monitored layer by layer. In this way the layer composition can be observed from the core (inner layer) to the shell (outer layer). It allows us to study how the metal arrangement changes as the synthesis advances. Likewise, the nanoparticle composition is also described by means of concentric spheres. The thickness of each sphere is proportional to the number of layers with a given % Au, keeping the same colour code.

3. Results and Discussion

3.1. Changing the Metal Salt Concentration: Structural Study on Metals Distribution in Final Nanoparticle. First of all, we will study the metal distribution in final nanoparticle for two different values of the reduction rates ratio of the two metals. To isolate this dependence, the microemulsion composition (characterized by $f = 30$, $k_{\text{ex}} = 5$) and the nucleation rates of both metals ($n_{\text{Au}}^* = n_{\text{Ag}}^* = n_{\text{Pt}}^* = 1$) must be kept constant. Figure 1 shows the predicted structures. In these figures, the reduction rate of the fast metal (Au) is considered instantaneous: that is, 100% Au salts inside the same micelle give rise to Au. The reduction rate of the slower metal (Pt or Ag) is decreased from $v_{\text{Au}}/v_{\text{Ag}} = 5$ (20% Ag salts react in each Monte Carlo step; see first column in Figure 1) to $v_{\text{Au}}/v_{\text{Pt}} = 10$ (10% Pt salts react; see second column in Figure 1). Each file

in Figure 1 shows results for different values of initial metal salts concentration.

Figure 1(a) shows the nanostructure obtained using a small difference in reduction rates and a low concentration ($v_{\text{Au}}/v_{\text{Pt}} = 5$, $\langle c \rangle = 4$ reactants per micelle). One can see that the composition of the inner layers (core) is enriched in the faster reduction metal (Au, see red bar on the left). By observing from the inner to the outer layers, the composition of the surrounded layers evolves to a mix of the two metals as the synthesis advances. At the end of the process, most of the particles have a shell which is composed of approximately 50% in each metal. When the reduction rate ratio is larger (see Figure 1(b), $v_{\text{Au}}/v_{\text{Pt}} = 10$, $\langle c \rangle = 4$), more Au is mainly located in the core, and the surrounding shells show a slight enrichment in the slower metal. It was shown that a further increase in $v_{\text{fast}}/v_{\text{slow}}$ gives rise to better segregated metals [22, 25, 26]. In contrast, a further decrease in reduction rate ratios leads to more mixed structures, so an alloy was obtained for equal reduction rates ($v_{\text{fast}}/v_{\text{slow}} = 1$) [25]. From these results, one could think that the ratios between both reduction rates $v_{\text{fast}}/v_{\text{slow}} = 5, 10$ are not large enough to give rise to a core-shell distribution. However, if concentration is increased (keeping constant the reduction rate ratio) the metal distribution changes drastically: most of the particles show an Au core, surrounded by mixed middle layers, finally covered by a slow metal-shell (see blue bar on the right in Figure 1). Two main features must be pointed out from this figure: First, independently of reactants concentration, the metal segregation is better as the reduction rate ratio is larger (see Figure 1, from left to right), as expected. Second, nanostructure can be modified by a change in concentration, as experimentally observed [23]. To provide a deeper insight into the influence of the initial reactant concentration on metal distribution, histograms in Figure 1 must be compared from the top to the bottom. The first column in Figure 1 clearly shows how, in spite of the small difference in chemical reduction rate ratio, the metal segregation is enhanced by high reactant concentration: from an Au-enriched core covered by an alloyed shell obtained at small concentration (see Figure 1(a), $\langle c \rangle = 4$ metal ions in a micelle) to the incipient formation of a shell at higher concentration (see Figure 1(c), $\langle c \rangle = 32$), which evolves to a better defined shell when concentration is increased (see blue bars on the right in Figure 1(e), $\langle c \rangle = 128$). The same qualitative behaviour is obtained at larger reduction rate ratio (see second column in Figure 1). One can conclude that the metal distribution in a bimetallic nanoparticle can be modified at nanometer resolution just by changing the reactants concentration. This is an unexpected result, which is supported by experimental observations [23]. It is well-known that the rate of a bimolecular reaction, such as reduction, increases with concentration. But the concentration of both metal salts was the same in all cases, so it may be expected that the influence of concentration on both reductions was similar. However, the analysis of the histograms proves that metal segregation in core-shell nanostructures depends on concentration. On the one hand, the shell is more pronounced at higher concentration. On the other hand, concerning the core, note that the larger the concentration, the larger the quantity of the slow metal

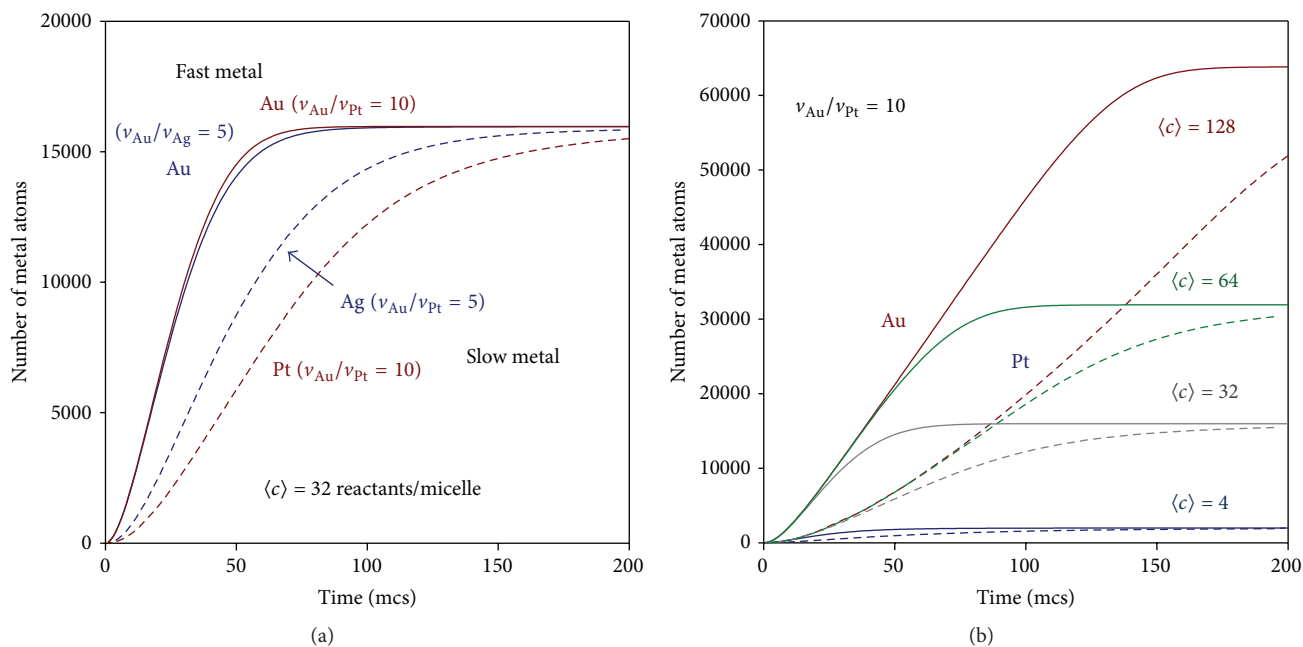


FIGURE 2: (a) Time evolution of the number of metal atoms obtained in micelles using different reduction rate ratio $v_{fast}/v_{slow} = 5, 10$. Continuous and discontinuous lines show the obtaining of fast (Au) and slow (Ag or Pt) metals, respectively. Synthesis conditions: flexible film ($k_{ex} = 5$, $f = 30$), average concentration $\langle c \rangle = 32$ metal salts in a micelle. Scheme colour: blue lines represent $v_{Au}/v_{Ag} = 5$; red lines represent $v_{Au}/v_{Pt} = 10$. (b) Number of metal atoms obtained in micelles versus time using different concentration and keeping constant the reduction rate ratio $v_{Au}/v_{Pt} = 10$.

forming the inner layers. That is, larger concentrations lead to more mixed cores (see Figure 1, from the top to the bottom). This would mean that the slow metal will be more accelerated by concentration compared to the faster one. Understanding this behaviour is not obvious. One must take into account that reverse micelles are demonstrated to be reaction medium that does not always obey classical assumptions. The dynamic properties of the microemulsion, which facilitates their use as confined reaction media, play a key role in the chemical kinetics. With the aim of explaining this unpredicted evolution of metal distribution in the nanostructure, a deeper kinetic study is explained below.

3.2. Changing the Metal Salt Concentration: Kinetic Study.

The whole speed at which nanoparticle is built up depends not only on the chemical reduction rates but also on the intermicellar exchange rate and concentration. The final nanoparticle was proven to be due to the particular combination of these three factors, which in turn determine the particular sequence of deposition of the two metals on the growing particle [38]. The simulation model allows us to monitor the number of metal atoms produced in all micelles as the synthesis advances. Continuous lines in Figure 2(a) represent the number of faster atoms (Au) and discontinuous lines correspond to slower ones (Ag, $v_{Au}/v_{Ag} = 5$ or Pt, $v_{Au}/v_{Pt} = 10$). These data were obtained keeping fixed concentration ($\langle c \rangle = 32$ atoms/micelle), that is, the synthesis conditions shown in Figures 1(c) and 1(d). The reduction rate ratios $v_{Au}/v_{Ag} = 5$ and $v_{Au}/v_{Pt} = 10$ are showed in blue and red, respectively. A plateau is reached when the reactants

have been exhausted. As expected, the slower reduced metal is produced later (see discontinuous lines). Fast and slow curves appear more separately as the second metal reduction rate is slowing down (compare blue and red lines). Concerning the influence of concentration on the curves, Figure 2(b) shows the results obtained at different initial concentrations for a reduction rate ratio $v_{Au}/v_{Pt} = 10$. As before, the quantities of Au and Pt produced at different concentrations as the synthesis advances are showed by continuous and discontinuous lines, respectively. One can observe that all Au curves have the same slope, except that concentration was very low. In this case, the reactant concentration appears to be the controlling factor, as expected. On the contrary, higher concentration does not result in a faster rate because the controlling step is the intermicellar exchange rate [47]. These data were obtained using an exchange parameter $k_{ex} = 5$, so only 5 molecules can be exchanged between micelles during each collision. That is, although the number of metal salts in one micelle was higher (e.g., $\langle c \rangle = 32$ atoms/micelle), only a maximum of 5 Au salts can be transferred in a collision. This implies that a maximum of 5 Au atoms can be produced if there is enough reducing agent located in the micelle. This restriction also governs the exchange of slow metal salts, but, in this case, only 10% of the pairs of Pt salt and reducing agent carried by the same micelle react. The remaining reactants stay in the micelle, resulting in a local accumulation due to cage-like effect. Previous studies suggest that micelle plays as a cage [37, 47, 50]. The hypothesis is that reactants located inside the same micelle can fail to react the first time, but they have more opportunities as long as they remain in the same

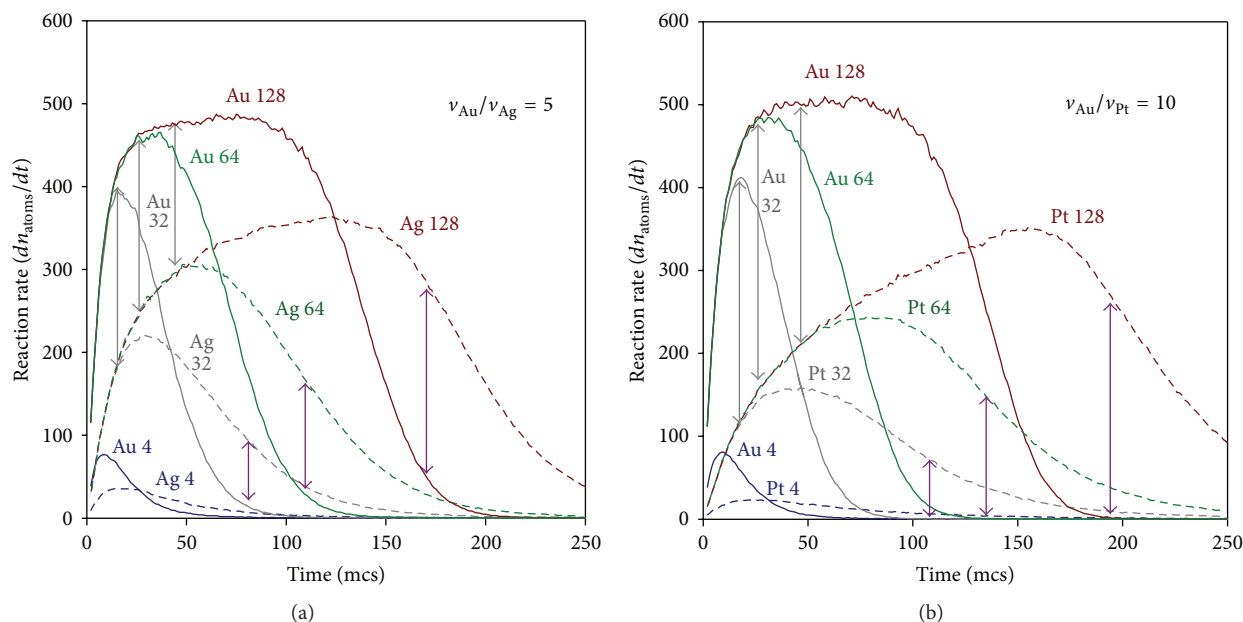


FIGURE 3: (a) Reaction rate versus time obtained using different reduction rate ratio: (a) $v_{\text{Au}}/v_{\text{Ag}} = 5$ and (b) $v_{\text{Au}}/v_{\text{Pt}} = 10$, and different average concentration in a micelle. Continuous and discontinuous lines show the obtaining of fast (Au) and slow (Ag or Pt) metals, respectively. Synthesis conditions: flexible film ($k_{\text{ex}} = 5$, $f = 30$). Scheme colour: $\langle c \rangle = 4, 32, 64$, and 128 metal salts in a micelle are represented by blue, grey, green, and red lines, respectively.

micelle. Consequently, the chemical reduction can continue independently from a new intermicellar collision. In this way micelles allow for less encounters between reactants than continuous reaction media, but reactants confined in micelles remain near each other for much longer. As a result, slower metal reaction rate increases due to a cage-like effect.

The cage effect in micelles can be proved by calculating the overall reaction rate of each metal from the slopes of the curves showed in Figure 2. The overall reaction rate, estimated as dn_{atom}/dt , takes into account not only the chemical reduction rate but also the material intermicellar exchange rate. The calculated Au and Pt reaction rates are showed in Figure 3 as continuous and discontinuous lines, respectively, keeping the same scheme color compared to that used in Figure 2(b). All curves show a maximum, from which the usual decay is obtained. The growing rate before the maximum is due to the reactants redistribution between micelles, because only when the metal salt and the reducing agent are carried by the same micelle, chemical reduction can take place. That is, as the reactants are redistributed, more intermicellar collisions can result in chemical reaction, so reaction rate increases. After the maximum, the usual decay versus time can be observed as reactants have been consumed. In spite of the similarities, the fast and the slow metals show different behaviour. In relation to Au, the fact that reactants are trapped inside micelles causes the Au reduction to be mainly controlled by the intermicellar exchange rate. This is reflected in the slopes of Au curves, which are equal before and after the peak for all concentration values and reduction rate ratios (see continuous lines in Figure 2). That is, Au reaction rate steadily increases while material has been exchanged between micelles and steadily

decreases while there are Au salts. When concentration is high enough, Au reaction rate reaches a threshold dictated by the intermicellar exchange rate from which it cannot increase anymore (see continuous red line). At this stage, Au reaction rate remains constant as long as the quantity of Au precursor is enough. It implies that the intuitive idea that larger concentration always gives rise to a faster reduction rate was proved to be not always true in reverse micelle [47]. Note that intermicellar control cannot be reached at low concentration because precursor salt is exhausted earlier.

Concerning slow metal reaction rates (see discontinuous lines in Figure 2), one could expect a behaviour similar to Au rate, because exchange restrictions are the same for both metals. Indeed, before the peak, the only effect of increasing concentration on the slow reaction is the obtaining of higher and later maxima. The maximum is higher because high concentration results in faster reaction rate, which is reached later because of intermicellar exchange restrictions. Nevertheless, the speed at which the slow rate falls after the peak is strongly dependent on concentration, contrary to Au reaction rate. This unexpected result can be explained by the effect of confinement on both metals: in relation to the faster metal, once the intermicellar exchange allows the location of both reactants enclosed in the same micelle, the reaction is very quick. But in the case of a slow reduction, the reactants which fail to react the first time remain in the micelle, so they will be close together for longer. They can react later, regardless of whether or not an intermicellar exchange takes place. It results in a faster slow reaction rate due to cage-like effect. It is important to point out that the fast reduction is not affected by the cage effect, because no reactants accumulation takes place. On the contrary, slow

rate depends on the exchange rate (as the Au case) and, in addition, depends on the accumulation of reactants, which will be higher as concentration is higher. Given that cage effect accelerates the slow reaction, it also results in a quicker decay of the slow reaction rate as observed in Figure 3.

3.3. Chemical Kinetics and Metal Distribution. The reaction rate profiles allow us to understand the influence of concentration and reduction rate ratio on resulting metal distribution in bimetallic nanostructures. The gap between the faster and the smaller reaction rates at the initial stages of the synthesis, when the core is building up, is shown by the grey arrows in Figure 3. Because the time required to reach equilibrium depends on concentration and reduction rate ratios, grey arrows are located at the stage at which 20% of total metal atoms have been deposited (the core is completed), for comparison purposes. The fact that the length of grey arrows is shorter as concentration is larger is directly related to metal distribution in the core: the shorter the gap, the smaller the difference between the reaction rates of the two metals, so the core is more mixed, as shown in Figure 1. That is, the high degree of mixture in the core observed at high concentrations is accounted for the acceleration of slow metal rate. In each pair of curves the factors affecting the rate (concentration, reduction rate ratio, and intermicellar exchange rate) are kept fixed, so the slow metal acceleration can be associated with the cage effect, which is more pronounced as concentration increases. By comparing Figures 3(a) and 3(b), one can observe that the gap is larger when $v_{\text{fast}}/v_{\text{slow}}$ ratio is higher, as expected. It results in a larger Au-enrichment in core, as observed in the structures shown in Figure 1.

Finally, the formation of the shell can also be explained on the basis of the differences between both rates. Pink arrows in Figure 3 show the gap between the faster and slower metals rates at later stages of the synthesis (90% of the total metals were deposited), that is, when the shell is forming. As expected, a larger $v_{\text{fast}}/v_{\text{slow}}$ ratio gives rise to a larger gap, directly related to better separated shell. Likewise, the fact that shell is better defined at high concentration is also accounted for by the increasing gap between both rates as concentration increases. A priori, one could think that the slow metal enriched shell, enhanced by higher concentration, is contrary to the acceleration caused by cage effect. Although slow metal acceleration favours earlier deposition, a high concentration also means that the available quantity of slow metal at later stage of the synthesis is higher. This delay in slow metal reduction determines the pure shell formation observed at high concentration (see Figure 1).

These results can be extended to oil in water micelles (e.g., in the preparation of hydrophobic particles solved inside micelles) because the main cause of the cage effect is the confinement of reactants inside micelles, which takes place independently of the kind of micelle.

4. Conclusions

The fact that reactants are trapped into micelles plays a key role in metal arrangement in bimetallic nanocatalysts,

because it affects the metals reduction in different ways. On the one hand, the intermicellar exchange rate is the controlling step of the fast metal reaction. On the other hand, slow metal reduction is also affected by the cage effect, which is more pronounced as concentration increases. It is reflected in the metal distribution of the nanocatalyst, which shows a more mixed core and a better defined shell as concentration is higher.

In summary, the surface composition of bimetallic nanocatalysts can be fine-tuned by choosing the adequate components of the microemulsion and reactant concentration. For a given couple of metals in a fixed microemulsion, the metal distribution of the final nanoparticle can be manipulated by changing the reactant concentration.

Conflict of Interests

The authors have no conflict of interests.

Acknowledgments

Works were supported by Ministerio de Ciencia e Innovación, Spain (MAT2012-36754-C02-01), and Xunta de Galicia (GRC2013-044, FEDER Funds, REDES 2014/019).

References

- [1] R. Ferrando, J. Jellinek, and R. L. Johnston, "Nanoalloys: from theory to applications of alloy clusters and nanoparticles," *Chemical Reviews*, vol. 108, no. 3, pp. 845–910, 2008.
- [2] S. Sun, C. B. Murray, D. Weller, L. Folks, and A. Moser, "Monodisperse FePt nanoparticles and ferromagnetic FePt nanocrystal superlattices," *Science*, vol. 287, no. 5460, pp. 1989–1992, 2000.
- [3] A. Habrioux, W. Vogel, M. Guinel et al., "Structural and electrochemical studies of Au-Pt nanoalloys," *Physical Chemistry Chemical Physics*, vol. 11, no. 18, pp. 3573–3579, 2009.
- [4] P. Hernández-Fernández, S. Rojas, P. Ocón et al., "Influence of the preparation route of bimetallic Pt-Au nanoparticle electrocatalysts for the oxygen reduction reaction," *The Journal of Physical Chemistry C*, vol. 111, no. 7, pp. 2913–2923, 2007.
- [5] M. Boutonnet, S. Lögdberg, and E. E. Svensson, "Recent developments in the application of nanoparticles prepared from w/o microemulsions in heterogeneous catalysis," *Current Opinion in Colloid and Interface Science*, vol. 13, no. 4, pp. 270–286, 2008.
- [6] J. R. Kitchin, J. K. Nørskov, M. A. Barteau, and J. G. Chen, "Role of strain and ligand effects in the modification of the electronic and chemical properties of bimetallic surfaces," *Physical Review Letters*, vol. 93, no. 15, pp. 156801–156804, 2004.
- [7] J. A. Rodriguez and D. W. Goodman, "The nature of the metal-metal bond in bimetallic surfaces," *Science*, vol. 257, no. 5072, pp. 897–903, 1992.
- [8] J. Suntivich, Z. Xu, C. E. Carlton et al., "Surface composition tuning of Au-Pt bimetallic nanoparticles for enhanced carbon monoxide and methanol electro-oxidation," *Journal of the American Chemical Society*, vol. 135, no. 21, pp. 7985–7991, 2013.
- [9] R. Y. Parapat, V. Parwoto, M. Schwarze, B. Zhang, D. S. Su, and R. Schomäcker, "A new method to synthesize very active and stable supported metal Pt catalysts: thermo-destabilization of

- microemulsions,” *Journal of Materials Chemistry*, vol. 22, no. 23, pp. 11605–11614, 2012.
- [10] Z. Yin, D. Ma, and X. Bao, “Emulsion-assisted synthesis of monodisperse binary metal nanoparticles,” *Chemical Communications*, vol. 46, no. 8, pp. 1344–1346, 2010.
- [11] E. Westsson and G. J. M. Koper, “How to determine the core-shell nature in bimetallic catalyst particles?” *Catalysts*, vol. 4, no. 4, pp. 375–396, 2014.
- [12] H. Zhang and N. Toshima, “Synthesis of Au/Pt bimetallic nanoparticles with a Pt-rich shell and their high catalytic activities for aerobic glucose oxidation,” *Journal of Colloid and Interface Science*, vol. 394, pp. 166–176, 2013.
- [13] H.-P. Liang, T. G. J. Jones, N. S. Lawrence, L. Jiang, and J. S. Barnard, “Understanding the role of nanoparticle synthesis on their underlying electrocatalytic activity,” *Journal of Physical Chemistry C*, vol. 112, no. 11, pp. 4327–4332, 2008.
- [14] M. A. López-Quintela, C. Tojo, M. C. Blanco, L. García Rio, and J. R. Leis, “Microemulsion dynamics and reactions in microemulsions,” *Current Opinion in Colloid and Interface Science*, vol. 9, no. 3–4, pp. 264–278, 2004.
- [15] M.-P. Pileni, “The role of soft colloidal templates in controlling the size and shape of inorganic nanocrystals,” *Nature Materials*, vol. 2, no. 3, pp. 145–150, 2003.
- [16] P. D. I. Fletcher, A. M. Howe, and B. H. Robinson, “The kinetics of solubilisation exchange between water droplets of a water-in-oil microemulsion,” *Journal of the Chemical Society, Faraday Transactions*, vol. 83, pp. 985–1006, 1987.
- [17] K. Holmberg, “Surfactant-templated nanomaterials synthesis,” *Journal of Colloid and Interface Science*, vol. 274, no. 2, pp. 355–364, 2004.
- [18] P. D. I. Fletcher, B. H. Robinson, F. Bermejo-Barrera, and D. G. Oakenfull, *Microemulsions*, Plenum Press, New York, NY, USA, 1982.
- [19] R. Touroude, P. Girard, G. Maire, J. Kizling, M. Boutonnet-Kizling, and P. Stenius, “Preparation of colloidal platinum/palladium alloy particles from non-ionic microemulsions: characterization and catalytic behaviour,” *Colloids and Surfaces A*, vol. 67, pp. 9–19, 1992.
- [20] M. Yashima, L. K. L. Falk, A. E. C. Palmqvist, and K. Holmberg, “Structure and catalytic properties of nanosized alumina supported platinum and palladium particles synthesized by reaction in microemulsion,” *Journal of Colloid and Interface Science*, vol. 268, no. 2, pp. 348–356, 2003.
- [21] C.-H. Chen, B.-J. Hwang, G.-R. Wang et al., “Nucleation and growth mechanism of Pd/Pt bimetallic clusters in sodium Bis(2-ethylhexyl)sulfosuccinate (AOT) reverse micelles as studied by in situ x-ray absorption spectroscopy,” *Journal of Physical Chemistry B*, vol. 109, no. 46, pp. 21566–21575, 2005.
- [22] L. M. Magno, W. Sigle, P. A. Van Aken, D. G. Angelescu, and C. Stubenrauch, “Microemulsions as reaction media for the synthesis of bimetallic nanoparticles: size and composition of particles,” *Chemistry of Materials*, vol. 22, no. 23, pp. 6263–6271, 2010.
- [23] D. Buceta, C. Tojo, M. Vukmirovik, F. L. Deepak, and M. A. López-Quintela, “Controlling bimetallic nanostructures by the microemulsion method with sub-nanometer resolution using a prediction model,” *Langmuir*, vol. 31, no. 27, pp. 7435–7439, 2015.
- [24] J. Feng and C.-P. Zhang, “Preparation of Cu-Ni alloy nanocrystallites in water-in-oil microemulsions,” *Journal of Colloid and Interface Science*, vol. 293, no. 2, pp. 414–420, 2006.
- [25] C. Tojo, M. de Dios, and M. A. López-Quintela, “On the structure of bimetallic nanoparticles synthesized in microemulsions,” *Journal of Physical Chemistry C*, vol. 113, no. 44, pp. 19145–19154, 2009.
- [26] D. G. Angelescu, L. M. Magno, and C. Stubenrauch, “Monte Carlo simulation of the size and composition of bimetallic nanoparticles synthesized in water in oil microemulsions,” *The Journal of Physical Chemistry C*, vol. 114, no. 50, pp. 22069–22078, 2010.
- [27] S. Schwamborn, L. Stoica, and W. Schuhmann, “Activation/inhibition effects during the coelectrodeposition of PtAg nanoparticles: application for ORR in alkaline media,” *ChemPhysChem*, vol. 12, no. 9, pp. 1741–1746, 2011.
- [28] E. V. Abkhalimov and B. G. Ershov, “Pt_{core}Ag_{shell} nanoparticle-catalyzed reduction of methylviologene with hydrogen in aqueous solution,” *Colloid Journal*, vol. 72, no. 4, pp. 441–445, 2010.
- [29] F. L. Deepak, G. Casillas-Garcia, R. Esparza, H. Barron, and M. Jose-Yacaman, “New insights into the structure of PdAu nanoparticles as revealed by aberration-corrected STEM,” *Journal of Crystal Growth*, vol. 325, no. 1, pp. 60–67, 2011.
- [30] T. Yonezawa and N. Toshima, “Mechanistic consideration of formation of polymer-protected nanoscopic bimetallic clusters,” *Journal of the Chemical Society, Faraday Transactions*, vol. 91, no. 22, pp. 4111–4119, 1995.
- [31] N. V. Long, T. D. Hien, T. Asaka, M. Ohtaki, and M. Nogami, “Synthesis and characterization of Pt-Pd alloy and core-shell bimetallic nanoparticles for direct methanol fuel cells (DMFCs): enhanced electrocatalytic properties of well-shaped core-shell morphologies and nanostructures,” *International Journal of Hydrogen Energy*, vol. 36, no. 14, pp. 8478–8491, 2011.
- [32] F. Tao, M. E. Grass, Y. Zhang et al., “Evolution of structure and chemistry of bimetallic nanoparticle catalysts under reaction conditions,” *Journal of the American Chemical Society*, vol. 132, no. 25, pp. 8697–8703, 2010.
- [33] F. Barroso and C. Tojo, “Modelling of nano-alloying and structural evolution of bimetallic core-shell nanoparticles obtained via the microemulsion route,” *Journal of Colloid and Interface Science*, vol. 363, no. 1, pp. 73–83, 2011.
- [34] F. Barroso and C. Tojo, “Designing bimetallic nanoparticle structures prepared from microemulsions,” *Journal of Physical Chemistry C*, vol. 117, no. 34, pp. 17801–17813, 2013.
- [35] J. Wang, H. F. M. Boelens, M. B. Thathagar, and G. Rothenberg, “In situ spectroscopic analysis of nanocluster formation,” *ChemPhysChem*, vol. 5, no. 1, pp. 93–98, 2004.
- [36] M.-L. Wu, D.-H. Chen, and T.-C. Huang, “Preparation of pd/pt bimetallic nanoparticles in water/AOT/isooctane microemulsions,” *Journal of Colloid and Interface Science*, vol. 243, no. 1, pp. 102–108, 2001.
- [37] O. F. Silva, M. A. Fernández, J. J. Silber, R. H. de Rossi, and N. M. Correa, “Inhibited phenol ionization in reverse micelles: confinement effect at the nanometer scale,” *ChemPhysChem*, vol. 13, no. 1, pp. 124–130, 2012.
- [38] C. Tojo, E. González, and N. Vila-Romeu, “The impact of the confinement of reactants on the metal distribution in bimetallic nanoparticles synthesized in reverse micelles,” *Beilstein Journal of Nanotechnology*, vol. 5, pp. 1966–1979, 2014.
- [39] P. Hernández-Fernández, S. Rojas, P. Ocón et al., “Influence of the preparation route of bimetallic Pt-Au nanoparticle electrocatalysts for the oxygen reduction reaction,” *Journal of Physical Chemistry C*, vol. 111, no. 7, pp. 2913–2923, 2007.

- [40] B. N. Wanjala, J. Luo, R. Loukrakpam et al., "Nanoscale alloying, phase-segregation, and core-shell evolution of gold-platinum nanoparticles and their electrocatalytic effect on oxygen reduction reaction," *Chemistry of Materials*, vol. 22, no. 14, pp. 4282–4294, 2010.
- [41] W. Zhang, L. Li, Y. Du, X. Wang, and P. Yang, "Gold/platinum bimetallic core/shell nanoparticles stabilized by a fréchet-type dendrimer: preparation and catalytic hydrogenations of phenylaldehydes and nitrobenzenes," *Catalysis Letters*, vol. 127, no. 3–4, pp. 429–436, 2009.
- [42] J. Luo, P. N. Njoki, Y. Lin, D. Mott, L. Wang, and C.-J. Zhong, "Characterization of carbon-supported AuPt nanoparticles for electrocatalytic methanol oxidation reaction," *Langmuir*, vol. 22, no. 6, pp. 2892–2898, 2006.
- [43] S. Tokonami, N. Morita, K. Takasaki, and N. Toshima, "Novel synthesis, structure, and oxidation catalysis of Ag/Au bimetallic nanoparticles," *Journal of Physical Chemistry C*, vol. 114, no. 23, pp. 10336–10341, 2010.
- [44] L. Feng, G. Gao, P. Huang et al., "Optical properties and catalytic activity of bimetallic gold-silver nanoparticles," *Nano Biomedicine and Engineering*, vol. 2, no. 4, pp. 258–267, 2010.
- [45] J. Santhanalakshmi and P. Venkatesan, "Mono and bimetallic nanoparticles of gold, silver and palladium-catalyzed NADH oxidation-coupled reduction of Eosin-Y," *Journal of Nanoparticle Research*, vol. 13, no. 2, pp. 479–490, 2011.
- [46] H. Zhang, J. Okuni, and N. Toshima, "One-pot synthesis of Ag-Au bimetallic nanoparticles with Au shell and their high catalytic activity for aerobic glucose oxidation," *Journal of Colloid and Interface Science*, vol. 354, no. 1, pp. 131–138, 2011.
- [47] C. Tojo, M. de Dios, D. Buceta, and M. A. López-Quintela, "Cage-like effect in Au-Pt nanoparticle synthesis in microemulsions: a simulation study," *Physical Chemistry Chemical Physics*, vol. 16, no. 36, pp. 19720–19731, 2014.
- [48] S. Quintillán, C. Tojo, M. C. Blanco, and M. A. López-Quintela, "Effects of the intermicellar exchange on the size control of nanoparticles synthesized in microemulsions," *Langmuir*, vol. 17, no. 23, pp. 7251–7254, 2001.
- [49] C. Tojo, M. C. Blanco, and M. A. López-Quintela, "Preparation of nanoparticles in microemulsions: a Monte Carlo study of the influence of the synthesis variable," *Langmuir*, vol. 13, no. 17, pp. 4527–4534, 1997.
- [50] N. J. Turro and G. C. Weed, "Micellar systems as 'supercages' for reactions of geminate radical pairs. Magnetic effects," *Journal of the American Chemical Society*, vol. 105, no. 7, pp. 1861–1868, 1983.

Research Article

Microwave-Assisted Synthesis of Porous ZnO/SnS₂ Heterojunction and Its Enhanced Photoactivity for Water Purification

A. B. Makama,¹ A. Salmiaton,¹ E. B. Saion,² T. S. Y. Choong,¹ and N. Abdullah¹

¹Department of Chemical and Environmental Engineering, Universiti Putra Malaysia (UPM), 43400 Serdang, Selangor, Malaysia

²Department of Physics, Universiti Putra Malaysia (UPM), 43400 Serdang, Selangor, Malaysia

Correspondence should be addressed to A. Salmiaton; mie@upm.edu.my

Received 12 January 2015; Accepted 15 March 2015

Academic Editor: Xin Zhang

Copyright © 2015 A. B. Makama et al. This is an open access article distributed under the Creative Commons Attribution License, which permits unrestricted use, distribution, and reproduction in any medium, provided the original work is properly cited.

Porous ZnO/SnS₂ nanocomposites with adjustable SnS₂ contents were prepared via microwave-assisted heating of different aqueous solutions of SnS₂ precursors in the presence of fixed amount of ZnCO₃ nanoparticles at pH 7. The structures, compositions, BET specific surface areas, and optical properties of the as-prepared products were characterized by X-ray diffraction, energy dispersive X-ray spectroscopy, transmission electron microscopy, N₂ adsorption, and UV-Vis absorption spectra. Photocatalytic activities of the samples were tested by the removal of aqueous ciprofloxacin, Cr^{VI}, and methylene blue under visible-light ($\lambda > 420$ nm) irradiation. The experimental results reveal that the as-prepared heterogeneous nanostructures exhibit much higher visible-light-driven photocatalytic activity for the degradation of the pollutants than pure SnS₂ nanocrystals. The photocatalytic degradation rates (C_t/C_0) of the pollutants for the most active heterogeneous nanostructure are about 10, 49, and 9 times higher than that of pure SnS₂. The enhanced photocatalytic activities exhibited by the heterojunctions could be ascribed to the synergetic effect of enhanced absorption in the visible region and the reduced rate of charge carrier recombination because of efficient separation and electron transfer from the SnS₂ to ZnO nanoparticles.

1. Introduction

The occurrence of subnano- to microquantities of the synthetic broad-based antibiotic ciprofloxacin (CIP) in surface and ground waters is an emerging source of high concern [1, 2]. The presence of CIP in aquatic environments, albeit at low concentrations, may lead to serious environmental issues. Of immediate concern is the high likelihood of inducing the evolution and proliferation of multidrug resistant bacteria [3]. On the mid and long term, the concern stems from not knowing the risks posed by CIP to ecosystems and human health. Because existing conventional water treatment plants are not designed to treat pharmaceutical products, there is the urgent need to develop cost-effective treatment technology to cope with this problem. In this context, advanced oxidation processes (AOPs) are being intensively investigated as possible remediation techniques. Advanced oxidation processes

hold much promise in this regard because of their ability to produce highly reactive oxidative species (ROS) that are capable of complete mineralization of recalcitrant organic, biological, and inorganic pollutants [4].

Many types of AOPs are being considered for water decontamination [5, 6]. These include electrochemical, photochemical, photocatalytic processes, or their combinations. The photochemical and electrochemical processes, such as ozonation [7, 8], photo/electro-Fenton [9, 10], and persulfate [11, 12], use expensive precursors (O₃, H₂O₂, and Fe²⁺ coupled with UV photons or electricity) to generate ROS. On the other hand, the photocatalytic decomposition (PCD) produces ROS without the need of any chemical and can be operated at ambient conditions. Furthermore, PCD has the inherent potential to be simple, reusable, efficient, and clean and can be designed to utilize a significant portion of the infinitely free energy from the sun. For these reasons,

PCD is widely regarded as a potentially viable AOP for water purification [13–15]. In heterogeneous photocatalytic decontamination (PCD) process, a semiconductor (SC) material harnesses energy from photons that pose energies equal to or greater than its band gap. The absorbed energy is utilized to excite electrons from the valence band to the conduction band of the semiconductor. The photogenerated electrons and holes then react with adsorbates such as O_2 , H_2O to initiate the production of ROS radicals that directly degrade pollutants [16–18].

The fate and economic viability of PCD in large-scale water purification process are contingent on the development of high-performance photocatalyst(s) [19]. From industrial perspective, the optimal catalyst must possess the ability to transform the pollutant(s) entirely to harmless molecule(s). Additionally, it must have a bandgap (with suitably positioned conduction and valence bands) that absorbs light in the visible range and remains stable in contact with the water matrix. Furthermore, it should be nontoxic, abundant, and cheap. Towards this goal, a considerable variety of semiconductor materials have been tested for this purpose in the past decades. Table 1 gives a summary of some of the most recent materials investigated as photocatalysts for CIP degradation.

Among the materials under consideration are SnS_2 and ZnO semiconductors with bulk band gaps of about 2.2 eV and 3.37 eV, respectively [20]. They are among the most promising photocatalysts, owing to their low cost, nontoxic nature, and high photocatalytic activity [21–23]. Moreover, they have matched band potentials; that is, both the valence band and conduction band potentials of SnS_2 are more negative than those of ZnO [24]. Thermodynamically, this allows the photogenerated electron to easily transfer from the conduction band of SnS_2 to the conduction band of ZnO under visible-light ($\lambda > 420$ nm) irradiation, hence, enhancing the separation of photogenerated electrons and holes in SnS_2 and bringing about the sensitization of ZnO. For this reason, the ZnO/ SnS_2 composites with appropriate compositions should have higher visible-light-driven photocatalytic activity than individual SnS_2 and ZnO.

On the basis of these considerations, we report a study on the synthesis of porous ZnO/ SnS_2 nanosphere heterojunctions via a three-step process, including (1) room temperature synthesis of $ZnCO_3$ in polyvinyl pyrrolidone-ethylene glycol solution, (2) microwave-assisted conformal deposition of SnS_2 layer on the $ZnCO_3$ nanospheres, and (3) calcination of the $ZnCO_3/SnS_2$ nanospheres at $360^\circ C$. The objectives are to evaluate the effectiveness of porous ZnO/ SnS_2 as a photocatalyst for the removal of (a) CIP and (b) hexavalent chromium ion and methylene blue. In addition, the source of enhanced photoactivity (if any) will be investigated. To the best of our knowledge, no such work on porous ZnO_3/SnS_2 was ever reported.

2. Materials and Methods

2.1. Chemicals. All chemicals and reagents used in this work were of analytical grade and they were used as-received without any purification. The materials are ammonium hydrogen

carbonate (NH_4HCO_3 , Friendemann Schimdt Chemical, Germany), tin (IV) chloride pentahydrate ($SnCl_4 \cdot 5H_2O$, Acros, New Jersey, US), sodium sulfide ($Na_2S \cdot xH_2O$, QRec, Thailand), ethylene glycol ($HOCH_2CH_2OH$, Merck, Germany), zinc sulfate heptahydrate ($ZnSO_4 \cdot 7H_2O$, R & M Chemicals, UK), and polyvinyl pyrrolidone (PVP 58000, Alfa Aesar, UK), and denatured absolute ethanol (CH_3OH , Globe Chemicals, Germany). Model pollutants purchased include ciprofloxacin hydrochloride ($C_{17}H_{18}FN_3O_3$ HCl, Cadila's Ciprodac, India), potassium dichromate ($K_2Cr_2O_7$, AR grade, System, Malaysia), and methylene blue (MB) whose structures and concentrations in test liquids are shown in Table 2. Distilled deionized water 18.2 m Ω -cm was prepared using TKA instrument and used to prepare all aqueous solutions.

2.2. Synthesis of $ZnCO_3$. Zinc carbonate ($ZnCO_3$) was prepared according to an earlier reported procedure with slight modification [25]. 2.9 g (0.01 g mol) of $ZnSO_4$ (Solution A) and 1.6 g (0.02 g mol) of NH_4HCO_3 (Solution B) were each dissolved in 50 mL of 5 wt% PVP-ethylene glycol solution at $70^\circ C$. Solution B was added in a dropwise manner to Solution A under magnetic stirring at 800 rpm. The mixture was stirred for 1 h, and the white precipitate formed was collected by centrifuge at 6 000 rpm for 3 min. The precipitate was washed with distilled deionized water (3 \times) and then with denatured absolute ethanol (3 \times). Finally, the moist $ZnCO_3$ precipitate obtained was dried in an oven at $70^\circ C$ for 6 h.

2.3. Microwave-Assisted Synthesis of ZnO/ SnS_2 . A predetermined mass of $ZnCO_3$ powder was dispersed by sonication for 30 min in 100 mL (NaOH neutralized) solution of $SnCl_4 \cdot 5H_2O$ (pH 7) in argon sparged distilled deionized (DDI) water. After that, 20 mL solution of Na_2S also in argon sparged DDI was dropped in the $ZnCO_3$ dispersion under vigorous stirring (800 rpm). The colloidal solution under vigorous stirring was irradiated using microwave in a pulsed regime of 5 s on, 20 s off at 20% power (180 W) in an oven for 10 min. The whitish brown $ZnCO_3/SnS_2$ precipitate formed was collected by centrifuge and washed as explained in Section 2.2. The cleaned solid was calcined in a stagnant air furnace at $360^\circ C$ for 3 h. Three different samples were prepared at various mass ratios of Sn^{4+} source and Zn^{2+} source that were controlled as 25, 50, and 75 wt%. Details of the experimental condition are given in Table 3. The as-prepared ZnO/ SnS_2 powders are designated ZOSS-1, ZOSS-2, and ZOSS-3, respectively, and referred to as such in the text.

For the purpose of comparison, ZnO and SnS_2 were also produced in 5% PVP-EG solution using microwave heating as above.

2.4. Characterization. Investigation of the crystallinity and the phase structures of the samples was carried out on a Phillips Analytical X-ray diffractometer. All measurements were done with $Cu_{K-\alpha}$ radiation between 2θ values of 20° and 80° at a scan rate of $0.033^\circ s^{-1}$ using accelerating voltage and current of 40 mV and 40 mA, respectively. Ultraviolet-Visible (UV-Vis) absorbance spectra of samples were obtained on a

TABLE 1: Photocatalysts and experimental conditions reported for the degradation of ciprofloxacin.

Photocatalyst	Catalyst load, mg	Concentration mg/L	Radiation	Illumination time, min	CIP removal, %	References
ZnO	20	5	UV-A	60	~50	[21]
Bio MgO _x	50	10	NG ^b	720	100	[52]
KMn ₈ O ₁₆	50 ^a	—	NG	30	>90	[53]
Ag/Pt@TiO ₂	80	10	Vis.	120	99	[54]
Ag@NC-TiO ₂	80	10	Vis.	150	98	[55]
TiO ₂	500	33	UV-Vis	—	—	[45]
rGO ^c -BiVO ₄	20	10	UV	60	68.2	[56]
TiO ₂ -P25	500	14	UV	—	—	[57]
Pt-BiO ₄	150	10	Vis.	60	91.97	[58]
Anatase-TiO ₂	1000	50	UV	120	—	[59]
NaCl/TiO ₂	100	10	Vis.	60	70.90	[13]

^aMolar ratio of catalyst to CIP; ^bNG = not given, ^crGO = reduced graphene oxide.

TABLE 2: Pollutants and some experimental conditions used in testing the photocatalytic activity of the porous ZnO/SnS₂ heterostructures. Unless otherwise indicated, reactions were performed at (30 ± 1)°C in a water-jacketed photoreactor, continuously air/argon-sparged and stirred at 400 rpm.

Model pollutant	Chemical structure	Initial concentration, mgL ⁻¹ (μmolL ⁻¹)	pH
Dichromate ion		35.5 (120.7)	5.21
Ciprofloxacin		40 (120.7)	6.10
Methylene blue		38.6 (120.7)	7.60

Shimadzu model UV-1800 spectrophotometer. Absorbance measurements are converted to absorption coefficient (α) from $\alpha = 2.303A/d$, where d is the path length of the quartz cuvette and A is the absorbance [26, 27]. The calculated α are used in Tauc equation [$\alpha h\nu = K(h\nu - E_{bg})^n$] to estimate the energy gap of the nanocomposite [28, 29]. Morphological structures of the samples were viewed and photographed on a Hitachi scanning electron microscope (FESEM) model S-3400N. Energy-dispersive X-ray spectrometry (EDS) was also taken on the same machine. Fine structural details were investigated with a Hitachi transmission electron microscope, model H-7100 STEM. Surface area of the samples was determined from BET measurements on a 3Flex Surface Characterization Analyzer (Micrometrics, USA). Isoelectric point (IEP) of ZOSS-2 was determined using ZetaSizer Nano ZS (Malvern, UK) instrument.

2.5. Batch Photocatalytic Activity Measurement. Photocatalytic activities of the nanocomposite were investigated by

photocatalytic degradation of ciprofloxacin (CIP) in 400 mL immersion well photoreactor (model RQ400, Photochemical Reactors, UK). In a run, 200 mg of a catalyst was added to 300 mL aqueous solution of the pollutant in the reaction flask at natural pH (see Table 2). The suspension was stirred at 400 rpm for 30 min (based on preliminary contact time test result) in the dark to allow for adsorption-desorption equilibrium. Visible-light irradiation ($\lambda > 420$ nm) was generated by a 200 W quartz tungsten halogen lamp (Osram Sylvania Inc., US) which was wrapped in a UV filtering plastic sheet (F20 UV Yellow, Fluorolite Plastics, US) to remove stray UV radiation. The lamp was switched on for 10 min–15 min to reach maximum output prior to coupling to the reaction flask. After that, the light source was coupled to the reaction flask to start the photoreaction under continuous stirring at 400 rpm and O₂ supply. The lamp and reactor temperature was maintained at (30 ± 1)°C by cooling water. About 3 mL of the reaction mixture was drawn from the reactor vessel at scheduled time intervals to the maximum specified time. The

TABLE 3: Designation and summary of synthesis conditions, BET specific area, BJH pore volume, band gaps, and valence band potential of the as-synthesized specimens.

Name	^a Zn ²⁺ mmol	^b Sn ⁴⁺ mmol	Na ₂ S mmol	^c Mass %	A _{BET} m ² /g	BJH cm ³ /g	E _g eV	E _{VB} eV
ZnO	40	0	0	0	62.7	0.823	3.3	2.9
ZOSS-1	40	3.6	7.2	25	39.4	0.571	2.9	2.2
ZOSS-2	40	7.1	14.3	50	109.1	0.767	2.8	2.1
ZOSS-3	40	10.7	21.4	75	69.7	0.229	2.6	2.0
SnS ₂	0	14.3	28.5	100	19.7	0.665	2.4	2.2

^aZnCO₃; ^bSnCl₄·5H₂O; ^cSnCl₄·5H₂O:ZnCO₃.

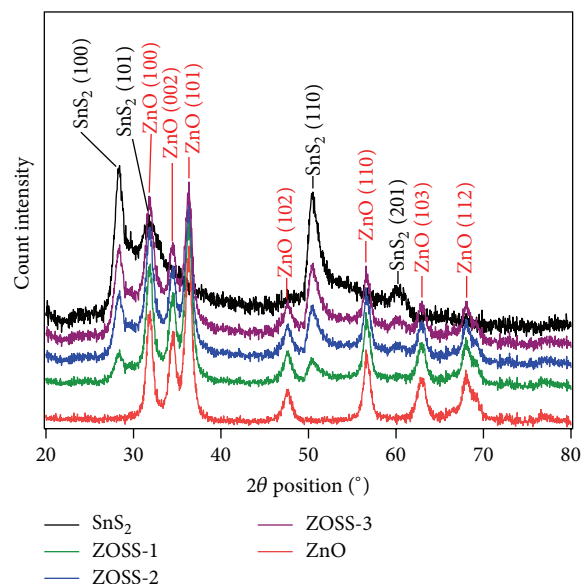


FIGURE 1: XRD patterns of the as-prepared ZnO and SnS₂ and the heterojunctions.

aliquots were immediately centrifuged at 6 000 rpm for 3 min to separate the photocatalyst from the supernatant.

2.6. Analytical Methods. The temporal concentrations of the pollutants in the different supernatants were determined using established methods in the technical literature based on optical absorbance measurements. Absorbance of Cr^{VI} was taken at 540 nm according to the 1,5-diphenylcarbazide (DPC) procedure [30]. Those of CIP and MB were taken at 275 nm [31] and 664 nm, respectively. Where necessary, the absorbances were converted to concentration using calibration curves for the different pollutants.

3. Results and Discussions

3.1. Characterization of As-Synthesized Photocatalysts

3.1.1. Crystallinity and Structural. The crystalline phases of the as-prepared samples were investigated with XRD and the results are shown in Figure 1. The peaks on the diffractogram of pure ZnO could be indexed to reflections from (100), (002), (101), (102), (110), (103), and (112) planes of pure wurtzite

structure of ZnO (PDF number: 36-1451). Those on the pure SnS₂ diffractogram were indexed to the (100), (101), (110), and (201) planes of pure hexagonal phase of SnS₂ (PDF number: 23-0677). On the other hand, the diffractograms of the heterojunctions (ZOSS-1, ZOSS-2, and ZOSS-3) show peaks coming from the planes of ZnO and those of SnS₂, hence confirming that the composite powders consist of ZnO and SnS₂ phases. All the XRD patterns exhibit strong reflections and no trace of impurity peaks could be detected indicating the high crystallinity and phase purity of the products. The SnS₂ peaks on the diffractograms of ZOSS-1, ZOSS-2, and ZOSS-3 exhibit an evolutionary development with increased SnS₂ content from ZOSS-1 to ZOSS-3. The evolutionary trend is a commonly observed XRD feature of composite materials [32].

3.1.2. Surface Morphological and Elemental Analysis. The morphology and structure of ZnO, heterojunctions, and SnS₂ are photographed with SEM as shown in Figures 2(a)–2(e), respectively. The SEM images of zincite and SnS₂ in Figures 2(a) and 2(e) show that they consist of uniformly shaped and sized spherical aggregates with sizes between 0.2 μm and

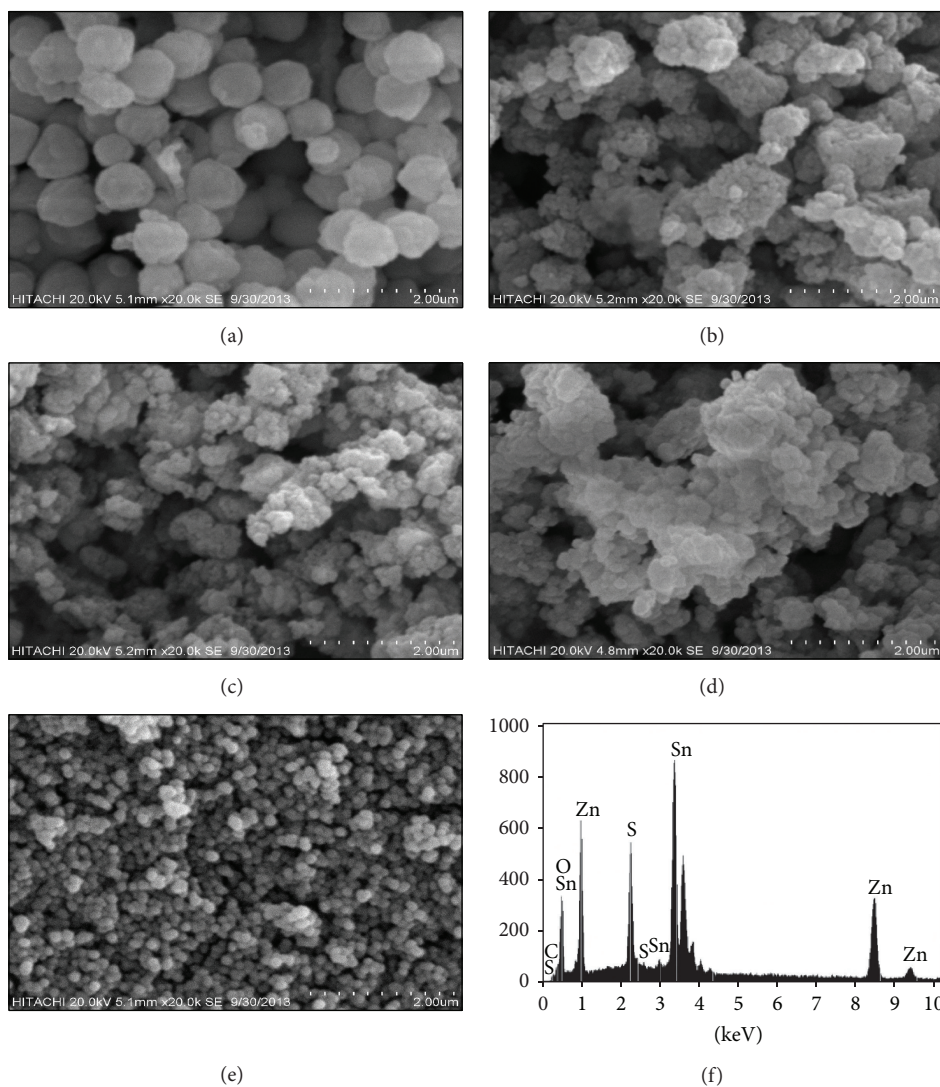


FIGURE 2: Low magnification SEM micrographs of (a) ZnO, (b) ZOSS-1, (c) ZOSS-2, (d) ZOSS-3, (e) SnS₂, and (f) EDX spectrum of ZOSS-2. Scale bar 2 μm .

0.8 μm . After compounding (Figures 2(b)–2(d)), the resulting composites show rough faced agglomerates that consist of spheres of ZnO covered and cemented together by mass of SnS₂. The degree of agglomeration increases with SnS₂ content from 25% to 75%. At 75%, petal like features of SnS₂ began to appear as shown in Figure 2(d).

The morphology of the smaller particles is further elucidated by the TEM micrograph. The TEM image of ZOSS-2 is shown in Figure 3(a). From this picture, it is clear that the ZOSS-2 heterostructure is made up of uniformly sized spheroidal particles. The dotted rectangular part in Figure 3(a) was further magnified, as shown in the inset. The enlarged portion displays that the surface of the ZnO (black spheroids) particles is entirely encased by SnS (gray mass) material. Particle size estimate obtained by counting shows the average diameter d_p of ZOSS-2 to be (10.9 ± 0.2) nm (Figure 3(b)). EDX analysis was performed to determine the elemental compositions of the ZOSS-surfaces. The analysis result for ZOSS-2 is shown on the EDX plot (Figure 2(f)), and

it further confirms the coexistence of the elements Zn, O, S, and Sn.

3.1.3. Optical Absorbance Analysis. Optical absorbance spectral studies in the UV-Vis region were done to estimate the band gaps of the synthesized photocatalysts. Figure 4 displays the plots for pristine ZnO and SnS₂ and for the ZnO/SnS₂ (ZOSS-1 to -3) heterojunctions. It is seen that zincite exhibits no optical absorption in visible-light region due to its large energy band gap (3.3 eV). The spectra of the heterojunctions showed steep absorption over the visible-light region, indicating that the visible-light response of ZnO/SnS₂ materials is a manifestation of the transition between the VB and CB not from hybrid energy levels [33, 34]. The band gaps estimated from the Tauc plot (inset of Figure 4) are tabulated in Table 3. They range from 2.6 eV to 2.9 eV. The visible-light absorption abilities of the heterojunctions gradually increased with increasing SnS₂. The present findings seem

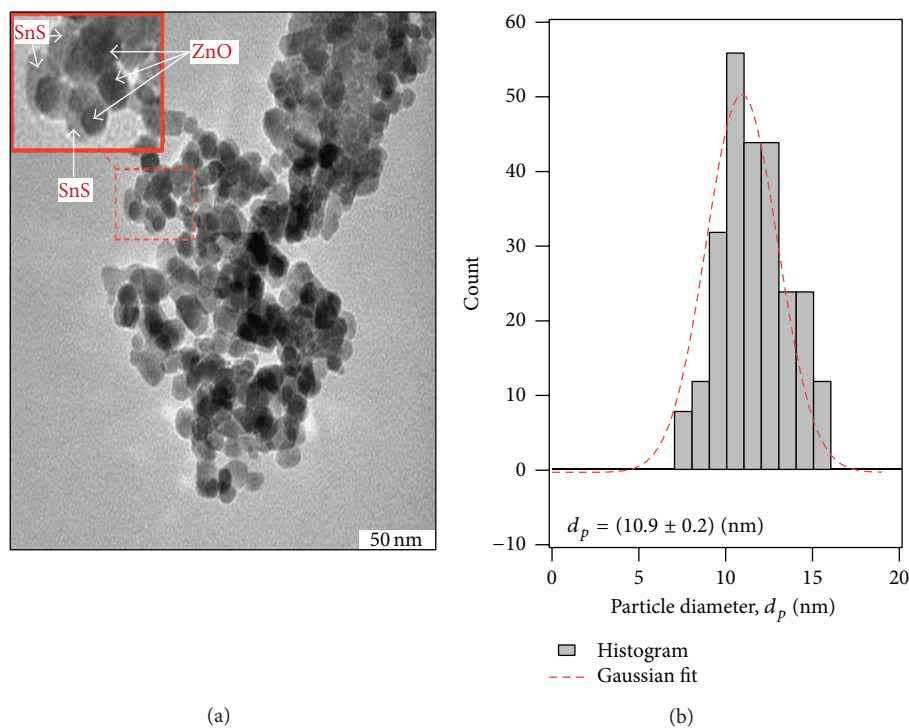


FIGURE 3: (a) TEM image and (b) particle size distribution of ZOSS-2.

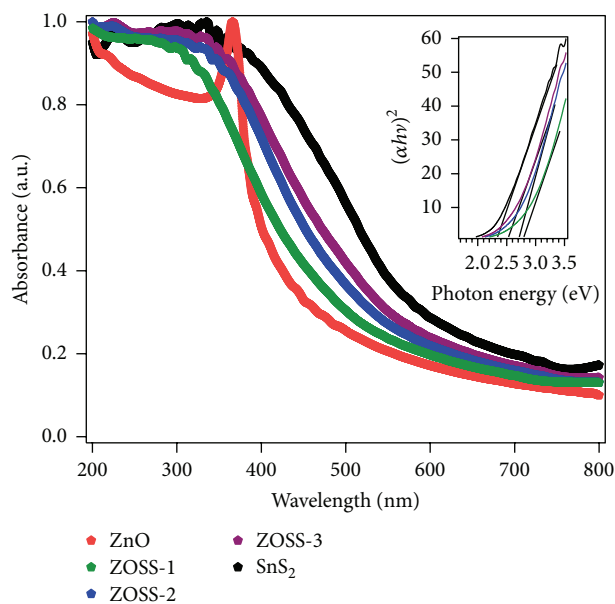


FIGURE 4: Room temperature optical absorbance spectra ZnO, ZOSSI-3, and SnS₂. Inset shows the Tauc $((\alpha h\nu)^2$ versus $h\nu$) plots and band gap estimates for the SnS₂ and the different heterojunctions. The band gap of ZnO was estimated from the onset of absorption on the main plot.

to be consistent with other research that reported similar visible-light absorption trend of semiconductor nanocomposite materials [35].

3.1.4. Surface Area and Pore Size Distribution. The specific surface areas and pore sizes of the different photocatalysts were determined by nitrogen adsorption-desorption

isotherms. The isotherms obtained revealed that all the pure phases and the heterojunctions have typical type IV isotherms according to the IUPAC classification of sorption isotherms. Figure 5(a) shows the adsorption-desorption isotherms for ZOSS-2. The isotherm with its characteristic type H1 hysteresis loop shows that the synthesized ZOSS-2 is purely a mesoporous material that contains similar sized

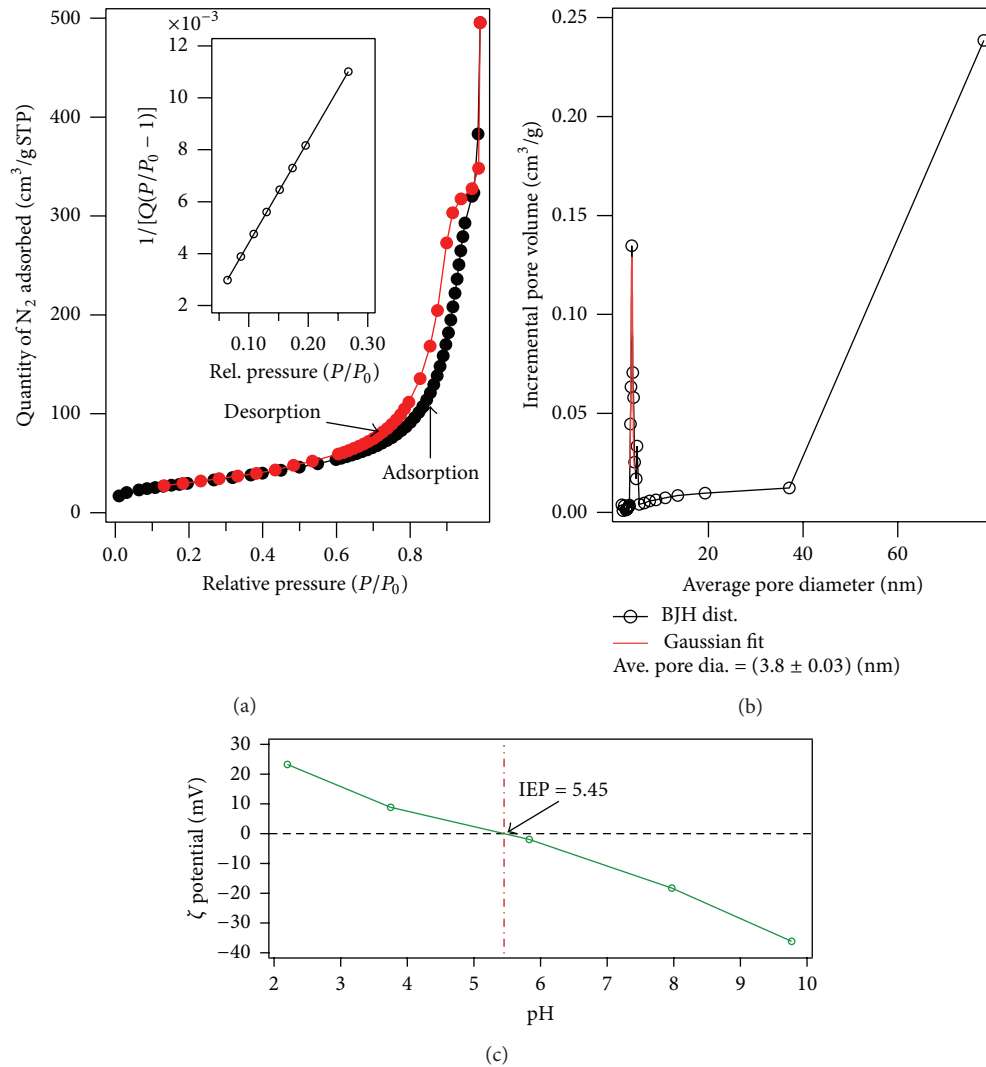


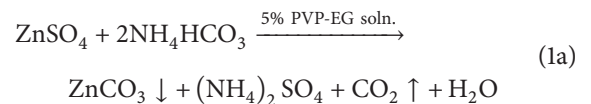
FIGURE 5: (a) Representative nitrogen adsorption-desorption isotherms and the BET surface area plot (inset) for ZOSS-2. (b) BJH pore size distribution. (c) ζ potential of porous ZnO/SnS₂ suspension as a function of pH showing the isoelectric point.

nonintersecting cylindrical mesopores [36]. The specific surface area for ZOSS-2 calculated according to the BET theory was found to be 109.1 m²g⁻¹. This is much bigger than the areas of pure ZnO (62.7 m²g⁻¹) and SnS₂ (19.7 m²g⁻¹). The monolayer capacity and the BET constant of ZOSS-2 were found to be 25.1 cm³g⁻¹ STP and 84.5, respectively. The material also shows a moderate pore volume of 0.72 cm³g⁻¹. The pore size distribution (inset of Figure 5(b)) calculated by BJH method shows that the pore diameters are in the mesoporous range with an average pore diameter equal to 3.8 nm. Similar properties for the other samples were calculated and summarized in Table 3. It is observed that the surface area increases SnS₂ < ZOSS-1 < ZnO < ZOSS-3 < ZOSS-2.

3.2. Proposed Mechanism for the Synthesis of Porous ZnO/SnS₂. Scheme 1 is a pictorial illustration of the

proposed steps for the formation of porous ZOSS-2 nanosphere heterojunctions.

First, uniformly shaped nanospheres of ZnCO₃ are produced by precipitation in 5% PVP-EG solution:



Secondly, SnS₂ nanocrystal layer is deposited on the ZnCO₃ nanospheres in an aqueous solution (pH 7) to produce the ZnCO₃/SnS₂ core-shell nanospheres according to the net ionic equation:



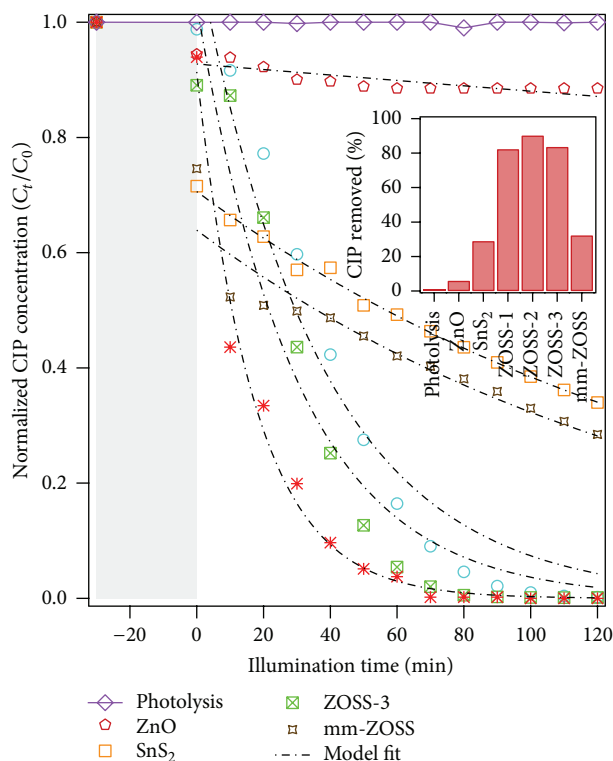
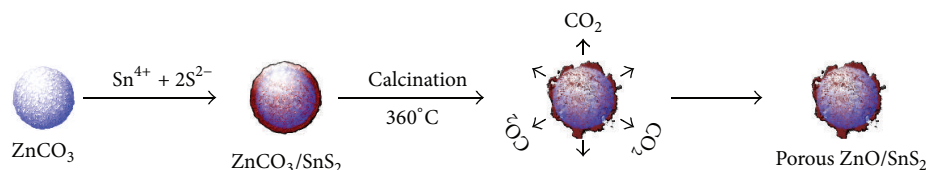


FIGURE 6: Visible-light ($\lambda > 420$ nm) induced photodegradation of CIP by photolysis and by photocatalysis over different catalysts. Inset shows the comparison of the quantity of CIP removed in 60 min by photocatalysis over the different catalysis. Rate coefficient for each reaction is tabulated in Table 4.



SCHEME 1: Schematic illustration of the conversion processes from ZnCO_3 nanospheres to porous ZnO/SnS_2 heterojunction.

Finally, the $\text{ZnCO}_3/\text{SnS}_2$ core-shell nanospheres are converted to porous ZnO/SnS_2 nanosphere heterojunctions by thermal decomposition at 360°C for 3 h:



3.3. Measurement of Photocatalytic Activity

3.3.1. Degradation of Ciprofloxacin. Figure 6 shows the decay in concentration of ciprofloxacin with time as a function of photocatalysts type under visible-light. It also shows that, in the absence of the catalyst, the degradation of CIP does not occur. In the presence of the as-synthesized photocatalysts (except ZnO) however, appreciable fall in the concentrations of the pollutant was observed, indicating that the catalysts are photoactive under visible-light. The negligible activity exhibited by ZnO could be attributed to its large band gap [21] which makes it most photoactive under UV light but not

under visible-light. The percentage removal of CIP over the different catalysts in 60 min is shown as inset of Figure 6. From the figure, it is clear that the photoactivity catalysts have various activities in removing CIP. The heterojunctions (ZOSS-1-3) exhibit much higher photocatalytic activities than single phase ZnO and SnS_2 . After 60 min of visible-light illumination, the CIP removal over ZnO and SnS_2 was <10% and about 30%, respectively. In contrast, the percentage decomposition in 60 min over each heterojunction was >80%. Moreover in 120 min, CIP was completely decomposed over the heterojunctions. It is worth noting that the coating of a small amount (25%) of SnS_2 on ZnO results in a sharp increase of CIP decomposition from 5.9% to 82.3% (ZOSS-1). As the SnS_2 content increases to 50% (ZOSS-2), the highest photocatalytic activity was recorded. A further increase in SnS_2 content to 75% (ZOSS-3) however results in a drop in photocatalytic activity.

The slight differences in activities of the heterojunctions under visible-light could be tied to the differences in their

SnS₂ content. When the content of SnS₂ is low as in ZOSS-1, it is very likely that a significant portion of ZnO is not covered. Thus, the visible-light response of this sample might be weak due to less SnS₂ content. On the other hand, more content of SnS₂ will result in greater SnS₂ coating and also lead to the development of high density of interfacial defects. Depending on the density of defects, they could either promote or impede charge carrier separation [37–39]. Low density of defects is believed to be beneficial to separation and mobility of charge carriers [40]. However, when the defects become more, they could act as electron-hole recombination centers. Consequently, electrons and holes are quenched at these centers instead of separating and thus lead to decrease of photocatalytic activity. Therefore, it is probable that the fall in activity noticed for ZOSS-3 could be ascribed to high density of charge defects as a result of more Sn⁴⁺ ions being incorporated into the structure of ZnO. Thus, there must exist an optimum composition for ZnO/SnS₂ nanocomposite to achieve the highest photocatalytic activity. For these reasons, ZOSS-2 with SnS₂ content of 50% possessed the highest photocatalytic activity among heterojunctions.

To evaluate the role of chemically induced interfacial binding on the photocatalytic activity of the heterojunction systems, 2 parts pure phase ZnO and 1 part pure phase SnS were mechanically mixed to produce a system with same composition as ZOSS-2 and used to photooxidized CIP under the same conditions. The activity recorded is also shown in Figure 6. The mechanically mixed specimen (mm-ZOSS) shows a rather low photocatalytic performance (32.2%) for decomposition of CIP compared to chemically produced heterojunctions. The performance of mm-ZOSS is marginally higher than the performance of the pure phase SnS₂ (28.2%). The low activity shown by mm-ZOSS could be explained by the relatively loose binding between the two semiconductors which hinders efficient charge transfer between them. As reported [39, 41], the main advantage of the wet synthesis of the heterojunctions is the formation of tight chemically bonded interfaces between the two materials (see Figure 3(a)). The tight binding between the two semiconductors makes charge transfer between them spatially smooth [42–44].

3.3.2. Multiactivity Test and Kinetics. In order to better assess the activity of ZOSS-2, its performance to transform anionic (hexavalent chromium Cr^{VI}) and cationic (methylene blue (MB)) pollutant was investigated. The results of the investigation are shown in Figure 7 and they show that ZOSS-2 interacts differently with the model pollutants under dark and illuminated conditions. Under the experimental conditions tabulated in Table 2, ZOSS-2 shows excellent interaction with the pollutants. It reversely adsorbed 15.2% of Cr^{VI} from its solution and when the solution was exposed to visible-light, 81.3% of the residual Cr^{VI} was reduced to Cr^{III} in 10 min. By 20th min of illumination, the amount of Cr^{VI} was practically reduced to zero. About 6.1% of CIP was adsorbed onto ZOSS-2 and upon irradiation with light, 90.2% of the residual CIP was removed. In the case of MB, 0.2% of the dye was adsorbed after 30 min and after 60 min of irradiation, 98.2%

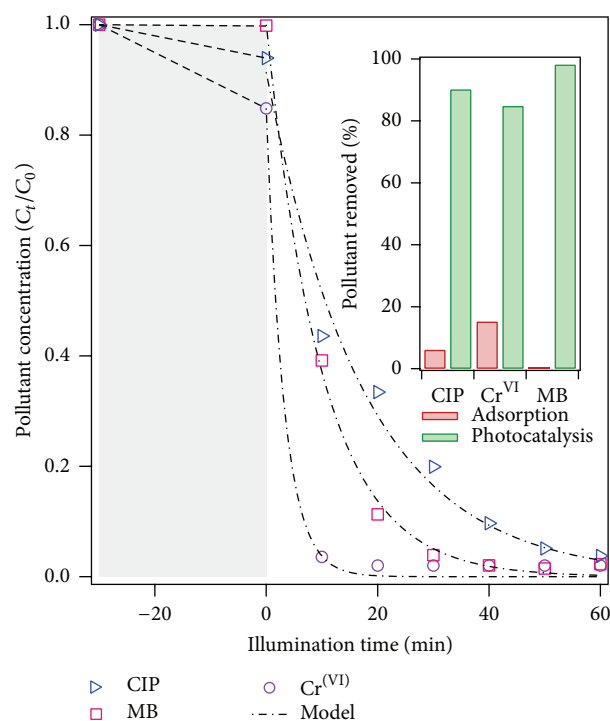


FIGURE 7: Visible-light ($\lambda > 420$ nm) photodegradation of Cr^{VI}, CIP, and MB over ZOSS-2 photocatalyst. Inset shows a comparison of CIP removed by adsorption and photocatalysis.

of the residual dye content was removed by photocatalysis. These findings show that adsorption plays only a nominal role in the transformation of the three model pollutants over ZOSS-2, suggesting that the transformation of the pollutants (especially for CIP and MB) mainly occurs in the bulk fluid, not on the catalyst surface.

To quantitatively understand the pollutants' transformation kinetics, experimental data were analyzed with the heterogeneous pseudo-first-order model as expressed by (2). The model has been applied successively [14, 16, 21, 42, 45] to represent the photocatalytic degradation process if the initial concentration of pollutant is low:

$$C_t = C_0 \exp(-k_r t), \quad (2)$$

where C_0 and C_t are the concentrations of each pollutant in solution at time 0 (optimum contact time to achieve adsorption-desorption equilibrium) and t , respectively, and k_r is the pseudo-first-order rate constant. The rate constants calculated from the nonlinear fit (NLF) of data to (2) and their corresponding χ^2 goodness of fit values for all the catalysts tested are tabulated in Table 4. A careful inspection of the χ^2 -values reveals that a reasonably good fit of experimental data to the kinetic model was achieved ($\chi^2 < 0.1$). It is clearly evident from the table that the rate constants of pollutant transformation by ZOSS-2 are much higher than the other catalysts. For the same initial molar concentration of pollutants, CIP, Cr^(VI), and MB, the rate of their removal over ZOSS-2 is about 9.2, 49, and 9 faster than by single phase SnS₂. The higher activity exhibited by ZOSS-2 could

TABLE 4: Pseudo-first-order rate constants and the respective chi-square test statistics of the model fit for the photocatalytic transformations of the model pollutants over the as-prepared catalysts.

Pollutant	ZnO		SnS ₂		ZOSS-1		ZOSS-2		ZOSS-3		mm-ZOSS	
	$10^{-3}k_r$ ^a	χ^2	$10^{-3}k_r$	χ^2	$10^{-3}k_r$	χ^2	$10^{-3}k_r$	χ^2	$10^{-3}k_r$	χ^2	$10^{-3}k_r$	χ^2
CIP	1.2 ^b	0.0002	6.2	0.0010	27.2	0.0785	57.1	0.0102	33.3	0.0867	6.8	0.0201
Cr ^{VI}	~0 ^c	—	6.8	0.0003	NA ^d	NA	311.9	0.0020	NA	NA	NA	NA
MB	~0	—	10.9	0.0017	NA	NA	99.4	0.0016	NA	NA	NA	NA

^aAll k_r have units of min^{-1} ; ^bsee text for explanation; ^cZnO is a large band gap semiconductor that is not active in visible-light. ^dExperiment not performed.

be attributed to its large surface area that offers more surface for visible-light absorption compared to the others. Similar findings have been reported in many reports [19, 42, 46–48]. Moreover, the dramatic increase in photoactivity of the nanocomposite is usually explained as a consequence of the formation of tight binding interface between the constituting semiconductors which favors charge carrier separation.

3.4. Apparent Quantum Yield. A measure of the energy utilization efficiency of the reactor-photocatalyst system was assessed using the apparent quantum yield (η_{app}) concept. On the basis of time required to achieve 90% conversion level, η_{app} is defined [49] as the ratio of the rate of 90% converted molecule over the number of photons with the required energy to cause excitation of the photocatalyst that enter the reactor. Accordingly, η_{app} for the degradation of CIP can be expressed mathematically as

$$\eta_{\text{app}}^{\lambda_1-\lambda_2} = \frac{N_{90\%}/t_{90\%}}{(A_{\text{irr}}/hc) \int_{\lambda_1}^{\lambda_2} I(\lambda) \lambda d\lambda}, \quad (3)$$

where $N_{90\%}$ is the number of pollutant molecules degraded at the 90% conversion level, $t_{90\%}$ is the time required to achieve 90% conversion in seconds, I ($\text{Wm}^{-2}\text{nm}^{-1}$) is the spectral irradiance intensity, A_{irr} (m^2) is the irradiated catalyst surface area ($= 50.2 \text{ m}^2$), h ($= 6.62 \times 10^{-34} \text{ Js}$) is Plank's constant, c ($= 2.997 \times 10^8 \text{ ms}^{-1}$) is the speed of light in vacuum, and λ_1 , λ_2 are the lower and upper wavelengths of the spectral band of interest. In this evaluation, the numerical integration of (3) is restricted within the 420 nm (λ_1)–443 nm (λ_2) spectral bandwidth for ZOSS-2. A visible high resolution spectra-photo radiometer (model BLK-HR-VIS, StellarNet Inc., US) was used to obtain the spectral distribution of the 200 W tungsten halogen lamp between 390 nm and 500 nm, as shown in Figure 8. The spectral irradiance of the lamp at the surface of outer wall of the immersion well was used to estimate the number of photons entering the reacting mixture. The apparent quantum yield was computed using (3) to be 0.225%.

3.5. Stability of the ZnO/SnS₂ Photocatalyst. Although the as-synthesized ZOSS-2 heterojunction has shown excellent photocatalytic activity, this positive characteristic will amount to naught if the catalyst is not stable for repeat operation. For this reason, its stability was investigated by recycling it over and over in the decomposition of CIP under visible-light. Before any new cycle of the experimental run, the

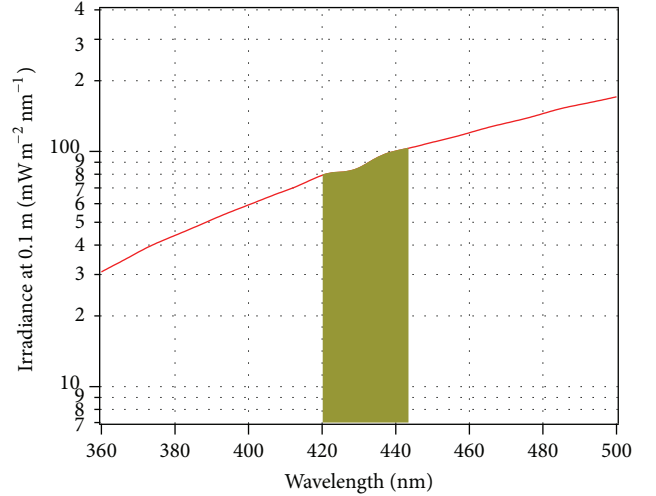


FIGURE 8: Spectral irradiance of the 200 W tungsten halogen lamp measured at the outer wall of the immersion wall ($\approx 10.0 \text{ cm}$ away from the lamp). Shaded area represents the spectral band of interest.

used catalyst was first cleaned, dried, and weighed. The result of the stability test is shown in Figure 9 and from it, it is apparent that there is very little lost in the activity of the ZOSS-2 photocatalyst after the first five reuse cycles. From this finding, it can be supposed that, under the current set of experimental conditions, ZOSS-2 is a stable photocatalyst.

3.6. Charge Transfer between the SnS₂ and ZnO Crystals and Enhancement of Photocatalytic Activity of ZnO/SnS₂. It is widely believed [19, 35, 39, 44] that the much better performance exhibited by composite semiconductor photocatalysts over single phase materials is mainly due to the phenomenon of electric-field-assisted photon induced charge separation and transfer across the systems' boundary. Thus, in order to understand the charge separation process between SnS₂ and ZnO interface, the valence band (VB) and conduction band (CB) potentials at the point of zero charge were calculated according to the electronegativity concept [50] using the empirical equations

$$E_{\text{VB}} = \psi - E^e + 0.5E_g, \quad (4a)$$

$$E_{\text{CB}} = E_{\text{VB}} - E_g, \quad (4b)$$

where ψ is the absolute electronegativity of the semiconductor, which is defined as the geometric mean of the absolute electronegativity of the constituent atoms. The absolute

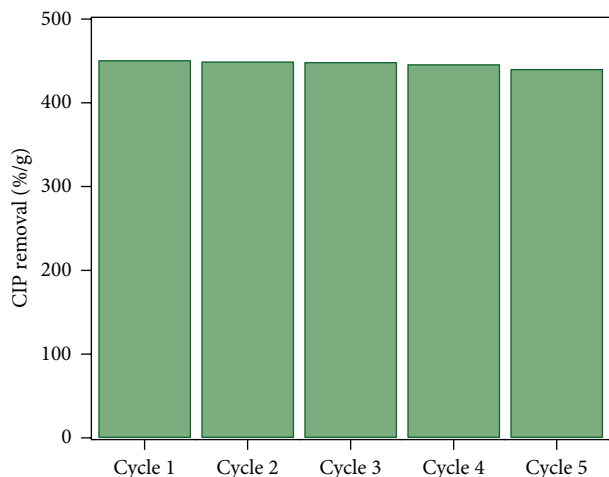
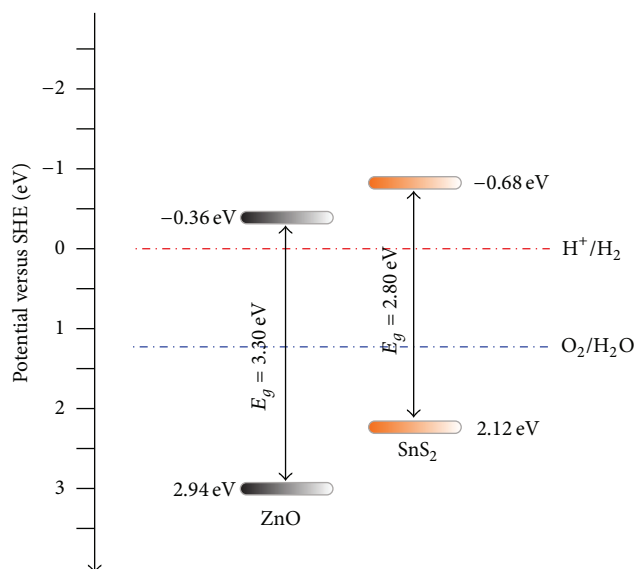


FIGURE 9: Photocatalytic performances of ZnO/SnS₂ in the first five reuse cycles.



SCHEME 2: Electronic band diagram of the ZnO/SnS₂ system.

electronegativity of the constituent atoms is defined as the arithmetic mean of the atomic electron affinity and the first ionization energy. The ψ values for SnS₂ and ZnO were calculated with data from Pearson [51] to be 5.17 eV and 5.79 eV, respectively. E° is the energy of free electrons on the hydrogen scale (ca. 4.5 eV) and E_g is the band gap of the semiconductor. The E_g values for ZnO and SnS₂ obtained in the experiments are 3.3 eV and 2.4 eV, respectively. Accordingly, the VB and CB energy values of SnS₂ crystals were calculated to be 1.87 eV and -0.53 eV while those for ZnO crystals were determined to be 2.89 eV and -0.36 eV, respectively.

Using the computed band potentials, the electronic band diagram of the heterojunction is drawn and shown in Scheme 2. As seen from the scheme, the ZnO/SnS₂ heterojunction is a “staggered” type II system. The CB edge potential of SnS₂ (-0.53 eV) is at a more negative potential than that of ZnO (-0.36 eV). Hence, visible-light excited

electrons in the CB of SnS₂ crystal can readily move across the system boundary to the CB of ZnO. At the other end, the holes (h⁺) created as a result of photon excitation of electrons remain in the VB of SnS₂ because it is at a lower potential than the VB of ZnO. In addition, the separation of electron-hole pairs is also aided by the internal electric fields generated within the depletion region of the two semiconductors. In other words, the small built-in voltage also induces the separation of electron-hole pairs both at the interface and in the individual semiconductors [43]. This also helps to reduce the probability of electron-hole recombination within the crystals. As a result, electrons are localized on the ZnO surface and holes on the SnS₂ surface. The separation and localization of electrons and holes in different semiconductors could effectively inhibit their recombination. Consequently, the lifetimes of these charge carriers are prolonged. This gives them the higher probability to partake in redox reactions which manifests as increased activity for the heterojunctions [42, 48].

4. Conclusions

Porous ZnO/SnS₂ heterostructures were synthesized through simple microwave-assisted heating chemical method at pH 7. The presence of SnS₂ extended the spectral response of ZnO from the UV to the visible region, enabling the heterostructures to efficiently remove ciprofloxacin, hexavalent chromium, and methylene blue from aqueous solutions under visible-light irradiation. The characterization results confirmed the formation of heterojunction and revealed that the heterojunction could promote the transfer of photoelectrons and thus inhibit their recombination with holes, leading to enhanced photocatalytic activity. The study suggests that the porous ZnO/SnS₂ heterostructures are new types of visible-light-driven photocatalysts for environmental applications.

Conflict of Interests

The authors declare that there is no conflict of interests regarding the publication of this paper.

Acknowledgments

The authors gratefully acknowledge the financial support provided by the Ministry of Education, Government of Malaysia, through Grant no. FGRS/1/11/TK/UPM/02/34, dated 1 August 2011, and RU Project Grant no. 05-02-12-2193RU.

References

- [1] M. Gros, M. Petrović, and D. Barceló, “Tracing pharmaceutical residues of different therapeutic classes in environmental waters by using liquid chromatography/quadrupole-linear ion trap mass spectrometry and automated library searching,” *Analytical Chemistry*, vol. 81, no. 3, pp. 898–912, 2009.
- [2] T. Christian, R. J. Schneider, H. A. Färber, D. Skutlarek, M. T. Meyer, and H. E. Goldbach, “Determination of antibiotic

- residues in manure, soil, and surface waters,” *Acta Hydrochimica et Hydrobiologica*, vol. 31, no. 1, pp. 36–44, 2003.
- [3] Z. Liu, P. Sun, S. G. Pavlostathis, X. Zhou, and Y. Zhang, “Adsorption, inhibition, and biotransformation of ciprofloxacin under aerobic conditions,” *Bioresource Technology*, vol. 144, pp. 644–651, 2013.
 - [4] C. Comninellis, A. Kapalka, S. Malato, S. A. Parsons, I. Poullos, and D. Mantzavinos, “Advanced oxidation processes for water treatment: advances and trends for R&D,” *Journal of Chemical Technology and Biotechnology*, vol. 83, no. 6, pp. 769–776, 2008.
 - [5] L. Feng, E. D. van Hullebusch, M. A. Rodrigo, G. Esposito, and M. A. Oturan, “Removal of residual anti-inflammatory and analgesic pharmaceuticals from aqueous systems by electrochemical advanced oxidation processes. A review,” *Chemical Engineering Journal*, vol. 228, pp. 944–964, 2013.
 - [6] J. Rivera-Utrilla, M. Sánchez-Polo, M. Á. Ferro-García, G. Prados-Joya, and R. Ocampo-Pérez, “Pharmaceuticals as emerging contaminants and their removal from water. A review,” *Chemosphere*, vol. 93, no. 7, pp. 1268–1287, 2013.
 - [7] C. Liu, V. Nanaboina, G. V. Korshin, and W. Jiang, “Spectroscopic study of degradation products of ciprofloxacin, norfloxacin and lomefloxacin formed in ozonated wastewater,” *Water Research*, vol. 46, no. 16, pp. 5235–5246, 2012.
 - [8] T. G. Vasconcelos, K. Kümmerer, D. M. Henriques, and A. F. Martins, “Ciprofloxacin in hospital effluent: degradation by ozone and photoprocesses,” *Journal of Hazardous Materials*, vol. 169, no. 1–3, pp. 1154–1158, 2009.
 - [9] S. Miralles-Cuevas, A. Arqués, M. I. Maldonado, J. A. Sánchez-Pérez, and S. Malato Rodríguez, “Combined nanofiltration and photo-Fenton treatment of water containing micropollutants,” *Chemical Engineering Journal*, vol. 224, no. 1, pp. 89–95, 2013.
 - [10] M. S. Yahya, N. Oturan, K. El Kacemi, M. El Karbane, C. Aravindakumar, and M. A. Oturan, “Oxidative degradation study on antimicrobial agent ciprofloxacin by electro-fenton process: kinetics and oxidation products,” *Chemosphere*, vol. 117, pp. 447–454, 2014.
 - [11] M. Mahdi-Ahmed and S. Chiron, “Ciprofloxacin oxidation by UV-C activated peroxydisulfate in wastewater,” *Journal of Hazardous Materials*, vol. 265, pp. 41–46, 2014.
 - [12] Y. Ji, C. Ferronato, A. Salvador, X. Yang, and J.-M. Chovelon, “Degradation of ciprofloxacin and sulfamethoxazole by ferrous-activated persulfate: implications for remediation of groundwater contaminated by antibiotics,” *Science of the Total Environment*, vol. 472, pp. 800–808, 2014.
 - [13] X. Liu, P. Lv, G. Yao et al., “Selective degradation of ciprofloxacin with modified NaCl/TiO₂ photocatalyst by surface molecular imprinted technology,” *Colloids and Surfaces A: Physicochemical and Engineering Aspects*, vol. 441, pp. 420–426, 2014.
 - [14] J. Ryu and W. Choi, “Substrate-specific photocatalytic activities of TiO₂ and multiactivity test for water treatment application,” *Environmental Science and Technology*, vol. 42, no. 1, pp. 294–300, 2008.
 - [15] H. Zhao, H.-J. Cui, and M.-L. Fu, “Synthesis of core-shell structured Fe₃O₄@ α -MnO₂ microspheres for efficient catalytic degradation of ciprofloxacin,” *RSC Advances*, vol. 4, no. 74, pp. 39472–39475, 2014.
 - [16] U. I. Gaya and A. H. Abdullah, “Heterogeneous photocatalytic degradation of organic contaminants over titanium dioxide: a review of fundamentals, progress and problems,” *Journal of Photochemistry and Photobiology C: Photochemistry Reviews*, vol. 9, no. 1, pp. 1–12, 2008.
 - [17] J.-M. Herrmann, C. Guillard, and P. Pichat, “Heterogeneous photocatalysis: an emerging technology for water treatment,” *Catalysis Today*, vol. 17, no. 1–2, pp. 7–20, 1993.
 - [18] A. Houas, H. Lachheb, M. Ksibi, E. Elaloui, C. Guillard, and J.-M. Herrmann, “Photocatalytic degradation pathway of methylene blue in water,” *Applied Catalysis B: Environmental*, vol. 31, no. 2, pp. 145–157, 2001.
 - [19] Y. C. Zhang, J. Li, and H. Y. Xu, “One-step in situ solvothermal synthesis of SnS₂/TiO₂ nanocomposites with high performance in visible light-driven photocatalytic reduction of aqueous Cr(VI),” *Applied Catalysis B: Environmental*, vol. 123–124, pp. 18–26, 2012.
 - [20] B. Ghosh, M. Das, P. Banerjee, and S. Das, “Fabrication of the SnS/ZnO heterojunction for PV applications using electrodeposited ZnO films,” *Semiconductor Science and Technology*, vol. 24, no. 2, Article ID 025024, 2009.
 - [21] M. El-Kemary, H. El-Shamy, and I. El-Mehasseb, “Photocatalytic degradation of ciprofloxacin drug in water using ZnO nanoparticles,” *Journal of Luminescence*, vol. 130, no. 12, pp. 2327–2331, 2010.
 - [22] Y. C. Zhang, J. Li, M. Zhang, and D. D. Dionysiou, “Size-tunable hydrothermal synthesis of SnS₂ nanocrystals with high performance in visible light-driven photocatalytic reduction of aqueous Cr(VI),” *Environmental Science and Technology*, vol. 45, no. 21, pp. 9324–9331, 2011.
 - [23] F. Liu, Y. H. Leung, A. B. Djurišić, A. M. C. Ng, and W. K. Chan, “Native defects in ZnO: effect on dye adsorption and photocatalytic degradation,” *Journal of Physical Chemistry C*, vol. 117, no. 23, pp. 12218–12228, 2013.
 - [24] Y. Xu and M. A. Schoonen, “The absolute energy positions of conduction and valence bands of selected semiconducting minerals,” *American Mineralogist*, vol. 85, no. 3–4, pp. 543–556, 2000.
 - [25] R. Zhang, F. Zhang, J. Feng, and Y. Qian, “Green and facile synthesis of porous ZnCO₃ as a novel anode material for advanced lithium-ion batteries,” *Materials Letters*, vol. 118, pp. 5–7, 2014.
 - [26] J. Sancho-Parramon, V. Janicki, and H. Zorc, “Compositional dependence of absorption coefficient and band-gap for Nb₂O₅-SiO₂ mixture thin films,” *Thin Solid Films*, vol. 516, no. 16, pp. 5478–5482, 2008.
 - [27] E. A. Davis and N. F. Mott, “Conduction in non-crystalline systems V. Conductivity, optical absorption and photoconductivity in amorphous semiconductors,” *Philosophical Magazine*, vol. 22, no. 179, pp. 0903–0922, 1970.
 - [28] A. B. Murphy, “Band-gap determination from diffuse reflectance measurements of semiconductor films, and application to photoelectrochemical water-splitting,” *Solar Energy Materials and Solar Cells*, vol. 91, no. 14, pp. 1326–1337, 2007.
 - [29] J. Tauc and A. Menth, “States in the gap,” *Journal of Non-Crystalline Solids*, vol. 8–10, pp. 569–585, 1972.
 - [30] A. D. Eaton, APHA, AWWA, and WEF, *Standard Methods for the Examination of Water and Wastewater*, APHA-AWWA-WEF, Washington, DC, USA, 20th edition, 1999.
 - [31] Y. Sun, Q. Yue, B. Gao et al., “Adsorption and cosorption of ciprofloxacin and Ni(II) on activated carbon-mechanism study,” *Journal of the Taiwan Institute of Chemical Engineers*, vol. 45, no. 2, pp. 681–688, 2014.
 - [32] J. Luo, L. Ma, T. He et al., “TiO₂/(CdS, CdSe, CdSeS) nanorod heterostructures and photoelectrochemical properties,” *Journal of Physical Chemistry C*, vol. 116, no. 22, pp. 11956–11963, 2012.

- [33] A. Kudo, "Photocatalyst materials for water splitting," *Catalysis Surveys from Asia*, vol. 7, no. 1, pp. 31–38, 2003.
- [34] Z. Lei, W. You, M. Liu et al., "Photocatalytic water reduction under visible light on a novel ZnIn_2S_4 catalyst synthesized by hydrothermal method," *Chemical Communications*, vol. 9, no. 17, pp. 2142–2143, 2003.
- [35] G. Yang, B. Yang, T. Xiao, and Z. Yan, "One-step solvothermal synthesis of hierarchically porous nanostructured CdS/TiO_2 heterojunction with higher visible light photocatalytic activity," *Applied Surface Science*, vol. 283, pp. 402–410, 2013.
- [36] K. S. W. Sing, D. Everet, R. Haul et al., "Reporting physisorption data for gas/solid systems with special reference to the determination of surface area and porosity (recomendations1984)," *Pure and Applied Chemistry*, vol. 54, no. 11, pp. 2201–2218, 1982.
- [37] H.-Y. Chen and D. H. Son, "Energy and charge transfer dynamics in doped semiconductor nanocrystals," *Israel Journal of Chemistry*, vol. 52, no. 11–12, pp. 1016–1026, 2012.
- [38] A. Kudo, "Recent progress in the development of visible light-driven powdered photocatalysts for water splitting," *International Journal of Hydrogen Energy*, vol. 32, no. 14, pp. 2673–2678, 2007.
- [39] X. Lin, J. Xing, W. Wang, Z. Shan, F. Xu, and F. Huang, "Photocatalytic activities of heterojunction semiconductors $\text{Bi}_2\text{O}_3/\text{BaTiO}_3$: a strategy for the design of efficient combined photocatalysts," *The Journal of Physical Chemistry C*, vol. 111, no. 49, pp. 18288–18293, 2007.
- [40] L. Yang, C.-W. Cheng, M. T. Bulsara, and E. A. Fitzgerald, "High mobility $\text{In}_{0.53}\text{Ga}_{0.47}\text{As}$ quantum-well metal oxide semiconductor field effect transistor structures," *Journal of Applied Physics*, vol. 111, no. 10, Article ID 104511, 2012.
- [41] J. Li, T. Wang, and X. Du, "Preparation of visible light-driven SnS/TiO_2 nanocomposite photocatalyst for the reduction of aqueous $\text{Cr}(\text{VI})$," *Separation and Purification Technology*, vol. 101, pp. 11–17, 2012.
- [42] W. Wang, J. Wang, Z. Wang et al., "p-n junction CuO/BiVO_4 heterogeneous nanostructures: synthesis and highly efficient visible-light photocatalytic performance," *Dalton Transactions*, vol. 43, no. 18, pp. 6735–6743, 2014.
- [43] W. Wang, F. Huang, and X. Lin, "x BiOI -(1-x) BiOCl as efficient visible-light-driven photocatalysts," *Scripta Materialia*, vol. 56, no. 8, pp. 669–672, 2007.
- [44] X. Zhang, L. Zhang, T. Xie, and D. Wang, "Low-temperature synthesis and high visible-light-induced photocatalytic activity of BiOI/TiO_2 heterostructures," *Journal of Physical Chemistry C*, vol. 113, no. 17, pp. 7371–7378, 2009.
- [45] T. Paul, P. L. Miller, and T. J. Strathmann, "Visible-light-mediated TiO_2 photocatalysis of fluoroquinolone antibacterial agents," *Environmental Science and Technology*, vol. 41, no. 13, pp. 4720–4727, 2007.
- [46] M. Farbod and M. Kajbafvala, "Effect of nanoparticle surface modification on the adsorption-enhanced photocatalysis of Gd/TiO_2 nanocomposite," *Powder Technology*, vol. 239, pp. 434–440, 2013.
- [47] A. Franco, M. C. Neves, M. M. L. R. Carrott, M. H. Mendonça, M. I. Pereira, and O. C. Monteiro, "Photocatalytic decolorization of methylene blue in the presence of TiO_2/ZnS nanocomposites," *Journal of Hazardous Materials*, vol. 161, no. 1, pp. 545–550, 2009.
- [48] W. Li, X. Cui, P. Wang, Y. Shao, D. Li, and F. Teng, "Enhanced photosensitized degradation of rhodamine B on CdS/TiO_2 nanocomposites under visible light irradiation," *Materials Research Bulletin*, vol. 48, no. 9, pp. 3025–3031, 2013.
- [49] H. Ibrahim and H. de Lasa, "Photo-catalytic degradation of air borne pollutants apparent quantum efficiencies in a novel photo-CREC-air reactor," *Chemical Engineering Science*, vol. 58, no. 3–6, pp. 943–949, 2003.
- [50] M. A. Butler and D. S. Ginley, "Prediction of flatband potentials at semiconductor-electrolyte interfaces from atomic electronegativities," *Journal of the Electrochemical Society*, vol. 125, no. 2, pp. 228–232, 1978.
- [51] R. G. Pearson, "Absolute electronegativity and hardness: application to inorganic chemistry," *Inorganic Chemistry*, vol. 27, no. 4, pp. 734–740, 1988.
- [52] J. Tu, Z. Yang, C. Hu, and J. Qu, "Characterization and reactivity of biogenic manganese oxides for ciprofloxacin oxidation," *Journal of Environmental Sciences*, vol. 26, no. 5, pp. 1154–1161, 2014.
- [53] X. Xiao, S.-P. Sun, M. B. McBride, and A. T. Lemley, "Degradation of ciprofloxacin by cryptomelane-type manganese(III/IV) oxides," *Environmental Science and Pollution Research*, vol. 20, no. 1, pp. 10–21, 2013.
- [54] Z. Jiang, J. Zhu, D. Liu, W. Wei, J. Xie, and M. Chen, "In situ synthesis of bimetallic Ag/Pt loaded single-crystalline anatase TiO_2 hollow nano-hemispheres and their improved photocatalytic properties," *CrystEngComm*, vol. 16, no. 12, pp. 2384–2394, 2014.
- [55] Z. Jiang, X. Lv, D. Jiang, J. Xie, and D. Mao, "Natural leaves-assisted synthesis of nitrogen-doped, carbon-rich nanodots-sensitized, Ag -loaded anatase TiO_2 square nanosheets with dominant 001 facets and their enhanced catalytic applications," *Journal of Materials Chemistry A*, vol. 1, no. 47, pp. 14963–14972, 2013.
- [56] Y. Yan, S. Sun, Y. Song et al., "Microwave-assisted in situ synthesis of reduced graphene oxide- BiVO_4 composite photocatalysts and their enhanced photocatalytic performance for the degradation of ciprofloxacin," *Journal of Hazardous Materials*, vol. 250–251, pp. 106–114, 2013.
- [57] X. van Doorslaer, K. Demeestere, P. M. Heynderickx, H. van Langenhove, and J. Dewulf, "UV-A and UV-C induced photolytic and photocatalytic degradation of aqueous ciprofloxacin and moxifloxacin: reaction kinetics and role of adsorption," *Applied Catalysis B: Environmental*, vol. 101, no. 3–4, pp. 540–547, 2011.
- [58] W. Shi, Y. Yan, and X. Yan, "Microwave-assisted synthesis of nano-scale BiVO_4 photocatalysts and their excellent visible-light-driven photocatalytic activity for the degradation of ciprofloxacin," *Chemical Engineering Journal*, vol. 215–216, pp. 740–746, 2013.
- [59] T. A. Gad-Allah, M. E. M. Ali, and M. I. Badawy, "Photocatalytic oxidation of ciprofloxacin under simulated sunlight," *Journal of Hazardous Materials*, vol. 186, no. 1, pp. 751–755, 2011.

Research Article

Electrochemical Glucose Oxidation Using Glassy Carbon Electrodes Modified with Au-Ag Nanoparticles: Influence of Ag Content

Nancy Gabriela García-Morales,¹ Luis Alfonso García-Cerda,²
Bertha Alicia Puente-Urbina,² Leonor María Blanco-Jerez,³
René Antaño-López,¹ and Federico Castañeda-Zaldivar¹

¹Centro de Investigación y Desarrollo Tecnológico en Electroquímica, Parque Tecnológico Querétaro, s/n, Sanfandila, 76703 Pedro Escobedo, QRO, Mexico

²Centro de Investigación en Química Aplicada, Bulevar Enrique Reyna 140, Colonia San José de los Cerritos, 25294 Saltillo, COAH, Mexico

³Laboratorio de Electroquímica, Facultad de Ciencias Químicas, Universidad Autónoma de Nuevo León, Guerrero y Progreso, s/n, Colonia Treviño, 64570 Monterrey, NL, Mexico

Correspondence should be addressed to Federico Castañeda-Zaldivar; fcastaneda@cideteq.mx

Received 12 May 2015; Revised 10 July 2015; Accepted 28 July 2015

Academic Editor: Xin Zhang

Copyright © 2015 Nancy Gabriela García-Morales et al. This is an open access article distributed under the Creative Commons Attribution License, which permits unrestricted use, distribution, and reproduction in any medium, provided the original work is properly cited.

This paper describes the application of glassy carbon modified electrodes bearing Au_x-Ag_y nanoparticles to catalyze the electrochemical oxidation of glucose. In particular, the paper shows the influence of the Ag content on this oxidation process. A simple method was applied to prepare the nanoparticles, which were characterized by transmission electron microscopy, Ultraviolet-Visible spectroscopy, X-ray diffraction spectroscopy, and cyclic voltammetry. These nanoparticles were used to modify glassy carbon electrodes. The effectiveness of these electrodes for electrochemical glucose oxidation was evaluated. The modified glassy carbon electrodes are highly sensitive to glucose oxidation in alkaline media, which could be attributed to the presence of Au_x-Ag_y nanoparticles on the electrode surface. The voltammetric results suggest that the glucose oxidation speed is controlled by the glucose diffusion to the electrode surface. These results also show that the catalytic activity of the electrodes depends on the Ag content of the nanoparticles. Best results were obtained for the Au₈₀-Ag₂₀ nanoparticles modified electrode. This electrode could be used for Gluconic acid (GA) production.

1. Introduction

Glucose electrooxidation, specifically on Au electrodes, has been extensively studied because it is a reaction of scientific and industrial interest [1–11]. Due to the high catalytic activity of modified electrodes bearing nanoparticles, Au nanoparticles have been studied for glucose fuel cells [12–14], for degradation of dyes [15–17], and, last but not least, for glucose sensor in medical applications [18–21]. Furthermore, bimetallic nanoparticles have received more and more attention because their amazing optical, electronic, and catalytic properties, leading to various applications, as,

indeed, sensors, catalysis, or SERS substrates [22–29], and so forth. Among these nanoparticles, Au_x-Ag_y or Au_x-Pt_y bimetallic nanoparticles have been extensively explored for different electrochemical reactions as methanol and glucose electrooxidation [30–34].

On the other hand, Gluconic acid (GA) is a high value added chemical used as intermediate in the food, pharmaceutical, and beverage industries. The only commercial/industrial method to produce GA is by glucose biochemical oxidation [35], whose main disadvantages are slow reaction rate, low space-time, and problematic enzyme-product separation. In the past few years, heterogeneous

TABLE 1: Composition of Au-Ag nanoparticles synthesized.

Sample	Composition	% wt Au	% wt Ag	HAuCl ₄ (mol)	AgNO ₃ (mol)
M1	Au ₁₀₀	100	0	$2.53 * 10^{-4}$	0
M2	Au ₉₀ Ag ₁₀	90	10	$2.28 * 10^{-4}$	$4.63 * 10^{-5}$
M3	Au ₈₀ Ag ₂₀	80	20	$2.03 * 10^{-4}$	$9.27 * 10^{-5}$
M4	Au ₇₀ Ag ₃₀	70	30	$1.77 * 10^{-4}$	$1.39 * 10^{-4}$

catalysis using Pt, Pd, or Au nanoparticles has attracted much attention [36, 37]. The selective glucose oxidation to GA has been reported using Au clusters as catalyst and O₂ as oxidant giving a yield of 98% at mild conditions, that is, 50°C and atmospheric pressure. Indeed, higher costs, electrode poisoning, and hard reuse of nanocatalyst make this process far from competitive GA production [38]. Some studies have been oriented to the use of bi- and trimetallic nanoparticles to overcome the noneconomic electrochemical GA production, at least to elucidate the best nanoparticle composition for the electrooxidation of glucose. In this sense, bimetallic Au-Ag nanoparticles show important synergistic effects in the catalytic properties; these properties depend upon metals ratio of nanoparticle, nanoparticle synthesis, nanoparticle size, form, and crystallographic orientation [39, 40]; indeed, it has been shown that the surface morphology and particularly the size of nanoparticles can be easily controlled by experimentally adjusting the synthesis conditions [41, 42].

In our previous work, we reported that Au nanoparticles supported on glassy carbon presented a catalytic activity and selectivity towards glucose oxidation, depending on the particle size and on the crystallographic orientation. Results also suggest that oxidation process in these conditions is taking place with lower poisoning of the surface in the case of the Au nanoparticles than for massive gold that the process is irreversible, and perhaps there are some chemical reactions involved in the overall oxidation process [25].

The aim of this work is to evaluate the catalytic properties of Au_x-Ag_yNPs towards the glucose electrooxidation; hence, we studied mainly the Au-Ag nanoparticles voltammetric response of different Au-Ag ratio.

2. Experimental Section

2.1. Preparation of Au_x-Ag_y Nanoparticles (Au_x-Ag_yNPs). Au_x-Ag_yNPs were prepared according to a previously published procedure [25]. The procedure has been modified in order to prepare bimetallic nanoparticles. Briefly, 30 mL of aqueous solutions containing the respective amount of HAuCl₄ and AgNO₃ to give nanoparticles Au₁₀₀ (M1), Au-Ag_{90/10} (M2), Au-Ag_{80/20} (M3), and Au-Ag_{70/30} (M4) was prepared (see Table 1) and was added to 10 mL of toluene (Aldrich) containing 0.34 mM of tetraoctylammonium bromide (TOAB 98%, Fluka) as a phase-transfer agent. Dodecanethiol (Aldrich) was incorporated to these different solutions as a stabilizing agent in an Au-Ag:thiol 2:1 ratio followed by the addition of an excess of NaBH₄ as an aqueous reducing agent. The reaction was allowed to proceed under constant stirring at controlled temperature (80°C), for

3 h. Finally, colored dispersions were obtained and purified several times in ethanol (J. T. Baker). The resulting Au-Ag nanoparticles were characterized by transmission electron microscopy (TEM), UV-Visible spectroscopy (UV-Vis), X-ray diffraction spectroscopy (XRD), and cyclic voltammetry (CV).

2.2. Preparation of Glassy Carbon Modified Electrodes. To remove the thiol stabilizing agent layer from Au_x-Ag_yNPs, the NPs were mixed with Vulcan XC-72 and were heated at 300°C for 2 hours under air atmosphere; the temperature was controlled within 2°C.

Then, Au_x-Ag_yNPs-modified electrodes were prepared as follows: 1 μL aliquot of thiol-Au_x-Ag_yNPs in hexane and Nafion (5% Electrochem) were mixed (1:10 ratio) and cast onto a carbon disk (CD) followed by natural evaporation at room temperature.

2.3. Characterization of Nanoparticles. Synthesized Au_x-Ag_yNPs were characterized using TEM, UV-Vis, XRD, and cyclic voltammetry (CV). TEM characterizations were performed on a TITAN 80-300 FEI microscope and the particle size distribution was measured from about 200 particles using the TEM images. Nanoparticles samples dissolved in hexane were cast onto a carbon-coated copper grid sample holder followed by natural evaporation at room temperature. UV-Vis measurements were carried out on HP spectrophotometer model 8453. XRD measurements were obtained using a Siemens D5000 diffractometer. Spectra were collected from 10 to 80° at a speed of 0.002°·seg⁻¹. Cyclic voltammetric measurements were performed in BioLogic VSP Modular 5 channels Potentiostat/Galvanostat using a three-electrode conventional cell. A separated compartment and an Ag/AgCl electrode were used as reference and a Pt wire as the counter electrode; all potentials were referred to this electrode. Glucose 0.01M in KOH 0.3M solution was used for the electrochemical characterization. The solution was purged for twenty minutes with high-purity nitrogen before taking measurements.

3. Results and Discussion

3.1. Characterization of Au_x-Ag_yNPs

3.1.1. TEM Characterization. Figures 1(a)–1(d) show TEM micrographs of the synthesized Au_x-Ag_y nanoparticles (labeled as M1 to M4) and their particle size distribution. Synthesis of Au_x-Ag_yNPs can be easily controlled to obtain narrow particle size distribution of spherical nanoparticles

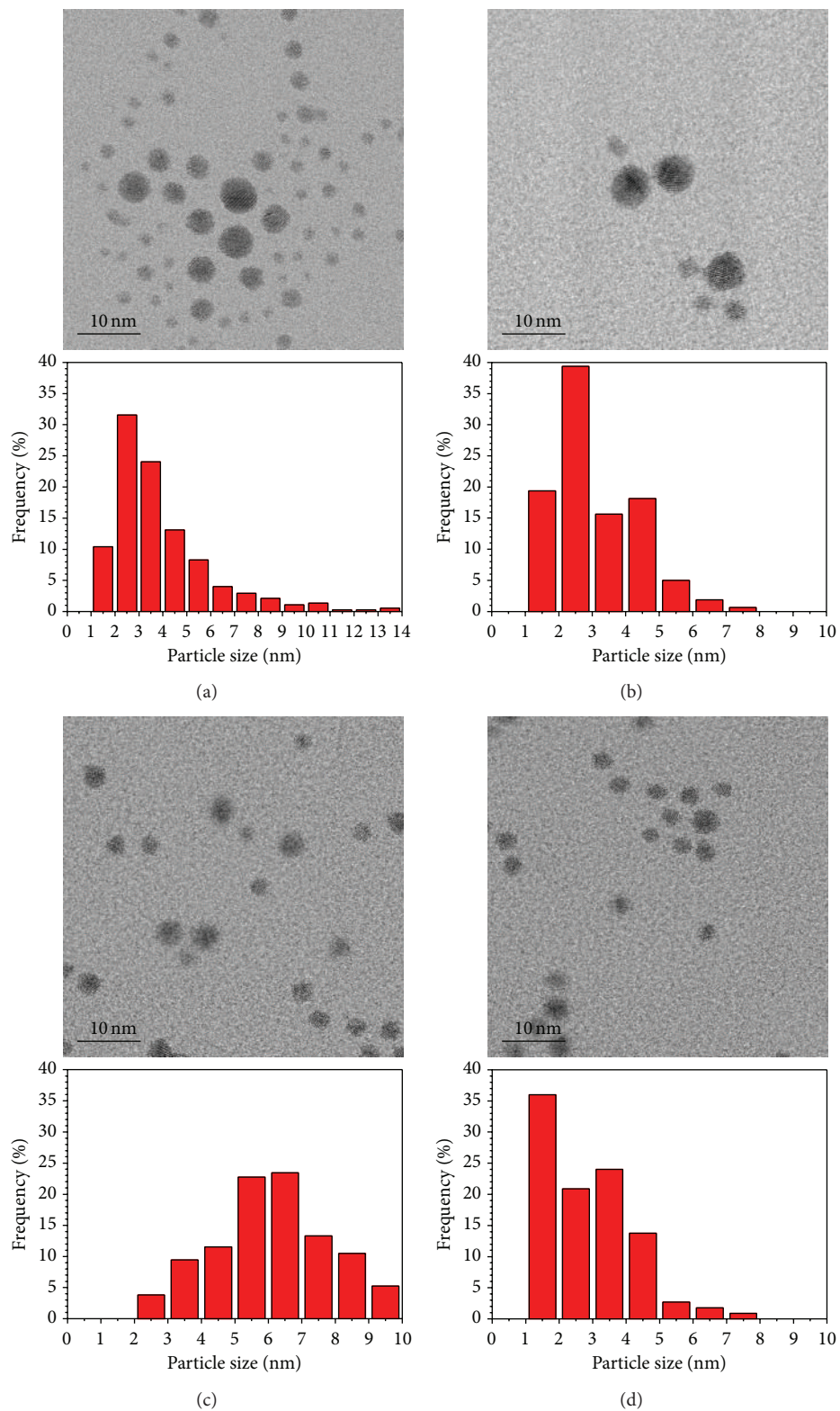


FIGURE 1: TEM images of thiol capped Au-Ag bimetallic nanoparticles. (a) $\text{Au}_{100}\text{Ag}_0$, (b) $\text{Au}_{90}\text{Ag}_{10}$, (c) $\text{Au}_{80}\text{Ag}_{20}$, and (d) $\text{Au}_{70}\text{Ag}_{30}$.

ranging from 1 to 7 nm. Figures 2(a)–2(d) show the Au_x-Ag_y NPs supported in Vulcan after heat treatment for thiol elimination. It can be seen that Au_x-Ag_y NPs keep their spherical form but at the same time there is an increase in size and distribution. The final size ranges from 6 to 40 nm; in spite of the size increase, the Au_x-Ag_y NPs are still small compared to other synthesis methods [33].

3.1.2. UV-Visible. It is well known that nanoparticles have surface plasmon (SP) resonance absorption bands in the visible region. SP resonance bands are strongly dependent on the size, shape, composition, and medium dielectric properties [43–46].

Figure 3 shows UV-Visible spectra from Au_x-Ag_y nanoparticles dispersed in hexane. Au and Ag nanoparticles are known to have plasmon bands in the visible region located at 520 and 420 nm, respectively. In the figure, distinct peaks are observed clearly at 530, 520, 512, and 506 nm; all these peaks are located at intermediate positions between the Au and Ag plasmon bands. The plasmon band is blue-shifted as the silver amount increases.

Two plasmon bands would be expected for a physical mixture of Au and Ag nanoparticles and the formation of an Au-Ag alloy could be deduced from the fact that the optical absorption spectrum shows only one plasmon band for all the samples [47, 48].

The formation of spherical Au_x-Ag_y NPs was demonstrated by TEM (Figure 1). Indeed, upon heat treatment for thiol elimination, the Au_x-Ag_y NPs, in spite of slight size increase, keep the spherical form as shown in Figure 2. Results are in agreement with the literature [25].

3.1.3. XRD Characterization. Figure 4 shows the XRD patterns of the different NPs synthesized. XRD analysis revealed in all the samples the presence of four representative diffraction peaks of face-centered cubic (fcc) structure that correspond to (111), (200), (220), and (311) planes. The angles of these diffraction peaks in all the samples were greater than those for pure Ag (38.11, 44.27, 64.42, and 77.47°) and lower than those for pure Au (38.18, 44.39, 64.57, and 77.54°) according to the standards for Ag [JCPDS 04-0783] and Au [JCPDS 04-0784]. These results confirm again the formation of an alloy of Au-Ag. No other impurity peak is detected in the samples.

The intensity of each signal respect to the other signals means the proportion of each orientation present in that particular nanoparticle. For nanoparticles synthesized by our method, the main factor influencing the orientation plane is the Au-Ag : thiol ratio [25]. In this case, we used a constant Au-Ag : thiol ratio of 2 : 1 in order to obtain a (111) : (200) plane ratio of 2.3–2.8.

3.1.4. Electrochemical Characterization. We have used cyclic voltammetry for the Au_x-Ag_y NPs electrochemical characterization. Figure 5 shows the response of both electrodes, Au polycrystalline (Poly-Au) (Figure 5(a)) and carbon disk Au_{100} nanoparticle-modified electrode (Figure 5(b)) in 0.3 M KOH. We can see the typical Au voltammetric response, that is,

the formation and reduction of Au oxides. The surface area of the Au_{100} NPs electrode was larger than that of a Poly-Au electrode by integrating the reduction charge of gold oxide monolayer. It indicated that there was nanostructured gold on the Au NPs electrode. The Au_{100} NPs electrode exhibited the same behavior of Poly-Au electrode, having higher current densities of relative peaks compared to that of Poly-Au electrode. Poly-Au and Au_{100} NPs electrodes exhibit the anodic peak located at 0.28 V corresponding to the oxidation of gold. The cathodic peak is located at 0.07 V for Au_{100} NPs and 0.1 V for Poly-Au corresponding to the subsequent reduction of the gold oxides. Nevertheless, there was a weak cathodic peak located at -0.2 V for Au_{100} NPs and -0.18 V for Poly-Au attributed to desorption of hydroxide anions.

As the content of Ag in nanoparticles increases ($Au_{80}Ag_{20}$ and $Au_{70}Ag_{30}$, Figures 5(c) and 5(d)), the voltammogram changes to take the form of that of Ag nanoparticles in alkaline media (Figures 5(e) and 6(f)) [49]. The cyclic voltammograms of the silver disk electrode or silver nanoparticle-modified electrode in alkaline media show three anodic peaks (Ox_1 , Ox_2 , and Ox_3) appearing at 0.25, 0.33, and 0.65 V, respectively (Figures 5(e) and 6(f)). During a reverse scan, two cathodic peaks (R_1 and R_2) appeared at 0.38 and 0.06 V, respectively, as reported in previous studies [49]. The first anodic peak (Ox_1) is due to the electroformation of the monolayer of Ag_2O . The second anodic peak (Ox_2) is due to the formation of the multilayer of Ag_2O . The third peak (Ox_3) is due to the oxidation of Ag_2O to AgO or direct oxidation of Ag to AgO.

The cathodic current peak R_1 is due to the reduction of AgO to Ag_2O , and R_2 corresponds to the reduction of Ag_2O to Ag. A small anodic peak (Ox_4) at 0.63 V appears during the cathodic scan, but it was dependent on the scan rate and occurred only when the scan rate is faster than 50 mV/s. Stonehart has suggested that peak Ox_4 is associated with autocatalytic oxidation process to convert Ag_2O to AgO [50]. When the nuclei of AgO formed at the Ag_2O surface during the anodic scan, further formation of AgO became easy and occurred at a lower potential than the initial formation of AgO nuclei. Therefore, during the cathodic scan, further formation of AgO resulted in the appearance of a small anodic peak.

It can be seen in Figure 5(c) ($Au_{80}Ag_{20}$) that the anodic scan shows three peaks probably due to the oxidation of gold (Ox_1), the electroformation of the monolayer of Ag_2O (Ox_2), and the oxidation of Ag_2O to AgO (Ox_3). The cathodic scan shows also three peaks probably corresponding to the reduction of AgO to a multilayer of Ag_2O (R_1), the reduction of Ag_2O to Ag (R_2), and the reduction of Au oxides (R_3).

As a consequence of the increase in Ag content, the anodic scan of $Au_{70}Ag_{30}$ NPs shows two peaks. The first one (Ox_1) is clearly due to the simultaneous formation of Au oxides and the formation of the Ag_2O monolayer because practically these two processes take place at the same potential resulting in one peak; the second anodic peak (Ox_2) is due to the oxidation of Ag_2O to AgO. The cathodic scan shows four peaks: R_1 is due to the reduction of AgO to a multilayer of Ag_2O , R_2 is due to the reduction of Ag_2O to Ag, and

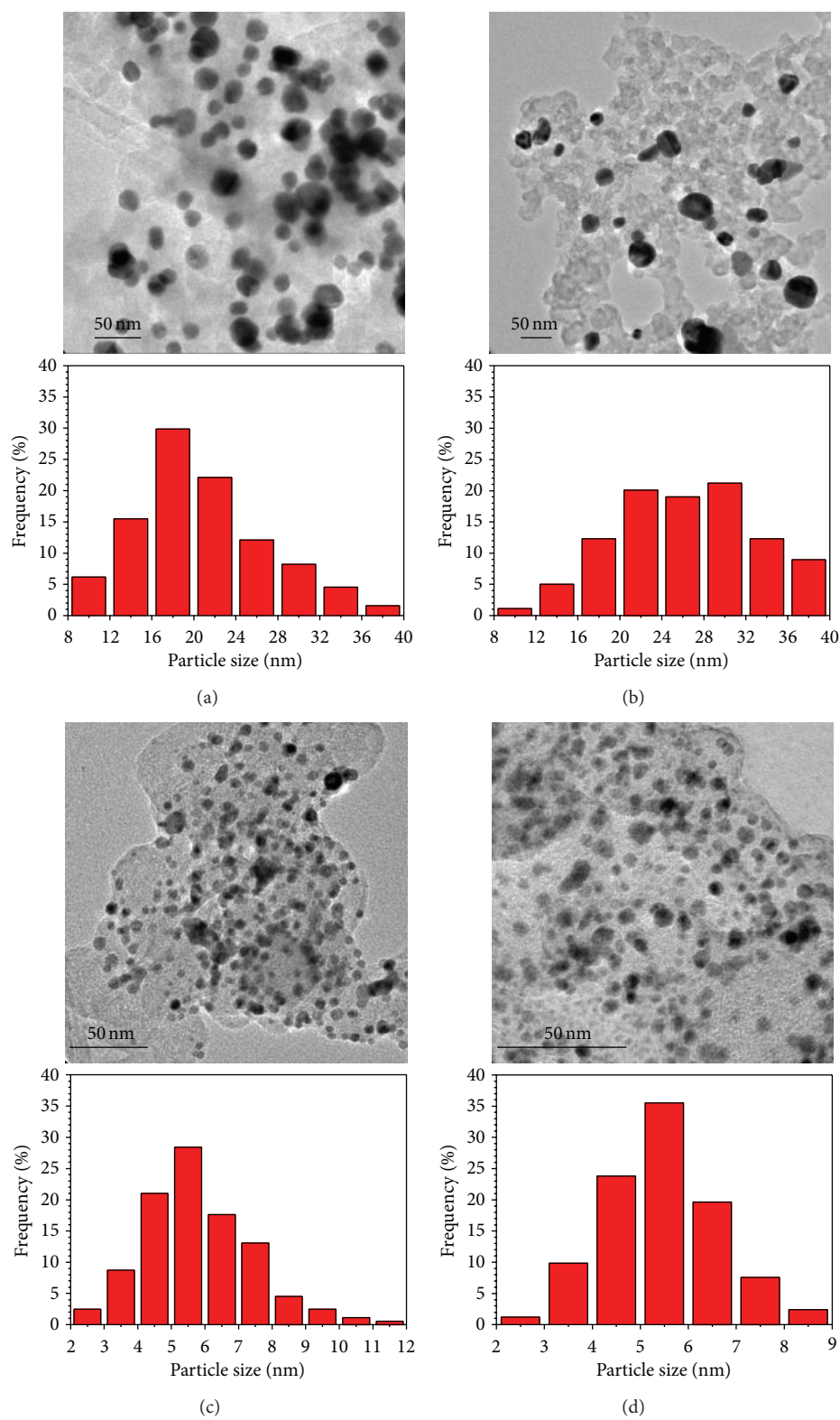


FIGURE 2: TEM images of Au-Ag bimetallic nanoparticles supported in Vulcan after heat treatment for thiol elimination. (a) $\text{Au}_{100}\text{Ag}_0$, (b) $\text{Au}_{90}\text{Ag}_{10}$, (c) $\text{Au}_{80}\text{Ag}_{20}$, and (d) $\text{Au}_{70}\text{Ag}_{30}$.

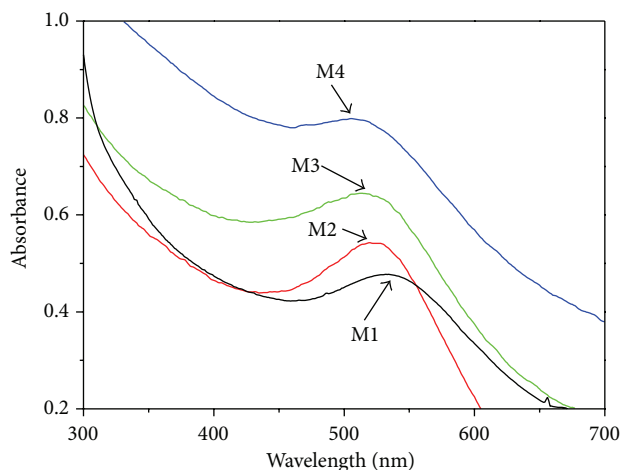


FIGURE 3: UV-vis spectra of bimetallic nanoparticles at different Au-Ag molar compositions. (M1) $\text{Au}_{100}\text{Ag}_0$, (M2) $\text{Au}_{90}\text{Ag}_{10}$, (M3) $\text{Au}_{80}\text{Ag}_{20}$, and (M4) $\text{Au}_{70}\text{Ag}_{30}$.

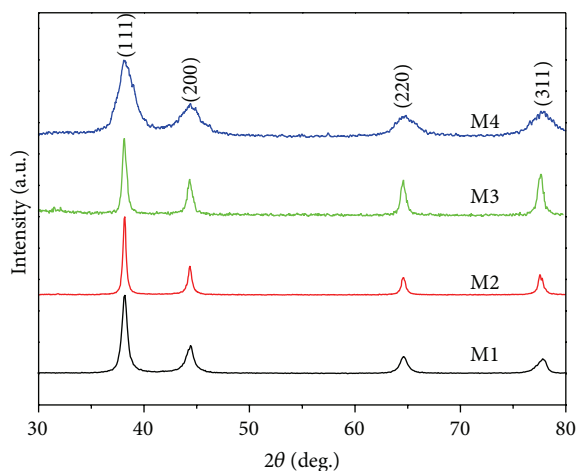


FIGURE 4: XRD patterns of different nanoparticles. (M1) $\text{Au}_{100}\text{Ag}_0$, (M2) $\text{Au}_{90}\text{Ag}_{10}$, (M3) $\text{Au}_{80}\text{Ag}_{20}$, and (M4) $\text{Au}_{70}\text{Ag}_{30}$.

peaks R_3 and R_4 are due to the reduction of the gold oxides and the desorption of hydroxide anions. These results are in agreement with others works [49, 51].

3.1.5. Electrochemical Oxidation of Glucose on AuNPs and Au-AgNPs. Figures 6(a)–6(e) compares the voltammograms obtained for the electrochemical oxidation of 10 mM glucose at the Poly-Au electrode and the $\text{Au}_x\text{-Ag}_y\text{NPs}$ electrodes in 0.3 M KOH solution. The Poly-Au and the $\text{Au}_x\text{-Ag}_y\text{NPs}$ electrodes demonstrated a typical voltammetric response for glucose. Interestingly, the current density of oxidation of glucose on the $\text{Au}_x\text{-Ag}_y\text{NPs}$ electrodes was higher than that on Poly-Au electrode; it could be attributed to the high surface area of $\text{Au}_x\text{-Ag}_y\text{NPs}$. However, the only $\text{Au}_x\text{-Ag}_y\text{NPs}$ electrode that did not show better performance is the M4 electrode ($\text{Au}_{70}\text{-Ag}_{30}$); hence, we discard it for further experiments and analysis.

TABLE 2: Oxidation peak and current density as a function of Ag content.

Sample	Potential, E/V versus Ag/AgCl/KCl sat'd	Current density (mAcm^{-2}) @ 0.49 V versus Ag/AgCl/KCl sat'd
Poly-Au	-0.52 ± 0.01	1.0 ± 0.1
M1 ($\text{Au}_{100}\text{-Ag}_0$)	-0.39 ± 0.03	1.2 ± 0.1
M2 ($\text{Au}_{90}\text{-Ag}_{10}$)	-0.41 ± 0.04	0.82 ± 0.1
M3 ($\text{Au}_{80}\text{-Ag}_{20}$)	-0.49 ± 0.04	1.9 ± 0.3
M4 ($\text{Au}_{70}\text{-Ag}_{30}$)	-0.54 ± 0.04	0.5 ± 0.1

There is also a shift of the glucose potential oxidation on the $\text{Au}_x\text{-Ag}_y\text{NPs}$ M1, M2, and M3 electrodes with respect to the Poly-Au electrode (see Table 2); the shift is to less-negative potentials and reveals that the $\text{Au}_x\text{-Ag}_y\text{NPs}$ electrodes could catalyze the oxidation of glucose. Indeed, we show in Table 2, for comparison purposes, the current density under the same potential for the electrode tested. These results are similar to that of Qiaofan's work on glucose oxidation in an alkaline electrolyte obtained at bimetallic Au-Ag/RGO/GC (bimetallic Au-Ag/reduced graphene oxide/glassy carbon) nanoparticles modified electrode [51].

The CV curves of the $\text{Au}_x\text{-Ag}_y\text{NPs}$ electrode presented a typical two-step oxidation process and three obvious oxidation peaks in the positive scan were observed. As the mechanism for the electrocatalytic oxidation of glucose at $\text{Au}_x\text{-Ag}_y\text{NPs}$ electrodes is a multistep one, the first step mediated the chemisorptions of hydroxide anions onto the electrode surface, leading to the formation of hydrous gold-silver oxide ($\text{Au}_x\text{-Ag}_y\text{OH}_{\text{ads}}$) which was believed to be the catalytic component of $\text{Au}_x\text{-Ag}_y\text{NPs}$ electrodes [52].

The glucose oxidation highly depends on the quantity of $\text{Au}_x\text{-Ag}_y\text{OH}_{\text{ads}}$ and the premonolayer oxidation was enhanced at $\text{Au}_x\text{-Ag}_y\text{NPs}$ surface. The first peak, Ox_1 , located between -0.54 and -0.39 V could be attributed to the electroadsorption of glucose to form adsorbed intermediate gluconolactone, releasing one proton per glucose molecule. At around these potentials, there could be a very limited number of $\text{Au}_x\text{-Ag}_y\text{OH}_{\text{ads}}$ sites on the $\text{Au}_x\text{-Ag}_y\text{NPs}$ surfaces due to the reductive nature of the electrodes potential. Glucose molecules interacted with the $\text{Au}_x\text{-Ag}_y\text{OH}_{\text{ads}}$ sites to give rise to the intermediate, gluconolactone [53, 54]. Nevertheless, the accumulation of gluconolactone blocks the active sites of the $\text{Au}_x\text{-Ag}_y\text{NPs}$ electrode surface inhibiting the direct oxidation of glucose, leading to the decrease of current density. The second oxidation peak Ox_2 appeared at a more positive potential located between 0.18 and 0.26 V depending on the Ag content in the electrode. When the potential reaches those values, the population of $\text{Au}_x\text{-Ag}_y\text{OH}_{\text{ads}}$ sites on the $\text{Au}_x\text{-Ag}_y\text{NPs}$ electrode increased; hence, catalytic oxidation of the intermediates takes place. A further positive increase in the potential to around 0.6 V gives rise to the formation of gold-silver oxides on the surface of $\text{Au}_x\text{-Ag}_y\text{NPs}$. The formation of Au-Ag oxides results in a decrease of the number of the $\text{Au}_x\text{-Ag}_y\text{OH}_{\text{ads}}$ sites on the surface $\text{Au}_x\text{-Ag}_y\text{NPs}$ and impedes the electrocatalytic oxidation of glucose and by-products. The

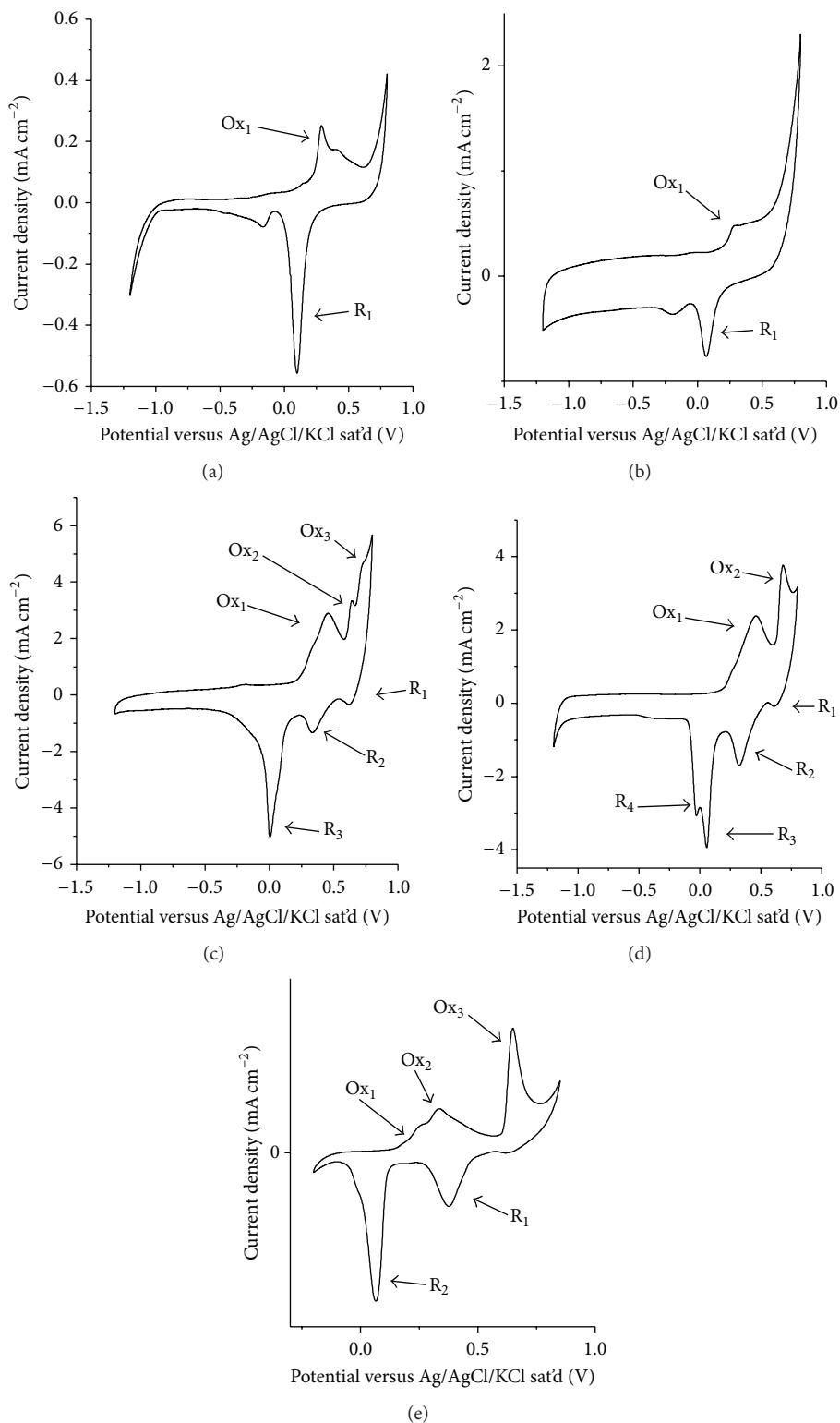


FIGURE 5: CV curves in 0.3 M KOH solution for (a) solid Au electrode, (b) Au₁₀₀, (c) Au₈₀Ag₂₀, (d) Au₇₀Ag₃₀, and (e) Au₀Ag₁₀₀. Scan rate, 50 mV s⁻¹. Scan direction →.

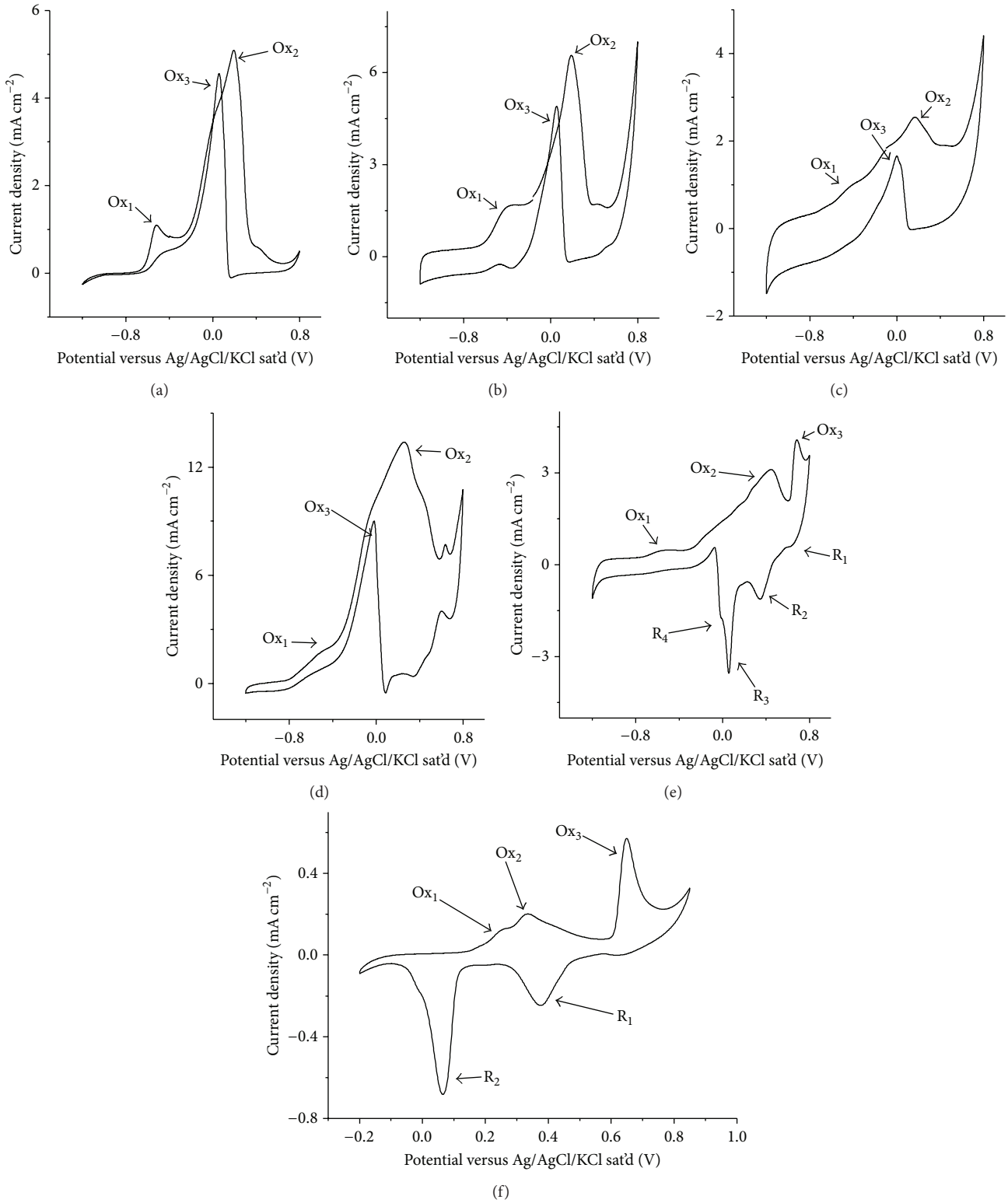


FIGURE 6: CV curves in 0.3 M KOH + 10 mM glucose solution for (a) solid Au electrode, (b) Au₁₀₀NP electrode, (c) Au₉₀Ag₁₀, (d) Au₈₀Ag₂₀, (e) Au₇₀Ag₃₀, and (f) Au₀Ag₁₀₀. Scan rate, 50 mVs⁻¹. Scan direction → .

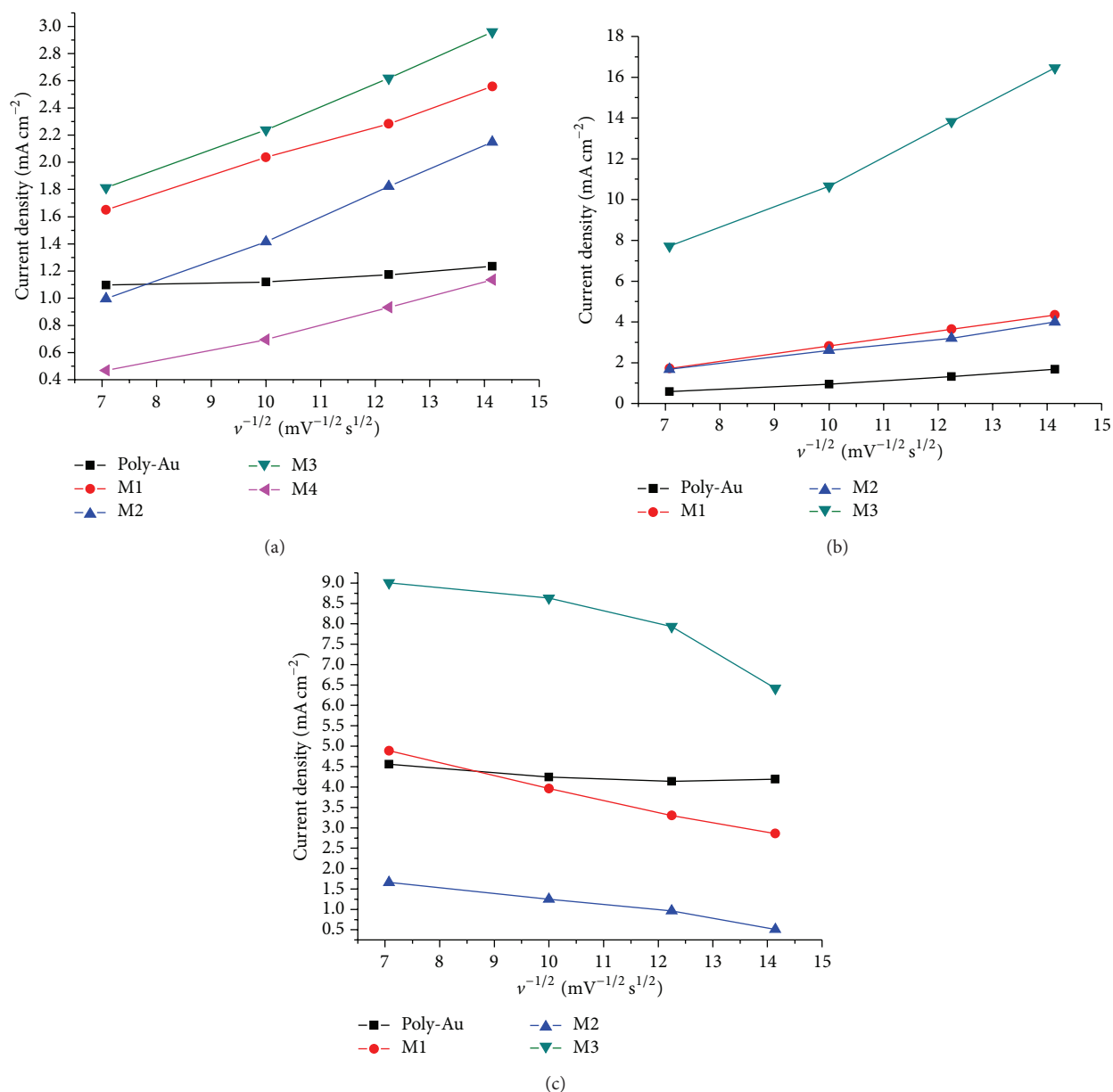


FIGURE 7: Plots of current density versus $V^{-1/2}$ (a) first oxidation scan peak, (b) second oxidation scan peak, and (c) oxidation cathodic peak.

current density, then, decreases dramatically at more positive values than 0.60 V, due to formation of gold and silver oxides. In the negative potential scan, the reduction of the surface gold and silver oxides would occur at the potential more negative than 0.16 V. Then, enough surface active sites would be available for the direct oxidation of glucose, resulting in a sharp increase in anodic current showing a peak (Ox_3), located between 0.001 and 0.15 V, depending on the Ag content in the electrode. Tang's group had reported a similar result; that is, there is a sharp increase in anodic current with a peak at 0.1 V [53]. The surface structure of a gold electrode influenced the electrooxidation of glucose via the influence on the adsorption of OH^- anions and gold oxide surface monolayer formation [55]. The as-prepared $\text{Au}_x\text{-Ag}_y\text{NPs}$

electrode exhibited better performance on electrocatalytic oxidation toward glucose than a Poly-Au electrode.

To evaluate the kinetics of the glucose oxidation on the $\text{Au}_x\text{-Ag}_y\text{NPs}$, the CVs of the electrodes in a 0.3 M KOH solution containing 10 mM glucose at different scan rates were recorded (figure not shown). The peak Ox_1 in the positive scan, located between -0.54 and -0.39 V, corresponds to the direct oxidation of glucose and the current density is proportional to the square root of scan rate for all the electrodes used (Poly-Au, M1, M2, M3, and M4, Figure 7(a)); this fact suggests a linear diffusion-controlled process. Indeed, it is in agreement with the proposed mechanism for peak Ox_1 , in which sufficient active sites on the hydroxyl coated gold surface allowed direct oxidation of

glucose to generate gluconolactone [25, 56]. We can see that the order from better to worst with respect to the glucose oxidation is M3 > M1 > M2 > Poly-Au > M4. As expected, the current density of all electrodes increases as scan rate rises but that of Poly-Au remains practically unchanged. Furthermore, the slope of Au_x-Ag_yNPs increases depending on the Ag content in the NPs. The Au₈₀-Ag₂₀ electrode has the highest slope, that is, the highest glucose oxidation rate.

In Figure 7(b), we can see the plot of current density versus square root of scan rate corresponding to the further oxidation of gluconolactone located between 0.18 and 0.26 V (Ox₂) on the same electrodes except that of M4. Figure 7(b) suggests again that the oxidation of gluconolactone is also a diffusion-controlled process. The order from better to worst is M3 > M1 > Poly-Au > M2. This time, the slope of Poly-Au increases as expected; we are working on the matter.

Finally, Figure 7(c) shows the plot of current density versus square root of scan rate for the oxidation peak Ox₃. Interestingly, as could be seen, peak Ox₃ corresponds to the direct oxidation of glucose in cathodic scan and is also linear versus scan rates. Indeed, this is a typical adsorption-controlled process corresponding to a fast electron-transfer behavior. In the negative potential scan, the reduction of the gold surface oxides provides enough surface active sites for the direct oxidation of glucose; they could account for the appearance of peak Ox₃. The order from better to worst is M3 > Poly-Au > M1 > M2. This time, the slope of Poly-Au remains again unchanged.

None of the straight lines of plots in Figures 7(a), 7(b), and 7(c) go through origin indicating a previous chemical step in the oxidation process; as noted above, this step is probably due to the chemisorption of hydroxide anions onto the gold and silver surface, leading to the formation of hydrous oxides (Au_x-Ag_yOH_{ads}), which are believed to be the catalytic component of Au_x-Ag_yNPs electrodes, particularly Au₈₀-Ag₂₀NPs electrode.

4. Conclusion

The nanoparticles applications, for instance, glucose oxidation, critically depend on their specific catalytic activity; unfortunately, it is still poorly understood [57]. Experimental evidence that can be found in literature points towards several variables affecting it, that is, nanoparticle size [57], nanoparticle crystal orientation [56], and composition of nanoparticle [51]. It is admitted that the glucose oxidation depends on the presence of what is known as monolayer or premonolayer of AuOH_{ads} or AgOH_{ads} [48]; at higher potential, the formation of Au and Ag oxides impedes the glucose oxidation. Nevertheless, Mikhlin et al. [57] found that the formation of AgO proceeded readily at the “primary” oxide for nanoparticles of about 12 nm but was retarded at the smaller ones. These findings are in agreement with our previous work where we have found a maximum in the catalytic activity for Au nanoparticles of about 6 nm and could explain the present findings; that is, smaller nanoparticles have the highest catalytic activity towards glucose oxidation.

Regarding nanoparticle composition, the experimental evidence strongly suggests that the best composition is around 80% Au and 20% Ag.

Indeed, we have performed the present study for a (111):(200) plane ratio of 2.3–2.8. Studies to optimizing the NPs size, Au-Ag ratio, and crystallographic orientation are underway.

Conflict of Interests

The authors declare that there is no conflict of interests regarding the publication of this paper.

Acknowledgments

Authors are grateful for financial support from CONACYT Project CB-2012-01 183463 and scholarship of Nancy Gabriela García Morales. Authors would also thank Azucena Osornio-Villa, Carlos Fernando Bautista Alegría, and Erick Montenegro Hernández for helping in preparing this paper.

References

- [1] Y. B. Vassilyev, O. A. Khazova, and N. N. Nikolaeva, “Kinetics and mechanism of glucose electrooxidation on different electrode-catalysts. Part II. Effect of the nature of the electrode and the electrooxidation mechanism,” *Journal of Electroanalytical Chemistry*, vol. 196, no. 1, pp. 127–144, 1985.
- [2] L. A. Larew and D. C. Johnson, “Concentration dependence of the mechanism of glucose oxidation at gold electrodes in alkaline media,” *Journal of Electroanalytical Chemistry and Interfacial Electrochemistry*, vol. 262, no. 1-2, pp. 167–182, 1989.
- [3] R. R. Adzic, M. W. Hsiao, and E. B. Yeager, “Electrochemical oxidation of glucose on single crystal gold surfaces,” *Journal of Electroanalytical Chemistry and Interfacial Electrochemistry*, vol. 260, no. 2, pp. 475–485, 1989.
- [4] K. B. Kokoh, J.-M. Léger, B. Beden, H. Huser, and C. Lamy, “On line’ chromatographic analysis of the products resulting from the electrocatalytic oxidation of d-glucose on pure and adatoms modified Pt and Au electrodes—Part II. Alkaline medium,” *Electrochimica Acta*, vol. 37, no. 11, pp. 1909–1918, 1992.
- [5] M. W. Hsiao, R. R. Adžić, and E. B. Yeager, “Electrochemical oxidation of glucose on single crystal and polycrystalline gold surfaces in phosphate buffer,” *Journal of the Electrochemical Society*, vol. 143, no. 3, pp. 759–767, 1996.
- [6] S. B. Aoun, Z. Dursun, T. Koga, G. S. Bang, T. Sotomura, and I. Taniguchi, “Effect of metal ad-layers on Au(111) electrodes on electrocatalytic oxidation of glucose in an alkaline solution,” *Journal of Electroanalytical Chemistry*, vol. 567, no. 2, pp. 175–183, 2004.
- [7] S. Ben Aoun, G. S. Bang, T. Koga, Y. Nonaka, T. Sotomura, and I. Taniguchi, “Electrocatalytic oxidation of sugars on silver-UPD single crystal gold electrodes in alkaline solutions,” *Electrochemistry Communications*, vol. 5, no. 4, pp. 317–320, 2003.
- [8] M. Tominaga, T. Shimazoe, M. Nagashima, and I. Taniguchi, “Electrocatalytic oxidation of glucose at gold nanoparticle-modified carbon electrodes in alkaline and neutral solutions,” *Electrochemistry Communications*, vol. 7, no. 2, pp. 189–193, 2005.

- [9] M. Tominaga, T. Shimazoe, M. Nagashima et al., "Electrocatalytic oxidation of glucose at gold-silver alloy, silver and gold nanoparticles in an alkaline solution," *Journal of Electroanalytical Chemistry*, vol. 590, no. 1, pp. 37–46, 2006.
- [10] M. Tominaga, M. Nagashima, K. Nishiyama, and I. Taniguchi, "Surface poisoning during electrocatalytic monosaccharide oxidation reactions at gold electrodes in alkaline medium," *Electrochemistry Communications*, vol. 9, no. 8, pp. 1892–1898, 2007.
- [11] M. Tominaga, T. Shimazoe, M. Nagashima, and I. Taniguchi, "Electrocatalytic oxidation of glucose at carbon electrodes modified with gold and gold-platinum alloy nanoparticles in an alkaline solution," *Chemistry Letters*, vol. 34, no. 2, pp. 202–203, 2005.
- [12] M. Guerra-Balcázar, D. Morales-Acosta, F. Castañeda, J. Ledesma-García, and L. G. Arriaga, "Synthesis of Au/C and Au/Pani for anode electrodes in glucose microfluidic fuel cell," *Electrochemistry Communications*, vol. 12, no. 6, pp. 864–867, 2010.
- [13] F. M. Cuevas-Muñiz, M. Guerra-Balcázar, F. Castañeda, J. Ledesma-García, and L. G. Arriaga, "Performance of Au and AuAg nanoparticles supported on Vulcan in a glucose laminar membraneless microfuel cell," *Journal of Power Sources*, vol. 196, no. 14, pp. 5853–5857, 2011.
- [14] M. Guerra-Balcázar, F. M. Cuevas-Muñiz, F. Castañeda et al., "Carbon nanotubes as catalyst support in a glucose microfluidic fuel cell in basic media," *Electrochimica Acta*, vol. 56, no. 24, pp. 8758–8762, 2011.
- [15] M. Meena Kumari, J. Jacob, and D. Philip, "Green synthesis and applications of Au-Ag bimetallic nanoparticles," *Spectrochimica Acta Part A: Molecular and Biomolecular Spectroscopy*, vol. 137, pp. 185–192, 2015.
- [16] Y. Feng, H. Yin, A. Wang, and W. Xue, "Selectively catalytic oxidation of 1,2-propanediol to lactic, formic, and acetic acids over Ag nanoparticles under mild reaction conditions," *Journal of Catalysis*, vol. 326, pp. 26–37, 2015.
- [17] D. Marković, Z. Šaponjić, M. Radoičić et al., "Sonophotocatalytic degradation of dye C.I. Acid Orange 7 by TiO₂ and Ag nanoparticles immobilized on corona pretreated polypropylene non-woven fabric," *Ultrasonics Sonochemistry*, vol. 24, pp. 221–229, 2015.
- [18] K. Tian, S. Alex, G. Siegel, and A. Tiwari, "Enzymatic glucose sensor based on Au nanoparticle and plant-like ZnO film modified electrode," *Materials Science and Engineering C*, vol. 46, pp. 548–552, 2015.
- [19] A. Samphao, P. Butmee, J. Jitcharoen, L. Švorc, G. Raber, and K. Kalcher, "Flow-injection amperometric determination of glucose using a biosensor based on immobilization of glucose oxidase onto Au seeds decorated on core Fe₃O₄ nanoparticles," *Talanta*, vol. 142, pp. 35–42, 2015.
- [20] N. German, A. Kausaite-Minkstimiene, A. Ramanavicius, T. Semashko, R. Mikhailova, and A. Ramanaviciene, "The use of different glucose oxidases for the development of an amperometric reagentless glucose biosensor based on gold nanoparticles covered by polypyrrole," *Electrochimica Acta*, vol. 169, pp. 326–333, 2015.
- [21] X. Wang, X. Li, C. Luo, M. Sun, L. Li, and H. Duan, "Ultrasensitive molecularly imprinted electrochemical sensor based on magnetism graphene oxide/ β -cyclodextrin/Au nanoparticles composites for chrysoidine analysis," *Electrochimica Acta*, vol. 130, pp. 519–525, 2014.
- [22] M. Harutal, H. Kageyama, N. Kamijo, T. Kobayashi, and F. Delannay, "Fine structure of novel gold catalysts prepared by coprecipitation," *Studies in Surface Science and Catalysis*, vol. 44, pp. 33–42, 1989.
- [23] J. M. Gottfried, K. J. Schmidt, S. L. M. Schroeder, and K. Christmann, "Adsorption of carbon monoxide on Au(1 1 0)-(1 \times 2)," *Surface Science*, vol. 536, no. 1–3, pp. 206–224, 2003.
- [24] M. S. El-Deab, T. Sotomura, and T. Ohsaka, "Oxygen reduction at electrochemically deposited crystallographically oriented Au (100)-like gold nanoparticles," *Electrochemistry Communications*, vol. 7, no. 1, pp. 29–34, 2005.
- [25] M. Guerra-Balcázar, J. Torres-González, I. Terol-Villalobos, J. Morales-Hernández, and F. Castañeda, "Glassy carbon electrode-supported Au nanoparticles for the glucose electrooxidation: on the role of crystallographic orientation," *Journal of Nanomaterials*, vol. 2012, Article ID 387581, 8 pages, 2012.
- [26] T. N. Huan, S. Kim, P. Van Tuong, and H. Chung, "Au-Ag bimetallic nanodendrite synthesized via simultaneous co-electrodeposition and its application as a SERS substrate," *RSC Advances*, vol. 4, no. 8, pp. 3929–3933, 2014.
- [27] C. Gao, Y. Hu, M. Wang, M. Chi, and Y. Yin, "Fully alloyed Ag/Au nanospheres: combining the plasmonic property of Ag with the stability of Au," *Journal of the American Chemical Society*, vol. 136, no. 20, pp. 7474–7479, 2014.
- [28] Y. Cui, B. Ren, J.-L. Yao, R.-A. Gu, and Z.-Q. Tian, "Synthesis of Ag_{core}Au_{shell} bimetallic nanoparticles for immunoassay based on surface-enhanced Raman spectroscopy," *The Journal of Physical Chemistry B*, vol. 110, no. 9, pp. 4002–4006, 2006.
- [29] S. E. Hunyadi and C. J. Murphy, "Bimetallic silver-gold nanowires: fabrication and use in surface-enhanced Raman scattering," *Journal of Materials Chemistry*, vol. 16, no. 40, pp. 3929–3935, 2006.
- [30] F. Xiao, F. Zhao, D. Mei, Z. Mo, and B. Zeng, "Nonenzymatic glucose sensor based on ultrasonic-electrodeposition of bimetallic PtM (M = Ru, Pd and Au) nanoparticles on carbon nanotubes-ionic liquid composite film," *Biosensors and Bioelectronics*, vol. 24, no. 12, pp. 3481–3486, 2009.
- [31] J. Suntivich, Z. Xu, C. E. Carlton et al., "Surface composition tuning of Au-Pt bimetallic nanoparticles for enhanced carbon monoxide and methanol electro-oxidation," *Journal of the American Chemical Society*, vol. 135, no. 21, pp. 7985–7991, 2013.
- [32] H. Zhang, M. Haba, M. Okumura, T. Akita, S. Hashimoto, and N. Toshima, "Novel formation of Ag/Au bimetallic nanoparticles by physical mixture of monometallic nanoparticles in dispersions and their application to catalysts for aerobic glucose oxidation," *Langmuir*, vol. 29, no. 33, pp. 10330–10339, 2013.
- [33] H. Yu and Y. He, "Seed-assisted synthesis of dendritic Au-Ag bimetallic nanoparticles with chemiluminescence activity and their application in glucose detection," *Sensors and Actuators B: Chemical*, vol. 209, pp. 877–882, 2015.
- [34] J. Huang, S. Vongehr, S. Tang, H. Lu, J. S. And, and X. Meng, "Ag dendrite-based Au/Ag bimetallic nanostructures with strongly enhanced catalytic activity," *Langmuir*, vol. 25, no. 19, pp. 11890–11896, 2009.
- [35] J. N. Chheda, G. W. Huber, and J. A. Dumesic, "Liquid-phase catalytic processing of biomass-derived oxygenated hydrocarbons to fuels and chemicals," *Angewandte Chemie—International Edition*, vol. 46, no. 38, pp. 7164–7183, 2007.
- [36] H. Zhang, T. Watanabe, M. Okumura, M. Haruta, and N. Toshima, "Catalytically highly active top gold atom on palladium nanocluster," *Nature Materials*, vol. 11, no. 1, pp. 49–52, 2012.

- [37] S. Biella, L. Prati, and M. Rossi, "Selective oxidation of D-glucose on gold catalyst," *Journal of Catalysis*, vol. 206, no. 2, pp. 242–247, 2002.
- [38] T. Ishida, N. Kinoshita, H. Okatsu, T. Akita, T. Takei, and M. Haruta, "Influence of the support and the size of gold clusters on catalytic activity for glucose oxidation," *Angewandte Chemie International Edition*, vol. 47, no. 48, pp. 9265–9268, 2008.
- [39] C. Jin and Z. Chen, "Electrocatalytic oxidation of glucose on gold-platinum nanocomposite electrodes and platinum-modified gold electrodes," *Synthetic Metals*, vol. 157, no. 13-15, pp. 592–596, 2007.
- [40] M. Tominaga, T. Shimazoe, M. Nagashima, and I. Taniguchi, "Composition-activity relationships of carbon electrode-supported bimetallic gold-silver nanoparticles in electrocatalytic oxidation of glucose," *Journal of Electroanalytical Chemistry*, vol. 615, no. 1, pp. 51–61, 2008.
- [41] N. German, A. Ramanavicius, J. Voronovic, and A. Ramanaviciene, "Glucose biosensor based on glucose oxidase and gold nanoparticles of different sizes covered by polypyrrole layer," *Colloids and Surfaces A: Physicochemical and Engineering Aspects*, vol. 413, pp. 224–230, 2012.
- [42] L. Liu, X. Zhang, and J. Chaudhuri, "Size control in the synthesis of 1–6 nm gold nanoparticles using folic acid-chitosan conjugate as a stabilizer," *Materials Research Express*, vol. 1, no. 3, p. 035033, 2014.
- [43] X. Zhang, Y. L. Chen, R.-S. Liu, and D. P. Tsai, "Plasmonic photocatalysis," *Reports on Progress in Physics*, vol. 76, no. 4, Article ID 046401, 41 pages, 2013.
- [44] S. Link and M. A. El-Sayed, "Spectral properties and relaxation dynamics of surface plasmon electronic oscillations in gold and silver nanodots and nanorods," *The Journal of Physical Chemistry B*, vol. 103, no. 40, pp. 8410–8426, 1999.
- [45] Y. Tian and T. Tatsuma, "Mechanisms and applications of plasmon-induced charge separation at TiO₂ films loaded with gold nanoparticles," *Journal of the American Chemical Society*, vol. 127, no. 20, pp. 7632–7637, 2005.
- [46] S. M. Yoo, S. B. Rawal, J. E. Lee et al., "Size-dependence of plasmonic Au nanoparticles in photocatalytic behavior of Au/TiO₂ and Au@SiO₂/TiO₂," *Applied Catalysis A: General*, vol. 499, pp. 47–54, 2015.
- [47] R. Kuladeep, L. Jyothi, K. S. Alee, K. L. N. Deepak, and D. N. Rao, "Laser-assisted synthesis of Au-Ag alloy nanoparticles with tunable surface plasmon resonance frequency," *Optical Materials Express*, vol. 2, no. 2, pp. 161–172, 2012.
- [48] A. Pal, S. Shah, and S. Devi, "Preparation of silver-gold alloy nanoparticles at higher concentration using sodium dodecyl sulfate," *Australian Journal of Chemistry*, vol. 61, no. 1, pp. 66–71, 2008.
- [49] H. Quan, S.-U. Park, and J. Park, "Electrochemical oxidation of glucose on silver nanoparticle-modified composite electrodes," *Electrochimica Acta*, vol. 55, no. 7, pp. 2232–2237, 2010.
- [50] P. Stonehart and F. P. Portante, "Potentiodynamic examination of surface processes and kinetics for the Ag₂O/AgO/OH⁻ system," *Electrochimica Acta*, vol. 13, no. 8, pp. 1805–1814, 1968.
- [51] Q. Shi, G. Diao, and S. Mu, "The electrocatalytic oxidation of glucose on the bimetallic Au-Ag particles-modified reduced graphene oxide electrodes in alkaline solutions," *Electrochimica Acta*, vol. 133, pp. 335–346, 2014.
- [52] L. D. Burke, "Premonolayer oxidation and its role in electrocatalysis," *Electrochimica Acta*, vol. 39, no. 11-12, pp. 1841–1848, 1994.
- [53] J. Wang, J. Gong, Y. Xiong et al., "Shape-dependent electrocatalytic activity of monodispersed gold nanocrystals toward glucose oxidation," *Chemical Communications*, vol. 47, no. 24, pp. 6894–6896, 2011.
- [54] L. Y. Chen, T. Fujita, Y. Ding, and M. W. Chen, "A three-dimensional gold-decorated nanoporous copper core-shell composite for electrocatalysis and nonenzymatic biosensing," *Advanced Functional Materials*, vol. 20, no. 14, pp. 2279–2285, 2010.
- [55] Z. Borkowska, A. Tymosiak-Zielinska, and G. Shul, "Electrooxidation of methanol on polycrystalline and single crystal gold electrodes," *Electrochimica Acta*, vol. 49, no. 8, pp. 1209–1220, 2004.
- [56] J. Wang, X. Cao, X. Wang, S. Yang, and R. Wang, "Electrochemical oxidation and determination of glucose in alkaline media based on Au (111)-like nanoparticle array on indium tin oxide electrode," *Electrochimica Acta*, vol. 138, pp. 174–186, 2014.
- [57] Y. L. Mikhlin, E. A. Vishnyakova, A. S. Romanchenko et al., "Oxidation of Ag nanoparticles in aqueous media: effect of particle size and capping," *Applied Surface Science*, vol. 297, pp. 75–83, 2014.

Review Article

Recent Developments in Environmental Photocatalytic Degradation of Organic Pollutants: The Case of Titanium Dioxide Nanoparticles—A Review

Mphilisi M. Mahlambi,¹ Catherine J. Ngila,¹ and Bhekile B. Mamba²

¹Department of Applied Chemistry, University of Johannesburg, P.O. Box 17011, Doornfontein 2028, South Africa

²Nanotechnology and Water Sustainable Unit, College of Science, Engineering and Technology, University of South Africa, Florida Campus, Johannesburg 17025, South Africa

Correspondence should be addressed to Mphilisi M. Mahlambi; mmahlambi@yahoo.co.uk

Received 29 April 2015; Revised 29 July 2015; Accepted 5 August 2015

Academic Editor: Xin Zhang

Copyright © 2015 Mphilisi M. Mahlambi et al. This is an open access article distributed under the Creative Commons Attribution License, which permits unrestricted use, distribution, and reproduction in any medium, provided the original work is properly cited.

The presence of both organic and inorganic pollutants in water due to industrial, agricultural, and domestic activities has led to the global need for the development of new, improved, and advanced but effective technologies to effectively address the challenges of water quality. It is therefore necessary to develop a technology which would completely remove contaminants from contaminated waters. TiO₂ (titania) nanocatalysts have a proven potential to treat “difficult-to-remove” contaminants and thus are expected to play an important role in the remediation of environmental and pollution challenges. Titania nanoparticles are intended to be both supplementary and complementary to the present water-treatment technologies through the destruction or transformation of hazardous chemical wastes to innocuous end-products, that is, CO₂ and H₂O. This paper therefore explores and summarizes recent efforts in the area of titania nanoparticle synthesis, modifications, and application of titania nanoparticles for water treatment purposes.

1. Introduction

The South African *National Water Act* (Act number 36 of 1998) specifically states that water resources must remain fit for use on a sustainable basis and that their quality must be constantly monitored [1]. Therefore the availability of water should be based not only on the quantity but also on the quality of the available water [2]. However, due to agricultural, industrial, and domestic activities the quality of river water or groundwater continues to deteriorate due to pollution by hazardous materials [3, 4]. Water pollution is defined as the direct or indirect introduction of substances into the water bodies. These pollutants may be harmful to human health or the quality of aquatic ecosystems thus affecting the use of amenities and other legitimate uses of water [1].

The sources of water pollution are categorised as either a point source or nonpoint source (diffuse sources). Point source water pollution occurs when the polluting substance

is emitted directly into the water system, for example, a pipe that spews sewage directly into a river, while nonpoint source (NPS) pollution refers to diffuse contamination which occurs when pollutants enter a water system through runoff, for example, when fertiliser is washed into a river by surface runoffs. Water pollutants can be classified as physical (odour, colour, solids, or temperature), biological (pathogens), or chemical (organic or inorganic compounds) [1, 2, 5–9]. Organic pollutants are of more concern than the other types because of their carcinogenic and mutagenic effects even after exposure to minute concentrations [10, 11].

1.1. Organic Pollutants. Organic contaminants have become of more concern due to the inability of conventional water-treatment technologies to completely decompose these contaminants in aqueous media [12, 13]. The ubiquitous appearance of organic contaminants in sewage effluents, groundwater, drinking water, and sludge poses a significant

threat to humans and aquatic organisms [14]. Volatile organic compounds (VOCs) are known to be toxic and carcinogenic and have been implicated in the depletion of the stratospheric ozone layer while also contributing to global warming [10, 15]. These pollutants have been reported as being mutagenic and hence are responsible for the emergence of antibiotic resistance bacteria and genes [16].

Some organic pollutants are referred to as persistent organic pollutants (POPs) because when they enter the environment, they do not readily break down and may remain there for very long periods of time, for example, polychlorinated biphenyls (PCBs), and may enter the food chains and accumulate to levels detrimental to organisms that are high up in the food chain [17]. Also organic pollutants are a serious threat because they can be transported from the source of contamination through air as vapour or as dust particles by water currents or sediments and released in a new environment [17]. Some of these organic pollutants eventually contaminate groundwater and surface waters; however, groundwater contamination is likely to be the primary source of human contact with these toxic chemicals [18]. Generally, exposure to organic contaminants could be through breathing, through ingestion, through drinking, or by skin contact.

1.2. Natural Organic Matter. Natural organic matter (NOM) is an agglomeration of organic compounds that naturally occur when animal and plant material break down [19–21]. NOM consists of a wide range of compounds with diverse chemical properties (due to geographic origin and age of the decomposing organism) and occurs in all natural water sources [20, 22, 23]. NOM components are a heterogeneous mixture of complex organic materials which consists of both hydrophilic and hydrophobic components. The hydrophilic components are microbial by-products and contain a higher proportion of aliphatic carbon and nitrogenous compounds with relatively high charge density such as amino acids and proteins as well as polysaccharides [22, 24, 25]. Humic substances (HS) constitute the more hydrophobic fraction of NOM and exhibit relatively high specific ultraviolet absorbance (SUVA) values due to the presence of a relatively large proportion of aromatic carbon, phenolic structures, and conjugated double bonds [5, 19, 21, 22, 24, 25].

Due to the complexity of NOM no single tool can give its definitive structural or functional information. Nondestructive spectroscopic techniques appear to be the most useful analytical techniques for NOM characterisation [20]. Treatment options for the removal of NOM include coagulation, the use of magnetic ion-exchange resins, activated carbon, membrane filtration, and advanced oxidation processes [22]. Characterisation of the structure and reactivity of NOM is vital because its presence creates problems in the quality of drinking water as well as in water-treatment processes [20, 26]. The presence of NOM results in an increased coagulant and disinfectant dosage resulting in increased sludge. It also increases biological growth in water-distribution networks and may also result in increased levels of heavy metal complexes and adsorbed organic pollutants [22]. Furthermore, the presence of NOM causes membrane fouling as well as

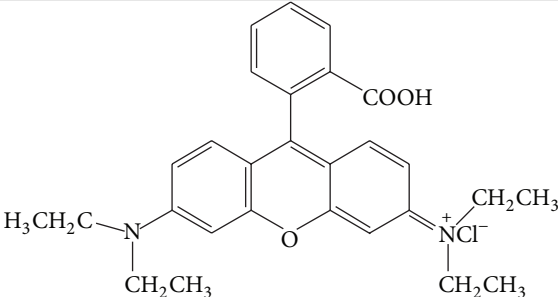
aesthetic and malodour problems in water. The organic acids that result from the oxidation of NOM have the capability to corrode turbines and engineering systems and this affects transportation of contaminants [19, 22, 27, 28]. Thus, understanding the impact of NOM in water-treatment processes is vital for human health and water-treatment plants as well as industrial processes where pure water is a prerequisite.

1.3. Disinfection By-Products. In the water-treatment processes, NOM may have adverse effects since it may react with disinfectants (e.g., chlorine or chloramines) resulting in the formation of disinfection by-products (DBPs), many of which are either carcinogenic or mutagenic [5, 25, 26, 29]. For example, haloacetic acids (HAAs) are a component of DBPs that are considered harmful to human health. These have been found to result in impaired reproductive and developmental retardation when tested on laboratory animals [24, 30–33]. Also, trihalomethanes (THMs) have been classified as possible carcinogens to humans [30, 32, 34, 35]. Nitrosamines are another group of DBPs, formed due to the reaction of NOM with disinfectants that have been reported to be a threat to human life due to its carcinogenicity [32, 36–38].

1.4. Industrial Effluents. Industrial development is directly related to the release of various toxic pollutants into the environment, especially to aqueous streams, and these pollutants are harmful and hazardous to the environment [12, 39–41]. Prevention of industrial pollution is currently a major focus of environmentalists and therefore treatment of industrial effluents before disposal into the ecosystem is imperative to protect human life and environmental quality [3, 40, 42]. Thus, a constant effort to protect water resources is being made by various government and nongovernmental organisations (e.g., US EPA, WHO, and DWAF) through the introduction of increasingly strict legislation covering pollutant release into the environment, with particular emphasis on liquid industrial effluents [5, 40, 43, 44]. There are major types of industries in the industrial complex, for example, pulp and paper mills, food, pharmaceutical, electroplating, textile, photographic, mining, and agriculture, to mention just a few, which do not generate uniform waste streams; industrial effluents are complex mixtures of chemical and biological compositions that have various environmental impacts depending on the source of the toxicant [45, 46].

1.4.1. Textile Industry Effluents. Textile-processing industries form the economic backbone of most developing countries. Effluents from textile industries are characterised by a variety of chemicals generated from the dyeing, bleaching, and washing processes [47, 48]. Wastewaters discharged from textile industries are a serious environmental threat due to their characteristic high colour, fluctuating pH, malodour, high biological oxygen demand (BOD) and chemical oxygen demand (COD), acids, and alkalis as well as various heavy metals that breach environmental standards [48–50]. Dyes are soluble in water and even a small amount of dye is highly visible and reduces the transparency of water bodies [49, 51].

TABLE 1: Molecular structure and chemical properties of Rhodamine B [6, 52–54].

Molecular structure	Chemical properties	
	Class Chemical formula Molecular weight UV absorption maximum	Triphenylmethane $C_{28}H_{31}ClN_2O_3$ $479.02 \text{ g}\cdot\text{mol}^{-1}$ 553 nm
Rhodamine B		

Also, dyes can be mutagens and carcinogens [49, 50], and thus they need to be removed from industrial effluents.

It is estimated that about 1% to 20% of the total world production of dyes is lost to the environment during synthesis and dyeing processes. These textile effluents are an environmental burden as they contain a large amount of azoic, anthraquinonic, and heteropolyaromatic dyes [6, 50]. The discharge of these highly pigmented synthetic dyes to the ecosystem causes aesthetic pollution, eutrophication, and perturbations in aquatic life as they hinder light penetration resulting in decreased photosynthesis [48, 49, 51]. Therefore textile wastewaters need to be treated to acceptable levels to meet the national discharge standard before being discharged to the environmental ecosystem.

1.4.2. Rhodamine B. Rhodamine B (Rh B) is a type of triphenylmethane dyes. Triphenylmethane (TPM) dyes are extensively used in textile, printing, food, photographic, and cosmetic industries [52]. TPM dyes can persist for long periods in the aquatic environment because they are resistant to chemical and biological (bacterial) attacks. Rh B is a common dye in the TPM family, which contains four (4) *N*-ethyl groups at either side of the xanthene rings (Table 1). It has achieved its prominent use due to its good stability as a laser material and is one of the major sources of pollution in the textile and photographic industry effluent streams [53]. Also, although Rhodamine B is a highly phosphorescent (fluorescent) dye, its toxicity is not dependent on the synergic effect of visible light [52, 54]. As a dye in the TPM family (i.e., azoic, anthraquinonic, and heteropolyaromatic dyes), the presence of Rh B in the ecosystem causes aesthetic pollution, eutrophication, and perturbations in aquatic life [6, 50, 52, 53].

1.4.3. Other Industrial Effluents. Other sources of industrial pollution are from surface treatment (mechanical and chemical surface-finishing processes), thermal power stations, and agricultural activities, to name but a few. Effluents originating from surface-treatment processes contain both organic and metal pollution from the washing and rinsing of process baths [43]. Fly ash is the by-product of combustion in thermal power plants using coal and lignite and is mainly used as landfills [39]. However, studies to characterise leachate originating from these landfills have indicated

that leachates contain hazardous pollutants like arsenides, PCBs, and sulfanilamides [14, 16, 55, 56]. Commonly used pesticides from agricultural activities (either domestic or large commercial scale) have high recalcitrant organic groups and hence are extremely difficult to break down through normal degradation [2, 38, 42, 57]. Also, the use of nitrogen-containing fertilisers causes acidification and eutrophication of ecosystems due to leaching [44, 58, 59]. These nitrogen-containing pollutants from agricultural activities are usually intermediates to the formation of refractory organic pollutants [44].

2. Refractory Organic Pollutants

Degradation of refractory organic pollutants is a challenge because these pollutants cannot be degraded using the current water-treatment technologies. They are resistant to aerobic microbial degradation in conventional biological treatment processes and the natural environment [44, 60, 61]. High-molecular-weight organics are the typical refractory pollutants. The presence of refractory pollutants in industrial wastewaters causes problems in the water-treatment system [46]. These pollutants cause biomass poisoning and die-off in conventional biological water-treatment systems. Other techniques such as flocculation, precipitation, or reverse osmosis require posttreatment to dispose of the pollutants while the use of chemical techniques either fails to adequately remove these organic pollutants or results in the formation of DBPs [28, 33, 36, 44, 62].

Current water-treatment technologies are designed to deal with either organic or inorganic pollutants in an aqueous medium, but not both. In addition, due to the diversity and varying chemical properties of organic pollutants these technologies fail to remove pollutants to the required levels. Furthermore, the presence of NOM in water-treatment processes may have adverse effects since it may react with disinfectants (e.g., chlorine or chloramines) and result in the formation of DBPs. Therefore the development of techniques that can remove both contaminants simultaneously without the production of DBPs would be ideal. Nanocatalysts have shown the ability to cost-effectively mineralise recalcitrant organic pollutants and reduce metal ions in aqueous media producing innocuous products, that is, H_2O and CO_2 , and

zero-valent metals, respectively. The approaches that we have undertaken in our laboratories in an attempt to address these problems are also described in this review.

3. Advanced Oxidation Processes (AOPs)

Due to the aforementioned limitations of the conventional water-treatment methods, there is an ongoing research interest to develop more efficient and environmentally friendly systems for the treatment of recalcitrant organic pollutants. Advanced oxidation processes (AOPs) have demonstrated the capability to develop such a green system. AOPs provide an effective remediation for the treatment of water since they have the ability to completely degrade a variety of organic pollutants, oxidise heavy metals, and destroy microbial substances. Advanced oxidation processes exploit the high reactivity of hydroxyl radicals as the oxidation driving force resulting in the formation of benign by-products (i.e., H_2O and CO_2); hence they are environmentally friendly [41, 63–67].

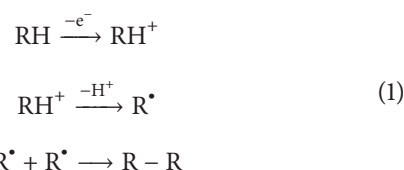
3.1. Supercritical Water Oxidation. Supercritical water oxidation (SCWO) is a technique that has been proven to destroy highly persistent organic pollutants without the production of harmful products. SCWO reactions are carried out above the critical point of water (374°C and 22.1 MPa) and at this point the volume of water is three times higher than at room temperature, with a density of $0.322\text{ g}\cdot\text{mL}^{-1}$ and a dielectric constant of 5.3 [68–71]. A homogeneous single phase results when oxygen and organic compounds are dissolved in supercritical water [69, 71, 72]. SCWO has been studied in the degradation of nitrogenated compounds (e.g., pyridine, aniline, nitrobenzene, and ammonia), phenolic compounds, and radioactive wastes [70].

SCWO is regarded as an environmentally friendly process, because not only does it produce CO_2 and H_2O during oxidation, but also none of the NO_x and SO_x compounds are produced due to the relatively mild operating conditions (340°C to 400°C and 22.29 MPa to 25.33 MPa) [69, 71]. However, during the degradation of halogenated hydrocarbons, the SCWO process is subject to corrosion problems due to the formation of acidic conditions as well as fouling problems due to the utilisation of neutralising processes and these are the major obstacles that have led to the noncommercialisation of SCWO [71, 73].

3.2. Wet Oxidation. Wet oxidation, also referred to as wet air oxidation (WAO), is used to oxidise organic and inorganic substances, in either suspension or solution forms, in the presence of an oxidant (water or air) at elevated temperature and pressure [44, 61, 74]. WAO technology has a high potential for the treatment of effluents containing a high content of organic matter and/or hazardous materials for which biological treatment is not feasible [44]. In WAO technology the organic pollutants are either partially oxidised into biodegradable intermediate products with low molecular weights or completely mineralised to water, carbon dioxide, and innocuous end-products at temperatures ranging between 125°C and 320°C and at pressures of between 0.5 MPa

and 20.0 MPa in the aqueous phase [44, 59]. The mechanism of wet oxidation seems to take place by means of a free radical. However, WAO is only effective for aliphatic and aromatic compounds that do not have halogenated groups. Moreover, investment and operation costs of WAO plants are not feasible due to excessive temperatures and pressures, while treatment of effluents containing refractory organic pollutants would further escalate the operating costs [75, 76].

3.3. Electrochemical Oxidation. Electrochemical oxidation processes employ an electrochemical cell to generate oxidising species which are used to destroy organic pollutants at ambient temperatures [60, 77–79]. The mechanism of electrochemical oxidation involves three stages which are electrocoagulation, electroflotation, and electrooxidation [79]:



Electrochemically, organic pollutants can be oxidised either directly or indirectly. In direct anodic oxidation, the pollutants are adsorbed on the anode before being destroyed by the oxidising species (mediator ions) produced at the anode while indirect electrochemical oxidation makes use of strong oxidising agents and the pollutants are oxidised in the bulk solution [77–79]. Although electrochemical oxidation processes offer an environmentally friendly prospect, the process is economically not viable due to high energy consumption. Furthermore, fouling of the electrodes has been observed due to either the deposition of oligomers formed during phenol oxidation or radical combination as an effect of pH [60, 80].

3.4. Photolysis. In photolysis, a chemical compound absorbs radiation energy, is elevated to a state of higher energy and an excited state, and produces radicals that carry out the photochemical reactions. The source of radiation is either solar energy or low and medium-pressure mercury lamps [27, 33, 81, 82]. In photolysis, the hydroxyl compounds are generated by water splitting:



These radicals then react with the organic pollutant, splitting it to smaller and more bioavailable compounds [27]. However, photolysis is a poor source of radicals and the radicals produced are not efficient enough to fully degrade refractory pollutants due to slow reaction kinetics observed in photolysis [8]. To accelerate these photochemical processes, metallic salts called semiconductors which act as catalysts to speed up the photochemical processes need to be added, giving rise to the so-called advanced oxidation processes [8, 83–85].

4. Semiconductor Photocatalysis

4.1. Introduction. Interest in semiconductor photocatalysis has recently risen exponentially because of the potential and

TABLE 2: Band gap energies of some semiconductor photocatalysts [8, 52, 89].

Photocatalyst	Band gap energy (eV)	Photocatalyst	Band gap energy (eV)
Si	1.1	SiC	3.0
WSe ₂	1.2	TiO ₂ rutile	3.02
α-Fe ₂ O ₃	2.2	Fe ₂ O ₃	3.1
CdS	2.4	TiO ₂ anatase	3.2
NaBiO ₃	2.62	ZnO	3.2
V ₂ O ₅	2.7	SrTiO ₃	3.4
B ₂ WO ₆	2.78	SnO ₂	3.5
WO ₃	2.8	ZnS	3.7

opportunities it offers in a variety of fields. These include treatment of environmental pollution, biotissue generation and biosensors, medicine (destruction of cancer and viruses), and pharmaceutical industries [7, 18, 86–90]. The major advantages of semiconductor photocatalysis are that it offers a good substitute for the energy-intensive treatment methods and has the capacity to use renewable and pollution-free solar energy. Also, unlike the conventional treatment methods, which not only transfer pollutants from one medium to another but also transform those to more refractory pollutants, semiconductor photocatalysis converts contaminants to innocuous products, such as CO₂ and H₂O. Furthermore, the reaction conditions are mild, and the reaction time is modest and can be applied to aqueous, gaseous, and solid-phase treatments with the possibility of being both supplementary and complementary to the present technologies [8, 18, 52, 83, 87, 88]. Semiconductor photocatalysts therefore have the advantage of not only minimising running costs but also generating the desired product in the most efficient and effective way.

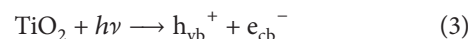
4.2. Properties of Semiconductor Photocatalysts. The defining property of a good semiconductor photocatalyst material is that the core element making up the material can reversibly change its valence state to accommodate a hole without decomposing the semiconductor (e.g., Ti³⁺ → Ti⁴⁺ in non-stoichiometric TiO₂) [8, 18, 91]. The photogenerated holes should be highly oxidizing to produce hydroxyl radicals ([•]OH) and the photogenerated electrons should be reducing enough to produce superoxides from the oxygen [92]. Also, the element should have more than one stable valence in the semiconductor so that it is not decomposed (photocorrosion) by the formation of holes (e.g., Zn²⁺ in ZnO and Cd²⁺ in CdS are photocorroded by the formation of holes) [8, 18, 93–95]. Furthermore, the semiconductor must have a suitable band gap, which is highly stable to chemical corrosion, nontoxic, and generally of low cost [8, 18, 92, 93, 96, 97]. The band gap energies of some semiconductor photocatalysts are shown in Table 2.

4.3. Mechanism of Photocatalysis. Semiconductor photocatalysts do not have a continuum of electronic states like metals,

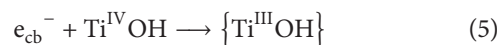
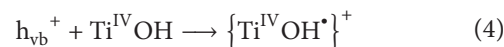
but they have a void region that extends from the top of the highest occupied molecular orbital (HOMO), that is, the valence band (VB), to the bottom of the lowest unoccupied molecular orbital (LUMO) which is also referred to as the conduction band (CB). This void region is called the band gap (E_g) [8, 18, 98–100]. When the semiconductor is illuminated with light, it absorbs a photon ($h\nu$) and when the energy of the photon is equal to or exceeds the band gap energy, an electron (e_{cb}^-) is promoted from the VB to the CB leaving a hole (h_{vb}^+) in the VB (Figure 1) [2, 18, 99–101]. The electron-hole pair then migrates to the surface of the photocatalyst where it can recombine and dissipate the energy as heat, get trapped in metastable surface states, or react with electron donors or acceptors adsorbed on the surface of the semiconductor [18]. Generally, the hole oxidises water to form hydroxyl radicals and initiates a chain reaction that then proceeds to oxidise organics while the electron can be donated to an electron acceptor, for example, O₂, leading to the formation of superoxides or a metal ion that is reduced to its lower valence state and deposited on the catalyst surface [8, 18, 98, 102, 103].

The mechanism for semiconductor photocatalysis (of a M(IV) lattice metal, e.g., TiO₂) can be summarised in the following reaction steps [8, 18]:

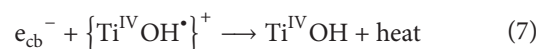
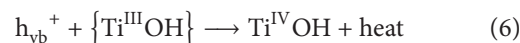
- (i) Excitation of photon greater than band gap resulting in the formation of electrons (e_{cb}^-) and holes (h_{vb}^+), that is, charge-carrier generation:



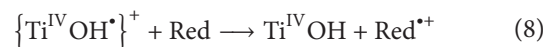
- (ii) Charge-carrier trapping:



- (iii) Charge-carrier recombination producing thermal energy:



- (iv) Interfacial charge transfer:



where Red is an electron donor (reductant) and Ox is an electron acceptor (oxidant).

- (v) Reduction of metal ions by e_{cb}^- , if present:



This fundamental phenomenon observed in semiconductor photocatalysts to oxidise (degrade) organic compounds and reduce metal ions is a promising technique in the treatment of refractory organic pollutants and heavy metals present in wastewater treatment plants.

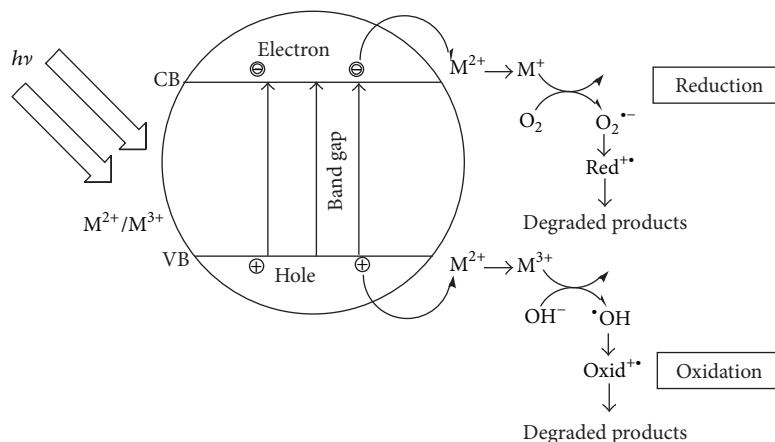


FIGURE 1: Mechanism for semiconductor photocatalysis [18].

5. Nanophotocatalysts in Water Treatment

Due to industrial and geographical reasons there is always a difference in the quality of water across the world. It is therefore acceptable that there is no possibility of one solution that can solve all the problems of water contamination. Thus, in the design for water-treatment technologies, nanotechnology will always play a key role. The intrigue of nanotechnology is the ability to control the manipulation of nanoscale (approximately 1 nm to 100 nm) structured materials and integrate them into large material components, systems, and architecture that have novel properties and functions [2, 86, 113, 114]. The merits of using semiconductor photocatalysts in their nanorange far outweigh their use in their bulk form [115]. For example, in the case of adsorption where surface sites of the adsorbent are utilised, diffusion is usually hindered due to the lack of a porous structure in the bulk materials. This is because the surface-to-volume ratio increases drastically with the decrease of the adsorbent from bulk to nanodimensions [2, 7, 11, 87, 113].

Also, new physical and chemical properties emerge when the size of a material is reduced to the nanoscale level. The surface energy per nanoparticle increases significantly in the nanorange. This increase in surface energy directly results in an increase in contaminant removal even at low concentrations. The use of nanocatalysts also results in less waste generation, especially in posttreatment, since less quantity of nanomaterial will be required compared to its bulk form. Furthermore, with the use of nanomaterials, novel reactions can be accomplished at nanoscale due to an increase in the number of surface atoms which is not possible with its analogous bulk material, for example, the degradation of pesticides by nanoparticles which cannot be done by the metals in their bulk form [2, 7, 93, 94, 113].

6. Titanium Dioxide/TiO₂/Titania Photocatalysts

6.1. Introduction. Among the nanophotocatalysts used in the treatment of environmental wastewater, titanium dioxide, also known as titania or TiO₂, has been extensively studied

[88, 116–119]. Since the discovery of the phenomenon of photocatalytic splitting of water on a TiO₂ electrode under UV light, enormous efforts devoted to titania research have led to promising applications in the fields of photovoltaics, photocatalysis, photoelectrochromics, ceramics, and sensors [120–126]. As the most promising semiconductor photocatalyst, TiO₂-based materials are therefore expected to play a major role to curb serious environmental and pollution challenges and ease the energy crisis through the use of renewable solar energy [93, 127–134].

6.2. Synthetic Methods for TiO₂ Nanoparticles. There are a number of available techniques for the synthesis of titania nanoparticles and these include sol-gel, sol, hydrothermal, solvothermal, and chemical vapour deposition, to name just a few [88, 135, 136]. These synthetic methods are highlighted in the following subsections. The method used plays a significant role in the shape, size, and photochemical properties of TiO₂.

6.2.1. Sol-Gel Method. The sol-gel method is the most commonly used technique for the synthesis of TiO₂ nanoparticles [137–140]. In a typical sol-gel process, a colloidal suspension (a sol) is formed from the hydrolysis of the precursors, usually inorganic metal salts or metal inorganic salts such as metal alkoxides [16, 88]. For titania synthesis, the sol-gel process usually proceeds via an acid-catalysed hydrolysis of titanium (IV) alkoxides followed by condensation [88, 138]. The sol-gel process has found more extensive use in the synthesis of titania because the reaction takes place at low temperatures, does not use complicated equipment, results in the formation of highly homogeneous and pure products, and allows for modification to produce specific desired products [138, 141–143].

Also, the sol-gel method results in the synthesis of high surface-area nanomaterials. It also allows for easy control of shape, size, and distribution, as well as the easy introduction of foreign materials into the catalyst lattice and at low temperatures [135, 141, 144–147]. Moreover, nanomaterials prepared by this method have a well-crystalline phase and a small crystalline size, which benefit thermal stability and photocatalytic activity. Hence, in this study, the sol-gel

process was used for the synthesis of TiO₂ nanoparticles as well as the introduction of metal ions into the crystal lattice of the TiO₂ nanoparticles.

6.2.2. Sol Method. This method is also referred to as the nonhydrolytic sol-gel process and usually involves the reaction of titanium chloride with oxygen donating materials, for example, metal alkoxides or organic ethers [88, 148–152]. The reaction between Ti–Cl and Ti–OR leads to the formation of Ti–O–Ti bridges. The alkoxide groups are formed *in situ* by the reaction of titanium chloride with alcohols or ethers. The length of the alkyl substituent of the alcohols affects the reaction speed (the longer the chain, the faster the reaction) but not the average particle size. However, the variation of the halogen (e.g., TiF₄ and TiI₄) affects the average particle size [88, 153]. Also, the shape and size of the titania nanoparticles can be controlled by the addition of a surfactant. For example, TiCl₃ was added to a solution of trioctylphosphine oxide (TOPO) and lauric acid and the reaction conditions controlled to produce either diamond-shaped, bullet-shaped nanocrystals or a mixture of branched and unbranched TiO₂ nanorods [88, 153–155].

6.2.3. Hydrothermal Method. Hydrothermal synthesis of nanoparticles takes place under controlled temperature and/or pressure in an autoclave [88, 127]. The reaction takes place in an aqueous medium. The hydrothermal process is effective for selective crystallisation of anatase titania from the amorphous phase. However, the presence of the Cl[−] ion (from the precursor, TiCl₃) results in the formation of a mixture of anatase and the brookite phases. Thermal treatment of the amorphous phase below 300°C results in a mixture of the anatase and the brookite phases due to a solid-state epitaxial growth mechanism. At temperatures above 300°C the formation of only the anatase phase is achieved because the dissolution/precipitation mechanism dominates [88, 127].

The hydrothermal process is thought to be environmentally friendly since the reactions are carried out in a closed system and the contents can be recovered and reused after cooling down to room temperature [53]. Moreover, proper and careful control of the hydrothermal processing conditions allows for the control over the physical properties of titania such as crystallite size and form, surface area, contamination, morphology and phase, uniform distribution and high-dispersion, and stronger interfacial adsorption properties [53, 88, 127].

6.2.4. Solvothermal Method. The solvothermal method is almost identical to the hydrothermal method except that it uses nonaqueous solvents [88, 156, 157]. However, in the solvothermal method the temperature can be elevated much higher than in the hydrothermal method and a variety of organic solvents with high boiling points can be used. With the solvothermal method there is a better control of the size, shape, and the crystallinity of the TiO₂ nanoparticle distributions than hydrothermal methods [158]. Thus the solvothermal method has been found to be a versatile method for the synthesis of a variety of nanoparticles with controlled

particle size, narrow size distribution, and dispersity [159–162]. Also the versatility of this method is seen in that it can be employed to synthesise TiO₂ nanoparticles and nanorods with or without the aid of surfactants.

6.2.5. Chemical Vapour Deposition (CVD) Method. Chemical vapour deposition (CVD) is a process in which materials in a vapour state are condensed to form a solid-phase material [88, 163]. This process alters the mechanical, electrical, thermal, optical, corrosion resistance, and wear-resistance properties of various substrates [163]. CVD has been used to form free-standing bodies, films, and fibres and to infiltrate fabric to form composite materials and, recently, in the fabrication of various nanomaterials [164, 165]. Chemical vapour deposition of titanium dioxide is usually carried out through the reaction of titanium tetrachloride (TiCl₄) with oxygen or through the thermal reaction of a titanium alkoxide such as Ti(OPri)₄, which already displays the Ti–O₄ tetrahedral motif of the titanium dioxide lattice in its chemical structure [165–167].

CVD processes usually take place within a vacuum chamber. If no chemical reaction occurs within the reaction chamber, the process is called physical vapour deposition (PVD). In CVD processes, the gaseous precursor compounds chemically react on a heated substrate surface and the deposition reaction is driven by thermal energy. The reactions usually happen in an inert atmosphere in the presence of a gas, for example, N₂, Ar, or He [163–165, 167]. Moreover, the reaction conditions in a CVD process can be tuned to determine the phase, size, and morphology of the TiO₂ nanostructures.

6.3. Properties of TiO₂ Nanoparticles. Titanium dioxide has gained prominence for use as an environmental remediation catalyst to completely mineralise organic and inorganic contaminants because of its outstanding characteristics. These include high thermal stability, high photocatalytic activity, high resistance to chemical and photocorrosion, nontoxicity, and dielectric properties as well as being inexpensive [168–172]. The photocatalytic activity of TiO₂ depends on its crystal phase, crystallinity, particle size, lattice impurities, density of surface hydroxyl groups, and the surface area. Titania has three (3) phases, namely, anatase (tetragonal), rutile (tetragonal), and brookite (orthorhombic), and the anatase phase of titania is the most photoreactive of the phases [121, 172–174]. Of the three phases, the anatase phase has the smallest particle sizes (<50 nm), high concentrations of surface hydroxyl (OH) groups, and a high surface area, hence the high photocatalytic activity [169].

However, the band gap of anatase TiO₂ is 3.2 eV and can only be activated under UV light irradiation with wavelength of 387 nm [117, 175–177]. This high-energy band gap rules out the use of solar energy as the photoactivity source. The UV source requires large quantities of electrical energy which would result in high costs in practical applications [52]. Moreover, titania is characterised by low quantum yields (i.e., low electron transfer rate) resulting in high electron-hole pair recombination which results in the termination of the photocatalytic reactions [41, 104, 168, 178–180]. As a result, a

number of reformative initiatives have been investigated as a means of overcoming these drawbacks.

6.4. TiO_2 Modifications. The main aim for titania modifications is to reduce the band gap of titania thus shifting its optical response to the visible-light region and to reduce the rate of electron-hole pair recombination to increase its photoreactivity [105, 132, 180]. TiO_2 modifications result in the “decrease” of the band gap by means of introducing a donor level on the valence band (Figure 2). The paramount condition for titania modification is to ensure that the anatase phase is maintained. The most common techniques used for TiO_2 modifications include anion doping, dye sensitizers, the use of binary oxides, and metal-ion doping. These are discussed in the following subsections.

6.4.1. Metal-Ion Doping. Doping of titanium dioxide nanoparticles with transition and noble metal ions for the degradation of organic pollutants is the most studied phenomenon and has been found to enhance both the photoresponse and photocatalytic activity of TiO_2 nanoparticles under visible-light irradiation [47, 96, 105, 142, 181–191]. The electronic states of titania can be decomposed into three parts: δ bonding of O p and Ti e_g orbitals or states that are located in the lower region, π bonding of O p_π and Ti e_g states in the middle energy region, and O p_π states in the higher energy region (Figure 3). The bottom of the lower CB has the Ti d_{xy} orbital and contributes to the metal-metal interactions due to δ bonding of the Ti t_{2g} -Ti t_{2g} states. The top of the lower CB consists of the Ti t_{2g} states that are antibonding with the O p_π states. The upper CB is characterised by the δ antibonding orbitals between the O p_δ and Ti e_g states [88].

During metal-ion doping, the energy due to the metal-ion dopant either lies at the top of the valence band or produces midgap states. When the atomic number of the dopants is increased, the localised level shifts to lower energy thus significantly contributing to the formation of the valence band with the O p and Ti 3d electrons. This results in the band gap narrowing due to the introduction of electron states into the band gap of TiO_2 resulting in the formation of a new lowest unoccupied molecular orbital (LUMO) [88]. Basically, metal ions provide a “cushion” on the valence band (the donor level) which results in the “decrease” in the band gap.

Metal doping should be differentiated from metal ions codissolved in a photodegraded solution and noble metals deposited on the semiconductor surface [88, 105]. Metal ions (dopants) are therefore incorporated into the TiO_2 lattice resulting in a “decrease” between the valence band and the conduction band hence altering the band gap energy thereby shifting the absorption band to the visible-light region [47]. Metal-ion dopants are nanoscale metal semiconductor contacts that act as electron scavengers hence resulting in increased photocatalysis [192, 193].

It is worth noting that although the introduction of metal-ion dopants on the titania lattice drastically shifts the absorption edge to the visible-light region, it can also result in reduced photocatalytic activities. Metal doping can increase

the rate of electron-hole pair recombination and the photocatalyst can also cause thermal instability [57, 176]. It is therefore imperative to avoid this by taking into consideration the adequate amount of the dopant (metal) when preparing doped titania [105, 194]. This is because when the dopant level passes the optimal limit, which usually lies at a very low dopant concentration, the metal ions act as recombination centres resulting in reduced photoactivity. The presence of adequate amounts of metal doping (optimal limit) also ensures that the metal particles only act as electron traps hence aiding electron-hole separation [105, 195].

6.4.2. Anion Doping. Anion doping of titania has increased recently and has been reported to shift the absorption edge towards the visible-light region and increase the photocatalytic activity [16, 102, 119, 176, 196–199]. The narrowing of the band gap is as a result of the mixing of either the p or the 2p states of the halogen (X) with the 2p states of the oxygen (O) atom in the valence band of the TiO_2 nanoparticles [88, 196, 197]. However, the mixing of the p states of the halogen and the 2p states of the O atom has the most positive effect on the band gap narrowing as it induces some states which act as shallow donors on the valence band [88]. The anion therefore traps holes resulting in less recombination of the electron-hole pair and displaces the surface OH groups increasing the rate of electron scavenging by O_2 resulting in the formation of an increased yield of superoxide radicals [103]. Anions therefore undergo innersphere ligand substitution reactions with surface hydroxyl groups.

6.4.3. Dye Sensitizers. Organic dyes have been widely employed as sensitizers for titanium dioxide nanomaterial to improve its optical properties as they are light absorbing chromophores [6, 84, 88, 125, 193, 200]. Organic dyes are usually transition-metal complexes with low-lying excited states, for example, polypyridine, phthalocyanine, and metalloporphyrin complexes. The metal centres for the dyes include Ru(II), Zn(II), Mg(II), Fe(II), and Al(III), while the ligands include nitrogen heterocycles with delocalised π or aromatic ring systems. The conduction band usually acts as a mediator for transferring the electrons from the excited sensitizer to the substrate on the titania surface [84, 125, 187].

These organic dyes act as both sensitizers and substrates and are normally linked to the TiO_2 nanoparticle surfaces via functional groups. The various interactions between the dyes and the TiO_2 nanoparticle substrates include covalent attachment by directly linking groups of interest or via linking agents, electrostatic interactions via ion-exchange, ion-pairing, or donor-acceptor interactions, hydrogen bonding, van der Waals forces, or hydroxyl groups [84, 88, 95]. Most dyes of interest link via direct covalent bonding with the functional groups that are on the TiO_2 surface. Carboxylic and phosphonic acid derivatives react with the hydroxyl groups to form esters, while amide linkages are obtained via the reaction of amine derivatives on TiO_2 [88, 95]. However, dye sensitizers are not stable and are usually prone to thermal instabilities which result in increased recombination centres. Furthermore, they are susceptible to damage from

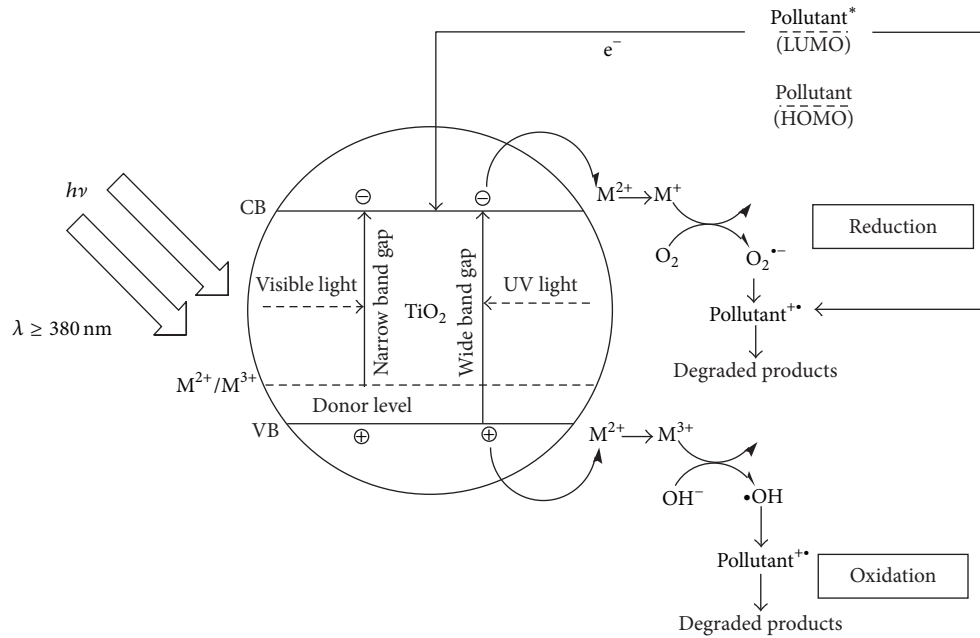


FIGURE 2: Band gap (effect of doping) and photocatalysis mechanism of TiO_2 [18, 104, 105].

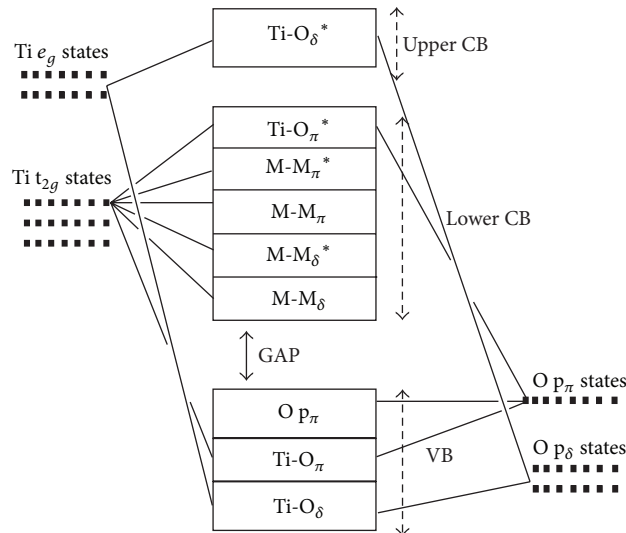


FIGURE 3: Bonding diagram of TiO_2 [18].

reactive oxygen species (ROS) which destroy the catalyst [92, 176].

6.4.4. Binary Oxides. Binary metal oxides like $\text{TiO}_2/\text{SiO}_2$, $\text{TiO}_2/\text{ZrO}_2$, TiO_2/WO_3 , $\text{TiO}_2/\text{Fe}_2\text{O}_3$, $\text{TiO}_2/\text{SnO}_2$, $\text{TiO}_2/\text{Ln}_2\text{O}_3$, and $\text{TiO}_2/\text{RuO}_2$ systems have been applied in the photocatalytic degradation of environmental pollutants under visible light [3, 95, 118, 124, 140, 201–207]. The photoactivity of these binary oxides was found to be enhanced because the metal oxides increased the acidity of the titania surface. The surface acidity takes the form of surface hydroxyls and accepts holes generated by illumination of the catalyst and oxidises the adsorbed molecules [118, 204]. Basically, since

the coupling oxide is activated under visible light, it is believed that the metal oxide will absorb visible light and the photocatalytic activity of the titanium dioxide will be used to mineralise organic pollutants. The metal oxides also enhance the separation properties of titania suspended particles from solution and thus decrease the effect of beam splitting by agglomerated particles [118]. Moreover, the metal oxides act as supports of the catalysts [10]. However, some of the metal oxides are thermodynamically unstable, for example, $\text{RuO}_2/\text{TiO}_2$, thus resulting in electron-hole pair recombination and significantly decreasing the photocatalytic activity [95].

Other techniques that have been used to shift the absorption edge of titania towards the visible-light region and

reduce the rate of electron-hole pair recombination include carbon nanotube-titania composites, metal-anion codoping, mounting TiO_2 on activated carbon exfoliated graphite, and polymeric substrates, for example, chitosan [116, 130, 208–213]. For the purposes of this research metal-ion-doped titania will be synthesised and investigated for its photocatalytic properties under visible-light irradiation.

6.5. TiO_2 Applications

6.5.1. Industrial Applications. The existing and potential applications of titanium dioxide nanomaterials include toothpaste, paint, UV protection, photovoltaics, photocatalysis, sensing, electrochromics, and photochromics. The photocatalytic properties of TiO_2 have found application, as well as potential application, in the manufacture of self-cleaning surfaces, air cleaning devices, and self-sterilising devices [88, 92, 194, 214, 215]. Photochromic and electrochromic compounds (with a redox potential above the conduction band edge of titania) exhibit different colours in different oxidation states, and TiO_2 acts as an electron conductor between the conduction band and the photo/electrochromic material. Electrochromic devices like electrochromic windows, displays, contact lenses, catheters, and spectacles with TiO_2 as the electron conductors have been synthesised and commercialised [131, 216–218]. Also, biomedically, TiO_2 has shown much potential in cancer therapy (endoscopic-like instruments) due to its antitumor activity [92].

6.5.2. Environmental Applications. The photocatalytic properties of TiO_2 make it an important semiconductor in applications in environmental remediation. Titanium dioxide has shown tremendous ability not only as a sensor for chemical, biological, and various gases (H_2 , NO_x , CO, etc.) even at low concentrations, but also to photocatalytically degrade and self-clean the contaminated environment [88, 200, 219–222]. Moreover, the degradation of organic pollutants and reduction of metals to their zero oxidation states have been earmarked as one of the peak applications of TiO_2 for the treatment of river water, groundwater, the drainage water from fish-feeding tanks, and industrial wastewater [57, 65, 91, 92, 117, 223, 224]. Furthermore, photodegradation of organic pollutants by titanium dioxide results in the formation of innocuous products and therefore eliminates the problems associated with the recalcitrant DBPs [18, 83, 174, 175, 225]. Although titania has the ability to completely degrade organic refractory pollutants and to be coupled with the existing water-treatment technologies, its large-scale industrial application in drinking-water treatment is still considered to be miles away.

6.6. Problems Associated with TiO_2 Applications. The use of TiO_2 in suspension form is efficient due to its large surface area but there are four major technical challenges that restrict its large-scale application and its use in water-treatment technologies. Firstly, it has a relatively wide band gap (~ 3.2 eV, which falls in the UV range of the solar spectrum), and therefore it is unable to harness visible light thus ruling out sunlight as the energy source of its photoactivation [9, 16,

211, 226–229]. Secondly, it has low quantum efficiency due to the low rate of electron transfer to oxygen resulting in a high recombination of the photogenerated electron-hole pairs [226, 227, 230]. Thirdly, when used in a suspension, titanium dioxide aggregates rapidly due to its small size (4 nm to 30 nm) and its aggregates may cause scattering of the light beam resulting in loss of catalytic efficiency [66, 211, 231]. And lastly, the application of powdered TiO_2 catalysts requires posttreatment separation to recover the catalyst from water. This is normally difficult, is energy consuming, and is economically not viable for use in water-treatment plants [12, 66, 156, 211, 230]. Therefore new research initiatives need to be explored to counter these challenges.

One of the major challenges facing scientists and government bodies is the development of materials using “clean” energy applications, the so-called Green Science, to relieve the environmental burden due to pollution. TiO_2 has the potential to be that green material and hence so much research has been ongoing to try and harness its potential applications. To achieve this, doping metals into the TiO_2 lattice is an effective strategy to reduce the band gap and shift the absorption edge towards the visible-light range [57, 84, 105, 107, 191, 227, 232, 233]. However, the amount of the metal-ion dopant when preparing doped titania is important. This is because when the dopant level passes the optimal limit, ($\sim 0.4\%$), the metal ions then act as recombination centres resulting in reduced photoactivity [105, 194].

Also, TiO_2 nanoparticles can be supported on catalyst supports. This would help improve the photocatalytic activity and potential application of the titania nanoparticles. Furthermore, to avoid the aggregation and posttreatment challenges, TiO_2 can also be assembled onto different substrates and fabricated into different types of titania thin films [150, 211, 214, 234–237]. The advantage of using thin films is that they are known to be chemically stable and possess a high dielectric constant, a high refractive index, and excellent transmittance; therefore they have the ability to retain the photocatalytic activity of the assembled catalysts [236].

7. Catalyst Supports

7.1. Introduction. A support material is very important in catalysis because it determines the catalytic activity of a catalyst [238, 239]. Catalyst supports are porous and have high surface areas [44, 240, 241]. The electronic interactions between the support and the catalyst bring about slightly acidic conditions which increases the rate of electron transfer thus reducing the rate of electron-hole combination. Also, supports result in an increased adsorption ability and stability of the catalyst and hence increase the rate of oxidation of organic pollutants [44, 76, 242, 243]. Moreover, catalyst support materials do not only shift the band edge towards the visible-light energy region but also have the ability to disperse the supported catalysts thus preventing them from agglomerating and also helping to improve catalyst separation from posttreatment wastes [130, 238, 243–247]. These conditions are therefore important since they enhance the photocatalytic activity and the application of the supported TiO_2 catalysts. The common types of supports used for catalysts include

alumina (γ -Al₂O₃) supports, carbon supports, and carbon-covered alumina (CCA) supports.

7.1.1. Alumina Supports. γ -Alumina as a catalyst support has a high surface area, good mechanical properties, and numerous pores as well as the ability to disperse the active metal phase [238, 239, 247, 248]. However, its exclusive use as a support has been found to have some disadvantages. For example, its acidity results in low catalytic activity of the supported catalysts. Furthermore, its reactive surfaces form unwanted metal oxides upon calcination. The reactive surfaces of alumina react with the promoter ions resulting in the formation of oxides which lower the catalytic activity of the catalysts [238, 247–249]. The strong interactions of the alumina support with the metal atoms are therefore undesirable since it is detrimental to the catalyst activity.

7.1.2. Carbon Supports. Carbon has also been used to support catalysts. Carbon supports have mild interactions with the supported metals and have a neutral surface, good thermal conductivity, and high surface area with controlled pore volume. Carbon is also resistant to nitrogen poisoning and contains variable surface functional groups [246, 248–251]. However, it also has some undesirable properties that limit its use as a catalyst support. It has poor mechanical properties and a low surface area. Moreover, it is also microporous and has poor adsorption properties and hence catalysts may be deposited on the micropores thus making their photocatalytic effect trivial [238, 246, 248–251]. These properties therefore make the sole use of carbon as a support material inapplicable.

7.2. Carbon-Covered Alumina (CCA) Supports. As described before, the sole use of either carbon or alumina as support materials has some shortcomings. A support system that exploits the merits of both carbon and alumina can provide an ideal support system. This is because it overcomes their shortcomings while improving their advantages. In this system, the alumina is coated with a thin layer of carbon prior to catalyst impregnation which results in a support material that possesses both the textural and mechanical properties of alumina and the favourable surface properties of carbon [238, 250, 252–255]. The properties of this carbon-covered alumina (CCA) support include reduction of the alumina acidity (~ by 90%) due to the presence of carbon; increased electron-charge transfer and reduced metal-support interactions resulting in increased catalytic activity; and increased mechanical strength and increased surface area [238, 239, 247, 252–254, 256, 257]. CCA supports are therefore superior catalyst supports due to the integration of the properties of both the carbon and alumina.

7.3. Synthesis of CCA Supports. The most common approach to the synthesis of CCA supports is based on the “pyrolyzability” of organic compounds, such as cyclohexene, acetylene, or ethane, on the surface of alumina at elevated temperatures (600°C to 700°C) in the flow of nitrogen, that is, chemical vapour deposition (CVD) of organic compounds [247, 249, 254, 258–260]. However, it has been found that the materials

synthesised by this method have some drawbacks. For example, their textural properties are dependent on the amount of carbon deposited and the type of the hydrocarbon used; hence the carbon coating is nonuniform [254]. Furthermore, increasing the degree of surface coverage of the alumina by carbon through CVD results in the aggregation of carbon on the alumina surface and this decreases the apparent surface area and pore volume which are key to catalytic activity of the supported catalysts.

Another method used to synthesise CCA involves the impregnation of alumina with sucrose solutions [198, 238, 250, 253, 257]. In this method the sucrose-impregnated alumina is dried in an oven and the pyrolysis of the sucrose takes place in an inert atmosphere at elevated temperatures (600°C to 700°C) to produce CCA supports. The CCA supports produced by the impregnation of sucrose have a uniform carbon layer; hence this is regarded as a better method than CVD of organic compounds. Lately, Sharanda et al. have synthesised CCA supports using an adsorption-equilibrium method [254, 261]. In this method highly reactive compounds like acetylacetone and isocyanates form surface complexes with the OH groups of the alumina via the C=O and N=C=O bond openings, respectively. Upon pyrolysis, a carbon coating is expected to form on the surface of the alumina. The equilibrium adsorption method has the advantage of forming better CCA supports since the interaction between the C and alumina is a chemical process and not a physical or mechanical one like in the case of CVD and sucrose impregnation. Hence, for the purposes of this study, the adsorption-equilibrium method was adopted for the synthesis of CCA supports.

7.4. Applications of CCA Supports. CCA supports have found utilisation as supports for hydrotreating catalysts in the Fischer-Tropsch conversion of heavy crude oil into light fractions [252, 258]. Also, CCA supports have a high surface area and high adsorption affinity for both organic and inorganic compounds (Al₂O₃ is a polar adsorbent and C is a nonpolar adsorbent). These properties have been exploited and CCA supports have been used as packing material for high-performance chromatography [249, 260, 261]. Recently, Jana and Ganesan [255] have synthesised CCA in the form of foams and increased its surface area and also enhanced its adsorptive properties. Due to their high catalytic activity and stability, CCA supports have been used to support Ru catalysts in the synthesis of NH₃ [262]. Ag nanoparticles have been used in CCA supports and used to remove bacteria in drinking water [239]. Since not much work has been done on the environmental application of CCA-supported catalysts, this research therefore seeks, for the first time, to support anatase TiO₂ nanoparticles on CCA supports and apply them in the degradation of organic pollutants.

8. CCA-Supported TiO₂ Nanoparticles

Titania nanoparticles have been recently attached on CCA supports and used for the photocatalytic degradation of Rhodamine B under visible-light irradiation [263]. Metal-doped titania has also been supported on these CCA supports. Ag,

Co, Ni, and Pd were used as the metal dopants [106]. The CCA supports were synthesised from glucose and an impregnation method was used to attach the nanoparticles on the supports. According to the results obtained, attaching the titania nanoparticles on the CCA supports greatly enhanced their photocatalytic activity. Both these CCA/TiO₂ and CCA/m-TiO₂ nanoparticles had a large surface area due to the porous nature of the CCA supports, and they were highly active under visible-light irradiation and exhibited less electron-hole combination due to the presence of C (which acts as electron traps) on the supports. Also, the band gap of the CCA-supported titania nanoparticles was highly reduced. The decrease in the band gap of the CCA-supported catalysts was found to be much higher than the decrease of 0.14 eV which is usually observed for carbon doped titania. The SEM images (Figure 4) revealed that the carbon formed a layer on top of the alumina and that the nanoparticles were successfully impregnated on the highly porous CCA supports.

Figure 5 showed that the catalysts were successfully impregnated onto the CCA supports. The authors also revealed that the catalysts were evenly distributed on the CCA supports. Uniform distribution is a distinguishing feature of CCA supports due to their high adsorption and porous nature. The CCA-supported catalysts were found not to have lost their crystallinity which would have inversely affected the photocatalytic activity of the catalysts.

9. Thin Films

As mentioned earlier, the tendency of titanium dioxide nanoparticles to aggregate and scatter incident light as well as the need for posttreatment recovery has made its large-scale application economically impractical [91, 211, 264]. This had led to the exploration of a number of techniques to try and immobilise TiO₂ nanoparticles on solid supports not only to solve posttreatment problems but also to facilitate the renewable use of the catalyst [66]. Also, TiO₂ thin films retain the photocatalytic properties of its powder form. TiO₂ thin films can still be applicable in gas sensors, electrodes for solar cells, electrochromic applications, as gate oxides of metal-oxide-semiconductor field transitions, laser applications, and photocatalytic degradation of pollutants [150, 264–267].

Although immobilised titania is less photocatalytically active than suspended titania particles due to reduced surface area and less porosity, the merits of using immobilised titania still far outweigh the disadvantages as it provides new avenues in the practical utilisation of titania. The techniques used for synthesis of TiO₂ thin films include CVD, dip coating, sol-gel, spin coating, spray pyrolysis, sputtering, liquid-phase deposition, and layer-by-layer (LbL) self-assembly. The substrates used include glass, single-crystal silicon, or polymeric substrates. Some of these thin-film synthesis techniques are discussed in the following subsections.

9.1. Chemical Vapour Deposition. Chemical vapour deposition (CVD) is a versatile method that can be used for the synthesis of a number of materials. To synthesise TiO₂ thin films by CVD, either a titanium alkoxide such as titanium isopropoxide (TTIP) is used, which already has the Ti–O₄

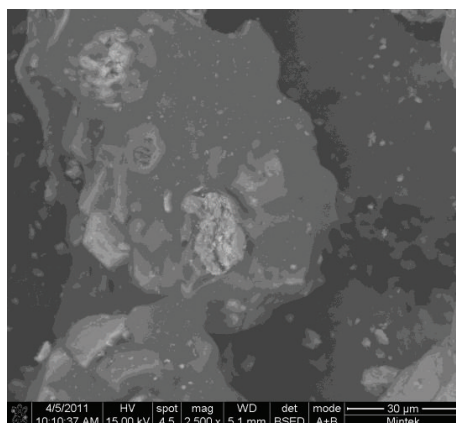
tetrahedral motif of the TiO₂ in its chemical structure, or TiCl₄ is reacted with oxygen to form the T–O₄ tetrahedral motif. These are thereafter deposited on a substrate at elevated temperatures in a vacuum to form the titania thin films [165, 236, 268, 269]. CVD offers good control of film structure and composition, excellent uniformity even on highly irregular substrates (conformal deposition), and a sufficiently high growth rate thus applicable for synthesis of multilayer structures [268, 270–272]. To realise the desired physicochemical properties of a material, a suitable substrate surface must be exposed to a suitable growth environment (temperature, pressure, and chemical composition) especially in the gas phase conditions close to the substrate surface [270].

The factors that affect the physicochemical properties of the thin films are the choice of precursors, carrier gas, and their respective flow rates, the total pressure in the reactor, the substrate temperature, the distance between the substrate and the nozzle head, and the water-vapour content in the whole reaction chamber [270, 273]. However, CVD is not a straightforward process and is complicated to control. The deposition rates, uniformity, and film properties change when one inert gas is replaced by another, a different-sized substrate is used, a different reactor loading is applied, or an identical process is applied in a different reactor setup [270]. Moreover, the vacuum equipment is expensive and due to the complicated nature of the reaction kinetics in the CVD reactors CVD processes developed in the laboratory are difficult to scale up to industrial scales [166, 235, 270].

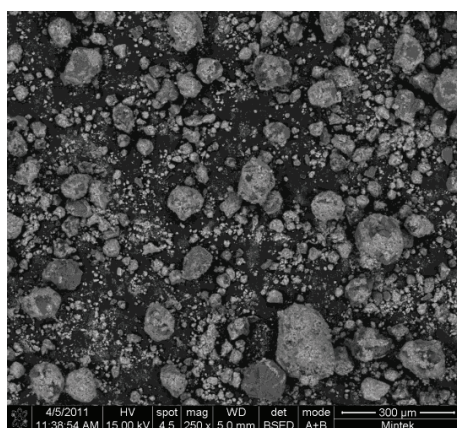
9.2. Liquid-Phase Deposition. Liquid-phase deposition (LPD), unlike CVD, is referred to as a unique soft process in which a metal oxide or hydroxide forms thin films through ligand-exchange (hydrolysis) equilibrium deposition at low temperatures [232, 274]. The substrate is immersed in the precursor solution (soft-solution deposition) and thereafter the substrate is calcined at high temperatures to obtain crystalline thin films [232, 275]. LPD is a cost-effective method, is regarded as environmentally friendly, and produces smooth, uniform, and dense thin films with good adherence [235, 275]. However, the thermal treatment of the thin films has been reported to affect the adhesion properties of the nanoparticles on the substrate [235].

9.3. Dip Coating. In dip coating the substrate is slowly immersed in a titanium dioxide precursor solution, for example, TTIP, TiCl₄, or TiCl₃ and then slowly pulled out at a fixed rate. The coated substrate is then immediately dried in furnace before calcination at elevated temperatures (400°C to 500°C) [65, 276–278]. Sometimes a complexing agent and a wetting additive are added to stabilise the solution and enhance film adherence [279]. Dip coating is also regarded as a simple, cost-effective technique and it produces uniform coatings with controllable film thickness [277, 280]. However, just like in LPD, the thermal treatment of the thin films affects the adhesion properties of the nanoparticles on the substrate [235].

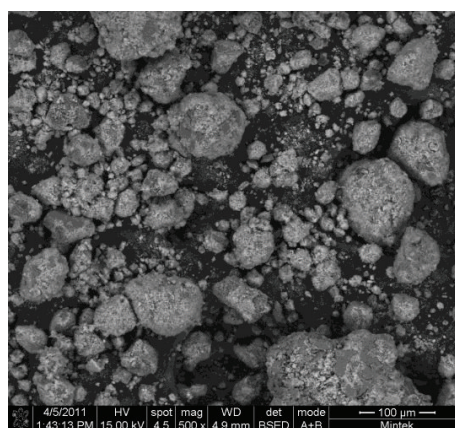
9.4. Spray Pyrolysis. Spray pyrolysis (SP) is a simple technique that requires a precursor solution (e.g., TiCl₃, TiCl₄,



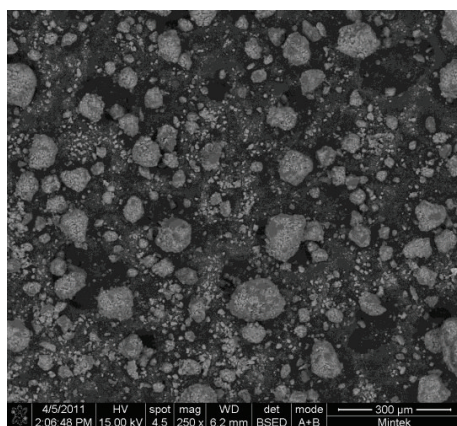
(a)



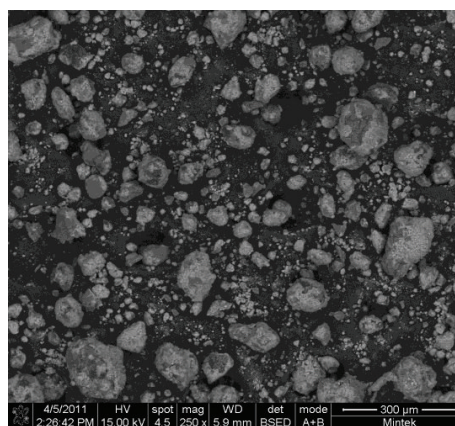
(b)



(c)



(d)



(e)

FIGURE 4: SEM images of CCA and CCA/TiO₂ nanoparticles [106].

Ti(OEt)₄, or TTIP dissolved in water, ethanol, or other solvents), an atomiser, and a heated substrate [156, 281]. In an SP process the solution is atomised into small droplets and the droplets are transported by a gas to the heated substrate where they form thin films upon immediate approach or impingement on the substrate (Figure 6). The source of the atomic mist (aerosol which produces large droplets or ultrasonic spraying which produces smaller droplets) determines the

surface morphology of the deposited films [281–283]. The SP method is attractive because it is inexpensive and uses simple facilities, results in rapid film growth, large surface-area substrate coverage, and homogeneity, and has the potential for mass production [156, 283–286].

However, SP has some drawbacks. Poor film quality is observed due to vapour convection in the hot zone because the vapour formed on the heated substrate may hinder the

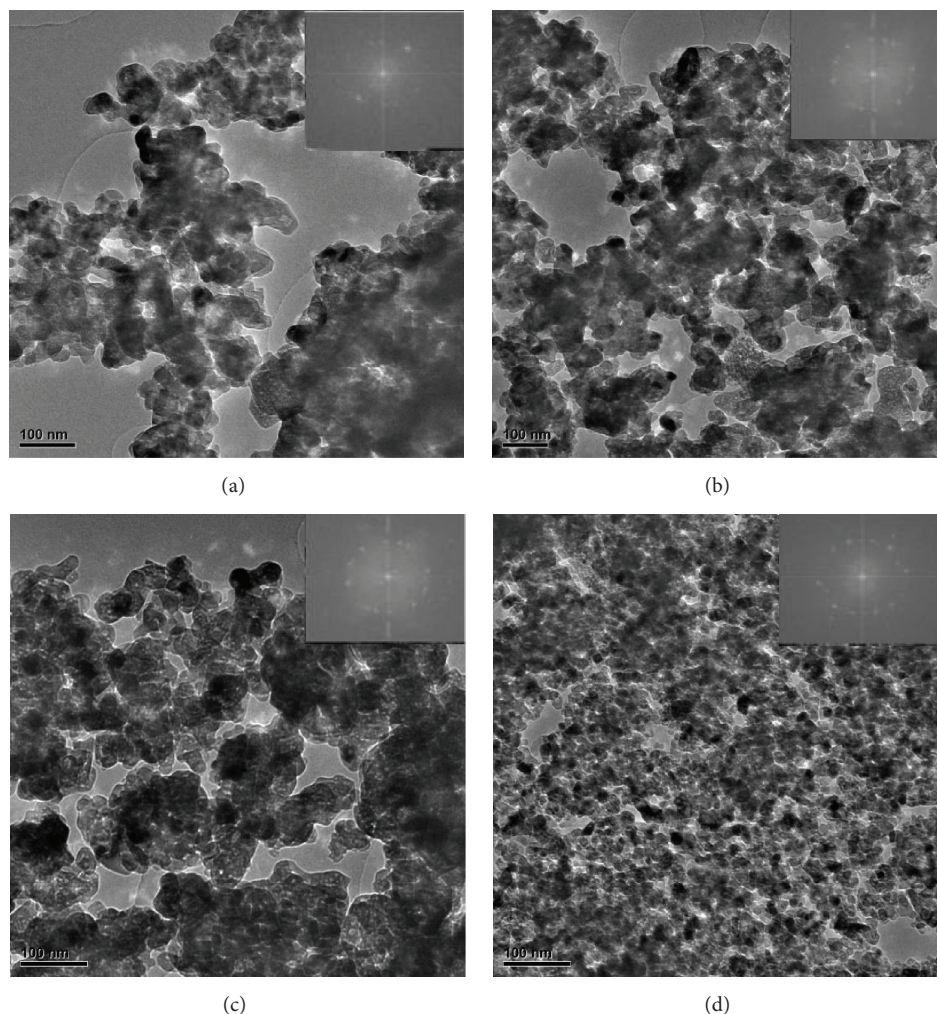


FIGURE 5: TEM images of the CCA-supported titania nanocatalysts [106].

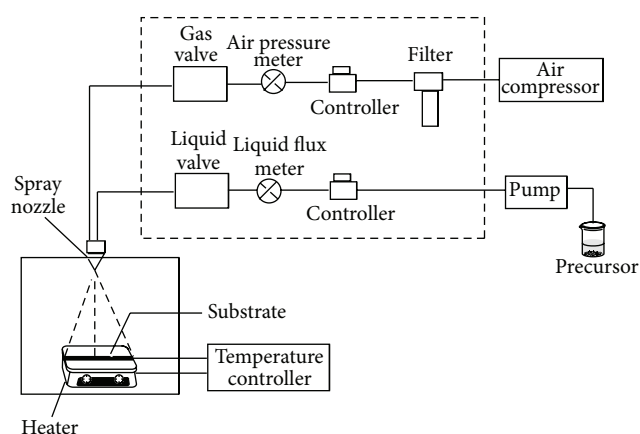


FIGURE 6: Schematic representation of the spray pyrolysis method [107].

source vapour from attaching to the substrate due to the temperature difference. Also, as the source liquid vaporises on the substrate due to thermal decomposition it may

result in the formation of thin films with many cracks due to precipitate shrinkage [284]. Also, SP can result in the deposition of powder on the substrate.

9.5. Sol-Gel Technique. The sol-gel technique is the most widely used method for the synthesis of TiO_2 thin films. The solution precursors are used to make the sol, and the substrate is immersed in the sol and substrate gelation occurs. These substrates are then aged and calcined at elevated temperatures to produce the thin films [185, 227, 234, 288–290]. The pH of the sol, the ageing time, amount of surfactant template, amount of hydrolysis retardant, and calcination temperature play an important role in the quality of the thin films produced [288]. However, the sol-gel method has some drawbacks. For example, during the ageing of gels and drying of films, the sols produce vapours which cause environmental pollution [287]. Also, the thermal treatment of the thin films

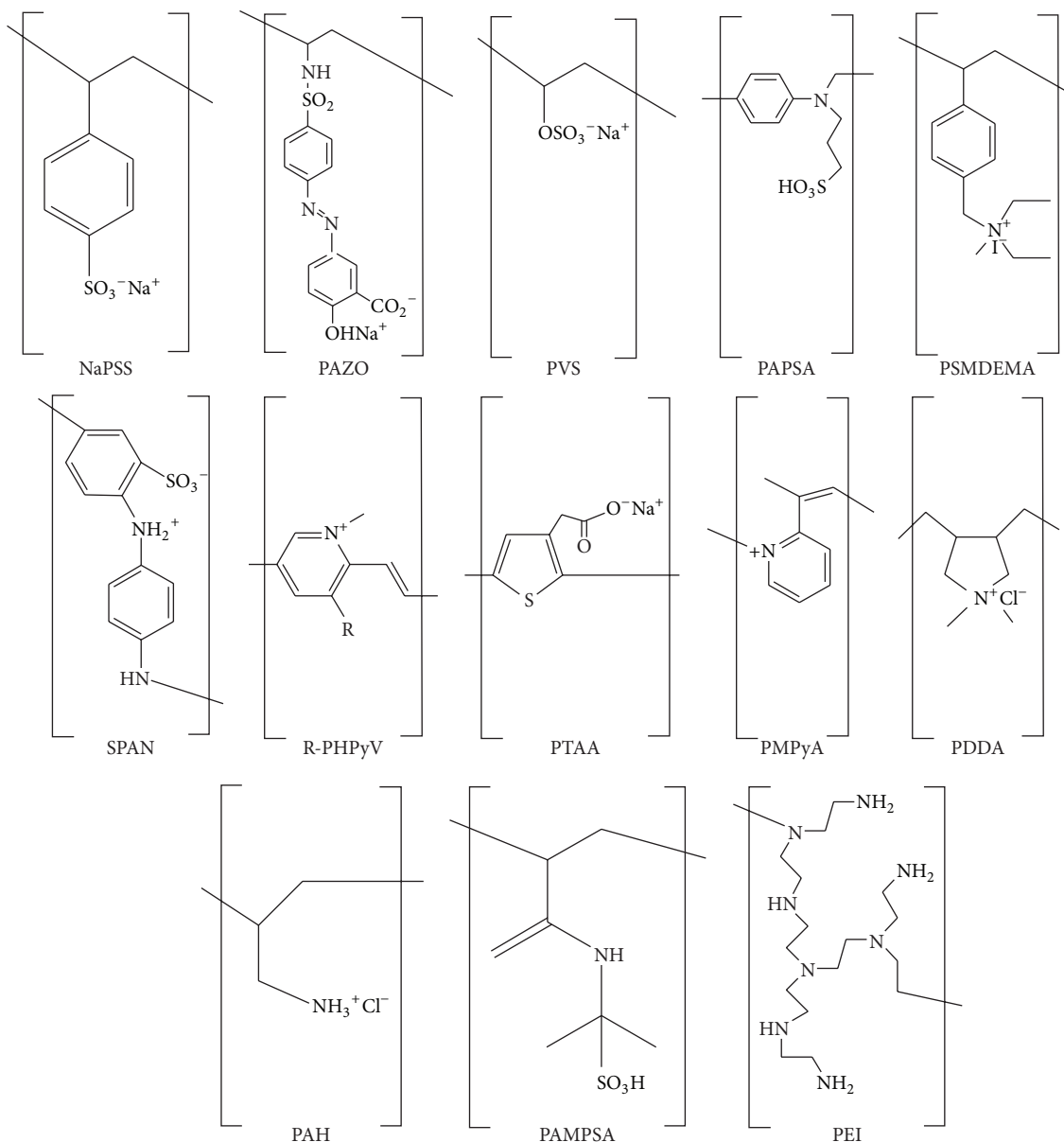


FIGURE 7: Examples of polyelectrolytes used in LbL thin-film synthesis.

affects the adhesion properties of the nanoparticles on the substrate [235].

9.6. Layer-by-Layer (LbL) Self-Assembly

9.6.1. Introduction. The layer-by-layer (LbL) self-assembly technique is a technology that enables the nanoconstruction of multifunctional films on solvent-accessible surfaces. It also allows for the design of functional surfaces and surface-based nanodevices in a “build-to-order” fashion, that is, the capacity to build standard or mass-customised products upon receipt of spontaneous orders without forecasts [109]. Furthermore, the LbL technique exceeds simple self-organisation under equilibrium conditions by making it possible to arrange many different materials at will with nanoscale precision [12, 109, 291–294]. The LbL technique

can thus provide solutions for surface modifications and fabrication of thin films; that is, it permits multifunctional assemblies of materials since it allows deposition on surfaces of almost any shape and kind [109, 295].

9.6.2. Fabrication of LbL Thin Films. Sequential deposition of polyelectrolytes (polyanions and polycations) on solid surfaces leads to the build-up of multilayer LbL thin films [108, 296, 297]. The LbL self-assembly technique is a physisorption process independent of size and topology of the substrate; however, parameters like solution concentration, ionic strength, solvent composition, and temperature play an important role in the multilayer build-up [292, 295, 298]. Examples of polyelectrolytes used for LbL thin-film fabrication are shown in Figure 7.

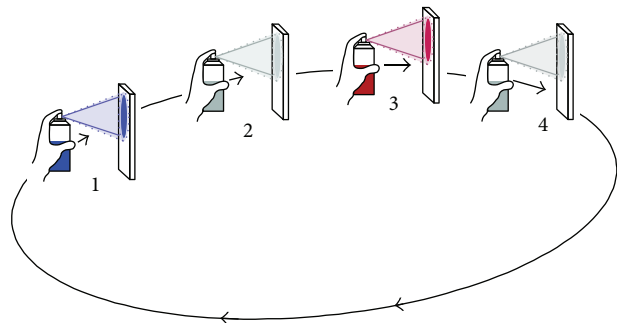


FIGURE 8: Schematic of the LbL electrolyte spraying deposition process [108].

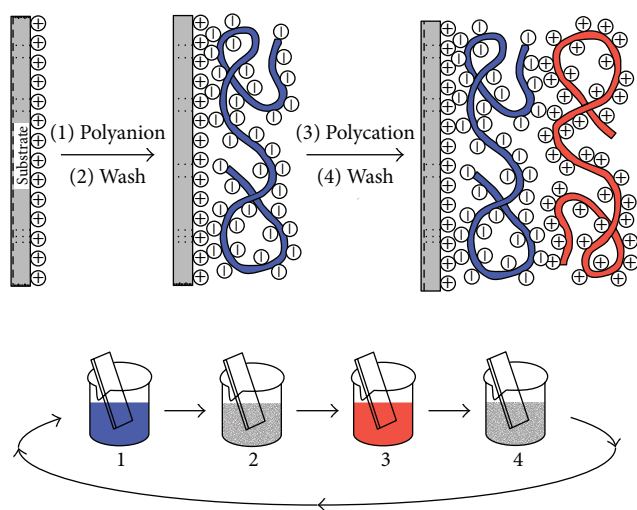


FIGURE 9: Schematic of the LbL electrolyte dipping deposition process [109].

To synthesise LbL thin films, a substrate is either dipped in or sprayed with oppositely charged polyelectrolytes. Also, solutions can be allowed to flow over the substrate. During spraying (Figure 8) the electrolyte sprayed on the substrate should not accumulate on the surface but flow away quickly, driven by gravity, and only a thin film of liquid which typically dries within minutes should initially remain on the surface. Because the thickness of the adhering solution is very thin, any spray droplet arriving at the surface immediately fuses with the liquid film and will replace liquid draining off. Spray coating is a fast and convenient application for large surface areas. Thus, this setup provides for mild but permanent agitation as driven by the draining solution [108].

During the dipping method (Figure 9), the substrate is dipped alternately in oppositely charged polyelectrolytes. Each dipping step is followed by a rinsing step to remove excess polyelectrolyte in contact with the surface. The washing is important because it avoids the formation of polyelectrolyte clusters in solution and hence it ensures homogeneity and uniformity of LbL films. Also, the dipping method forms thicker films than the spraying method [108, 109]. Thus for

the purposes of this study the dipping deposition process was preferred.

9.6.3. Applications of LbL Thin Films. There are a number of unprecedented “reagents” or materials for LbL film deposition and these include polymers (linear or branched), colloids (polymeric, metallic, or oxidic), biomacromolecules (DNA/proteins, polynucleotides, bioaggregates, and contact lenses), and nanoparticles (for environmental application) [293, 296, 297, 299]. Due to the variety of materials used for LbL thin-film fabrication, its application is therefore spread across a variety of disciplines which include electric and electronic devices (rectifiers, transistors, and switches), film coating, micropatterning, nanobioreactors, photocatalysis, and drug-delivery systems [300–302]. Biomedically, thin-film coating on medical devices can improve biocompatibility, reduce immunological response, and enhance targeted drug delivery [294]. The LbL self-assembly technique has also been applied in the synthesis of thin-film microcapsules that disintegrate on the target site hence improving drug or DNA delivery to their active site [298, 299, 303–307]. Also, LbL thin films have been applied to assemble semiconductor catalysts (especially TiO_2) and applied in the degradation of organic pollutants for environmental remediation [12, 293, 308]. LbL self-assembly of TiO_2 on thin films can therefore go a long way to overcome the problems associated with the practical application of suspended TiO_2 nanoparticles.

9.7. Layer-by-Layer TiO_2 Thin Films. The use of titania in powder form has the tendency to aggregate and scatter incident light and there are difficulties associated with the recovery of powdered titania after treatment; hence its large-scale application is economically not viable. TiO_2 has been assembled on substrates using different methods and applied in catalytic environmental remediation processes. However, since the other TiO_2 thin-film fabrication methods have some drawbacks like film cracking, poor adhesion to substrate, the use of high temperatures, expensive equipment, and a high level of expertise required, the LbL self-assembly provides a better alternative. LbL thin films are synthesised at low temperature (room temperature), simple equipment is used, the films require no thermal treatment, and strong adhesion between nanoparticles, electrolyte, and substrate is ensured due to the strong electrostatic interactions [12].

The TiO_2 nanoparticles assembled by the LbL self-assembly technique were found to be well separated and highly accessible for the photocatalytic processes. Also, the amount of the nanoparticles deposited was easily controllable [12, 293]. When compared to other methods like drop-casting and spin-coating, the LbL assembled TiO_2 show superiority in terms of film stability and catalyst reusability (thin film can be used a number of times with the same efficiency). Also, the LbL method has no limit to the number of TiO_2 layers that can be assembled and the higher the number of the layers the more the catalytic activity [12]. The use of LbL synthesised thin films therefore overcomes the problems associated with the use of powdered TiO_2 as well as the other thin-film assembly techniques and is attractive for practical application in continuous water-treatment and

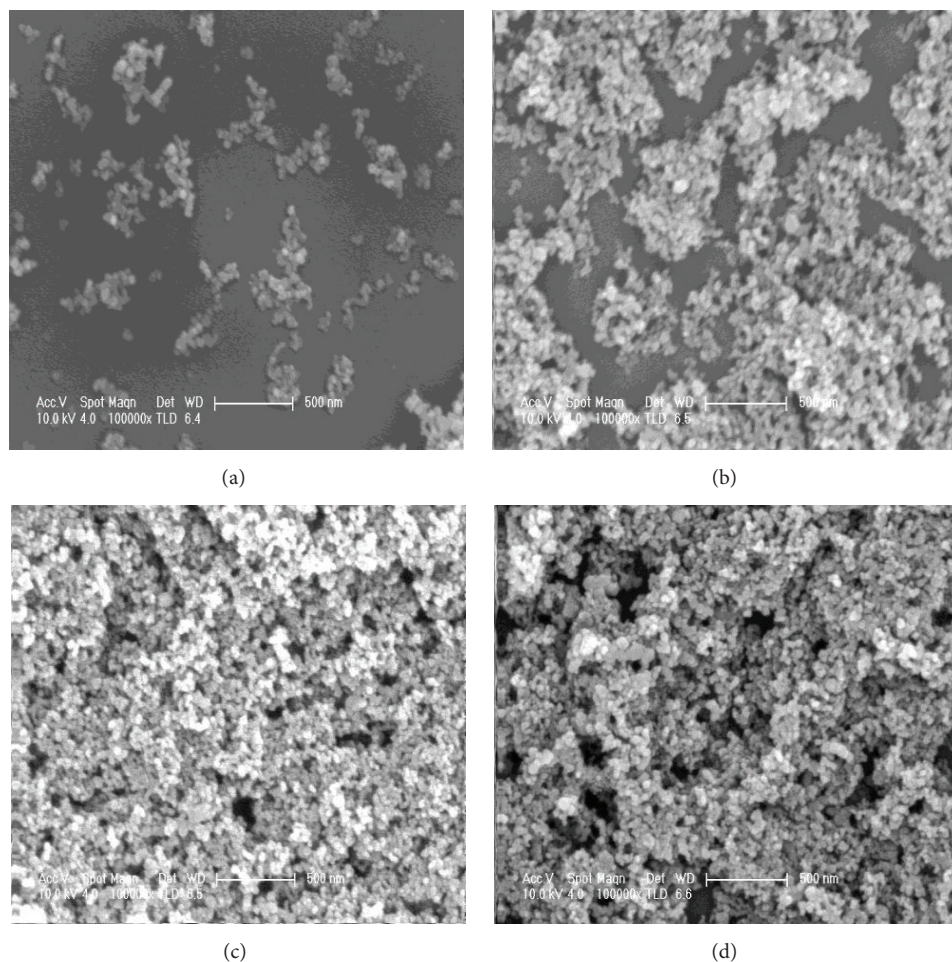


FIGURE 10: SEM images of 1, 3, 5, and 10 bilayers of the m-TiO₂ nanoparticles thin films [110].

environmental remediation processes. However, little have been reported in recent literature on the assembly and use of metal-doped titania by the LbL method.

10. Metal-Ion-Doped TiO₂ LbL Thin Films

The immobilization of metal-ion-doped titania on glass slides by the LbL method has been reported recently [110]. This study reveals that the metal-ion-doped titanium dioxide nanoparticles were successfully attached on glass slides and there was an increase in the number of particles and thin-film thickness with increase in the number of bilayers (Figure 10). PAH and PSS electrolytes were used to immobilise these m-TiO₂ nanoparticles on the glass slides as thin films. The photocatalytic efficiency of the PAH (PSS/mTiO₂) thin films was studied using Rhodamine B under visible-light illumination. These thin films were highly active towards the photocatalytic degradation of Rhodamine B under visible-light illumination and did not lose their photocatalytic activity and strength even after five cycles. This study shows a great stride in the use of metal-doped titania nanoparticles as it eliminates the problems associated with aggregation and posttreatment and thus increases the chances for easy use in water treatment.

11. Titania Mixed-Matrix Membranes

Recently, membrane separation technologies have been found to be cheap and fast, chemically stable, and highly selective. They can also be easily integrated with other water-treatment strategies [309–311]. Because of these properties, they have been found more favourable to be used for water-treatment processes. Membrane techniques do not require addition of chemical substances and therefore it is easy to increase their capacity (modular system). The separation process is in a continuous mode and therefore applicable in mild environmental conditions [312]. Membrane processes can therefore be used in diverse industrial sectors such as pharmaceutical, water treatment, chemical, food processing, electronics (fuel cells), metallurgy, and biotechnology [311, 313–317].

Although using polymeric membranes has major benefits over the conventional water-treatment technologies, their susceptibility to fouling is a major drawback [309, 318]. Foulants may be either crystalline, particulate, thermal, colloidal, microbial (biofouling), or organic fouling [309, 314, 318]. Polysulfone (PS) has been widely used to synthesise membranes. PS membranes are relatively cheap, have a

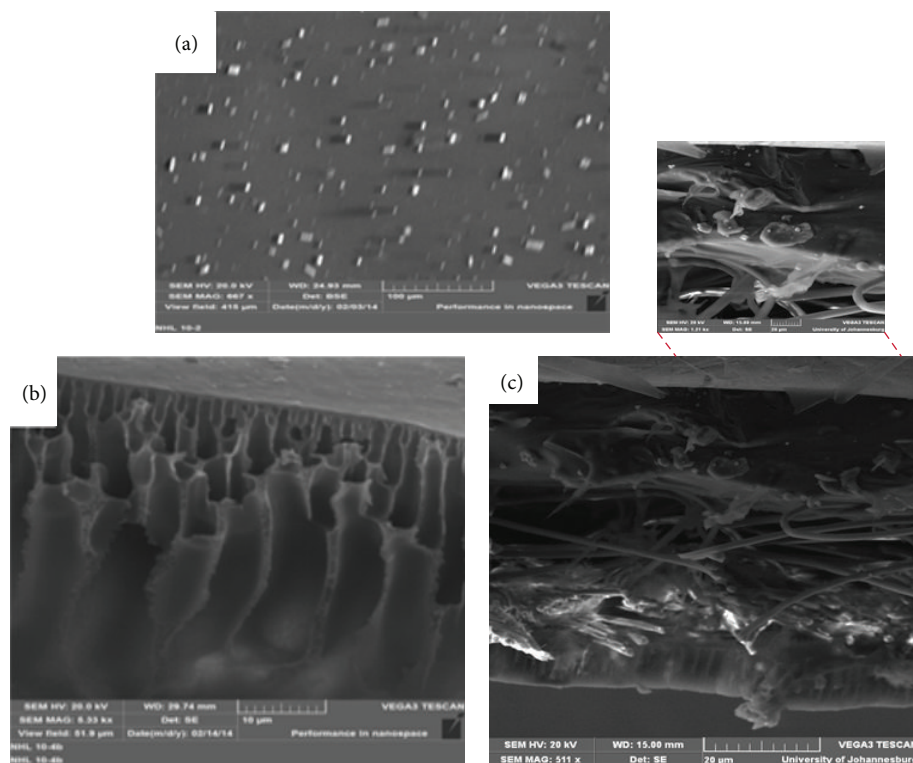


FIGURE 11: SEM micrographs of the CCA/TiO₂ mixed matrix membranes: (a) surface morphology, (b) cross section, and (c) nanoparticles within the polymer matrix [111, 112].

superior film-forming ability, strong thermal and chemical stability, and acidic and alkaline resistance, and hence have been widely used in many applications [318, 319]. These membranes have good mechanical and anticompression properties. However, like any other membranes, PS membranes have limitations to be used in water-treatment processes because they easily get fouled, have a low permeate flux, and are hydrophobic in nature [310, 311, 320], hence the need to modify their properties.

Current research in membrane technology development is focussed on the improvement of antifouling and hydrophilicity properties while maintaining or improving their throughput characteristics [310, 311, 319, 321]. This can be attained by either bulk or surface modification which changes the chemical structure of the membranes. Also, inorganic nanoparticles can be incorporated through the membrane matrix or on the surface [309]. Although this phenomenon is still under debate, it is widely accepted that the thermodynamic state and kinetic properties of the system and how they vary during processing govern the structure formation pathway of the membrane. Also, physical parameters like the temperature, the composition of the casting solution, the composition of the nonsolvent bath, and the surrounding atmosphere play a pivotal role in determining the synthetic pathway as well as the final membrane structure [322, 323]. Incorporating inorganic nanomaterials into polymeric membranes has been found to improve the chemical stability, the thermal stability, the permeation, and the mechanical as well as the antifouling resistance of membranes [313, 318, 321, 324].

For such purposes, nanoparticles like TiO₂, Al₂O₃, ZrO₂, Cu, Ag, and SiO₂ have been utilised in the past [309, 311, 318, 325].

Recently CCA-supported free TiO₂ (CCA/TiO₂/PSf) and Pd-doped titania (CCA/Pd-TiO₂/PSf) nanoparticles have been embedded within a polysulfone matrix to synthesise mixed matrix membranes [111, 112]. In these studies, both the CCA/TiO₂/PSf and the (CCA/TiO₂/PSf) membranes were found to be highly photoactive for the discolouration of Rhodamine B under visible-light irradiation. The CCA-supported nanoparticles were distributed both within and on the surface of the membranes (Figure 11). These studies revealed that only a minimal amount of the nanoparticles can be incorporated within the polymer matrix without compromising the mechanical properties. Increasing the amount of the nanoparticles to about 0.5% resulted in weakening of the mechanical properties of the nanoparticles. The presence of the nanoparticles also enhanced the permeate flux as well as the fouling behaviour of the PSf membranes. This is thus a great step that eliminates not only the problems associated with posttreatment and aggregation but also fouling of the membranes and thus provides a better alternative in finding means to deal with water-treatment problems.

12. Conclusion

From the literature discussed, the health risks associated with the presence of pollutants in water due to the failure of conventional water-treatment technologies to effectively remove organic and inorganic pollutants have been highlighted. It

has been revealed that TiO₂ nanoparticles have demonstrated the ability to completely degrade organic pollutants in an aqueous medium resulting in the formation of innocuous products and thus have tremendous potential to be used in water-treatment processes. Reformative processes to shift the absorption edge of titania to the visible-light region have been discussed. Supporting the TiO₂ on CCA supports has proven to drastically enhance the dispersion of the nanoparticles, reduce electron-hole pair recombination, and increase the surface area resulting in an increased photocatalytic activity. Also, CCA supports were found to play a major role in shifting the absorption edge of titania towards visible-light irradiation. Also, the LbL self-assembly of the metal-ion-doped TiO₂ on glass substrates overcame the problems associated with the need for the application of costly post-treatment processes needed when using suspended TiO₂. The embedding of the titania nanoparticles within the a polymer matrix has proved to be the recent pivotal advancement in the application of titania nanoparticles for environmental remediation processes.

Overall, this review brings to attention the advancements of titania nanoparticles in their use for water-treatment processes. These advancements thus serve as techniques that can be used in conjunction with the present water-treatment technologies to alleviate the problems associated with pollutants in drinking water systems. Also, since titania can degrade organic pollutants while simultaneously oxidising heavy metal species, it serves as a cheap dual process that can be further explored to realize the potential of TiO₂ in water-treatment processes. Furthermore, titania provides a cheaper alternative that can be used in conjunction with the already existing water-treatment technologies, especially membranes. Also the use of titania based systems is a better alternative for the use since it harnesses the green solar energy and thus reduces the environmental waste due to the use of chemicals. The ability of TiO₂ nanoparticles to completely deal with organic pollutants without producing recalcitrant by-products has thus opened new research avenues to be pursued.

Conflict of Interests

The authors declare that there is no conflict of interests regarding the publication of this paper.

Acknowledgment

The authors are grateful to the Department of Applied Chemistry, University of Johannesburg, South Africa, for constantly supporting our research program on nanomaterials, especially their financial support.

References

- [1] K. Murray, L. Slabbert, and B. Moloi, "Needs assessment and development framework for a tested implementation plan for the initialisation and execution of a National Toxicants Monitoring Programme (NTMP)," Final Report, Department of Water Affairs and Forestry (DWAF), Pretoria, South Africa, 2003.
- [2] T. Pradeep and Anshup, "Noble metal nanoparticles for water purification: a critical review," *Thin Solid Films*, vol. 517, no. 24, pp. 6441–6478, 2009.
- [3] M. Sun, D. Li, Y. Chen et al., "Synthesis and photocatalytic activity of calcium antimony oxide hydroxide for the degradation of dyes in water," *Journal of Physical Chemistry C*, vol. 113, no. 31, pp. 13825–13831, 2009.
- [4] X. Wang, Z. Gai, B. Yu et al., "Degradation of carbazole by microbial cells immobilized in magnetic gellan gum gel beads," *Applied and Environmental Microbiology*, vol. 73, no. 20, pp. 6421–6428, 2007.
- [5] S. Hong and M. Elimelech, "Chemical and physical aspects of natural organic matter (NOM) fouling of nanofiltration membranes," *Journal of Membrane Science*, vol. 132, no. 2, pp. 159–181, 1997.
- [6] T. S. Natarajan, M. Thomas, K. Natarajan, H. C. Bajaj, and R. J. Tayade, "Study on UV-LED/TiO₂ process for degradation of Rhodamine B dye," *Chemical Engineering Journal*, vol. 169, no. 1–3, pp. 126–134, 2011.
- [7] N. Savage and M. S. Diallo, "Nanomaterials and water purification: opportunities and challenges," *Journal of Nanoparticle Research*, vol. 7, no. 4–5, pp. 331–342, 2005.
- [8] K. Kabra, R. Chaudhary, and R. L. Sawhney, "Treatment of hazardous organic and inorganic compounds through aqueous-phase photocatalysis: a review," *Industrial and Engineering Chemistry Research*, vol. 43, no. 24, pp. 7683–7696, 2004.
- [9] P. Romero-Gómez, V. Rico, J. P. Espinós, A. R. González-Elipe, R. G. Palgrave, and R. G. Egdell, "Nitridation of nanocrystalline TiO₂ thin films by treatment with ammonia," *Thin Solid Films*, vol. 519, no. 11, pp. 3587–3595, 2011.
- [10] Z. J. Bo, G. Maochu, W. J. Li, L. Z. Min, Z. Ming, and Y. Chen, "Effect of metal doping into Ce_{0.5}Zr_{0.5}O₂ on photocatalytic activity of TiO₂/Ce_{0.45}Zr_{0.45}M_{0.1}O_x (M = Y, La, Mn)," *Journal of Hazardous Materials*, vol. 143, no. 1–2, pp. 516–521, 2007.
- [11] I. Dror, D. Baram, and B. Berkowitz, "Use of nanosized catalysts for transformation of chloro-organic pollutants," *Environmental Science and Technology*, vol. 39, no. 5, pp. 1283–1290, 2005.
- [12] D. N. Priya, J. M. Modak, and A. M. Raichur, "LbL fabricated poly(styrene sulfonate)/TiO₂ multilayer thin films for environmental applications," *ACS Applied Materials & Interfaces*, vol. 1, no. 11, pp. 2684–2693, 2009.
- [13] H. Choi, E. Stathatos, and D. D. Dionysiou, "Photocatalytic TiO₂ films and membranes for the development of efficient wastewater treatment and reuse systems," *Desalination*, vol. 202, no. 1–3, pp. 199–206, 2007.
- [14] G. V. Lowry and K. M. Johnson, "Congener-specific dechlorination of dissolved PCBs by microscale and nanoscale zerovalent iron in a water/methanol solution," *Environmental Science and Technology*, vol. 38, no. 19, pp. 5208–5216, 2004.
- [15] W. Nam, J. H. Park, and G. Y. Han, "Enhanced photocatalytic oxidation properties in Pt-TiO₂ thin films by grounding," *Korean Journal of Chemical Engineering*, vol. 26, no. 2, pp. 392–397, 2009.
- [16] P. Wang, T. Zhou, R. Wang, and T.-T. Lim, "Carbon-sensitized and nitrogen-doped TiO₂ for photocatalytic degradation of sulfanilamide under visible-light irradiation," *Water Research*, vol. 45, no. 16, pp. 5015–5026, 2011.
- [17] A. Faroon and J. Olson, *Toxicological Profile for Polychlorinated Biphenyls (PCBs)*, Agency for Toxic Substances and Disease Registry, US Department of Health and Human Security, 2000.

- [18] M. R. Hoffmann, S. T. Martin, W. Choi, and D. W. Bahnemann, "Environmental applications of semiconductor photocatalysis," *Chemical Reviews*, vol. 95, no. 1, pp. 69–96, 1995.
- [19] T. I. Nkambule, R. W. Krause, B. B. Mamba, and J. Haarhoff, "Removal of natural organic matter from water using ion-exchange resins and cyclodextrin polyurethanes," *Physics and Chemistry of the Earth*, vol. 34, no. 13–16, pp. 812–818, 2009.
- [20] J. Chen, B. Gu, E. J. LeBoeuf, H. Pan, and S. Dai, "Spectroscopic characterization of the structural and functional properties of natural organic matter fractions," *Chemosphere*, vol. 48, no. 1, pp. 59–68, 2002.
- [21] H. C. Hong, M. H. Wong, A. Mazumder, and Y. Liang, "Trophic state, natural organic matter content, and disinfection by-product formation potential of six drinking water reservoirs in the Pearl River Delta, China," *Journal of Hydrology*, vol. 359, no. 1–2, pp. 164–173, 2008.
- [22] A. Matilainen, E. T. Gjessing, T. Lahtinen, L. Hed, A. Bhatnagar, and M. Sillanpää, "An overview of the methods used in the characterisation of natural organic matter (NOM) in relation to drinking water treatment," *Chemosphere*, vol. 83, no. 11, pp. 1431–1442, 2011.
- [23] B. Gu, J. Schmitt, Z. Chen, L. Liang, and J. F. McCarthy, "Adsorption and desorption of natural organic matter on iron oxide: mechanisms and models," *Environmental Science and Technology*, vol. 28, no. 1, pp. 38–46, 1994.
- [24] V. Kanokkantapong, T. F. Marhaba, P. Pavasant, and B. Panyapinyophol, "Characterization of haloacetic acid precursors in source water," *Journal of Environmental Management*, vol. 80, no. 3, pp. 214–221, 2006.
- [25] S. Mattaraj, C. Jarusutthirak, and R. Jiratananon, "A combined osmotic pressure and cake filtration model for crossflow nanofiltration of natural organic matter," *Journal of Membrane Science*, vol. 322, no. 2, pp. 475–483, 2008.
- [26] T. I. Nkambule, R. W. M. Krause, J. Haarhoff, and B. B. Mamba, "Treatability and characterization of natural organic matter (NOM) in South African waters using newly developed methods," *Physics and Chemistry of the Earth*, vol. 36, no. 14–15, pp. 1159–1166, 2011.
- [27] S. McDonald, A. G. Bishop, P. D. Prenzler, and K. Robards, "Analytical chemistry of freshwater humic substances," *Analytica Chimica Acta*, vol. 527, no. 2, pp. 105–124, 2004.
- [28] J. Kim, Z. Cai, and M. M. Benjamin, "Effects of adsorbents on membrane fouling by natural organic matter," *Journal of Membrane Science*, vol. 310, no. 1–2, pp. 356–364, 2008.
- [29] H. Zhang, J. Qu, H. Liu, and X. Zhao, "Characterization of isolated fractions of dissolved organic matter from sewage treatment plant and the related disinfection by-products formation potential," *Journal of Hazardous Materials*, vol. 164, no. 2–3, pp. 1433–1438, 2009.
- [30] C. M. M. Bougeard, E. H. Goslan, B. Jefferson, and S. A. Parsons, "Comparison of the disinfection by-product formation potential of treated waters exposed to chlorine and monochloramine," *Water Research*, vol. 44, no. 3, pp. 729–740, 2010.
- [31] A. Kanan and T. Karanfil, "Formation of disinfection by-products in indoor swimming pool water: the contribution from filling water natural organic matter and swimmer body fluids," *Water Research*, vol. 45, no. 2, pp. 926–932, 2011.
- [32] T. Bond, J. Huang, M. R. Templeton, and N. Graham, "Occurrence and control of nitrogenous disinfection by-products in drinking water—a review," *Water Research*, vol. 45, no. 15, pp. 4341–4354, 2011.
- [33] B. Chen, W. Lee, P. K. Westerhoff, S. W. Krasner, and P. Herckes, "Solar photolysis kinetics of disinfection byproducts," *Water Research*, vol. 44, no. 11, pp. 3401–3409, 2010.
- [34] H. Zhang, J. Qu, H. Liu, and D. Wei, "Characterization of dissolved organic matter fractions and its relationship with the disinfection by-product formation," *Journal of Environmental Sciences*, vol. 21, no. 1, pp. 54–61, 2009.
- [35] I. Kristiana, C. Joll, and A. Heitz, "Powdered activated carbon coupled with enhanced coagulation for natural organic matter removal and disinfection by-product control: application in a western Australian water treatment plant," *Chemosphere*, vol. 83, no. 5, pp. 661–667, 2011.
- [36] R. Shen and S. A. Andrews, "Demonstration of 20 pharmaceuticals and personal care products (PPCPs) as nitrosamine precursors during chloramine disinfection," *Water Research*, vol. 45, no. 2, pp. 944–952, 2011.
- [37] S. H. Mhlongo, B. B. Mamba, and R. W. Krause, "Monitoring the prevalence of nitrosamines in South African waters and their removal using cyclodextrin polyurethanes," *Physics and Chemistry of the Earth, Parts A/B/C*, vol. 34, no. 13–16, pp. 819–824, 2009.
- [38] J. Nawrocki and P. Andrzejewski, "Nitrosamines and water," *Journal of Hazardous Materials*, vol. 189, no. 1–2, pp. 1–18, 2011.
- [39] V. V. B. Rao and S. R. M. Rao, "Adsorption studies on treatment of textile dyeing industrial effluent by flyash," *Chemical Engineering Journal*, vol. 116, no. 1, pp. 77–84, 2006.
- [40] S. N. Husaini, J. H. Zaidi, F. Malik, and M. Arif, "Application of nuclear track membrane for the reduction of pollutants in the industrial effluent," *Radiation Measurements*, vol. 43, no. 1, pp. S607–S611, 2008.
- [41] X.-H. Ou, C.-H. Wu, and S.-L. Lo, "Photodegradation of 4-chlorophenol by UV/photocatalysts: the effect of the interparticle electron transfer process," *Reaction Kinetics and Catalysis Letters*, vol. 88, no. 1, pp. 89–95, 2006.
- [42] S. M. Ali, S. Z. Sabae, M. Fayez, M. Monib, and N. A. Hegazi, "The influence of agro-industrial effluents on River Nile pollution," *Journal of Advanced Research*, vol. 2, no. 1, pp. 85–95, 2011.
- [43] B. Sancey, G. Trunfio, J. Charles et al., "Heavy metal removal from industrial effluents by sorption on cross-linked starch: chemical study and impact on water toxicity," *Journal of Environmental Management*, vol. 92, no. 3, pp. 765–772, 2011.
- [44] K.-H. Kim and S.-K. Ihm, "Heterogeneous catalytic wet air oxidation of refractory organic pollutants in industrial wastewaters: a review," *Journal of Hazardous Materials*, vol. 186, no. 1, pp. 16–34, 2011.
- [45] B. Hajem, H. Hamzaoui, and A. M'nif, "Chemical interaction between industrial acid effluents and the hydrous medium," *Desalination*, vol. 206, no. 1–3, pp. 154–162, 2007.
- [46] L.-C. Chiang, J.-E. Chang, and S.-C. Tseng, "Electrochemical oxidation pretreatment of refractory organic pollutants," *Water Science and Technology*, vol. 36, no. 2–3, pp. 123–130, 1997.
- [47] S. Ghasemi, S. Rahimnejad, S. R. Setayesh, S. Rohani, and M. R. Gholami, "Transition metal ions effect on the properties and photocatalytic activity of nanocrystalline TiO₂ prepared in an ionic liquid," *Journal of Hazardous Materials*, vol. 172, no. 2–3, pp. 1573–1578, 2009.
- [48] A. Kaur, S. Vats, S. Rekhi et al., "Physico-chemical analysis of the industrial effluents and their impact on the soil microflora," *Procedia Environmental Sciences*, vol. 2, pp. 595–599, 2010.
- [49] B. Kayan, B. Gözmen, M. Demirel, and A. M. Gizir, "Degradation of acid red 97 dye in aqueous medium using wet oxidation

- and electro-Fenton techniques," *Journal of Hazardous Materials*, vol. 177, no. 1–3, pp. 95–102, 2010.
- [50] L. Lei, Q. Dai, M. Zhou, and X. Zhang, "Decolorization of cationic red X-GRL by wet air oxidation: performance optimization and degradation mechanism," *Physics and Chemistry of the Earth, Parts A/B/C*, vol. 68, no. 13–16, pp. 1135–1142, 2007.
- [51] H. Y. He, W. X. Dong, and G. H. Zhang, "Photodegradation of aqueous methyl orange on MnTiO₃ powder at different initial pH," *Research on Chemical Intermediates*, vol. 36, no. 9, pp. 995–1001, 2010.
- [52] K. Yu, S. Yang, H. He, C. Sun, C. Gu, and Y. Ju, "Visible light-driven photocatalytic degradation of rhodamine B over NaBiO₃: Pathways and mechanism," *Journal of Physical Chemistry A*, vol. 113, no. 37, pp. 10024–10032, 2009.
- [53] A. Murat, A. Meltem, S. Funda, K. Nadir, A. Ertugrul, and S. Hikmet, "A novel approach to the hydrothermal synthesis of anatase titania nanoparticles and the photocatalytic degradation of rhodamine B," *Turkish Journal of Chemistry*, vol. 30, pp. 333–343, 2006.
- [54] N. C. Respicio and J. Heitz, "Comparative toxicity of rhodamine B and rhodamine 6G to the house fly (*Musca domestica* L.)," *Bulletin of Environmental Contamination and Toxicology*, vol. 27, no. 2, pp. 274–281, 1981.
- [55] T. Masciangioli and W.-X. Zhang, "Environmental technologies at the nanoscale," *Environmental Science and Technology*, vol. 37, no. 5, pp. 102–108, 2003.
- [56] S. Suárez, N. Arconada, Y. Castro et al., "Photocatalytic degradation of TCE in dry and wet air conditions with TiO₂ porous thin films," *Applied Catalysis B: Environmental*, vol. 108–109, pp. 14–21, 2011.
- [57] Y. Cao, H. Tan, T. Shi, T. Shi, T. Tang, and J. Li, "Preparation of Ag-doped TiO₂ nanoparticles for photocatalytic degradation of acetamiprid in water," *Journal of Chemical Technology and Biotechnology*, vol. 83, no. 4, pp. 546–552, 2008.
- [58] J. Sá and J. A. Anderson, "FTIR study of aqueous nitrate reduction over Pd/TiO₂," *Applied Catalysis B: Environmental*, vol. 77, no. 3–4, pp. 409–417, 2008.
- [59] C.-M. Hung, "Catalytic wet oxidation of ammonia solution: activity of the nanoscale platinum-palladium-rhodium composite oxide catalyst," *Journal of Hazardous Materials*, vol. 163, no. 1, pp. 180–186, 2009.
- [60] Z. Wu and M. Zhou, "Partial degradation of phenol by advanced electrochemical oxidation process," *Environmental Science and Technology*, vol. 35, no. 13, pp. 2698–2703, 2001.
- [61] J. Mucha and R. Zarzycki, "Analysis of wet oxidation process after initial thermohydrolysis of excess sewage sludge," *Water Research*, vol. 42, no. 12, pp. 3025–3032, 2008.
- [62] A. W. Zularisam, A. F. Ismail, and R. Salim, "Behaviours of natural organic matter in membrane filtration for surface water treatment—a review," *Desalination*, vol. 194, no. 1–3, pp. 211–231, 2006.
- [63] M. Anpo, "Utilization of TiO₂ photocatalysts in green chemistry," *Pure and Applied Chemistry*, vol. 72, no. 7, pp. 1265–1270, 2000.
- [64] J.-Y. Li, W.-H. Ma, P.-X. Lei, and J.-C. Zhao, "Detection of intermediates in the TiO₂-assisted photodegradation of Rhodamine B under visible light irradiation," *Journal of Environmental Sciences*, vol. 19, no. 7, pp. 892–896, 2007.
- [65] K. Sunada, Y. Kikuchi, K. Hashimoto, and A. Fujishima, "Bactericidal and detoxification effects of TiO₂ thin film photocatalysts," *Environmental Science and Technology*, vol. 32, no. 5, pp. 726–728, 1998.
- [66] A. Bhattacharyya, S. Kawi, and M. B. Ray, "Photocatalytic degradation of orange II by TiO₂ catalysts supported on adsorbents," *Catalysis Today*, vol. 98, no. 3, pp. 431–439, 2004.
- [67] V. Mirkhani, S. Tangestaninejad, M. Moghadam, M. H. Habibi, and A. R. Vartooni, "Photodegradation of aromatic amines by Ag-TiO₂ photocatalyst," *Journal of the Iranian Chemical Society*, vol. 6, no. 4, pp. 800–807, 2009.
- [68] P. E. Savage, "Organic chemical reactions in supercritical water," *Chemical Reviews*, vol. 99, no. 2–3, pp. 603–621, 1999.
- [69] H. E. Barner, C. Y. Huang, T. Johnson, G. Jacobs, M. A. Martch, and W. R. Killilea, "Supercritical water oxidation: an emerging technology," *Journal of Hazardous Materials*, vol. 31, no. 1, pp. 1–17, 1992.
- [70] V. Marulanda and G. Bolaños, "Supercritical water oxidation of a heavily PCB-contaminated mineral transformer oil: Laboratory-scale data and economic assessment," *Journal of Supercritical Fluids*, vol. 54, no. 2, pp. 258–265, 2010.
- [71] S.-H. Son, J.-H. Lee, and C.-H. Lee, "Corrosion phenomena of alloys by subcritical and supercritical water oxidation of 2-chlorophenol," *Journal of Supercritical Fluids*, vol. 44, no. 3, pp. 370–378, 2008.
- [72] T. Fujii, R. Hayashi, S.-I. Kawasaki, A. Suzuki, and Y. Oshima, "Water density effects on methanol oxidation in supercritical water at high pressure up to 100 MPa," *Journal of Supercritical Fluids*, vol. 58, no. 1, pp. 142–149, 2011.
- [73] P. A. Marrone and G. T. Hong, "Corrosion control methods in supercritical water oxidation and gasification processes," *Journal of Supercritical Fluids*, vol. 51, no. 2, pp. 83–103, 2009.
- [74] R. Hayashi, M. Onishi, M. Sugiyama, S. Koda, and Y. Oshima, "Kinetic analysis on alcohol concentration and mixture effect in supercritical water oxidation of methanol and ethanol by elementary reaction model," *The Journal of Supercritical Fluids*, vol. 40, no. 1, pp. 74–83, 2007.
- [75] F. Stüber, J. Font, A. Fortuny, C. Bengoa, A. Eftaxias, and A. Fabregat, "Carbon materials and catalytic wet air oxidation of organic pollutants in wastewater," *Topics in Catalysis*, vol. 33, no. 1–4, pp. 3–50, 2005.
- [76] N. Li, C. Descorme, and M. Besson, "Catalytic wet air oxidation of chlorophenols over supported ruthenium catalysts," *Journal of Hazardous Materials*, vol. 146, no. 3, pp. 602–609, 2007.
- [77] D. Prabhakaran, T. Kannadasan, and C. Ahmed Basha, "Mediated electrochemical oxidation process for destruction of TOC in a batch recirculation reactor," *International Journal of ChemTech Research*, vol. 1, no. 4, pp. 962–969, 2009.
- [78] D. Nematollahi and L. Mohammadi-Behzad, "Electrochemical oxidation of catechol in the presence of some azacrown ethers and transition metal ions in acetonitrile," *International Journal of Electrochemical Science*, vol. 4, no. 11, pp. 1583–1592, 2009.
- [79] L.-C. Chiang, J.-E. Chang, and T.-C. Wen, "Indirect oxidation effect in electrochemical oxidation treatment of landfill leachate," *Water Research*, vol. 29, no. 2, pp. 671–678, 1995.
- [80] J. D. Rodgers, W. Jedral, and N. J. Bunce, "Electrochemical oxidation of chlorinated phenols," *Environmental Science and Technology*, vol. 33, no. 9, pp. 1453–1457, 1999.
- [81] S. Jiao, S. Zheng, D. Yin, L. Wang, and L. Chen, "Aqueous photolysis of tetracycline and toxicity of photolytic products to luminescent bacteria," *Chemosphere*, vol. 73, no. 3, pp. 377–382, 2008.
- [82] L. Fang, J. Huang, G. Yu, and X. Li, "Quantitative structure-property relationship studies for direct photolysis rate constants and quantum yields of polybrominated diphenyl ethers in

- hexane and methanol," *Ecotoxicology and Environmental Safety*, vol. 72, no. 5, pp. 1587–1593, 2009.
- [83] B. Abramović, D. Šojić, and V. Anderluh, "Visible-light-induced photocatalytic degradation of herbicide mecoprop in aqueous suspension of TiO_2 ," *Acta Chimica Slovenica*, vol. 54, no. 3, pp. 558–564, 2007.
- [84] E. Bae and W. Choi, "Highly enhanced photoreductive degradation of perchlorinated compounds on dye-sensitized metal/ TiO_2 under visible light," *Environmental Science & Technology*, vol. 37, no. 1, pp. 147–152, 2003.
- [85] F. Zhang, J. Zhao, T. Shen, H. Hidaka, E. Pelizzetti, and N. Serpone, " TiO_2 -assisted photodegradation of dye pollutants. II. Adsorption and degradation kinetics of eosin in TiO_2 dispersions under visible light irradiation," *Applied Catalysis B: Environmental*, vol. 15, no. 1-2, pp. 147–156, 1998.
- [86] L. Zhang and T. J. Webster, "Nanotechnology and nanomaterials: promises for improved tissue regeneration," *Nano Today*, vol. 4, no. 1, pp. 66–80, 2009.
- [87] B. F. G. Johnson, "Nanoparticles in catalysis," *Topics in Catalysis*, vol. 24, no. 1-4, pp. 147–159, 2003.
- [88] X. Chen and S. S. Mao, "Titanium dioxide nanomaterials: Synthesis, properties, modifications and applications," *Chemical Reviews*, vol. 107, no. 7, pp. 2891–2959, 2007.
- [89] Z. He, C. Sun, S. Yang, Y. Ding, H. He, and Z. Wang, "Photocatalytic degradation of rhodamine B by Bi_2WO_6 with electron accepting agent under microwave irradiation: mechanism and pathway," *Journal of Hazardous Materials*, vol. 162, no. 2-3, pp. 1477–1486, 2009.
- [90] W. Dong and C. Zhu, "Optical properties of surface-modified Bi_2O_3 nanoparticles," *Journal of Physics and Chemistry of Solids*, vol. 64, no. 2, pp. 265–271, 2003.
- [91] F. Meng, F. Lu, Z. Sun, and J. Lü, "A mechanism for enhanced photocatalytic activity of nano-size silver particle modified titanium dioxide thin films," *Science China Technological Sciences*, vol. 53, no. 11, pp. 3027–3032, 2010.
- [92] A. Fujishima, T. N. Rao, and D. A. Tryk, "Titanium dioxide photocatalysis," *Journal of Photochemistry and Photobiology C: Photochemistry Reviews*, vol. 1, no. 1, pp. 1–21, 2000.
- [93] M. Ni, M. K. H. Leung, D. Y. C. Leung, and K. Sumathy, "A review and recent developments in photocatalytic water-splitting using TiO_2 for hydrogen production," *Renewable and Sustainable Energy Reviews*, vol. 11, no. 3, pp. 401–425, 2007.
- [94] W. Tang, Q. Wang, X. Zeng, and X. Chen, "Photocatalytic degradation on Disperse Blue with modified nano- TiO_2 film electrode," *Journal of Solid State Electrochemistry*, vol. 16, no. 4, pp. 1429–1445, 2012.
- [95] U. Diebold, "The surface science of titanium dioxide," *Surface Science Reports*, vol. 48, no. 5–8, pp. 53–229, 2003.
- [96] A. Kudo, R. Niishiro, A. Iwase, and H. Kato, "Effects of doping of metal cations on morphology, activity, and visible light response of photocatalysts," *Chemical Physics*, vol. 339, no. 1–3, pp. 104–110, 2007.
- [97] A. R. Malagutti, H. A. J. L. Mourão, J. R. Garbin, and C. Ribeiro, "Deposition of TiO_2 and $\text{Ag}:\text{TiO}_2$ thin films by the polymeric precursor method and their application in the photodegradation of textile dyes," *Applied Catalysis B: Environmental*, vol. 90, no. 1-2, pp. 205–212, 2009.
- [98] K. M. Reddy, S. V. Manorama, and A. R. Reddy, "Bandgap studies on anatase titanium dioxide nanoparticles," *Materials Chemistry and Physics*, vol. 78, no. 1, pp. 239–245, 2003.
- [99] R. Pode, "On the problem of open circuit voltage in metal phthalocyanine/ C_{60} organic solar cells," *Advanced Materials Letters*, vol. 2, pp. 3–11, 2011.
- [100] R. Ferrando, J. Jellinek, and R. L. Johnston, "Nanoalloys: from theory to applications of alloy clusters and nanoparticles," *Chemical Reviews*, vol. 108, no. 3, pp. 845–910, 2008.
- [101] L. Shivalingappa, J. Sheng, and T. Fukami, "Photocatalytic effect in platinum doped titanium dioxide films," *Vacuum*, vol. 48, no. 5, pp. 413–416, 1997.
- [102] C. Minero, G. Mariella, V. Maurino, D. Vione, and E. Pelizzetti, "Photocatalytic transformation of organic compounds in the presence of inorganic ions. 2. Competitive reactions of phenol and alcohols on a titanium dioxide-fluoride system," *Langmuir*, vol. 16, no. 23, pp. 8964–8972, 2000.
- [103] C. Minero, G. Mariella, V. Maurino, and E. Pelizzetti, "Photocatalytic transformation of organic compounds in the presence of inorganic anions. 1. Hydroxyl-mediated and direct electron-transfer reactions of phenol on a titanium dioxide-fluoride system," *Langmuir*, vol. 16, no. 6, pp. 2632–2641, 2000.
- [104] S. Wang, L. Ji, B. Wu, Q. Gong, Y. Zhu, and J. Liang, "Influence of surface treatment on preparing nanosized TiO_2 supported on carbon nanotubes," *Applied Surface Science*, vol. 255, no. 5, pp. 3263–3266, 2008.
- [105] P. Bouras, E. Stathatos, and P. Lianos, "Pure versus metal-ion-doped nanocrystalline titania for photocatalysis," *Applied Catalysis B: Environmental*, vol. 73, no. 1-2, pp. 51–59, 2007.
- [106] M. M. Mahlambi, A. K. Mishra, S. B. Mishra, R. W. Krause, B. B. Mamba, and A. M. Raichur, "Effect of metal ions (Ag, Co, Ni, and Pd) on the visible light degradation of Rhodamine B by carbon-covered alumina-supported TiO_2 in aqueous solutions," *Industrial and Engineering Chemistry Research*, vol. 52, no. 5, pp. 1783–1794, 2013.
- [107] W. Weng, M. Ma, P. Du et al., "Superhydrophilic Fe doped titanium dioxide thin films prepared by a spray pyrolysis deposition," *Surface and Coatings Technology*, vol. 198, no. 1–3, pp. 340–344, 2005.
- [108] A. Izquierdo, S. S. Ono, J.-C. Voegel, P. Schaaf, and G. Decher, "Dipping versus spraying: exploring the deposition conditions for speeding up layer-by-layer assembly," *Langmuir*, vol. 21, no. 16, pp. 7558–7567, 2005.
- [109] G. Decher, "Fuzzy nanoassemblies: toward layered polymeric multicomposites," *Science*, vol. 277, no. 5330, pp. 1232–1237, 1997.
- [110] M. M. Mahlambi, A. K. Mishra, S. B. Mishra, A. M. Raichur, B. B. Mamba, and R. W. Krause, "Layer-by-layer self-assembled metal-ion- (Ag-, Co-, Ni-, and Pd-) doped TiO_2 nanoparticles: synthesis, characterisation, and visible light degradation of rhodamine B," *Journal of Nanomaterials*, vol. 2012, Article ID 302046, 12 pages, 2012.
- [111] M. M. Mahlambi, O. T. Mahlangu, G. D. Vilakati, and B. B. Mamba, "Visible light photodegradation of rhodamine B dye by two forms of carbon-covered alumina supported TiO_2 /polysulfone membranes," *Industrial and Engineering Chemistry Research*, vol. 53, no. 14, pp. 5709–5717, 2014.
- [112] M. M. Mahlambi, G. D. Vilakati, and B. B. Mamba, "Synthesis, characterization, and visible light degradation of rhodamine B dye by carbon-covered alumina supported Pd- TiO_2 /polysulfone membranes," *Separation Science and Technology*, vol. 49, no. 14, pp. 2124–2134, 2014.
- [113] A. N. Guz and Y. Y. Rushchitskii, "Nanomaterials: on the mechanics of nanomaterials," *International Applied Mechanics*, vol. 39, no. 11, pp. 1271–1293, 2003.

- [114] J. D. Mackenzie and E. P. Bescher, "Chemical routes in the synthesis of nanomaterials using the sol-gel process," *Accounts of Chemical Research*, vol. 40, no. 9, pp. 810–818, 2007.
- [115] C. E. Allmond, A. T. Sellinger, K. Gogick, and J. M. Fitzgerald, "Photo-chemical synthesis and deposition of noble metal nanoparticles," *Applied Physics A*, vol. 86, no. 4, pp. 477–480, 2007.
- [116] K. Ramanathan, D. Avnir, A. Modestov, and O. Lev, "Sol-gel derived ormosil-exfoliated graphite-TiO₂ composite floating catalyst: photodeposition of copper," *Chemistry of Materials*, vol. 9, no. 11, pp. 2533–2540, 1997.
- [117] J. Wang, R. Li, Z. Zhang et al., "Degradation of hazardous dyes in wastewater using nanometer mixed crystal TiO₂ powders under visible light irradiation," *Water, Air, and Soil Pollution*, vol. 189, no. 1–4, pp. 225–237, 2008.
- [118] D. Beydoun and R. Amal, "Implications of heat treatment on the properties of a magnetic iron oxide-titanium dioxide photocatalyst," *Materials Science and Engineering B*, vol. 94, no. 1, pp. 71–81, 2002.
- [119] W. Ho, J. C. Yu, and S. Lee, "Synthesis of hierarchical nanoporous F-doped TiO₂ spheres with visible light photocatalytic activity," *Chemical Communications*, no. 10, pp. 1115–1117, 2006.
- [120] J. Yu and J. Zhang, "A simple template-free approach to TiO₂ hollow spheres with enhanced photocatalytic activity," *Dalton Transactions*, vol. 39, no. 25, pp. 5860–5867, 2010.
- [121] H. D. Jang, S.-K. Kim, and S.-J. Kim, "Effect of particle size and phase composition of titanium dioxide nanoparticles on the photocatalytic properties," *Journal of Nanoparticle Research*, vol. 3, no. 2–3, pp. 141–147, 2001.
- [122] A. Pottier, C. Chanéac, E. Tronc, L. Mazerolles, and J.-P. Jolivet, "Synthesis of brookite TiO₂ nanoparticles by thermolysis of TiCl₄ in strongly acidic aqueous media," *Journal of Materials Chemistry*, vol. 11, no. 4, pp. 1116–1121, 2001.
- [123] D.-S. Seo, J.-K. Lee, E.-G. Lee, and H. Kim, "Effect of aging agents on the formation of TiO₂ nanocrystalline powder," *Materials Letters*, vol. 51, no. 2, pp. 115–119, 2001.
- [124] M. Afuyoni, G. Nashed, and I. M. Nasser, "TiO₂ doped with SnO₂ and studying its structural and electrical properties," *Energy Procedia*, vol. 6, pp. 11–20, 2011.
- [125] S. Nakade, M. Matsuda, S. Kambe et al., "Dependence of TiO₂ nanoparticle preparation methods and annealing temperature on the efficiency of dye-sensitized solar cells," *Journal of Physical Chemistry B*, vol. 106, no. 39, pp. 10004–10010, 2002.
- [126] M. Subramanian, S. Vijayalakshmi, S. Venkataraj, and R. Jayavel, "Effect of cobalt doping on the structural and optical properties of TiO₂ films prepared by sol-gel process," *Thin Solid Films*, vol. 516, no. 12, pp. 3776–3782, 2008.
- [127] J. Ovenstone, "Preparation of novel titania photocatalysts with high activity," *Journal of Materials Science*, vol. 36, no. 6, pp. 1325–1329, 2001.
- [128] Y. Zhang, A. Weidenkaff, and A. Reller, "Mesoporous structure and phase transition of nanocrystalline TiO₂," *Materials Letters*, vol. 54, no. 5–6, pp. 375–381, 2002.
- [129] M. Behpour, S. M. Ghoreishi, and F. S. Razavi, "Photocatalytic activity of TiO₂/Ag nanoparticles on degradation of water pollutions," *Digest Journal of Nanomaterials and Biostructures*, vol. 5, no. 2, pp. 467–475, 2010.
- [130] J. Araña, J. M. Doña-Rodríguez, E. Tello Rendón et al., "TiO₂ activation by using activated carbon as a support: part I. Surface characterisation and decantability study," *Applied Catalysis B: Environmental*, vol. 44, no. 2, pp. 161–172, 2003.
- [131] P. C. Lansåker, J. Backholm, G. A. Niklasson, and C. G. Granqvist, "TiO₂/Au/TiO₂ multilayer thin films: novel metal-based transparent conductors for electrochromic devices," *Thin Solid Films*, vol. 518, no. 4, pp. 1225–1229, 2009.
- [132] M.-S. Wong, S.-W. Hsu, K. K. Rao, and C. P. Kumar, "Influence of crystallinity and carbon content on visible light photocatalysis of carbon doped titania thin films," *Journal of Molecular Catalysis A: Chemical*, vol. 279, no. 1, pp. 20–26, 2008.
- [133] T. Peng, D. Zhao, K. Dai, W. Shi, and K. Hirao, "Synthesis of titanium dioxide nanoparticles with mesoporous anatase wall and high photocatalytic activity," *Journal of Physical Chemistry B*, vol. 109, no. 11, pp. 4947–4952, 2005.
- [134] J. P. Vicente, T. Gacoin, P. Barboux, J.-P. Boilot, M. Rondet, and L. Guéneau, "Photocatalytic decomposition of fatty stains by TiO₂ thin films," *International Journal of Photoenergy*, vol. 5, no. 2, pp. 95–98, 2003.
- [135] P. Kiri, G. Hyett, and R. Binions, "Solid state thermochromic materials," *Advanced Materials Letters*, vol. 1, no. 2, pp. 86–105, 2010.
- [136] M. I. Zaki, G. A. H. Mekhemer, N. E. Fouad, T. C. Jagadale, and S. B. Ogale, "Surface texture and specific adsorption sites of sol-gel synthesized anatase TiO₂ nanoparticles," *Materials Research Bulletin*, vol. 45, no. 10, pp. 1470–1475, 2010.
- [137] A. S. Barnard and P. Zapol, "Predicting the energetics, phase stability, and morphology evolution of faceted and spherical anatase nanocrystals," *Journal of Physical Chemistry B*, vol. 108, no. 48, pp. 18435–18440, 2004.
- [138] J. Zhu, J. Zhang, F. Chen, K. Iino, and M. Anpo, "High activity TiO₂ photocatalysts prepared by a modified sol-gel method: characterization and their photocatalytic activity for the degradation of XRG and X-GL," *Topics in Catalysis*, vol. 35, no. 3–4, pp. 261–268, 2005.
- [139] J. A. Navío, G. Colón, M. Macías, C. Real, and M. I. Litter, "Iron-doped titania semiconductor powders prepared by a sol-gel method. Part I: synthesis and characterization," *Applied Catalysis A: General*, vol. 177, no. 1, pp. 111–120, 1999.
- [140] V. Panić, A. Dekanski, S. Milonjić, R. Atanasoski, and B. Nikolić, "The influence of the aging time of RuO₂ and TiO₂ sols on the electrochemical properties and behavior for the chlorine evolution reaction of activated titanium anodes obtained by the sol-gel procedure," *Electrochimica Acta*, vol. 46, no. 2–3, pp. 415–421, 2000.
- [141] J. Zarzycki, "Past and present of sol-gel science and technology," *Journal of Sol-Gel Science and Technology*, vol. 8, no. 1–3, pp. 17–22, 1997.
- [142] A. Ahmad, J. Thiel, and S. I. Shah, "Structural effects of niobium and silver doping on titanium dioxide nanoparticles," *Journal of Physics: Conference Series*, vol. 61, no. 1, pp. 11–15, 2007.
- [143] K.-R. Zhu, M.-S. Zhang, J.-M. Hong, and Z. Yin, "Size effect on phase transition sequence of TiO₂ nanocrystal," *Materials Science and Engineering A*, vol. 403, no. 1–2, pp. 87–93, 2005.
- [144] T. Sugimoto, K. Okada, and H. Itoh, "Synthesis of uniform spindle-type titania particles by the gel-sol method," *Journal of Colloid and Interface Science*, vol. 193, no. 1, pp. 140–143, 1997.
- [145] T. Sugimoto, X. Zhou, and A. Muramatsu, "Synthesis of uniform anatase TiO₂ nanoparticles by gel-sol method: 1. Solution chemistry of Ti(OH)_n⁽⁴⁻ⁿ⁾⁺ complexes," *Journal of Colloid and Interface Science*, vol. 252, pp. 339–346, 2002.
- [146] T. Sugimoto, X. Zhou, and A. Muramatsu, "Synthesis of uniform anatase TiO₂ nanoparticles by gel-sol method. 4. Shape control," *Journal of Colloid and Interface Science*, vol. 259, no. 1, pp. 53–61, 2003.

- [147] T. Sugimoto, X. Zhou, and A. Muramatsu, "Synthesis of uniform anatase TiO₂ nanoparticles by gel-sol method: 3. Formation process and size control," *Journal of Colloid and Interface Science*, vol. 259, no. 1, pp. 43–52, 2003.
- [148] W. Chen and W. Gao, "Sol-enhanced electroplating of nanostructured Ni-TiO₂ composite coatings—the effects of sol concentration on the mechanical and corrosion properties," *Electrochimica Acta*, vol. 55, no. 22, pp. 6865–6871, 2010.
- [149] Y. Lei, L. D. Zhang, and J. C. Fan, "Fabrication, characterization and Raman study of TiO₂ nanowire arrays prepared by anodic oxidative hydrolysis of TiCl₃," *Chemical Physics Letters*, vol. 338, no. 4–6, pp. 231–236, 2001.
- [150] X.-S. Zhou, L.-J. Li, Y.-H. Lin, and C.-W. Nan, "Characterization and properties of anatase TiO₂ film prepared via colloidal sol method under low temperature," *Journal of Electroceramics*, vol. 21, no. 1–4, pp. 795–797, 2008.
- [151] J. Zhu, J. Ren, Y. Huo, Z. Bian, and H. Li, "Nanocrystalline Fe/TiO₂ visible photocatalyst with a mesoporous structure prepared via a nonhydrolytic sol-gel route," *Journal of Physical Chemistry C*, vol. 111, no. 51, pp. 18965–18969, 2007.
- [152] G. Guo, J. K. Whitesell, and M. A. Fox, "Synthesis of TiO₂ photocatalysts in supercritical CO₂ via a non-hydrolytic route," *Journal of Physical Chemistry B*, vol. 109, no. 40, pp. 18781–18785, 2005.
- [153] Y.-W. Jun, M. F. Casula, J.-H. Sim, S. Y. Kim, J. Cheon, and A. P. Alivisatos, "Surfactant-assisted elimination of a high energy facet as a means of controlling the shapes of TiO₂ nanocrystals," *Journal of the American Chemical Society*, vol. 125, no. 51, pp. 15981–15985, 2003.
- [154] T. J. Trentler, T. E. Denler, J. F. Bertone, A. Agrawal, and V. L. Colvin, "Synthesis of TiO₂ nanocrystals by nonhydrolytic solution-based reactions," *Journal of the American Chemical Society*, vol. 121, no. 7, pp. 1613–1614, 1999.
- [155] B. Koo, J. Park, Y. Kim, S.-H. Choi, Y.-E. Sung, and T. Hyeon, "Simultaneous phase- and size-controlled synthesis of TiO₂ nanorods via non-hydrolytic sol-gel reaction of syringe pump delivered precursors," *Journal of Physical Chemistry B*, vol. 110, no. 48, pp. 24318–24323, 2006.
- [156] A. López, D. Acosta, A. I. Martínez, and J. Santiago, "Nanostructured low crystallized titanium dioxide thin films with good photocatalytic activity," *Powder Technology*, vol. 202, no. 1–3, pp. 111–117, 2010.
- [157] J. Liu, Y. Zhao, L. Shi et al., "Solvothermal synthesis of crystalline phase and shape controlled Sn⁴⁺-Doped TiO₂ nanocrystals: Effects of reaction solvent," *ACS Applied Materials and Interfaces*, vol. 3, no. 4, pp. 1261–1268, 2011.
- [158] J. Liao, L. Shi, S. Yuan, Y. Zhao, and J. Fang, "Solvothermal synthesis of TiO₂ nanocrystal colloids from peroxotitanate complex solution and their photocatalytic activities," *Journal of Physical Chemistry C*, vol. 113, no. 43, pp. 18778–18783, 2009.
- [159] W. Q. Fang, J. Z. Zhou, J. Liu et al., "Hierarchical structures of single-crystalline anatase TiO₂ nanosheets dominated by 001 facets," *Chemistry*, vol. 17, no. 5, pp. 1423–1427, 2011.
- [160] X. Wang, J. Zhuang, Q. Peng, and Y. Li, "A general strategy for nanocrystal synthesis," *Nature*, vol. 437, no. 7055, pp. 121–124, 2005.
- [161] X.-L. Li, Q. Peng, J.-X. Yi, X. Wang, and Y. Li, "Near monodisperse TiO₂ nanoparticles and nanorods," *Chemistry—A European Journal*, vol. 12, no. 8, pp. 2383–2391, 2006.
- [162] J. Xu, J.-P. Ge, and Y.-D. Li, "Solvothermal synthesis of monodisperse PbSe nanocrystals," *The Journal of Physical Chemistry B*, vol. 110, no. 6, pp. 2497–2501, 2006.
- [163] K. S. Yeung and Y. W. Lam, "A simple chemical vapour deposition method for depositing thin TiO₂ films," *Thin Solid Films*, vol. 109, no. 2, pp. 169–178, 1983.
- [164] H. Yoshitake, T. Sugihara, and T. Tatsumi, "Preparation of wormhole-like mesoporous TiO₂ with an extremely large surface area and stabilization of its surface by chemical vapor deposition," *Chemistry of Materials*, vol. 14, no. 3, pp. 1023–1029, 2002.
- [165] H. Nizard, M. L. Kosinova, N. I. Fainer, Y. M. Rumyantsev, B. M. Ayupov, and Y. V. Shubin, "Deposition of titanium dioxide from TTIP by plasma enhanced and remote plasma enhanced chemical vapor deposition," *Surface and Coatings Technology*, vol. 202, no. 17, pp. 4076–4085, 2008.
- [166] Y. Guo, X.-W. Zhang, W.-H. Weng, and G.-R. Han, "Structure and properties of nitrogen-doped titanium dioxide thin films grown by atmospheric pressure chemical vapor deposition," *Thin Solid Films*, vol. 515, no. 18, pp. 7117–7121, 2007.
- [167] P. G. Karlsson, J. H. Richter, M. P. Andersson et al., "TiO₂ chemical vapor deposition on Si(111) in ultrahigh vacuum: transition from interfacial phase to crystalline phase in the reaction limited regime," *Surface Science*, vol. 605, no. 13–14, pp. 1147–1156, 2011.
- [168] W.-Y. Ahn, S. A. Sheeley, T. Rajh, and D. M. Cropek, "Photocatalytic reduction of 4-nitrophenol with arginine-modified titanium dioxide nanoparticles," *Applied Catalysis B: Environmental*, vol. 74, no. 1–2, pp. 103–110, 2007.
- [169] B. Neppolian, H. Yamashita, Y. Okada, H. Nishijima, and M. Anpo, "Preparation of unique TiO₂ nano-particle photocatalysts by a multi-gelation method for control of the physico-chemical parameters and reactivity," *Catalysis Letters*, vol. 105, no. 1–2, pp. 111–117, 2005.
- [170] H. Liu, W. Yang, Y. Ma et al., "Synthesis and characterization of titania prepared by using a photoassisted sol-gel method," *Langmuir*, vol. 19, no. 7, pp. 3001–3005, 2003.
- [171] Y. Bessekhouad, D. Robert, and J. V. Weber, "Synthesis of photocatalytic TiO₂ nanoparticles: optimization of the preparation conditions," *Journal of Photochemistry and Photobiology A: Chemistry*, vol. 157, no. 1, pp. 47–53, 2003.
- [172] G. Tian, H. Fu, L. Jing, and C. Tian, "Synthesis and photocatalytic activity of stable nanocrystalline TiO₂ with high crystallinity and large surface area," *Journal of Hazardous Materials*, vol. 161, no. 2–3, pp. 1122–1130, 2009.
- [173] A. Daßler, A. Feltz, J. Jung, W. Ludwig, and E. Kaisersberger, "Characterization of rutile and anatase powders by thermal analysis," *Journal of Thermal Analysis*, vol. 33, no. 3, pp. 803–809, 1988.
- [174] W. Fu, H. Yang, M. Li, M. Li, N. Yang, and G. Zou, "Anatase TiO₂ nanolayer coating on cobalt ferrite nanoparticles for magnetic photocatalyst," *Materials Letters*, vol. 59, no. 27, pp. 3530–3534, 2005.
- [175] N. Chitose, S. Ueta, S. Seino, and T. A. Yamamoto, "Radiolysis of aqueous phenol solutions with nanoparticles. 1. Phenol degradation and TOC removal in solutions containing TiO₂ induced by UV, γ -ray and electron beams," *Chemosphere*, vol. 50, no. 8, pp. 1007–1013, 2003.
- [176] X. Li, R. Xiong, and G. Wei, "S-N co-doped TiO₂ photocatalysts with visible-light activity prepared by sol-gel method," *Catalysis Letters*, vol. 125, no. 1–2, pp. 104–109, 2008.
- [177] K. Mori, K. Maki, S. Kawasaki, S. Yuan, and H. Yamashita, "Hydrothermal synthesis of TiO₂ photocatalysts in the presence of NH₄F and their application for degradation of organic

- compounds," *Chemical Engineering Science*, vol. 63, no. 20, pp. 5066–5070, 2008.
- [178] M.-C. Wang, H.-J. Lin, C.-H. Wang, and H.-C. Wu, "Effects of annealing temperature on the photocatalytic activity of N-doped TiO₂ thin films," *Ceramics International*, vol. 38, no. 1, pp. 195–200, 2012.
- [179] D.-S. Bae, K.-S. Han, and J. H. Adair, "Synthesis of Cu/SiO₂ nanosize particles by a reverse micelle and sol-gel processing," *Journal of Materials Science Letters*, vol. 21, no. 1, pp. 53–54, 2002.
- [180] S.-W. Wei, B. Peng, L.-Y. Chai, Y.-C. Liu, and Z.-Y. Li, "Preparation of doping titania antibacterial powder by ultrasonic spray pyrolysis," *Transactions of Nonferrous Metals Society of China*, vol. 18, no. 5, pp. 1145–1150, 2008.
- [181] C.-C. Chan, C.-C. Chang, W.-C. Hsu, S.-K. Wang, and J. Lin, "Photocatalytic activities of Pd-loaded mesoporous TiO₂ thin films," *Chemical Engineering Journal*, vol. 152, no. 2-3, pp. 492–497, 2009.
- [182] M. Hamadian, A. Reisi-Vanani, and A. Majedi, "Sol-gel preparation and characterization of Co/TiO₂ nanoparticles: application to the degradation of methyl orange," *Journal of the Iranian Chemical Society*, vol. 7, no. 1, pp. S52–S58, 2010.
- [183] S. Klosek and D. Raftery, "Visible light driven V-doped TiO₂ photocatalyst and its photooxidation of ethanol," *Journal of Physical Chemistry B*, vol. 105, no. 14, pp. 2815–2819, 2002.
- [184] G. N. Kryukova, G. A. Zenkovets, A. A. Shutilov et al., "Structural peculiarities of TiO₂ and Pt/TiO₂ catalysts for the photocatalytic oxidation of aqueous solution of acid orange 7 dye upon ultraviolet light," *Applied Catalysis B: Environmental*, vol. 71, no. 3-4, pp. 169–176, 2007.
- [185] R. Mechiakh, N. B. Sedrine, and R. Chtourou, "Sol-gel synthesis, characterization and optical properties of mercury-doped TiO₂ thin films deposited on ITO glass substrates," *Applied Surface Science*, vol. 257, no. 21, pp. 9103–9109, 2011.
- [186] D. Jing, Y. Zhang, and L. Guo, "Study on the synthesis of Ni doped mesoporous TiO₂ and its photocatalytic activity for hydrogen evolution in aqueous methanol solution," *Chemical Physics Letters*, vol. 415, no. 1–3, pp. 74–78, 2005.
- [187] J. Nair, P. Nair, F. Mizukami, Y. Oosawa, and T. Okubo, "Microstructure and phase transformation behavior of doped nanostructured titania," *Materials Research Bulletin*, vol. 34, no. 8, pp. 1275–1290, 1999.
- [188] S. S. Samal, P. Jeyaraman, and V. Vishwakarma, "Sonochemical coating of Ag-TiO₂ nanoparticles on textile fabrics for stain repellency and self-cleaning—the Indian scenario: a review," *Journal of Minerals and Materials Characterization and Engineering*, vol. 9, no. 6, pp. 519–525, 2010.
- [189] M. Takahashi, K. Mita, H. Toyuki, and M. Kume, "Pt-TiO₂ thin films on glass substrates as efficient photocatalysts," *Journal of Materials Science*, vol. 24, no. 1, pp. 243–246, 1989.
- [190] A. Towata, Y. Uwamino, M. Sando, K. Iseda, and H. Taoda, "Synthesis of titania photocatalysts dispersed with nickel nanosized particles," *Nanostructured Materials*, vol. 10, no. 6, pp. 1033–1042, 1998.
- [191] T. Umebayashi, T. Yamaki, H. Itoh, and K. Asai, "Analysis of electronic structures of 3d transition metal-doped TiO₂ based on band calculations," *Journal of Physics and Chemistry of Solids*, vol. 63, no. 10, pp. 1909–1920, 2002.
- [192] N. Serpone, D. Lawless, J. Disdier, and J.-M. Herrmann, "Spectroscopic, photoconductivity, and photocatalytic studies of TiO₂ colloids. Naked and with the lattice doped with Cr³⁺, Fe³⁺, and V⁵⁺ cations," *Langmuir*, vol. 10, no. 3, pp. 643–652, 1994.
- [193] E. Stathatos, T. Petrova, and P. Lianos, "Study of the efficiency of visible-light photocatalytic degradation of basic blue adsorbed on pure and doped mesoporous titania films," *Langmuir*, vol. 17, no. 16, pp. 5025–5030, 2001.
- [194] M. Stir, R. Nicula, and E. Burkel, "Pressure-temperature phase diagrams of pure and Ag-doped nanocrystalline TiO₂ photocatalysts," *Journal of the European Ceramic Society*, vol. 26, no. 9, pp. 1547–1553, 2006.
- [195] Y. Ao, J. Xu, D. Fu, and C. Yuan, "Preparation of Ag-doped mesoporous titania and its enhanced photocatalytic activity under UV light irradiation," *Journal of Physics and Chemistry of Solids*, vol. 69, no. 11, pp. 2660–2664, 2008.
- [196] C. Burda, Y. Lou, X. Chen, A. C. S. Samia, J. Stout, and J. L. Gole, "Enhanced nitrogen doping in TiO₂ nanoparticles," *Nano Letters*, vol. 3, no. 8, pp. 1049–1051, 2003.
- [197] S. S. Srinivasan, J. Wade, E. K. Stefanakos, and Y. Goswami, "Synergistic effects of sulfation and co-doping on the visible light photocatalysis of TiO₂," *Journal of Alloys and Compounds*, vol. 424, no. 1-2, pp. 322–326, 2006.
- [198] L. Lin, W. Lin, Y. X. Zhu et al., "Uniform carbon-covered titania and its photocatalytic property," *Journal of Molecular Catalysis A: Chemical*, vol. 236, no. 1-2, pp. 46–53, 2005.
- [199] Y. Ao, J. Xu, D. Fu, and C. Yuan, "Synthesis of C,N,S-tridoped mesoporous titania with enhanced visible light-induced photocatalytic activity," *Microporous and Mesoporous Materials*, vol. 122, no. 1–3, pp. 1–6, 2009.
- [200] J.-A. He, R. Mosurkal, L. A. Samuelson, L. Li, and J. Kumar, "Dye-sensitized solar cell fabricated by electrostatic layer-by-layer assembly of amphoteric TiO₂ nanoparticles," *Langmuir*, vol. 19, no. 6, pp. 2169–2174, 2003.
- [201] M. Sorescu and T. Xu, "The effect of ball-milling on the thermal behavior of anatase-doped hematite ceramic system," *Journal of Thermal Analysis and Calorimetry*, vol. 103, no. 2, pp. 479–484, 2011.
- [202] A. A. Ismail, I. A. Ibrahim, M. S. Ahmed, R. M. Mohamed, and H. El-Shall, "Sol-gel synthesis of titania-silica photocatalyst for cyanide photodegradation," *Journal of Photochemistry and Photobiology A: Chemistry*, vol. 163, no. 3, pp. 445–451, 2004.
- [203] D. Beydoun, R. Amal, G. Low, and S. McEvoy, "Occurrence and prevention of photodissolution at the phase junction of magnetite and titanium dioxide," *Journal of Molecular Catalysis A: Chemical*, vol. 180, no. 1-2, pp. 193–200, 2002.
- [204] J. C. Yu, J. Lin, and R. W. M. Kwok, "Enhanced photocatalytic activity of Ti_{1-x}V_xO₂ solid solution on the degradation of acetone," *Journal of Photochemistry and Photobiology A: Chemistry*, vol. 111, no. 1–3, pp. 199–203, 1997.
- [205] D. Han, Y. Li, and W. Jia, "Preparation and characterization of molecularly imprinted SiO₂-TiO₂ and photo-catalysis for 2, 4-dichlorophenol," *Advanced Materials Letters*, vol. 1, no. 3, pp. 188–192, 2010.
- [206] A. Ulgen and W. F. Hoelderich, "Conversion of glycerol to acrolein in the presence of WO₃/TiO₂ catalysts," *Applied Catalysis A: General*, vol. 400, no. 1-2, pp. 34–38, 2011.
- [207] K. T. Ranjit, H. Cohen, I. Willner, S. Bossmann, and A. M. Braun, "Lanthanide oxide-doped titanium dioxide: effective photocatalysts for the degradation of organic pollutants," *Journal of Materials Science*, vol. 34, no. 21, pp. 5273–5280, 1999.
- [208] L. Chen, X. Pang, G. Yu, and J. Zhang, "In-situ coating of MWNTs with sol-gel TiO₂ nanoparticles," *Advanced Materials Letters*, vol. 1, no. 1, pp. 75–78, 2010.

- [209] L. H. Huang, C. Sun, and Y. L. Liu, "Pt/N-codoped TiO₂ nanotubes and its photocatalytic activity under visible light," *Applied Surface Science*, vol. 253, no. 17, pp. 7029–7035, 2007.
- [210] J. Matos, J. Laine, and J.-M. Herrmann, "Synergy effect in the photocatalytic degradation of phenol on a suspended mixture of titania and activated carbon," *Applied Catalysis B: Environmental*, vol. 18, no. 3-4, pp. 281–291, 1998.
- [211] M. A. Nawi, A. H. Jawad, S. Sabar, and W. S. W. Ngah, "Immobilized bilayer TiO₂/chitosan system for the removal of phenol under irradiation by a 45watt compact fluorescent lamp," *Desalination*, vol. 280, no. 1-3, pp. 288–296, 2011.
- [212] B. Tryba, A. W. Morawski, and M. A. Inagaki, "A new route for preparation of TiO₂-mounted activated carbon," *Applied Catalysis B: Environmental*, vol. 46, no. 1, pp. 203–208, 2003.
- [213] T. Tsumura, N. Kojitani, H. Umemura, M. Toyoda, and M. Inagaki, "Composites between photoactive anatase-type TiO₂ and adsorptive carbon," *Applied Surface Science*, vol. 196, no. 1-4, pp. 429–436, 2002.
- [214] J. Yu, X. Zhao, and Q. Zhao, "Effect of film thickness on the grain size and photocatalytic activity of the sol-gel derived nanometer TiO₂ thin films," *Journal of Materials Science Letters*, vol. 19, no. 12, pp. 1015–1017, 2000.
- [215] W. Yuan, J. Ji, J. Fu, and J. Shen, "A facile method to construct hybrid multilayered films as a strong and multifunctional antibacterial coating," *Journal of Biomedical Materials Research—Part B: Applied Biomaterials*, vol. 85, no. 2, pp. 556–563, 2008.
- [216] Y. Lai, H. Zhuang, K. Xie et al., "Fabrication of uniform Ag/TiO₂ nanotube array structures with enhanced photoelectrochemical performance," *New Journal of Chemistry*, vol. 34, no. 7, pp. 1335–1340, 2010.
- [217] S. Li, I. N. Germanenko, and M. S. El-Shall, "Nanoparticles from the vapor phase: synthesis and characterization of Si, Ge, MoO₃, and WO₃ nanocrystals," *Journal of Cluster Science*, vol. 10, no. 4, pp. 533–547, 1999.
- [218] J. Zhao, X. Wang, Y. Kang, X. Xu, and Y. Li, "Photoelectrochemical activities of W-doped titania nanotube arrays fabricated by anodization," *IEEE Photonics Technology Letters*, vol. 20, no. 14, pp. 1213–1215, 2008.
- [219] M. Epifani, A. Helwig, J. Arbiol et al., "TiO₂ thin films from titanium butoxide: synthesis, Pt addition, structural stability, microelectronic processing and gas-sensing properties," *Sensors and Actuators B: Chemical*, vol. 130, no. 2, pp. 599–608, 2008.
- [220] Y. Li, X. Yu, and Q. Yang, "Fabrication of TiO₂ nanotube thin films and their gas sensing properties," *Journal of Sensors*, vol. 2009, Article ID 402174, 19 pages, 2009.
- [221] A. Serra, M. Re, M. Palmisano et al., "Assembly of hybrid silver-titania thin films for gas sensors," *Sensors and Actuators B: Chemical*, vol. 145, no. 2, pp. 794–799, 2010.
- [222] M. H. Yaacob, A. Z. Sadek, K. Latham, K. Kalantar-Zadeh, and W. Wlodarski, "Optical H₂ sensing performance of anodized nanoporous TiO₂ thin films," *Procedia Chemistry*, vol. 1, pp. 951–954, 2009.
- [223] D. Chen and A. K. Ray, "Removal of toxic metal ions from wastewater by semiconductor photocatalysis," *Chemical Engineering Science*, vol. 56, no. 4, pp. 1561–1570, 2001.
- [224] D. G. Shchukin, E. A. Ustinovich, D. V. Sviridov, and A. I. Kulak, "Titanium and iron oxide-based magnetic photocatalysts for oxidation of organic compounds and sulfur dioxide," *High Energy Chemistry*, vol. 38, no. 3, pp. 167–173, 2004.
- [225] D.-E. Gu, B.-C. Yang, and Y.-D. Hu, "A novel method for preparing V-doped titanium dioxide thin film photocatalysts with high photocatalytic activity under visible light irradiation," *Catalysis Letters*, vol. 118, no. 3-4, pp. 254–259, 2007.
- [226] X. Hou, X. Wu, and A. Liu, "Studies on photocatalytic activity of Ag/TiO₂ films," *Frontiers of Chemistry in China*, vol. 1, no. 4, pp. 402–407, 2006.
- [227] B. Zhao and Y.-W. Chen, "Ag/TiO₂ sol prepared by a sol-gel method and its photocatalytic activity," *Journal of Physics and Chemistry of Solids*, vol. 72, no. 11, pp. 1312–1318, 2011.
- [228] M. C. Kao, H. Z. Chen, S. L. Young, C. Y. Kung, C. C. Lin, and Z. Y. Hong, "Microstructure and optical properties of tantalum modified TiO₂ thin films prepared by the sol-gel process," *Journal of Superconductivity and Novel Magnetism*, vol. 23, no. 5, pp. 843–845, 2010.
- [229] A. Bai, W. Liang, G. Zheng, and J. Xue, "Preparation and enhanced daylight-induced photo-catalytic activity of transparent C-doped TiO₂ thin films," *The Journal of Wuhan University of Technology-Material Science Edition*, vol. 25, pp. 738–742, 2010.
- [230] L. Ge, M. Xu, and H. Fang, "Synthesis and characterization of the Pd/InVO₄-TiO₂ co-doped thin films with visible light photocatalytic activities," *Applied Surface Science*, vol. 253, no. 4, pp. 2257–2263, 2006.
- [231] J. Yu, J. C. Yu, B. Cheng, and X. Zhao, "Photocatalytic activity and characterization of the sol-gel derived Pb-doped TiO₂ thin films," *Journal of Sol-Gel Science and Technology*, vol. 24, no. 1, pp. 39–48, 2002.
- [232] N. S. Begum, H. M. F. Ahmed, and K. R. Gunashekar, "Effects of Ni doping on photocatalytic activity of TiO₂ thin films prepared by liquid phase deposition technique," *Bulletin of Materials Science*, vol. 31, no. 5, pp. 747–751, 2008.
- [233] F. Meng, X. Song, and Z. Sun, "Photocatalytic activity of TiO₂ thin films deposited by RF magnetron sputtering," *Vacuum*, vol. 83, no. 9, pp. 1147–1151, 2009.
- [234] C. Zhang, R. Chen, J. Zhou, J. Cheng, and Q. Xia, "Synthesis of TiO₂ films on glass slides by the sol-gel method and their photocatalytic activity," *Rare Metals*, vol. 28, no. 4, pp. 378–384, 2009.
- [235] Z. He, Z. Yu, H. Miao, G. Tan, and Y. Liu, "Preparation of TiO₂ thin film by the LPD method on functionalized organic self-assembled monolayers," *Science in China, Series E: Technological Sciences*, vol. 52, no. 1, pp. 137–140, 2009.
- [236] G. A. Battiston, R. Gerbasi, M. Porchia, and A. Marigo, "Influence of substrate on structural properties of TiO₂ thin films obtained via MOCVD," *Thin Solid Films*, vol. 239, no. 2, pp. 186–191, 1994.
- [237] F. Ren, K. He, Y. Ling, and J. Feng, "Novel fabrication of net-like and flake-like Fe doped TiO₂ thin films," *Applied Surface Science*, vol. 257, no. 22, pp. 9621–9625, 2011.
- [238] M. Zheng, Y. Shu, J. Sun, and T. Zhang, "Carbon-covered alumina: a superior support of noble metal-like catalysts for hydrazine decomposition," *Catalysis Letters*, vol. 121, no. 1-2, pp. 90–96, 2008.
- [239] V. Shashikala, V. Siva Kumar, A. H. Padmasri et al., "Advantages of nano-silver-carbon covered alumina catalyst prepared by electro-chemical method for drinking water purification," *Journal of Molecular Catalysis A: Chemical*, vol. 268, no. 1-2, pp. 95–100, 2007.
- [240] D. R. Uhlmann, G. Teowee, and J. Boulton, "The future of sol-gel science and technology," *Journal of Sol-Gel Science and Technology*, vol. 8, no. 1-3, pp. 1083–1091, 1997.

- [241] J.-X. Wang, L.-X. Wen, Z.-H. Wang, M. Wang, L. Shao, and J.-F. Chen, "Facile synthesis of hollow silica nanotubes and their application as supports for immobilization of silver nanoparticles," *Scripta Materialia*, vol. 51, no. 11, pp. 1035–1039, 2004.
- [242] T. I. Halkides, D. I. Kondarides, and X. E. Verykios, "Catalytic reduction of NO by C₃H₆ over Rh/TiO₂ catalysts effect of W⁶⁺-cation doping of TiO₂ on morphological characteristics and catalytic performance," *Applied Catalysis B: Environmental*, vol. 41, no. 4, pp. 415–426, 2003.
- [243] N. L. V. Carreño, I. T. S. Garcia, L. S. S. M. Carreño et al., "Synthesis of titania/carbon nanocomposites by polymeric precursor method," *Journal of Physics and Chemistry of Solids*, vol. 69, no. 8, pp. 1897–1904, 2008.
- [244] D. Dumitriu, A. R. Bally, C. Ballif et al., "Photocatalytic degradation of phenol by TiO₂ thin films prepared by sputtering," *Applied Catalysis B: Environmental*, vol. 25, no. 2-3, pp. 83–92, 2000.
- [245] M. Vondrova, T. Klimczuk, V. L. Miller et al., "Supported superparamagnetic Pd/Co alloy nanoparticles prepared from a silica/cyanogel co-gel," *Chemistry of Materials*, vol. 17, no. 25, pp. 6216–6218, 2005.
- [246] P. M. Boorman, K. Chong, R. A. Kydd, and J. M. Lewis, "A comparison of alumina, carbon, and carbon-covered alumina as supports for Ni-Mo-F additives: carbon deposition and model compound reaction studies," *Journal of Catalysis*, vol. 128, no. 2, pp. 537–550, 1991.
- [247] J. P. R. Vissers, F. P. M. Mercx, S. M. A. M. Bouwens, V. H. J. de Beer, and R. Prins, "Carbon-covered alumina as a support for sulfide catalysts," *Journal of Catalysis*, vol. 114, no. 2, pp. 291–302, 1988.
- [248] P. M. Boorman and K. Chong, "Preparation of carbon-covered alumina using fluorohydrocarbons. A new acidic support material," *Applied Catalysis A, General*, vol. 95, no. 2, pp. 197–210, 1993.
- [249] L. Lin, W. Lin, Y. X. Zhu et al., "Uniformly carbon-covered alumina and its surface characteristics," *Langmuir*, vol. 21, no. 11, pp. 5040–5046, 2005.
- [250] M. Błachnio, P. Staszczuk, G. Grodzicka, L. Lin, and Y. X. Zhu, "Adsorption and porosity properties of carbon-covered alumina surfaces," *Journal of Thermal Analysis and Calorimetry*, vol. 88, no. 2, pp. 601–606, 2007.
- [251] P. M. Boorman, R. A. Kydd, T. S. Sorensen, K. Chong, J. M. Lewis, and W. S. Bell, "A comparison of alumina, carbon and carbon-covered alumina as supports for NiMoF additives: gas oil hydroprocessing studies," *Fuel*, vol. 71, no. 1, pp. 87–93, 1992.
- [252] P. M. Boorman and K. Chong, "A comparative gas oil hydroprocessing study of alumina, carbon, and carbon-covered alumina supported nickel-molybdenum catalysts: effect of quinoline, thiophene, and vanadium spiking," *Energy & Fuels*, vol. 6, no. 3, pp. 300–307, 1992.
- [253] L. Lin, W. Lin, P. Wang, Y.-X. Zhu, B.-Y. Zhao, and Y.-C. Xie, "Uniform carbon-covered alumina synthesized by pyrolysis of sucrose/ γ -Al₂O₃," *Acta Physico-Chimica Sinica*, vol. 20, no. 10, pp. 1179–1181, 2004.
- [254] L. F. Sharanda, Y. V. Plyuto, I. V. Babich et al., "Synthesis and characterisation of hybrid carbon-alumina support," *Applied Surface Science*, vol. 252, no. 24, pp. 8549–8556, 2006.
- [255] P. Jana and V. Ganesan, "The production of a carbon-coated alumina foam," *Carbon*, vol. 49, no. 10, pp. 3292–3298, 2011.
- [256] K. S. R. Rao, P. K. Rao, S. K. Masthan, L. Kaluschnaya, and V. B. Shur, "New type of carbon coated alumina supports for the preparation of highly active ruthenium catalysts for ammonia synthesis," *Applied Catalysis*, vol. 62, no. 1, pp. L19–L22, 1990.
- [257] Y. Zhu, X. Pan, and Y. Xie, "Dispersion of sucrose on the surface of alumina," *Acta Physico-Chimica Sinica*, vol. 15, no. 9, pp. 830–833, 1999.
- [258] S. K. Maity, L. Flores, J. Ancheyta, and H. Fukuyama, "Carbon-modified alumina and alumina-carbon-supported hydrotreating catalysts," *Industrial and Engineering Chemistry Research*, vol. 48, no. 3, pp. 1190–1195, 2009.
- [259] D. B. Murphy, R. W. Carroll, and J. E. Klonowski, "Analysis of products of high-temperature pyrolysis of various hydrocarbons," *Carbon*, vol. 35, no. 12, pp. 1819–1823, 1997.
- [260] C. Paek, A. V. McCormick, and P. W. Carr, "Preparation and evaluation of carbon coated alumina as a high surface area packing material for high performance liquid chromatography," *Journal of Chromatography A*, vol. 1217, no. 42, pp. 6475–6483, 2010.
- [261] L. F. Sharanda, Y. V. Plyuto, I. V. Babich, Y. A. Babich, and J. A. Moulijn, "Preparation of carbon-coated alumina by pyrolysis of adsorbed acetylacetone," *Mendeleev Communications*, vol. 9, no. 3, pp. 95–96, 1999.
- [262] S. K. Masthan, P. S. S. Prasad, K. S. R. Rao, and P. K. Rao, "Hysteresis during ammonia synthesis over promoted ruthenium catalysts supported on carbon-covered alumina," *Journal of Molecular Catalysis*, vol. 67, no. 2, pp. L1–L5, 1991.
- [263] M. M. Mahlambi, A. K. Mishra, S. B. Mishra, R. W. Krause, B. B. Mamba, and A. M. Raichur, "Synthesis and characterization of carbon-covered alumina (CCA) supported TiO₂ nanocatalysts with enhanced visible light photodegradation of Rhodamine B," *Journal of Nanoparticle Research*, vol. 14, article 790, 2012.
- [264] J. Medina-Valtierra, J. García-Servín, C. Frausto-Reyes, and S. Calixto, "The photocatalytic application and regeneration of anatase thin films with embedded commercial TiO₂ particles deposited on glass microrods," *Applied Surface Science*, vol. 252, no. 10, pp. 3600–3608, 2006.
- [265] S.-Y. Lin, Y.-C. Chen, C.-M. Wang, and C.-C. Liu, "Effect of heat treatment on electrochromic properties of TiO₂ thin films," *Journal of Solid State Electrochemistry*, vol. 12, no. 11, pp. 1481–1486, 2008.
- [266] D. J. Kim, D. S. Kim, S. Cho, S. W. Kim, S. H. Lee, and J. C. Kim, "Measurement of thermal conductivity of TiO₂ thin films using 3 ω method," *International Journal of Thermophysics*, vol. 25, no. 1, pp. 281–289, 2004.
- [267] B. R. Sankapal, M. C. Lux-Steiner, and A. Ennaoui, "Synthesis and characterization of anatase-TiO₂ thin films," *Applied Surface Science*, vol. 239, no. 2, pp. 165–170, 2005.
- [268] C. Sarantopoulos, A. N. Gleizes, and F. Maury, "Chemical vapor deposition and characterization of nitrogen doped TiO₂ thin films on glass substrates," *Thin Solid Films*, vol. 518, no. 4, pp. 1299–1303, 2009.
- [269] L. Sedláková, M. Horáková, P. Hájková, A. Kolouch, J. Karásek, and P. Špatenka, "Photocatalytic properties of titanium oxide-based films deposited by PECVD," *Journal of Superhard Materials*, vol. 29, no. 3, pp. 162–165, 2007.
- [270] C. R. Kleijn, R. Dorsman, K. J. Kuijlaars, M. Okkerse, and H. van Santen, "Multi-scale modeling of chemical vapor deposition processes for thin film technology," *Journal of Crystal Growth*, vol. 303, no. 1, pp. 362–380, 2007.
- [271] H. Y. Ha, S. W. Nam, T. H. Lim, I.-H. Oh, and S.-A. Hong, "Properties of the TiO₂ membranes prepared by CVD of titanium tetraisopropoxide," *Journal of Membrane Science*, vol. 111, no. 1, pp. 81–92, 1996.

- [272] V. G. Bessergenev, I. V. Khmelinskii, R. J. F. Pereira, V. V. Krisuk, A. E. Turgambaeva, and I. K. Igumenov, "Preparation of TiO₂ films by CVD method and its electrical, structural and optical properties," *Vacuum*, vol. 64, no. 3-4, pp. 275-279, 2002.
- [273] K. Kamata, K. Maruyama, S. Amano, and H. Fukazawa, "Rapid formation of TiO₂ films by a conventional CVD method," *Journal of Materials Science Letters*, vol. 9, no. 3, pp. 316-319, 1990.
- [274] N. S. Begum, H. M. Farveez Ahmed, and O. M. Hussain, "Characterization and photocatalytic activity of boron-doped TiO₂ thin films prepared by liquid phase deposition technique," *Bulletin of Materials Science*, vol. 31, no. 5, pp. 741-745, 2008.
- [275] S.-Q. Sun, B. Sun, W. Zhang, and D. Wang, "Preparation and antibacterial activity of Ag-TiO₂ composite film by liquid phase deposition (LPD) method," *Bulletin of Materials Science*, vol. 31, no. 1, pp. 61-66, 2008.
- [276] M. N. Ghazzal, N. Barthen, and N. Chaoui, "Photodegradation kinetics of stearic acid on UV-irradiated titania thin film separately followed by optical microscopy and Fourier transform infrared spectroscopy," *Applied Catalysis B: Environmental*, vol. 103, no. 1-2, pp. 85-90, 2011.
- [277] B. J. Brasjen, A. W. V. Cuijk, and A. A. Darhuber, "Dip-coating of chemically patterned surfaces," *Chemical Engineering and Processing*, vol. 50, no. 5-6, pp. 565-568, 2011.
- [278] N. Negishi, K. Takeuchi, and T. Ibusuki, "Surface structure of the TiO₂ thin film photocatalyst," *Journal of Materials Science*, vol. 33, no. 24, pp. 5789-5794, 1998.
- [279] R. Bayón, G. San Vicente, C. Maffiotte, and Á. Morales, "Characterization of copper-manganese-oxide thin films deposited by dip-coating," *Solar Energy Materials and Solar Cells*, vol. 92, no. 10, pp. 1211-1216, 2008.
- [280] Z. Wang, K. Sun, S. Shen, N. Zhang, J. Qiao, and P. Xu, "Preparation of YSZ thin films for intermediate temperature solid oxide fuel cells by dip-coating method," *Journal of Membrane Science*, vol. 320, no. 1-2, pp. 500-504, 2008.
- [281] A. Nakaruk and C. C. Sorrell, "Conceptual model for spray pyrolysis mechanism: fabrication and annealing of titania thin films," *Journal of Coatings Technology Research*, vol. 7, no. 5, pp. 665-676, 2010.
- [282] M. Okuya, K. Nakade, and S. Kaneko, "Porous TiO₂ thin films synthesized by a spray pyrolysis deposition (SPD) technique and their application to dye-sensitized solar cells," *Solar Energy Materials and Solar Cells*, vol. 70, no. 4, pp. 425-435, 2002.
- [283] M. Okuya, K. Shiozaki, N. Horikawa et al., "Porous TiO₂ thin films prepared by spray pyrolysis deposition (SPD) technique and their application to UV sensors," *Solid State Ionics*, vol. 172, no. 1-4, pp. 527-531, 2004.
- [284] B.-H. Kim, J.-Y. Lee, Y.-H. Choa, M. Higuchi, and N. Mizutani, "Preparation of TiO₂ thin film by liquid sprayed mist CVD method," *Materials Science and Engineering: B*, vol. 107, no. 3, pp. 289-294, 2004.
- [285] D. R. Acosta, A. I. Martinez, A. A. Lopez, and C. R. Magana, "Titanium dioxide thin films: the effect of the preparation method in their photocatalytic properties," *Microscopy*, vol. 228, pp. 183-188, 2005.
- [286] L. Castañeda, A. Maldonado, and M. de la L. Olvera, "Sensing properties of chemically sprayed TiO₂ thin films using Ni, Ir, and Rh as catalysts," *Sensors and Actuators B: Chemical*, vol. 133, no. 2, pp. 687-693, 2008.
- [287] R. S. Sonawane and M. K. Dongare, "Sol-gel synthesis of Au/TiO₂ thin films for photocatalytic degradation of phenol in sunlight," *Journal of Molecular Catalysis A: Chemical*, vol. 243, no. 1, pp. 68-76, 2006.
- [288] L. Sun, T. An, S. Wan et al., "Effect of synthesis conditions on photocatalytic activities of nanoparticulate TiO₂ thin films," *Separation and Purification Technology*, vol. 68, no. 1, pp. 83-89, 2009.
- [289] M. Vishwas, S. K. Sharma, K. N. Rao, S. Mohan, K. V. A. Gowda, and R. P. S. Chakradhar, "Influence of surfactant and annealing temperature on optical properties of sol-gel derived nanocrystalline TiO₂ thin films," *Spectrochimica Acta Part A: Molecular and Biomolecular Spectroscopy*, vol. 75, no. 3, pp. 1073-1077, 2010.
- [290] R. Zaroni, G. Righini, A. Montenero et al., "XPS analysis of sol-gel processed doped and undoped TiO₂ films for sensors," *Surface and Interface Analysis*, vol. 22, no. 1, pp. 376-379, 1994.
- [291] Y. Guo, W. Geng, and J. Sun, "Layer-by-layer deposition of polyelectrolyte-polyelectrolyte complexes for multilayer film fabrication," *Langmuir*, vol. 25, no. 2, pp. 1004-1010, 2009.
- [292] G. Decher, J. D. Hong, and J. Schmitt, "Buildup of ultrathin multilayer films by a self-assembly process: III. Consecutively alternating adsorption of anionic and cationic polyelectrolytes on charged surfaces," *Thin Solid Films*, vol. 210-211, no. 2, pp. 831-835, 1992.
- [293] T.-H. Kim and B.-H. Sohn, "Photocatalytic thin films containing TiO₂ nanoparticles by the layer-by-layer self-assembling method," *Applied Surface Science*, vol. 201, no. 1-4, pp. 109-114, 2002.
- [294] H. Ai, S. A. Jones, and Y. M. Lvov, "Biomedical applications of electrostatic layer-by-layer nano-assembly of polymers, enzymes, and nanoparticles," *Cell Biochemistry and Biophysics*, vol. 39, no. 1, pp. 23-43, 2003.
- [295] J. B. Schlenoff and S. T. Dubas, "Mechanism of polyelectrolyte multilayer growth: charge overcompensation and distribution," *Macromolecules*, vol. 34, no. 3, pp. 592-598, 2001.
- [296] T. Sasaki, Y. Ebina, T. Tanaka, M. Harada, M. Watanabe, and G. Decher, "Layer-by-layer assembly of titania nanosheet/polycation composite films," *Chemistry of Materials*, vol. 13, no. 12, pp. 4661-4667, 2001.
- [297] B. Schoeler, G. Kumaraswamy, and F. Caruso, "Investigation of the influence of polyelectrolyte charge density on the growth of multilayer thin films prepared by the layer-by-layer technique," *Macromolecules*, vol. 35, no. 3, pp. 889-897, 2002.
- [298] M. M. De Villiers, D. P. Otto, S. J. Strydom, and Y. M. Lvov, "Introduction to nanocoatings produced by layer-by-layer (LbL) self-assembly," *Advanced Drug Delivery Reviews*, vol. 63, no. 9, pp. 701-715, 2011.
- [299] G. Decher, B. Lehr, K. Lowack, Y. Lvov, and J. Schmitt, "New nanocomposite films for biosensors: layer-by-layer adsorbed films of polyelectrolytes, proteins or DNA," *Biosensors and Bioelectronics*, vol. 9, no. 9-10, pp. 677-684, 1994.
- [300] N. I. Kovtyukhova, B. R. Martin, J. K. N. Mbindyo, T. E. Mallouk, M. Cabassi, and T. S. Mayer, "Layer-by-layer self-assembly strategy for template synthesis of nanoscale devices," *Materials Science and Engineering C*, vol. 19, no. 1-2, pp. 255-262, 2002.
- [301] Y. Liu, Y. Wang, and R. O. Claus, "Layer-by-layer ionic self-assembly of Au colloids into multilayer thin-films with bulk metal conductivity," *Chemical Physics Letters*, vol. 298, no. 4-6, pp. 315-319, 1998.
- [302] K. Ariga, J. P. Hill, and Q. Ji, "Layer-by-layer assembly as a versatile bottom-up nanofabrication technique for exploratory research and realistic application," *Physical Chemistry Chemical Physics*, vol. 9, no. 19, pp. 2319-2340, 2007.

- [303] A. A. Antipov, G. B. Sukhorukov, E. Donath, and H. Möhwald, "Sustained release properties of polyelectrolyte multilayer capsules," *Journal of Physical Chemistry B*, vol. 105, no. 12, pp. 2281–2284, 2001.
- [304] F. Wang, J. Feng, and C. Gao, "Manipulating the properties of coacervated polyelectrolyte microcapsules by chemical cross-linking," *Colloid and Polymer Science*, vol. 286, no. 8-9, pp. 951–957, 2008.
- [305] S. Anandhakumar and A. M. Raichur, "A facile route to synthesize silver nanoparticles in polyelectrolyte capsules," *Colloids and Surfaces B: Biointerfaces*, vol. 84, no. 2, pp. 379–383, 2011.
- [306] S. Anandhakumar, M. Debapriya, V. Nagaraja, and A. M. Raichur, "Polyelectrolyte microcapsules for sustained delivery of water-soluble drugs," *Materials Science and Engineering C*, vol. 31, no. 2, pp. 342–349, 2011.
- [307] S. Anandhakumar, V. Nagaraja, and A. M. Raichur, "Reversible polyelectrolyte capsules as carriers for protein delivery," *Colloids and Surfaces B: Biointerfaces*, vol. 78, no. 2, pp. 266–274, 2010.
- [308] N. A. Kotov, I. Dekany, and J. H. Fendler, "Layer-by-layer self-assembly of polyelectrolyte-semiconductor nanoparticle composite films," *Journal of Physical Chemistry*, vol. 99, no. 35, pp. 13065–13069, 1995.
- [309] A. Mollahosseini, A. Rahimpour, M. Jahamshahi, M. Peyravi, and M. Khavarpour, "The effect of silver nanoparticle size on performance and antibacteriability of polysulfone ultrafiltration membrane," *Desalination*, vol. 306, pp. 41–50, 2012.
- [310] D. Y. Koseoglu-Imer, B. Kose, M. Altinbas, and I. Koyuncu, "The production of polysulfone (PS) membrane with silver nanoparticles (AgNP): physical properties, filtration performances, and biofouling resistances of membranes," *Journal of Membrane Science*, vol. 428, pp. 620–628, 2013.
- [311] Z. Fan, Z. Wang, N. Sun, J. Wang, and S. Wang, "Performance improvement of polysulfone ultrafiltration membrane by blending with polyaniline nanofibers," *Journal of Membrane Science*, vol. 320, no. 1-2, pp. 363–371, 2008.
- [312] E. Saljoughi and S. M. Mousavi, "Preparation and characterization of novel polysulfone nanofiltration membranes for removal of cadmium from contaminated water," *Separation and Purification Technology*, vol. 90, pp. 22–30, 2012.
- [313] R. J. Wang, Y. Chen, H. M. Xie, G. Q. Kai, Z. Y. Wang, and J. Pan, "Polysaccharide separation mechanism in polysulfone-Fe₃O₄ magnetic composite membranes," *Chinese Science Bulletin*, vol. 56, no. 18, pp. 1951–1956, 2011.
- [314] N. A. A. Hamid, A. F. Ismail, T. Matsuura et al., "Morphological and separation performance study of polysulfone/titanium dioxide (PSF/TiO₂) ultrafiltration membranes for humic acid removal," *Desalination*, vol. 273, no. 1, pp. 85–92, 2011.
- [315] N. Y. Abu-Thabit, S. A. Ali, and S. M. J. Zaidi, "New highly phosphonated polysulfone membranes for PEM fuel cells," *Journal of Membrane Science*, vol. 360, no. 1-2, pp. 26–33, 2010.
- [316] S. Ramaswamy, C. Gopalakrishnan, N. S. Kumar, A. Littleflower, and M. Ponnaivaikko, "Fabrication of Ni nanodots templated by nanoporous polysulfone membrane: structural and magnetic properties," *Applied Physics A: Materials Science and Processing*, vol. 98, no. 3, pp. 481–485, 2010.
- [317] Y. Devrim, S. Erkan, N. Baç, and I. Eroğlu, "Preparation and characterization of sulfonated polysulfone/titanium dioxide composite membranes for proton exchange membrane fuel cells," *International Journal of Hydrogen Energy*, vol. 34, no. 8, pp. 3467–3475, 2009.
- [318] Y. Yang, H. Zhang, P. Wang, Q. Zheng, and J. Li, "The influence of nano-sized TiO₂ fillers on the morphologies and properties of PSF UF membrane," *Journal of Membrane Science*, vol. 288, no. 1-2, pp. 231–238, 2007.
- [319] M. Padaki, A. M. Isloor, A. F. Ismail, and M. S. Abdullah, "Synthesis, characterization and desalination study of novel PSAB and mPSAB blend membranes with Polysulfone (PSf)," *Desalination*, vol. 295, pp. 35–42, 2012.
- [320] N. Ghaemi, S. S. Madaeni, A. Alizadeh et al., "Fabrication and modification of polysulfone nanofiltration membrane using organic acids: morphology, characterization and performance in removal of xenobiotics," *Separation and Purification Technology*, vol. 96, pp. 214–228, 2012.
- [321] S. Rajesh, S. Senthilkumar, A. Jayalakshmi, M. T. Nirmala, A. F. Ismail, and D. Mohan, "Preparation and performance evaluation of poly (amide-imide) and TiO₂ nanoparticles impregnated polysulfone nanofiltration membranes in the removal of humic substances," *Colloids and Surfaces A: Physicochemical and Engineering Aspects*, vol. 418, pp. 92–104, 2013.
- [322] M. J. Eckelman, M. S. Mauter, J. A. Isaacs, and M. Elimelech, "New perspectives on nanomaterial aquatic ecotoxicity: production impacts exceed direct exposure impacts for carbon nanotubes," *Environmental Science and Technology*, vol. 46, no. 5, pp. 2902–2910, 2012.
- [323] A. Tiraferri, N. Y. Yip, W. A. Phillip, J. D. Schiffman, and M. Elimelech, "Relating performance of thin-film composite forward osmosis membranes to support layer formation and structure," *Journal of Membrane Science*, vol. 367, no. 1-2, pp. 340–352, 2011.
- [324] S. Liang, Y. Kang, A. Tiraferri, E. P. Giannelis, X. Huang, and M. Elimelech, "Highly hydrophilic polyvinylidene fluoride (PVDF) ultrafiltration membranes via postfabrication grafting of surface-tailored silica nanoparticles," *ACS Applied Materials and Interfaces*, vol. 5, no. 14, pp. 6694–6703, 2013.
- [325] M. S. Mauter, Y. Wang, K. C. Okemgbo, C. O. Osuji, E. P. Giannelis, and M. Elimelech, "Antifouling ultrafiltration membranes via post-fabrication grafting of biocidal nanomaterials," *ACS Applied Materials and Interfaces*, vol. 3, no. 8, pp. 2861–2868, 2011.

Review Article

Three-Dimensional Graphene-Based Nanomaterials as Electrocatalysts for Oxygen Reduction Reaction

Xuan Ji,¹ Xin Zhang,² and Xianwen Zhang³

¹*Shanxi Research Institute of Applied Chemistry, Taiyuan 030027, China*

²*Department of Chemical Engineering, Texas Tech University, 6th Street and Canton Avenue, Lubbock, TX 79409, USA*

³*Institute of Advanced Energy Technology and Equipment, Hefei University of Technology, 193rd Tunxi Road, Hefei 230009, China*

Correspondence should be addressed to Xin Zhang; xin.zhang@ttu.edu and Xianwen Zhang; xianwen.zhang@ttu.edu

Received 14 May 2015; Accepted 15 July 2015

Academic Editor: Nay Ming Huang

Copyright © 2015 Xuan Ji et al. This is an open access article distributed under the Creative Commons Attribution License, which permits unrestricted use, distribution, and reproduction in any medium, provided the original work is properly cited.

In recent years, three-dimensional (3D) graphene-based nanomaterials have been demonstrated to be efficient and promising electrocatalysts for oxygen reduction reaction (ORR) in fuel cells application. This review summarizes and categorizes the recent progress on the preparation and performance of these novel materials as ORR catalysts, including heteroatom-doped 3D graphene network, metal-free 3D graphene-based nanocomposites, nonprecious metal-containing 3D graphene-based nanocomposites, and precious metal-containing 3D graphene-based nanocomposites. The challenges and future perspective of this field are also discussed.

1. Introduction

As a novel nanomaterial, graphene is a one-atom-thick carbon sheet with a hexagonal packed lattice structure. Since the first direct observation and characterization of a mechanically exfoliated graphene by Geim and Novoselov in 2004, this “miracle material” has attracted tremendous attention and research interest owing to its many unique properties, such as extraordinarily high in-plane electrical mobility, thermal conductivity, mechanical strength, and ultralarge specific surface area [1–4]. Over the past decade, graphene and graphene-based nanomaterials as gifted carbonaceous materials have found a multifunctional application in the fields of photocatalysis, electrocatalysis, water treatment, electrochemical sensor, optical sensor, fiber optic sensor, and so on [5–18]. Among these applications, graphene-based nanomaterials have been actively studied as promising electrode materials in electrochemical devices such as supercapacitors, rechargeable lithium-ion batteries, fuel cells, and solar cells [19–23]. In these studies, graphene may play the role of either the conducting substrate or electroactive center.

Although 2D graphene-based nanomaterials have been demonstrated to be promising in the above electrochemical applications, a huge challenge and need still remain for

the efficient use of graphene's large specific surface area and extraordinary electrical, chemical, and mechanical properties. For instance, for electrodes, large surface area and fast electrolyte transfer near electrode surface are required, in order to obtain high rate of electrochemical reaction. However, the graphene sheets on the electrode tend to form irreversible agglomerates or restack due to the strong π - π stacking and van der Waals interactions between the graphene sheets, which will dramatically reduce the surface area of electrode, hinder the rapid electrolyte diffusion, and consequently limit its practical application in energy devices.

Recently, integrating nanomonolayer graphene into macroscopic 3D porous interconnected networks has attracted significant attention, since the nonagglomerated 3D structure can provide graphene-based nanomaterials with high specific surface areas, strong mechanical strengths, and fast mass and electron transport kinetics due to the combination of 3D porous structures and the excellent intrinsic properties of graphene [24–29].

On the other hand, the greenhouse gas emissions from the depletion of traditional fossil fuels become the primary cause for global warming and climate change. In this context, increasing demand for sustainable energy has stimulated intense research on energy conversion and storage systems

that are highly efficient, of low cost, and environmentally friendly. Among the various promising energy conversion technologies, fuel cell, which converts chemical energy from fuels into electricity, is a clean and high-efficiency device with low or zero emissions from operation and has drawn a great deal of attention in terms of both fundamentals and applications [30, 31]. In a fuel cell, the fuel (such as hydrogen, methanol, and ethanol) is oxidized at the anode, and the released electrons are transferred to cathode where oxygen is reduced. Because the oxygen reduction reaction (ORR) at the cathode has sluggish reaction kinetics, which limits the cell performance, the electrocatalysts are necessary to facilitate the ORR. Consequently, the electrocatalyst for the ORR is a key component for fuel cell and plays a vital role in determining the performance of fuel cells, such as power output, open circuit, energy efficiency, and circling life [32–34]. Over the past few years, various 3D graphene-based nanomaterials have been extensively designed, prepared, and investigated as efficient electrocatalysts for ORR in fuel cells application. However, as far as we know, though it is much needed, a specific and timely review on this area is missing. Accordingly, this review article is provided to categorize and summarize the recent advances in the development of 3D graphene-based nanomaterials as catalysts for ORR in fuel cells, with focus on introducing and understanding the “preparation-structure-performance” relationship of these novel materials. The challenges and perspective of these emerging materials as ORR catalysts are discussed as well.

2. Preparation Methods

In the past several years, tremendous efforts have been devoted to the development of synthetic methods for 3D graphene-based materials with various morphologies, structures, and properties, in order to satisfy the requirements arising from various applications. Considering the existence of several excellent reviews highlighting the classification and summarization of the recent progress in the preparation methods of these materials, the reader should be referred to these reviews to obtain in-depth coverage of the various preparation procedures [35–38]. The subject of the present review is the application of 3D graphene-based materials in ORR catalysis; thus, only the relevant preparation methods towards this subject are briefly introduced here.

Self-assembly, among the main strategies for the construction of 3D graphene architecture, is the most promising and widely used strategy to obtain 3D graphene-based materials as catalysts for ORR. As a typical example, 3D graphene structures can be fabricated through the gelation process of a graphene oxide (GO) suspension followed by reduction to convert GO to reduced graphene oxide (rGO). Both chemical and physical treatments, such as adding various kinds of cross-linkers, changing the pH value or temperature of the GO suspension, hydrothermal treatment, direct freeze-drying, and electrochemical reduction, could trigger the gelation of a GO suspension. Hydrogels, organogels, and aerogels are the main forms of 3D graphene usually as products of the self-assembly process, and aerogels are obtained from

hydrogels and organogels via freeze-drying or supercritical CO₂ drying. To create 3D graphene-based materials, including doped 3D graphene and 3D graphene-based composite, dopant-containing precursor and precursor ions are usually added during or after the GO gelation process followed by reduction for intrinsically doped 3D graphene and for *in situ* decoration of NPs/nanomaterials on 3D graphene, respectively. Since GO can be synthesized in large quantities with low cost and easily reduced by different methods, the preparation of 3D graphene-based materials from GO by self-assembly is a promising and practical way for the mass production of these materials for ORR catalysis.

3. Applications and Performances of 3D Graphene-Based Nanomaterials as ORR Electrocatalyst

Although Pt-based electrocatalysts are the most active and popular catalysts for ORR at the cathode in fuel cells, large-scale commercialization is still restricted due to high cost, poor durability, and sluggish electron transfer kinetics. Therefore, the development of alternative catalysts, including metal-free catalysts and nonprecious metal catalysts (NPMC), has drawn tremendous attention in the past decades. In 3D graphene-based electrocatalysts for ORR, 3D graphene may play the role of either inherent and single catalysts such as heteroatom-doped 3D graphene network (discussed in Section 3.1) or supporting materials for other nanocatalysts such as metal-free or metal-containing 3D graphene-based nanocomposites (discussed in Sections 3.2–3.4). The following subsections will mainly focus on the preparation and performance of these 3D graphene-based materials as electrocatalysts for ORR.

3.1. Heteroatom-Doped 3D Graphene Network. More recently, heteroatom-doped carbon nanomaterials (e.g., carbon nanotubes, nanotube cups, ordered mesoporous graphitic arrays, and graphene) have been emerged as a new class of metal-free catalysts or supporting materials for NPMC for ORR [39]. Among these carbon materials, 2D graphene doped with foreign nonmetallic atoms (N-doped graphene in particular) has been demonstrated both experimentally and theoretically as a promising ORR catalyst owing to its excellent electrocatalytic activities as well as low cost, good durability, and being environmentally friendly [40]. However, the practical applications of 2D graphene as an electrode material in energy device are still limited, because graphene sheets tend to form irreversible agglomerates or restack due to the strong π - π stacking and van der Waals interactions between the graphene sheets. In this context, the nonagglomerated 3D graphene has been rapidly developed in recent years because its unique structures, which integrate nanomonolayer graphene into macroscopic 3D porous interconnected networks, could effectively translate the excellent intrinsic properties of graphene at the nanoscale into those at the macroscopic level, thus making this doped 3D graphene as promising catalysts for ORR.

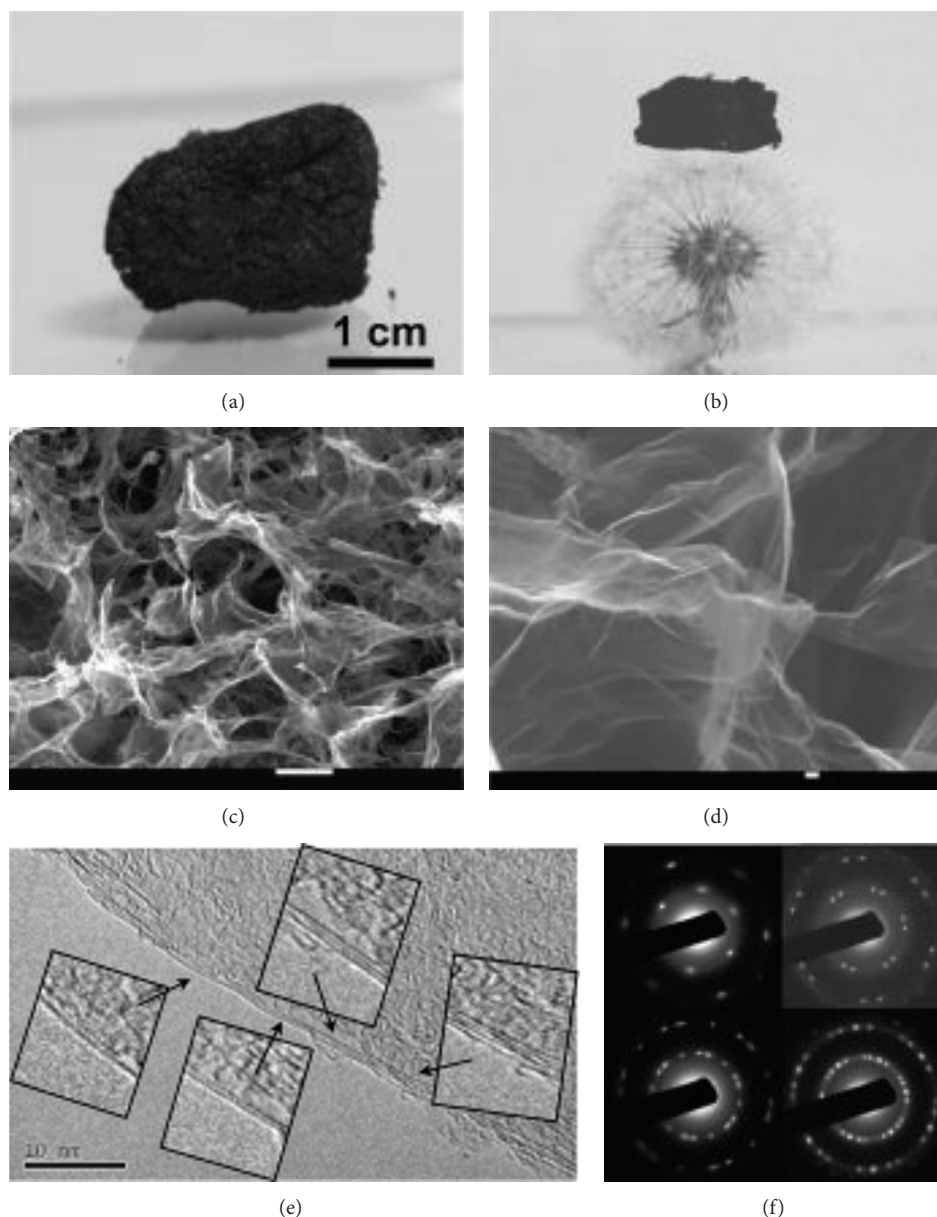


FIGURE 1: (a, b) Photographs of an as-prepared superlight GF and one with a piece of GF size of $1.8\text{ cm} \times 1.1\text{ cm} \times 1.2\text{ cm}$ standing on a dandelion. (c, d) SEM images of the sample in (a). (e, f) Typical TEM images of the walls of GF and the corresponding electron diffraction patterns consistent with 1–4 crystalline graphene layers (reprinted from [41]; copyright 2012 WILEY-VCH).

In 2012, Zhao and coworkers developed a method to prepare versatile, N-doped, ultralight 3D graphene framework (GF), which is demonstrated to be a promising metal-free catalyst for ORR in an alkaline solution (Figures 1(a)–1(b)) [41]. The N-doped 3D GF was synthesized through hydrothermal treatment of GO and pyrrole and subsequent freeze-drying and annealing the composition. Different from the conventional 2D stacked graphene film, this doped GF provides a unique 3D pore-rich structure with maximum access to the N sites within highly exposed graphene sheets and multidimensional electron transport pathways (Figures 1(c)–1(f)). Results from electrochemical measurements showed that this N-containing electrode has high catalytic

activity and a four-electron pathway for ORR as compared with that of Pt/C electrode. In addition, this N-doped 3D GF exhibited excellent tolerance to the methanol crossover effect and good stability for ORR. Notably, due to its excellent performances in adsorption and capacitance, this N-doped 3D GF also shows a great promise both as a super adsorption material for high-efficiency recyclable sorbent applications and as a new type of electrode material or supporting material for high performance supercapacitors.

In 2013, Su and coworkers developed 3D nitrogen and sulfur codoped graphene frameworks (N/S-GFs) as efficient electrocatalysts under alkaline conditions [42]. These N/S-GFs were prepared by the hydrothermal treatment of

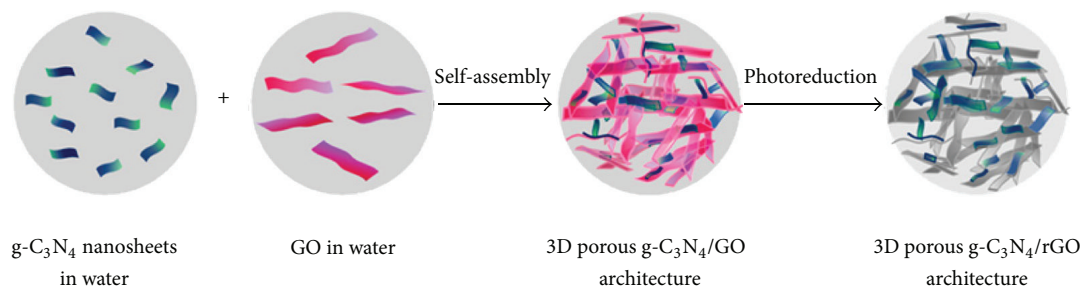


FIGURE 2: Schematic diagram to illustrate the fabrication process of 3D porous supramolecular architecture of g-C₃N₄ nanosheets and rGO (reprinted from [44]; copyright 2014 American Chemical Society).

ammonium thiocyanate (NH₄SCN) and GO at 443 K. In the hydrothermal process, NH₄SCN was decomposed into highly reactive N/S-rich species, such as NH₃, H₂S, and CS₂, which can react with the defective sites and oxygen-containing groups of GO; simultaneously, GO was reduced to graphene and assembled into 3D GFs. The as-prepared N/S-GFs, with large surface area (220 m² g⁻¹ BET surface area) and high heteroatom weight content (12.3% N content and 18.4% S content), were observed to be an interconnected framework of ultrathin graphene nanosheets with porous architecture. According to the study, ORR catalyzed by N/S-GFs was mainly through the four-electron transfer pathway while ORR catalyzed by N-doped GF revealed only two electron transfer mechanism. Moreover, N/S-GFs showed a kinetic-limiting current density of 3.9 mA/cm², which is comparable to that of commercial Pt/C catalyst (4.2 mA/cm²) and is much higher than 2.8 mA/cm² for N-doped GF measured at -0.36 V. In addition to the high electrocatalytic activity, N/S-GFs also exhibited superior stability and tolerance to methanol crossover effect as compared with those of Pt/C catalyst.

Although the aforementioned nonmetallic heteroatom-doped 3D graphene networks are claimed as inherent “metal-free” electrocatalysts for ORR, it should be pointed out that the specific catalytic sites as well as the catalytic mechanisms are still unclear. Moreover, because the starting material GO contains metallic impurities brought by its preparation method and it has been demonstrated that even a slight trace of Mn metallic impurities in graphene materials is sufficient to alter or dominate their electrocatalytic properties towards ORR, Wang and coworkers argued that the “metal-free” electrocatalysis of the ORR on heteroatom-doped graphene is caused by trace levels (ppm) of metallic impurities (manganese oxide in particular) present within the graphene materials [43]. Therefore, more future works are encouraged to study and prove that the doping atoms other than the residual metallic impurities in these 3D GF played a dominant role in the electrocatalysis of the ORR on electrodes.

3.2. Metal-Free 3D Graphene-Based Nanocomposites. As mentioned above, N-doped carbon materials have been reported to be efficient metal-free electrocatalysts for ORR; however, the low level of nitrogen concentration limited by their preparation methods may affect further improvements in

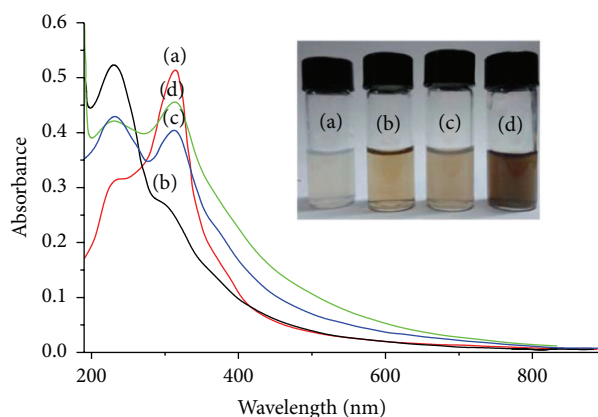


FIGURE 3: UV-vis absorption spectra and corresponding photographs (inset) of aqueous dispersions of g-C₃N₄ nanosheets (a), GO (b), g-C₃N₄/GO (c), and g-C₃N₄/rGO (reprinted from [44]; copyright 2014 American Chemical Society).

their catalytic performances. Graphitic carbon nitride (g-C₃N₄), which possesses high nitrogen content including both pyridinic and graphitic nitrogen moieties which could be potential active sites for ORR, is thus considered to be a potential catalyst or an effective component in composite catalyst for ORR.

In 2014, Tian and coworkers constructed a novel 3D porous supramolecular architecture of ultrathin g-C₃N₄ nanosheets and rGO (g-C₃N₄/rGO) by solution self-assembly of g-C₃N₄ and GO followed by photoreduction catalyzed by g-C₃N₄ (Figure 2) [44]. The π -stacking interactions between the sp² lattice of g-C₃N₄ and the sp² graphene lattice as well as the hydrogen-bonding interactions between the N-containing groups in g-C₃N₄ and O functional groups of GO were believed to be responsible for the self-assembly formation of the 3D porous frameworks in solution—this presumption could be further confirmed by the shift of the UV-vis absorption band of g-C₃N₄ in the presence of GO (Figure 3). The as-prepared g-C₃N₄/rGO hybrid possessed high surface area, multilevel porous structure, good electrical conductivity, efficient electron transport network, and fast charge transfer kinetics at g-C₃N₄/rGO interfaces, which facilitate the diffusion of O₂, electrolyte, and electrons in the porous frameworks during ORR. As a novel ORR catalyst, g-C₃N₄/rGO

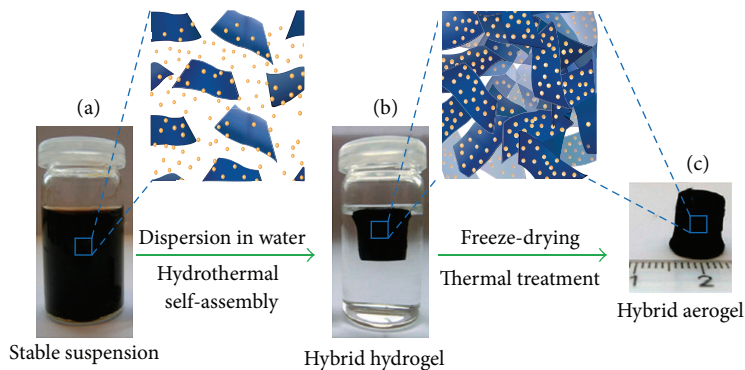


FIGURE 4: Fabrication process for the 3D $\text{Fe}_3\text{O}_4/\text{N-GAs}$ catalyst. (a) Stable suspension of GO, iron ions, and PPy dispersed in a vial. (b) Fe- and PPy-supporting graphene hybrid hydrogel prepared by hydrothermal self-assembly and floating on water in a vial and its ideal assembled model. (c) Monolithic $\text{Fe}_3\text{O}_4/\text{N-GAs}$ hybrid aerogel obtained after freeze-drying and thermal treatment (reprinted from [46]; copyright 2012 American Chemical Society).

exhibited superior ORR catalytic activity over single component, physical mixed or *in situ* immobilized composite or previously reported $\text{g-C}_3\text{N}_4/\text{C}$ composites in alkaline mediums. In comparison with Pt/C catalyst, $\text{g-C}_3\text{N}_4/\text{rGO}$ showed comparable ORR catalytic activity, higher stability, and better tolerance toward methanol poisoning, with a four-electron dominated ORR process. This work exemplifies a new way to prepare metal-free, 3D graphene-based composite as ORR catalyst which combines the advantages of 3D graphene (high surface area, good electrical conductivity, etc.) with those of metal-free catalysts (sustainability, low cost, etc.).

Besides the aforementioned metal-free 3D graphene/inorganic composite as ORR catalyst, Zhuang and coworkers reported a graphene/biofilm composite with a 3D structure as biocathode in microbial fuel cell (MFC) [45]. This composite was fabricated by a novel one-pot method that the microbially reduced graphene was implanted into cathode biofilm, leading to the *in situ* construction of graphene/biofilm composite. As an effective biocathode catalyst for ORR, this graphene/biofilm composite could enhance the electrocatalytic activity and facilitate the electron transfer between bacteria and electrode, thus showing higher maximum power density of MFC, faster electron transfer kinetics, and less internal resistance as compared with those of carbon cloth-biocathode.

3.3. Nonprecious Metal-Containing 3D Graphene-Based Nanocomposites. As alternative ORR catalysts for Pt-based materials, nonprecious metals (Fe, Co, etc.) or metal oxides (Fe_3O_4 , Co_3O_4 , etc.) have been actively studied; however, these catalysts tend to degrade during operation of the fuel cell due to dissolution, sintering, and agglomeration. Supporting these nonprecious metal/metal oxide nanoparticles (NPs) on 3D graphene networks would be an attractive way to solve these problems, as a geometric confinement of these NPs within graphene layers would enhance their interface contact and suppress the dissolution and agglomeration of NPs, thereby promoting the electrochemical activity and stability of the hybrids.

In 2012, Wu and coworkers reported 3D N-doped graphene aerogel- (N-GA-) supported Fe_3O_4 nanoparticles ($\text{Fe}_3\text{O}_4/\text{N-GAs}$) as efficient cathode catalysts for ORR [46]. These 3D monolithic $\text{Fe}_3\text{O}_4/\text{N-GAs}$ hybrids were fabricated via a combined hydrothermal self-assembly, freeze-drying, and thermal treatment process, using GO, iron acetate, and polypyrrole as starting materials (Figure 4). Because of the 3D macroporous structure, high surface area, and uniform deposition of Fe_3O_4 NPs, the resulting $\text{Fe}_3\text{O}_4/\text{N-GAs}$ exhibited a more positive onset potential, higher cathodic density, lower H_2O_2 yield, and higher electron transfer number ($4e^-$) for the ORR in alkaline media than Fe_3O_4 NPs supported on N-doped carbon black or N-doped 2D graphene sheets. Furthermore, $\text{Fe}_3\text{O}_4/\text{N-GAs}$ showed better durability than the commercial Pt/C catalyst. This 3D N-GA is also demonstrated to be a universal carbon support that is superior to other carbon supports for loading of other nonprecious metal electrocatalysts (e.g., Fe NPs).

Iron porphyrin plays a vital role in oxygen transport and reduction reactions in biological system. Thus, it would be attractive to consider if supporting iron porphyrin on graphene could function as an alternative to Pt-based electrode in fuel cells for ORR. In 2012, Jahan and coworkers synthesized an electrocatalytically active 3D graphene-iron porphyrin metal organic framework (MOF) composite for ORR by reacting the pyridine-functionalized graphene with iron porphyrin [47]. According to their study, the addition of functionalized rGO sheets influenced the crystallization process of MOF, increased its porosity and electroactive surface area, and enhanced the electrochemical charge transfer rate of iron porphyrin. The synergistic effect of the rGO, pyridinium linker, and the iron porphyrin for the improvements in electrocatalytic activities was demonstrated by a series of control experiments. With a four-electron ORR pathway, this graphene-metalloporphyrin hybrid also possessed significantly reduced methanol crossover effects and superior durability compared to Pt catalysts, showing its potential for use as a promising Pt-free cathode in alkaline direct methanol fuel cell.

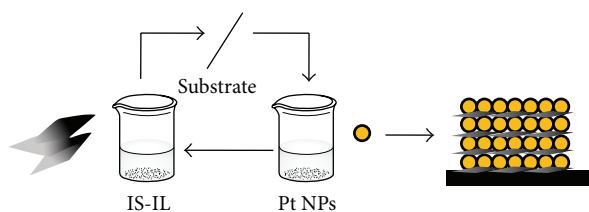


FIGURE 5: Schematic representation of the assembling process of the IS-IL modified graphene/Pt NPs multilayer films (reprinted from [49]; copyright 2010 American Chemical Society).

Recently, Mao and coworkers reported a 3D N-doped crumpled graphene- (N-CG-) cobalt oxide nanohybrids (N-CG-CoO) with a stable structure for use as bifunctional catalysts for both ORR and oxygen evolution reaction (OER) in alkaline solutions [48]. The N-CG-CoO nanocrystal hybrid, showing a hollow structure with uniform nanocrystal decoration on both the external and internal surfaces of the CG balls, was produced by an aerosolization/high-temperature-induced GO crumpling and nanocrystal growth method. With a four-electron ORR process, the N-CG-CoO hybrid exhibited excellent ORR catalytic activity that is comparable with that of commercial Pt/C catalyst (and is much higher than that of nondoped CG-CoO, rGO, and CoO) and good durability superior to that of Pt/C in an alkaline electrolyte and thus is believed to be a promising candidate for fuel cell and water splitting applications.

3.4. Noble Metal-Containing 3D Graphene-Based Nanocomposites. Although great contribution has been made to devise various nonnoble metal electrocatalysts, the demands of the high catalytic activity for the four-electron ORR and the acidic environment of the fuel cell electrode still make noble metal-based nanostructures the most promising for practical application. In this context, it is a realistic strategy to further maximize the activity of noble metal-based nanostructures and minimize the use of precious noble metal by loading these highly active nanomaterials on the surface of supporting materials with low cost, high surface area, and good electrical conductivity, which not only maximizes the availability of surface area for electron transfer and decreases the aggregation of these electrocatalysts, but also provides better mass transport of reactants to the electrocatalysts. As expected, 3D graphene network, among the catalyst supports for ORR, is believed to be the most promising candidate owing to its unique properties such as high electrical and thermal conductivities, great mechanical strength, inherent flexibility, and huge specific surface area.

In 2010, Zhu and coworkers constructed a hybrid 3D nanocomposite film by alternatively assembling the graphene nanosheets modified by imidazolium salt-based ionic liquid (IS-IL) and Pt NPs through electrostatic interaction (Figure 5) [49]. The introduction of IS-IL on the surface of graphene nanosheets not only increases the dissolubility of graphene nanosheets, but also provides the catalyst support with higher conductivity and abundant positive charge desired in this layer-by-layer (LBL) self-assembly of

nanocomposites. This multilayer film exhibited prominent electrocatalytic activity and stability toward ORR. Furthermore, the content of Pt NPs—and thus the electrocatalytic activity—of the films could be tailored by tuning the number of bilayers in the LBL process.

In 2013, Sattayasamitsathit and coworkers reported for the first time on the use of lithographically defined 3D graphene microstructure as support for catalytic metal NPs (Figure 6) [50]. Various noble metal NPs (Au, Pd, and Pt) were deposited on these multilayered highly ordered 3D graphene structures by either electrochemical or electroless method. The size, morphology, and distribution of the NPs over the 3D graphene structure could be tailored by changing the preparation conditions (e.g., deposition potential or time for electrochemical method; metal concentration, pH, or temperature for chemical reduction method). The catalytic activity toward ORR of Pt NPs on 3D graphene was superior to that of Pt NPs on a 3D carbon substrate and on a glassy carbon electrode, bare 3D graphene, and Pt black. This enhancement of catalytic activity could be ascribed to the macroporosity of 3D graphene which allows deposition of a high surface area of catalytic NPs and the nanosize dimensions of the connecting arms and nodes in 3D graphene structure which provides a highly favorable mass transport environment for delivery of fuels.

4. Conclusions and Perspective

In fuel cells, an effective electrocatalyst for ORR at the cathode plays a crucial role in improving their energy conversion efficiency and enhancing the high energy and power density. In recent years, the newly developed 3D graphene-based materials have been demonstrated to be promising as efficient electrocatalysts for ORR. In this paper, we have reviewed the primary preparation method of these novel materials and their performances as catalysts for ORR. From the viewpoint of whether containing precious metals or not, Sections 3.1–3.3 have introduced the development of noble metal-free 3D graphene-based electrocatalysts, which is among the current efforts to develop the alternative to Pt-based catalysts for ORR. The success in this direction would significantly weaken or fully eliminate the dependency on noble metals, thereby greatly reducing the cost of fuel cells. On the other hand, Section 3.4 has introduced the development of low-noble metal 3D graphene-based electrocatalysts, which belongs to another class of efforts to maximize the utilization of noble metal in fuel cells application. As mentioned earlier, 3D graphene could function as either single catalyst or catalyst support for ORR. As the single catalyst, heteroatom-doped 3D graphene-based materials could render stable and durable catalytic performance compared with other composite electrocatalysts for ORR. As the catalyst support, compared to another carbonaceous support, 3D graphene combines the advantages of traditional 2D graphene (such as high conductivity and large specific surface area) with its nonagglomerated morphology and porous structure, which could facilitate the loading and dispersion of catalysts. Moreover, the interconnected graphene networks could promote fast electron transport between the reaction sites and

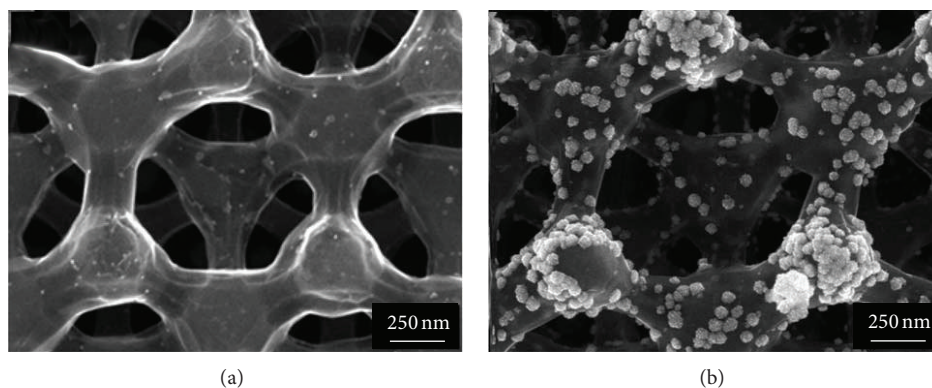


FIGURE 6: SEM images of (a) bare 3D graphene substrate before modification with metal nanoparticles and (b) 3D graphene after modification with Pt NPs using electrodeposition at 0.4 V for 750 s (reproduced from [50] with permission of the Royal Society of Chemistry).

the electrode and efficiently maximize the electroactive surface area of catalysts, all of which would greatly improve the catalytic activity and durability of these 3D graphene-based electrocatalysts for ORR [51–54].

In spite of significant progress made in this area within only several years, the research of 3D graphene-based materials still remains at its initial stage and at least two aspects of challenges for practical application of these materials in fuel cells should be addressed. First, the systematic exploration and deeper understanding of the different catalytic mechanisms of various 3D graphene-based materials for ORR are required for optimum material design and device performance optimization. For example, for N-doped 3D graphene as inherent ORR catalyst, though the critical role of N dopant for the catalytic enhancement is proved, the precise relationship between catalytic activity and N species is still controversial, while, for 3D-graphene-based nanocomposites, more experimental and theoretical studies are needed to reveal the interactions between the 3D graphene and loaded active nanomaterials. Second, the development of facile, green, cost-effective, and controllable preparation method is still a significant issue, because the current assembly process usually needs to be carried out in rigorous conditions (such as high temperature or pressure) or involves tedious procedures, which increases the degree of preparation difficulty. Thus, much further research is needed to realize the aim of final industrial implementation, large scale, low cost, and simple production of 3D graphene-based materials with high catalytic activity and practical durability for ORR. This review is anticipated to encourage more future works to achieve this aim and to promote sustainability.

Conflict of Interests

The authors declare that there is no conflict of interests regarding the publication of this paper.

Acknowledgments

This work was supported by the Natural Science Foundation of Shanxi (no. 2015021081), the Project for Construction of

Science and Technology Innovation Team of Shanxi (no. 2015013001-04), and the Provincial Science and Technology Major Project of Shanxi (no. 0111101059).

References

- [1] V. Dhand, K. Y. Rhee, H. Ju Kim, and D. Ho Jung, “A comprehensive review of graphene nanocomposites: research status and trends,” *Journal of Nanomaterials*, vol. 2013, Article ID 763953, 14 pages, 2013.
- [2] A. K. Geim and K. S. Novoselov, “The rise of graphene,” *Nature Materials*, vol. 6, no. 3, pp. 183–191, 2007.
- [3] K. S. Novoselov, V. I. Fal’Ko, L. Colombo, P. R. Gellert, M. G. Schwab, and K. Kim, “A roadmap for graphene,” *Nature*, vol. 490, no. 7419, pp. 192–200, 2012.
- [4] K. S. Novoselov, A. K. Geim, S. V. Morozov et al., “Electric field effect in atomically thin carbon films,” *Science*, vol. 306, no. 5696, pp. 666–669, 2004.
- [5] X. Huang, X. Qi, F. Boey, and H. Zhang, “Graphene-based composites,” *Chemical Society Reviews*, vol. 41, no. 2, pp. 666–686, 2012.
- [6] X. Zhang, K. S. Ziemer, K. Zhang et al., “Large-area preparation of high-quality and uniform three-dimensional graphene networks through thermal degradation of graphene oxide-nitrocellulose composites,” *ACS Applied Materials and Interfaces*, vol. 7, no. 2, pp. 1057–1064, 2015.
- [7] Y. Zhu, S. Murali, W. Cai et al., “Graphene and graphene oxide: synthesis, properties, and applications,” *Advanced Materials*, vol. 22, no. 35, pp. 3906–3924, 2010.
- [8] X. Zhang, X. Ji, R. Su, B. L. Weeks, Z. Zhang, and S. Deng, “Aerobic oxidation of 9h-fluorenes to 9-fluorenonees using mono-/multilayer graphene-supported alkaline catalyst,” *ChemPlusChem*, vol. 78, no. 7, pp. 703–711, 2013.
- [9] A. Aziz, H. N. Lim, S. H. Girei et al., “Silver/graphene nanocomposite-modified optical fiber sensor platform for ethanol detection in water medium,” *Sensors and Actuators B: Chemical*, vol. 206, pp. 119–125, 2015.
- [10] S. P. Lim, A. Pandikumar, Y. S. Lim, N. M. Huang, and H. N. Lim, “In-situ electrochemically deposited polypyrrole nanoparticles incorporated reduced graphene oxide as an efficient counter electrode for platinum-free dye-sensitized solar cells,” *Scientific Reports*, vol. 4, article 5305, 2014.

- [11] G. T. S. How, A. Pandikumar, H. N. Ming, and L. H. Ngee, "Highly exposed 001 facets of titanium dioxide modified with reduced graphene oxide for dopamine sensing," *Scientific Reports*, vol. 4, article 5044, 2014.
- [12] K. Zangeneh Kamali, A. Pandikumar, G. Sivaraman et al., "Silver@graphene oxide nanocomposite-based optical sensor platform for biomolecules," *RSC Advances*, vol. 5, no. 23, pp. 17809–17816, 2015.
- [13] M. M. Shahid, A. Pandikumar, A. M. Golsheikh, N. M. Huang, and H. N. Lim, "Enhanced electrocatalytic performance of cobalt oxide nanocubes incorporating reduced graphene oxide as a modified platinum electrode for methanol oxidation," *RSC Advances*, vol. 4, no. 107, pp. 62793–62801, 2014.
- [14] A. Pandikumar, G. T. S. How, T. P. See et al., "Graphene and its nanocomposite material based electrochemical sensor platform for dopamine," *RSC Advances*, vol. 4, no. 108, pp. 63296–63323, 2014.
- [15] J. K. Gan, Y. S. Lim, A. Pandikumar, N. M. Huang, and H. N. Lim, "Graphene/polypyrrole-coated carbon nanofiber core-shell architecture electrode for electrochemical capacitors," *RSC Advances*, vol. 5, no. 17, pp. 12692–12699, 2015.
- [16] F. A. Jumeri, H. N. Lim, Z. Zainal, N. M. Huang, A. Pandikumar, and S. P. Lim, "Dual functional reduced graphene oxide as photoanode and counter electrode in dye-sensitized solar cells and its exceptional efficiency enhancement," *Journal of Power Sources*, vol. 293, pp. 712–720, 2015.
- [17] S. P. Lim, A. Pandikumar, N. M. Huang, and H. N. Lim, "Reduced graphene oxide-titania nanocomposite-modified photoanode for efficient dye-sensitized solar cells," *International Journal of Energy Research*, vol. 39, no. 6, pp. 812–824, 2015.
- [18] T. Peik-See, A. Pandikumar, L. H. Ngee, H. N. Ming, and C. C. Hua, "Magnetically separable reduced graphene oxide/iron oxide nanocomposite materials for environmental remediation," *Catalysis Science & Technology*, vol. 4, no. 12, pp. 4396–4405, 2014.
- [19] B. Xia, Y. Yan, X. Wang, and X. W. Lou, "Recent progress on graphene-based hybrid electrocatalysts," *Materials Horizons*, vol. 1, no. 4, pp. 379–399, 2014.
- [20] C. Huang, C. Li, and G. Shi, "Graphene based catalysts," *Energy & Environmental Science*, vol. 5, no. 10, pp. 8848–8868, 2012.
- [21] B. F. MacHado and P. Serp, "Graphene-based materials for catalysis," *Catalysis Science and Technology*, vol. 2, no. 1, pp. 54–75, 2012.
- [22] F. Liu, C. W. Lee, and J. S. Im, "Graphene-based carbon materials for electrochemical energy storage," *Journal of Nanomaterials*, vol. 2013, Article ID 642915, 11 pages, 2013.
- [23] L. Chen, M. Zhang, and W. Wei, "Graphene-based composites as cathode materials for lithium ion batteries," *Journal of Nanomaterials*, vol. 2013, Article ID 940389, 8 pages, 2013.
- [24] X. Cao, Z. Yin, and H. Zhang, "Three-dimensional graphene materials: preparation, structures and application in supercapacitors," *Energy and Environmental Science*, vol. 7, no. 6, pp. 1850–1865, 2014.
- [25] B. Luo and L. Zhi, "Design and construction of three dimensional graphene-based composites for lithium ion battery applications," *Energy & Environmental Science*, vol. 8, no. 2, pp. 456–477, 2015.
- [26] S. Mao, G. Lu, and J. Chen, "Three-dimensional graphene-based composites for energy applications," *Nanoscale*, vol. 7, no. 16, pp. 6924–6943, 2015.
- [27] S. Nardecchia, D. Carriazo, M. L. Ferrer, M. C. Gutiérrez, and F. Del Monte, "Three dimensional macroporous architectures and aerogels built of carbon nanotubes and/or graphene: synthesis and applications," *Chemical Society Reviews*, vol. 42, no. 2, pp. 794–830, 2013.
- [28] Y. Shen, Q. Fang, and B. Chen, "Environmental applications of three-dimensional graphene-based macrostructures: adsorption, transformation, and detection," *Environmental Science — Technology*, vol. 49, no. 1, pp. 67–84, 2015.
- [29] J. Zai and X. Qian, "Three dimensional metal oxides-graphene composites and their applications in lithium ion batteries," *RSC Advances*, vol. 5, no. 12, pp. 8814–8834, 2015.
- [30] Y. J. Wang, N. Zhao, B. Fang, H. Li, X. T. Bi, and H. Wang, "Carbon-supported pt-based alloy electrocatalysts for the oxygen reduction reaction in polymer electrolyte membrane fuel cells: particle size, shape, and composition manipulation and their impact to activity," *Chemical Reviews*, vol. 115, no. 9, pp. 3433–3467, 2015.
- [31] C. Wang, N. M. Markovic, and V. R. Stamenkovic, "Advanced platinum alloy electrocatalysts for the oxygen reduction reaction," *ACS Catalysis*, vol. 2, no. 5, pp. 891–898, 2012.
- [32] K. Chen, L. Chen, Y. Chen, H. Bai, and L. Li, "Three-dimensional porous graphene-based composite materials: electrochemical synthesis and application," *Journal of Materials Chemistry*, vol. 22, no. 39, pp. 20968–20976, 2012.
- [33] Z. Yang, H. Nie, X. Chen, X. Chen, and S. Huang, "Recent progress in doped carbon nanomaterials as effective cathode catalysts for fuel cell oxygen reduction reaction," *Journal of Power Sources*, vol. 236, pp. 238–249, 2013.
- [34] C. Zhu and S. Dong, "Recent progress in graphene-based nanomaterials as advanced electrocatalysts towards oxygen reduction reaction," *Nanoscale*, vol. 5, no. 5, pp. 1753–1767, 2013.
- [35] Q. Fang, Y. Shen, and B. Chen, "Synthesis, decoration and properties of three-dimensional graphene-based macrostructures: a review," *Chemical Engineering Journal*, vol. 264, pp. 753–771, 2015.
- [36] C. Li and G. Shi, "Three-dimensional graphene architectures," *Nanoscale*, vol. 4, no. 18, pp. 5549–5563, 2012.
- [37] Z. Yan, W. Yao, L. Hu, D. Liu, C. Wang, and C. Lee, "Progress in the preparation and application of three-dimensional graphene-based porous nanocomposites," *Nanoscale*, vol. 7, no. 13, pp. 5563–5577, 2015.
- [38] M. Zeng, W.-L. Wang, and X.-D. Bai, "Preparing three-dimensional graphene architectures: review of recent developments," *Chinese Physics B*, vol. 22, no. 9, Article ID 098105, 2013.
- [39] X.-K. Kong, C.-L. Chen, and Q.-W. Chen, "Doped graphene for metal-free catalysis," *Chemical Society Reviews*, vol. 43, no. 8, pp. 2841–2857, 2014.
- [40] H. Wang, T. Maiyalagan, and X. Wang, "Review on recent progress in nitrogen-doped graphene: synthesis, characterization, and its potential applications," *ACS Catalysis*, vol. 2, no. 5, pp. 781–794, 2012.
- [41] Y. Zhao, C. Hu, Y. Hu, H. Cheng, G. Shi, and L. Qu, "A versatile, ultralight, nitrogen-doped graphene framework," *Angewandte Chemie International Edition*, vol. 51, no. 45, pp. 11371–11375, 2012.
- [42] Y. Su, Y. Zhang, X. Zhuang et al., "Low-temperature synthesis of nitrogen/sulfur co-doped three-dimensional graphene frameworks as efficient metal-free electrocatalyst for oxygen reduction reaction," *Carbon*, vol. 62, pp. 296–301, 2013.

- [43] L. Wang, A. Ambrosi, and M. Pumera, "Metal-free catalytic oxygen reduction reaction on heteroatom-doped graphene is caused by trace metal impurities," *Angewandte Chemie—International Edition*, vol. 52, no. 51, pp. 13818–13821, 2013.
- [44] J. Tian, R. Ning, Q. Liu, A. M. Asiri, A. O. Al-Youbi, and X. Sun, "Three-dimensional porous supramolecular architecture from ultrathin g-C₃N₄ nanosheets and reduced graphene oxide: solution self-assembly construction and application as a highly efficient metal-free electrocatalyst for oxygen reduction reaction," *ACS Applied Materials & Interfaces*, vol. 6, no. 2, pp. 1011–1017, 2014.
- [45] L. Zhuang, Y. Yuan, G. Yang, and S. Zhou, "In situ formation of graphene/biofilm composites for enhanced oxygen reduction in biocathode microbial fuel cells," *Electrochemistry Communications*, vol. 21, no. 1, pp. 69–72, 2012.
- [46] Z.-S. Wu, S. Yang, Y. Sun, K. Parvez, X. Feng, and K. Müllen, "3D nitrogen-doped graphene aerogel-supported Fe₃O₄ nanoparticles as efficient electrocatalysts for the oxygen reduction reaction," *Journal of the American Chemical Society*, vol. 134, no. 22, pp. 9082–9085, 2012.
- [47] M. Jahan, Q. Bao, and K. P. Loh, "Electrocatalytically active graphene-porphyrin MOF composite for oxygen reduction reaction," *Journal of the American Chemical Society*, vol. 134, no. 15, pp. 6707–6713, 2012.
- [48] S. Mao, Z. Wen, T. Huang, Y. Hou, and J. Chen, "High-performance bi-functional electrocatalysts of 3D crumpled graphene-cobalt oxide nanohybrids for oxygen reduction and evolution reactions," *Energy & Environmental Science*, vol. 7, no. 2, pp. 609–616, 2014.
- [49] C. Zhu, S. Guo, Y. Zhai, and S. Dong, "Layer-by-layer self-assembly for constructing a graphene/platinum nanoparticle three-dimensional hybrid nanostructure using ionic liquid as a linker," *Langmuir*, vol. 26, no. 10, pp. 7614–7618, 2010.
- [50] S. Sattayasamitsathit, Y. Gu, K. Kaufmann et al., "Highly ordered multilayered 3D graphene decorated with metal nanoparticles," *Journal of Materials Chemistry A*, vol. 1, no. 5, pp. 1639–1645, 2013.
- [51] D. Geng, N. Ding, T. S. Andy Hor, Z. Liu, X. Sun, and Y. Zong, "Potential of metal-free 'graphene alloy' as electrocatalysts for oxygen reduction reaction," *Journal of Materials Chemistry A*, vol. 3, no. 5, pp. 1795–1810, 2015.
- [52] D.-W. Wang and D. Su, "Heterogeneous nanocarbon materials for oxygen reduction reaction," *Energy & Environmental Science*, vol. 7, no. 2, pp. 576–591, 2014.
- [53] Y. Nie, L. Li, and Z. Wei, "Recent advancements in Pt and Pt-free catalysts for oxygen reduction reaction," *Chemical Society Reviews*, vol. 44, no. 8, pp. 2168–2201, 2015.
- [54] L. Dai, Y. Xue, L. Qu, H.-J. Choi, and J.-B. Baek, "Metal-free catalysts for oxygen reduction reaction," *Chemical Reviews*, vol. 115, no. 11, pp. 4823–4892, 2015.

Research Article

Rice Husk Supported Catalysts for Degradation of Chlorobenzenes in Capillary Microreactor

**Abdulelah Thabet, Chanbasha Basheer, Than Htun Maung,
Hasan Ali Al-Muallem, and Abdul Nasar Kalanthen**

Department of Chemistry, King Fahd University of Petroleum and Minerals, Dhahran 31261, Saudi Arabia

Correspondence should be addressed to Chanbasha Basheer; cbasheer@kfupm.edu.sa

Received 16 January 2015; Revised 21 May 2015; Accepted 4 June 2015

Academic Editor: Maofeng Zhang

Copyright © 2015 Abdulelah Thabet et al. This is an open access article distributed under the Creative Commons Attribution License, which permits unrestricted use, distribution, and reproduction in any medium, provided the original work is properly cited.

Chlorinated organic pollutants are persistent, toxic, and ubiquitously distributed environmental contaminants. These compounds are highly bioaccumulative and adversely affect the ozone layer in the atmosphere. As such, their widespread usage is a major cause of environmental and health concern. Therefore, it is important to detoxify such compounds by environment friendly methods. In this work, rice husk supported platinum (RHA-Pt) and titanium (RHA-Ti) catalysts were used, for the first time, to investigate the detoxification of chlorobenzenes in a glass capillary microreactor. High potential (in kV range) was applied to a reaction mixture containing buffer solution in the presence of catalyst. Due to high potential, hydroxyl and hydrogen radicals were produced, and the reaction was monitored by gas chromatography-mass spectrometry. The main advantage of this capillary reactor is the in situ generation of hydrogen for the detoxification of chlorobenzene. Various experimental conditions influencing detoxification were optimized. Reaction performance of capillary microreactor was compared with conventional catalysis. Only 20 min is sufficient to completely detoxify chlorobenzene in capillary microreactor compared to 24 h reaction time in conventional catalytic method. The capillary microreactor is simple, easy to use, and suitable for the detoxification of a wide range of chlorinated organic pollutants.

1. Introduction

Chlorinated organic compounds (COCs) are a large class of synthetic and natural organic molecules that contain one or more chlorine atoms. They are one of the most versatile and widely used classes of compounds in the industrial world [1]. For example, COCs are used as anesthetics, pesticides and herbicides, fungicides, dyes, pharmaceuticals, plant growth regulators, heat-transfer medium, and industrial solvents and are byproducts of several industries (e.g., oil refining, paper industry, plastics or adhesives manufacturing, etc.) [1–6]. The importance of these chlorinated chemicals lies in the fact that chlorine bonds strongly to other elements, and this makes chlorine an important ingredient and precursor in building new compounds. Unfortunately, this property is also one of the reasons why chlorinated compounds, once formed, are hazardous. Due to this strong bonding, it is hard to break down COCs and hence they persist in nature. Chlorine-containing compounds also adversely affect the ozone layer in the atmosphere. As such, their widespread usage is a major

cause of environmental and health concern. Moreover, COCs are among the most widely distributed pollutants in wastewaters and contaminated ground waters [7]. They are listed as priority pollutant by the U.S. Environmental Protection Agency (USEPA) [8]. Due to their lipophilic nature (i.e., easy to concentrate in fats of animals, which leads to biomagnification), polychlorinated aromatic compounds which are environmentally stable and persistent in nature tend to bioaccumulate in the food chain [9]. Bioaccumulation indirectly affects human as residues of these compound are detected in food and human adipose tissues, milk, and serum fat [10]. COCs can cause serious environmental problems because they are difficult to be decomposed biologically. Exposure to them can lead to kidney, liver, blood, and central nervous system damages. Therefore, there is an urgent need to develop efficient and cost-effective methods to detoxify and destroy them [11]. Several remediation methods have been developed to eliminate COCs, such as oxidation methods and incineration [12, 13]; mechanochemical methods and reductive

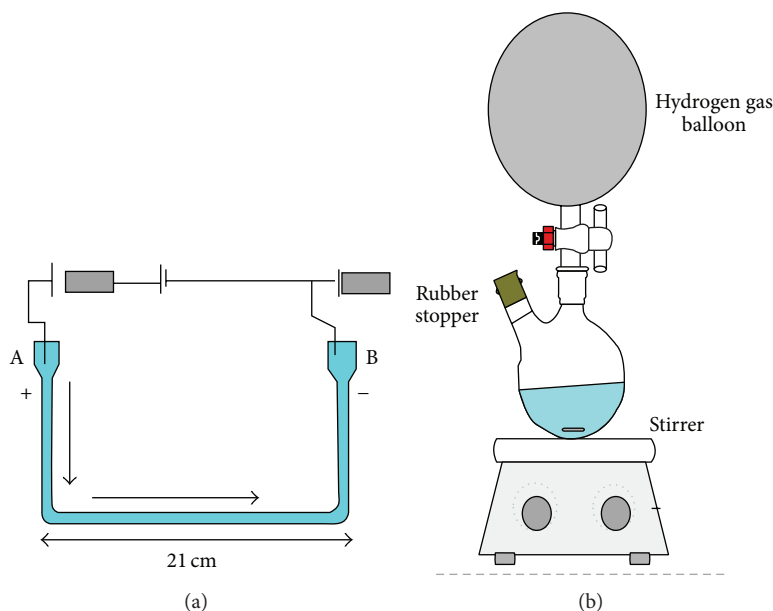
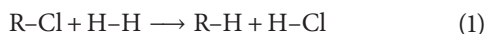


FIGURE 1: Schematics of (a) the glass capillary microreactor for transfer hydrogenolysis reaction. (b) Conventional experimental set up for hydrodechlorination reaction with external supplied hydrogen gas source.

methods such as electrochemical [14], photochemical [15], ultrasonic [16], microbial [17], and radiolytic and thermal [18] reductive methods have been developed. Besides reductive methods, bioremediation using natural biological activity by means of aerobic and anaerobic biodegradation of chlorinated compounds has also been extensively studied [19–21]. Catalytic hydrodechlorination (HDC), which involves the reductive cleavage of a C–Cl bond by highly reactive atomic hydrogen (H), is a green (environmentally friendly) and cost-effective technique. So far, the effective degradation of various COCs, including CBs and CPs (chlorophenols), has been successfully achieved [11]. HDC is one of the most promising alternative methods for the detoxification of COCs; it operates in liquid or gas phase using different catalytic systems yielding none or partially chlorinated hydrocarbons and HCl as products. Basically, HDC is the reaction of COCs (R–Cl) with hydrogen to form a carbon-hydrogen bond and HCl. It can be represented by the following chemical equation:



Moreover, this reaction can be done in mild ambient conditions and it forms no harmful side-products and could eventually be selective towards chloride removal [22, 23]. HDC is a simple, efficient and clean method. The hydrogen source in the HDC reaction can be molecular hydrogen (H_2) or any other hydrogen donors such as formic acid and its salts or alcohols such as isopropanol and hydrazine [7, 24, 25]. This reaction is quite exothermic and thus requires the presence of a catalyst to drive it to completion. The reaction also requires selective cleavage of C–Cl bond and therefore requires selective catalysts. Several hydrodechlorination metallic catalysts and support have been reported in the literature [26, 27]. For example, palladium, ruthenium, rhodium, iridium, rhenium, titanium, platinum, and Raney nickel [2, 28–30] were used

as catalysts. Where alumina, activated carbon [2], Ni–Mo/C [5], and silica are among the catalyst supports for the most commonly used ones in the HDC reactions, the catalytic activity of HDC does not only depend on the size of the metals but also on the nature of the support and the preparation method of the support [31].

Rice husk (RH) is an agricultural waste and the ash contains about 92–95% silica (SiO_2). It is highly porous with lightweight and high surface area. Many publications reported the use of rice husk ash as catalyst support for metals [32]. HDC processes can be performed in batch reactors for small and medium-scale processes and/or continuous-flow reactors for large-scale processes. A glass capillary-based microreactor (as shown in Figure 1(a)) was fabricated for this study and the glass is chemically inert, optically clear, and nonporous, hence making it a suitable material [33, 34]. The present study investigates detoxification of chlorinated aromatic compounds over silica-platinum and silica-titanium supported catalysts under mild condition by using buffered solutions in a capillary microreactor.

2. Experimental

2.1. Materials. Platinum chloride (PtCl_2) used as the source of platinum and titanium dioxide (TiO_2) as the source of titanium were purchased from Merck, Darmstadt, Germany. Other materials used are nitric acid (65% purity), sodium hydroxide pellets (99%), and acetone (99.5%) (Sigma-Aldrich, St Louis). Cetyltrimethylammonium bromide (CTAB, 98%) and methylene blue were purchased from Sigma Aldrich. Rice husk (RH) was obtained from a rice milling company in Penang. A 100 ppm standards of 1,2-dichlorobenzene (1,2-DCB), 3-dichlorobenzene (1,3-DCB), 1,4-dichlorobenzene

(1,4-DCB), 1,2,4-trichlorobenzene (1,2,4-TCB), hexachlorobenzene (HCB) and benzene (Sigma-Aldrich, $\geq 99.0\%$) were prepared.

2.2. Preparation of the Catalysts. 30 g of clean rice husk was stirred with 750 mL of 1.0 M HNO_3 at room temperature for 24 h. The cleaned RH was washed with copious amount of distilled water to constant pH, then dried in an oven at 100°C for 24 h, and burned in a muffle furnace at 600°C for 6 h so as to obtain white rice husk ash (RHA) [32]. About 3.0 g of RHA was added to 350 mL of 1.0 mol L^{-1} NaOH in a plastic container and stirred for 24 h at room temperature to get sodium silicate solution. About 3.6 g of CTAB (1:1.2, Si:CTAB molar ratio) was added into the sodium silicate solution and stirred to dissolve completely. This solution was titrated with 3.0 mol L^{-1} HNO_3 at a rate of ca. 1.0 mL min^{-1} with constant stirring until pH 3.0. The resulting gel was aged for 5 days, then filtered and washed thoroughly with distilled water, and finally washed with acetone. The gel was dried at 110°C for 24 h, ground to fine powder, and calcined at 500°C in a muffle furnace for 5 h and then labeled as RHA-silica powder. Same procedure was followed for the preparation of RHA-silica solution of 10 wt.% Pt of PtCl_2 which was dissolved in 50 mL of 3 mol L^{-1} HNO_3 and titrated. Similarly, solution of 10.0 wt.% Ti of TiO_2 was dissolved in 50 mL of 3 mol L^{-1} HNO_3 and titrated. The resulting gels were treated as described above. The resulting powders were labeled as RHA-Pt and RHA-Ti, respectively.

2.3. Catalysts Characterization. The prepared RHA-Pt and RHA-Ti samples were characterized using Fourier transform infrared (FTIR) spectroscopy, N_2 adsorption-desorption analysis, Field-Emission Scanning Electron Microscope (FESEM), and energy dispersive spectrometry (EDX).

2.4. HDC Reaction in a Capillary Microreactor. The capillary microreactor was used for studying the detoxification of chlorinated organic compounds. Several glass capillary microreactores (7 cm, 14 cm, and 21 cm) were designed for the HDC reaction as shown in Figure 1(a). The capillary microreactor and reservoirs A and B were filled with 2.5 mmol of buffer solution of different pH (2, 7 and 10) and 12.5 mg of catalyst and $100 \mu\text{L}$ of the mixture standard (8270 MagaMix) were introduced into the capillary microreactor at the reservoir A. Platinum wires were used as the electrodes and high voltage (1–5 kV) was applied. No air bubbles were found inside the capillary tube during the reaction. A reaction potential (1–5 kV) and $200 \mu\text{A}$ current were applied to reservoir A, while reservoir B was connected to ground. HDC reaction was carried out at room temperature and ambient pressure, all experiments were repeated three times, to get more accurate results, and the reaction time was controlled manually. The basic arrangement of the capillary microreactor, in which the experimental studies for the detoxification of chlorinated organic compounds were carried out, is depicted in Figure 1(a). The setup of the capillary microreactor system is composed of a high voltage power supply, glass capillary microreactor, and platinum wires.

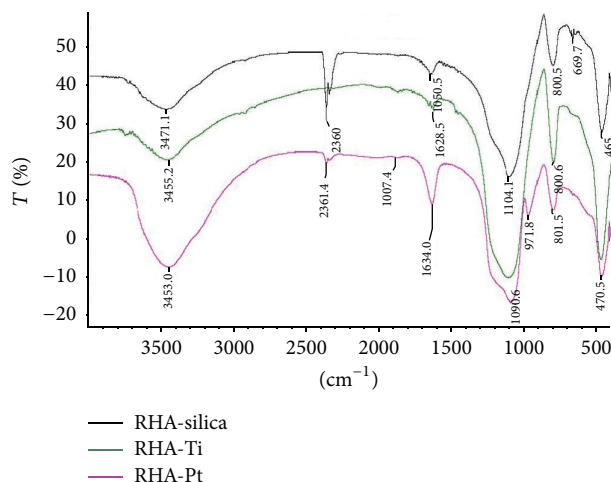


FIGURE 2: The FT-IR spectra of RHA-silica and metal modified silica by loading (Ti and Pt) (a) RHA- SiO_2 , (b) RHA-Ti, and (c) RHA-Pt.

2.5. Catalytic Hydrodechlorination (HDC) by Conventional Method. HDC reactions of 8270 MagaMix with molecular hydrogen gas were carried out at room temperature and ambient pressure by using buffered solutions in a round bottom flask. Hydrogen was introduced by balloon (Figure 1(b)). In a typical HDC procedure, 10 mL of buffer solution was spiked with 100 ppm chlorobenzenes, and 50 mg of supported Pt catalyst RHA-Pt, or 50 mg of RHA-Ti was added [2]. The mixture was magnetically stirred at 100 rpm with a stirring bar and after the desired time (2 h, 16 h, 24 h), the samples reaction mixtures were collected, and separated by 1.5 mL heptane for 5 min. The identification and quantification of all CBs was performed by GC-MS, and catalytic conversion was calculated by analyzing the peak areas of the target compounds. The setup is displayed in Figure 1(b). The buffer solutions used in the HDC reactions were prepared as follows: (a) phosphate buffer: phosphoric acid H_3PO_4 (2 mol L^{-1}) was added to a solution of K_2HPO_4 (2 mol L^{-1}) until the pH reaches 2; (b) phosphate buffer: a solution of NaH_2PO_4 (0.021 mol L^{-1}) was added to a solution of Na_2HPO_4 (0.029 mol L^{-1}) until the pH reaches 7; (c) borate buffer: a solution of sodium tetraborate (0.013 mol L^{-1}) was added to a solution of NaOH (0.018 mol L^{-1}) until the pH reaches 10.

3. Result and Discussion

3.1. Catalysts Characterization. The FT-IR analysis was carried out in Nicolet 6700 FT-IR using the KBr pellet method. Figure 2 shows the FT-IR spectra of the catalysts RHA-Ti and RHA-Pt and RHA- SiO_2 obtained in the wavenumber range $400\text{--}4000 \text{ cm}^{-1}$. The broad band in the range $3471\text{--}3455 \text{ cm}^{-1}$ is due to the stretching vibration of O–H bonds in Si–OH and the HO–H of water molecules adsorbed on the materials surface. The band at $1628\text{--}1650 \text{ cm}^{-1}$ is due to the bending vibration of H_2O trapped in the silica matrix. The band around 1104 cm^{-1} was shifted to a lower wavenumber for metal incorporated RHA. The band at $1090\text{--}1104 \text{ cm}^{-1}$ is attributed to asymmetric Si–O–Si stretching vibration, from

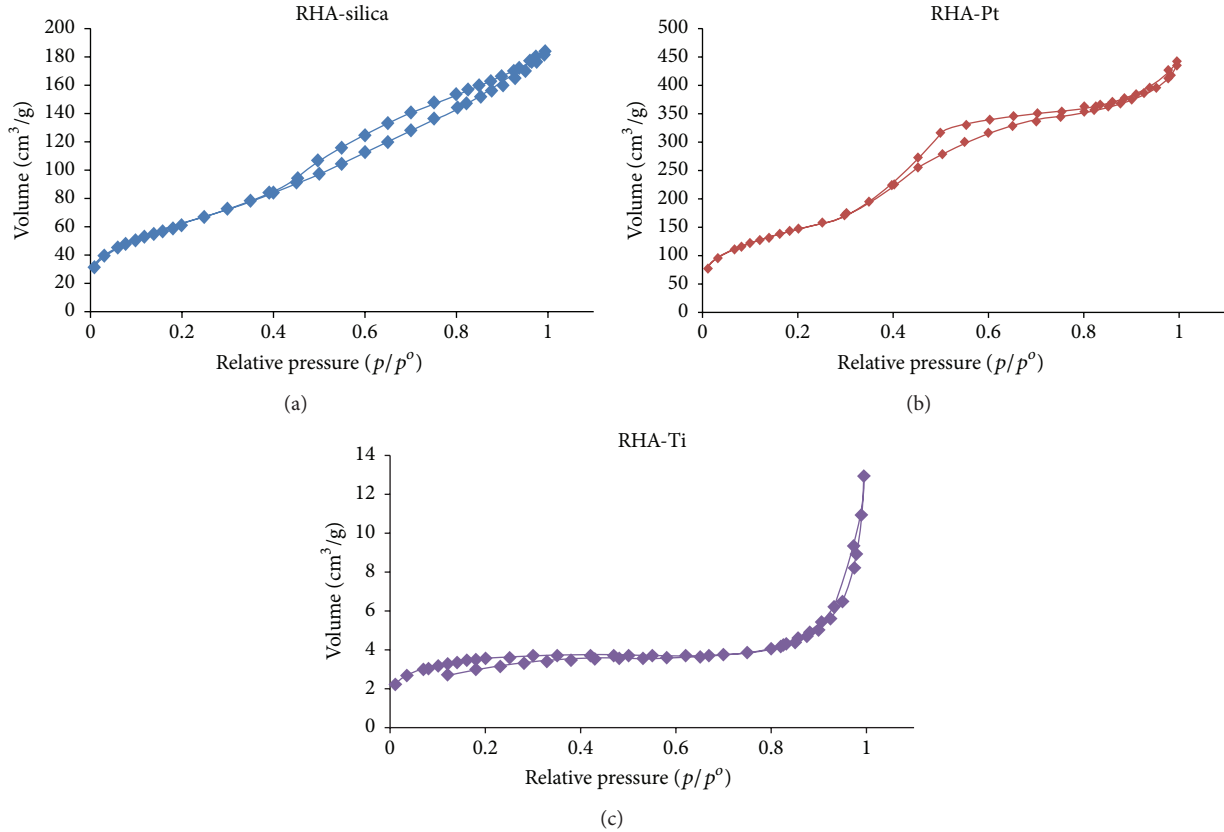


FIGURE 3: The nitrogen adsorption-desorption analysis of materials (a) RHA-silica, (b) RHA-Pt, and (c) RHA-Ti.

the structural siloxane bond. The band at 971.8 cm^{-1} can be attributed to the symmetric stretching vibration of Si-OH [32]. The intensity of this peak decreased in RHA-Ti and appears as a shoulder. This might indicate that some metal ions are attached on the surface of the silica as Si-O-M from the original Si-O-H or Si-O-Si silica structure. The absorption bands at about 465 cm^{-1} and 470.5 cm^{-1} are due to Si-O-Si bending vibrations [32]. The bands at $800\text{--}802\text{ cm}^{-1}$ are due to the deformation and bending modes of Si-O-Si.

The specific surface area, pore volume, and pore size distribution of the prepared catalysts were determined using N_2 adsorption-desorption on a Micromeritics ASAP 2020 volumetric instrument. Nitrogen sorption isotherms were performed at liquid nitrogen temperature (-195.786°C). The N_2 adsorption-desorption isotherm of RHA-silica, RHA-Pt, and RHA-Ti is shown in Figure 3. The surface area, pore diameter, and pore volume were calculated using Barrett-Joyner-Halenda model and the results are displayed in Table 1. The average mesopore size was, for all catalysts, around 4 to 4.85 nm. We see that RHA-silica has high surface area of $225.4306\text{ m}^2/\text{g}$ while RHA-Ti catalyst has associated BET surface area and pore volume of $12.6548\text{ m}^2/\text{g}$ and $0.012738\text{ cm}^3/\text{g}$, respectively. The incorporation of Ti into silica reduced its surface area and pore volume compared to RHA-silica due to the pore blocking by the agglomerated particles [35]. However, in the RHA-Pt supported catalyst,

TABLE 1: The nitrogen adsorption-desorption analysis parameters of materials.

Catalyst	BET surface area (m^2/g)	Pore volume (cm^3/g)	Average pore size (nm)
RHA-silica	225.4306	0.273179	4.84725
RHA-Pt	538.0725	0.637532	4.73938
RHA-Ti	12.6548	0.012738	4.02638

the incorporation of Pt into silica matrix increased its surface area ($538.0725\text{ m}^2/\text{g}$) and pore volume ($0.637532\text{ cm}^3/\text{g}$) compared to those of the support RHA-silica. This could be good dispersion of Pt particles within the silica matrix [32].

Field-Emission Scanning Electron Microscope (FESEM) (Tescan Lyra-3) was used to investigate the surface morphology and the general morphological features of the prepared RHA-silica and RHA-Pt nanoparticles. The EDX measurements were also used to confirm the percentage and the atomic ratio of the components in the prepared catalyst. Figure 4 shows the FESEM and EDX images of (a) RHA-silica sample, (b) RHA-Pt, and (c) RHA-Ti. The RHA-silica particles have flakes structure whereas the RHA-Pt particles have spherical structure with porous surfaces. While the RHA-Ti particles have rod-like morphology and less porous surfaces compared to RHA-silica.

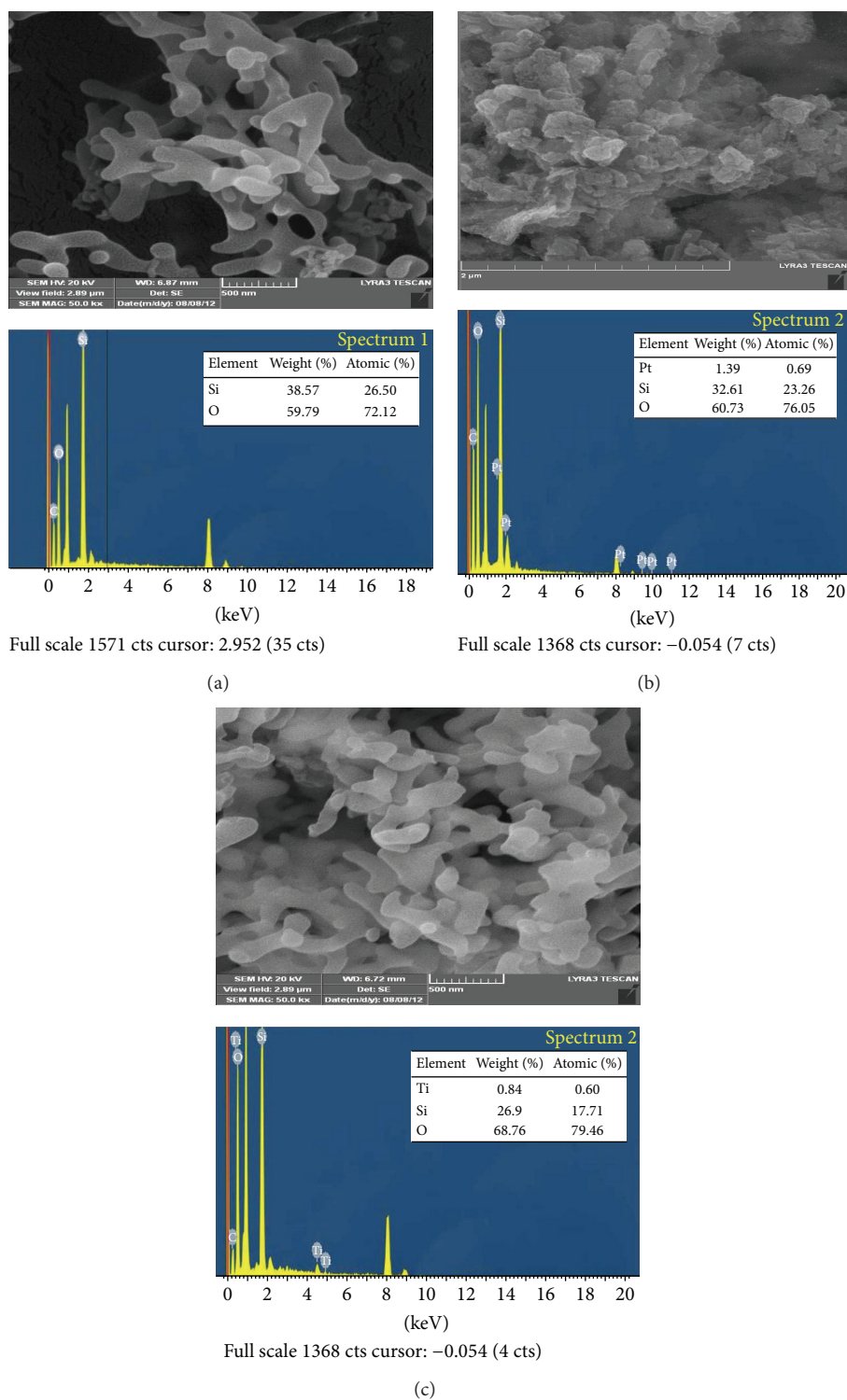


FIGURE 4: The FESEM and EDX images of (a) RHA-silica, (b) RHA-Pt, and (c) RHA-Ti.

3.2. Detoxification of COCs Using Capillary Microreactor. To optimize the HDC reactions in the capillary microreactor, analytical factors like applied potential, reaction time, length of the capillary, and pH of buffer solution were investigated to determine the most favorable reaction conditions. Temperature was kept constant at room temperature throughout

the reactions. The results were then compared with those of the conventional method. The identification and quantitative results were determined from GC-MS data.

3.2.1. Effect of Reaction Time. Reaction time is one of the most important factors in the HDC reactions. Therefore, various

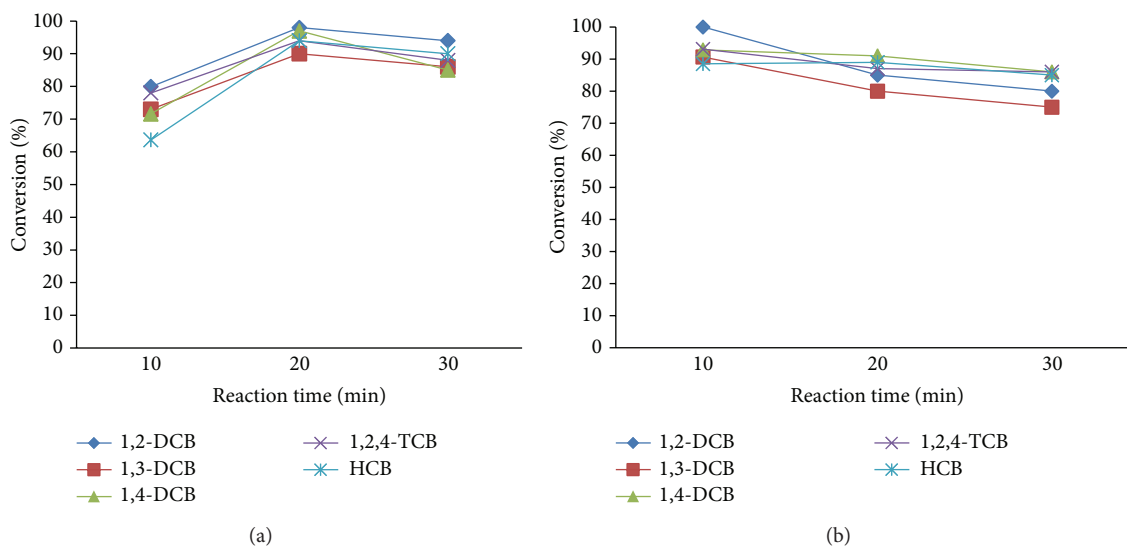


FIGURE 5: Effect of different reaction times on the conversion ratio of chlorobenzenes (CBs) in the capillary microreactor of 21 cm length, applied potential 3 kV (a) using pH 7 and RHA-Pt catalyst and (b) using pH 10 and RHA-Ti catalyst.

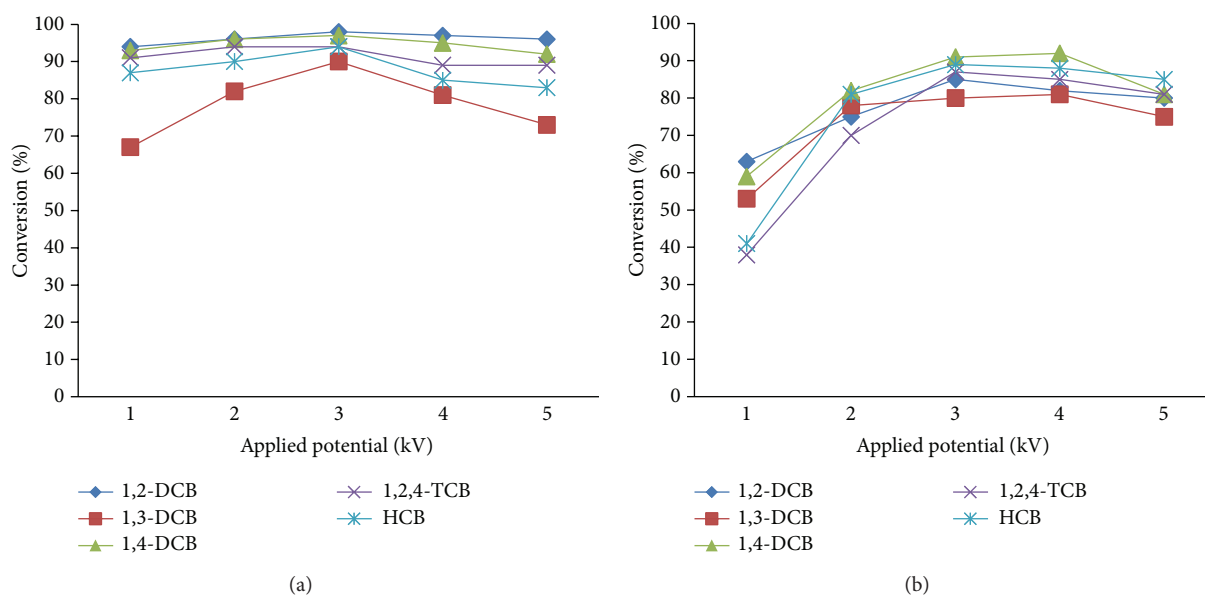


FIGURE 6: Effect of different applied potentials on the conversion ratio of chlorobenzenes (CBs) in the capillary microreactor at reaction time 20 min and pH 10 by using (a) RHA-Pt and (b) RHA-Ti.

reaction times (10 min, 20 min, and 30 min) were applied. The reaction time was controlled manually; Figure 5 shows the conversion percentage of CBs with respect to these times. The dechlorination increases with the increase in reaction time up to 20 min, by using RHA-Pt catalyst (Figure 5(a)), while the best time for the dechlorination of CBs by using RHA-Ti as catalyst was 10 min (Figure 5(b)).

3.2.2. Applied Potential. In order to achieve a high detoxification of COCs, different potentials were applied in the range of 1–5 kV at a constant current of 200 μ A. Figure 6 shows the influence of the applied potential on the HDC reactions. As can be seen, a maximum detoxification of COCs by both

catalysts (RHA-Pt and RHA-Ti) was obtained by using 3 kV. In a glass capillary microreactor, high potential (in kV range) was applied to create in situ generation of hydrogen as well as to expedite the activation of catalysts for the detoxification of chlorobenzene. Moreover, the higher applied potential increases the analyte interaction with the catalyst particles and enhances the hydrodechlorination (HDC) reaction to detoxify chlorobenzene [33, 34].

3.2.3. Length of the Capillary Microreactor. We have reported in a previous study that for microdevices, using an electrophoretic separation at constant field, resolution is proportional to the square of the channel length [33]. Various lengths

TABLE 2: Conversion ratio of CBs by the capillary-microreactor and the conventional method.

Catalyst	Method							
	Glass capillary microreactor			Conventional method				
	RHA-Ti 10 min	RHA-Pt 20 min	2 h	RHA-Pt 16 h	24 h	2 h	RHA-Ti 16 h	24 h
Compound name								
1,2-DCB	100	98	38	95	99	56	97	97
1,3-DCB	91	90	29	92	96	52	91	95
1,4-DCB	93	97	35	93	97	50	95	100
1,2,4-TCB	93	94	28	90	96	48	100	99
HCB	89	94	25	87	92	42	88	95

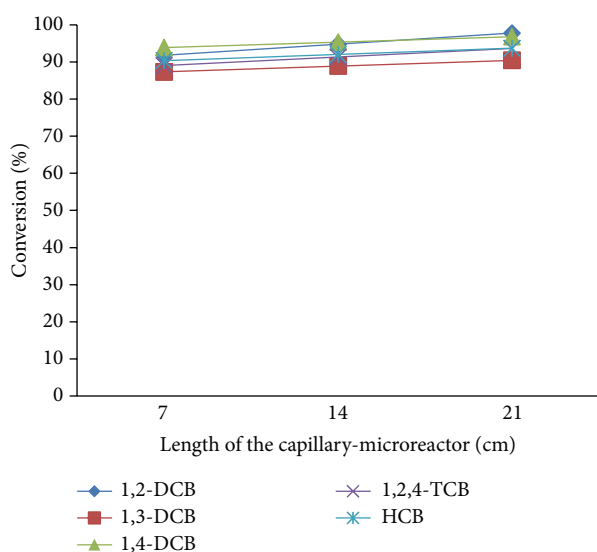


FIGURE 7: Effect of length of the capillary microreactor on the conversion ratio of CBs.

(7 cm, 14 cm, and 21 cm) of the capillary were studied and significant improvement was obtained in the dechlorination of CBs when the length of the capillary was increased from 7 cm to 21 cm as shown in Figure 7.

3.2.4. Reaction pH. The pH of the solution is an important parameter which controls the rate of the dechlorination of CBs and CPs in the capillary microreactor. The pH values of the solution studied were 2.0, 7.0, and 10. The conversions of CBs and CPs by catalytic HDC in the capillary microreactor by different buffer solutions are used to neutralize the HCl which forms during the HDC reaction. Figure 8 shows the conversion of COCs involving different catalysts. The maximum conversion by using RHA-Pt catalyst was observed in the neutral range (pH 7) compared to other buffer solutions. This might be due to the dissolution of platinum particles [26]. However, when RHA-Ti was used as catalyst, the maximum conversion was obtained in alkaline range (pH 10).

3.2.5. Quantitative Determination of Detoxification of COCs Using Microreactor with GC-MS Compared to Conventional Method. In order to evaluate the most favorable reaction conditions, the optimum dechlorination conditions were set as follows: reaction time of 20 min, and pH 7 when using RHA-Pt as the catalyst and 10 min applied potential of 3 kV was used with a 21 cm long capillary microreactor, and pH 7 when the catalyst was RHA-Ti. The results are summarized in Table 2. Compared with conventional detoxification method, the capillary microreactor provided high conversion ratios of CBs in shorter reaction time (20 min) with very little amount of the reactants.

In a glass capillary microreactor, high potential (in kV range) was applied to cause in situ generation of hydrogen as well as to expedite the activation of catalysts in the reaction for the detoxification of chlorobenzene. Moreover, the higher applied potential increases the analyte interaction with the nanoparticles and enhances the hydrodechlorination (HDC) reaction to detoxify chlorobenzene and chlorophenols. In our reactor, we believe that the electron density on the surface of the catalysts and the efficiency/performance of HDC reaction increase by the applied potential and thereby enhance conversion and dechlorination of CBs.

4. Conclusions

In this work, for the first time rice husk supported platinum (RHA-Pt) and titanium (RHA-Ti) catalysts were used to investigate the detoxification of chlorobenzenes in a glass capillary microreactor. RHA-Ti and RHA-Pt supported catalysts showed very interesting catalytic activity in the detoxification of chlorobenzenes in ambient conditions. The main advantage of capillary reactor is the in situ generation of hydrogen for the detoxification of chlorobenzenes. Only 20 min is sufficient when compared to 24 h reaction time in conventional method. The proposed method is simple, easy to use, and suitable for the detoxification of a wide range of chlorinated organic pollutants in environmental remediation applications.

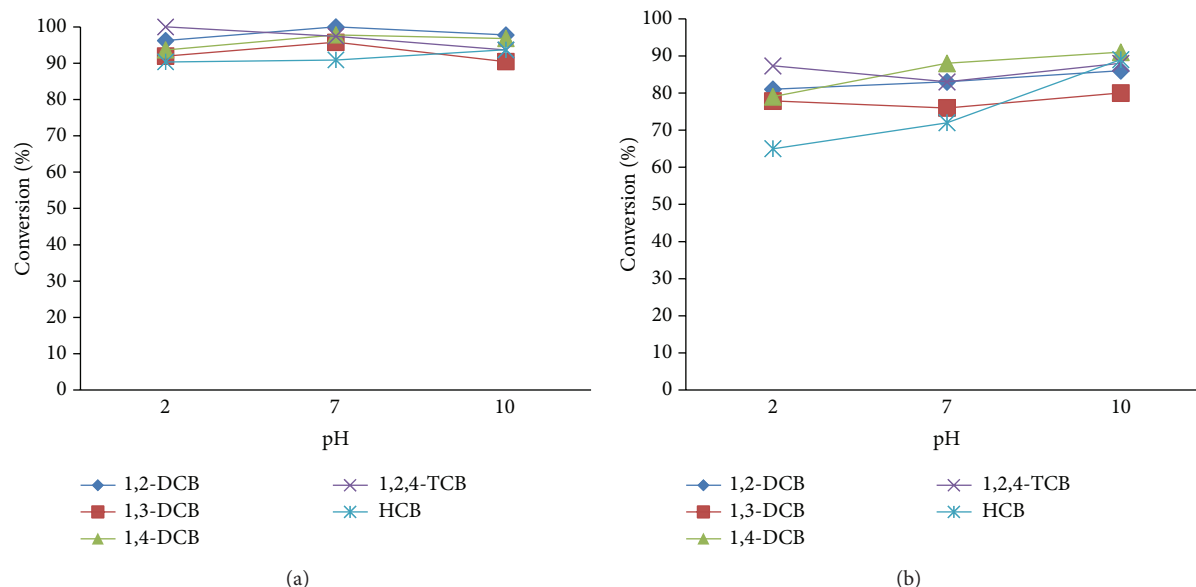


FIGURE 8: Effect of reaction pH on the conversion ratio of chlorobenzenes (CBs) in the capillary microreactor at 20 min and applied potential (3 kV) by using (a) RHA-Pt and (b) RHA-Ti.

Conflict of Interests

The authors declare that there is no conflict of interests regarding the publication of this paper.

Acknowledgment

The authors gratefully acknowledge the support provided by the King Abdul Aziz City for Science and Technology through the Science and Technology Unit at King Fahd University of Petroleum and Minerals for funding Project no. 13-ENE277-04, as a part of the National Science Technology and Innovation Plan.

References

- [1] V. Felis, P. Fouilloux, C. de Bellefon, and D. Schweich, "Three-step catalytic detoxification process of wastewater containing chlorinated aromatic compounds: experimental results and modeling issues," *Industrial & Engineering Chemistry Research*, vol. 38, no. 11, pp. 4213–4219, 1999.
- [2] I. M. Nangoi, P. K. Kiyohara, and L. M. Rossi, "Catalytic hydrodechlorination of chlorobenzene over supported palladium catalyst in buffered medium," *Applied Catalysis B: Environmental*, vol. 100, no. 1-2, pp. 42–46, 2010.
- [3] C. Cui, X. Quan, S. Chen, and H. Zhao, "Adsorption and electrocatalytic dechlorination of pentachlorophenol on palladium-loaded activated carbon fibers," *Separation and Purification Technology*, vol. 47, no. 1-2, pp. 73–79, 2005.
- [4] L. Calvo, M. A. Gilarranz, J. A. Casas, A. F. Mohedano, and J. J. Rodríguez, "Hydrodechlorination of 4-chlorophenol in water with formic acid using a Pd/activated carbon catalyst," *Journal of Hazardous Materials*, vol. 161, no. 2-3, pp. 842–847, 2009.
- [5] S. Gryglewicz and W. Piechocki, "Hydrodechlorination of dichlorobenzenes and their derivatives over Ni–Mo/C catalyst: kinetic analysis and effect of molecular structure of reactant," *Chemosphere*, vol. 83, no. 3, pp. 334–339, 2011.
- [6] W. F. Jardim, S. G. Moraes, and M. M. K. Takiyama, "Photocatalytic degradation of aromatic chlorinated compounds using TiO₂: toxicity of intermediates," *Water Research*, vol. 31, no. 7, pp. 1728–1732, 1997.
- [7] F.-D. Kopinke, K. Mackenzie, R. Koehler, and A. Georgi, "Alternative sources of hydrogen for hydrodechlorination of chlorinated organic compounds in water on Pd catalysts," *Applied Catalysis A: General*, vol. 271, no. 1-2, pp. 119–128, 2004.
- [8] US Environmental Protection Agency (US.EPA), *National Pollutant Discharge Elimination System*, Code of Federal Regulations, 40(122), US Government Printing Office, Washington, DC, USA, 1980–1988.
- [9] W. J. Hayes and E. R. Laws, "Chlorinated hydrocarbon insecticides," in *Handbook of Pesticide Toxicology, Classes of Pesticides*, J. Hopkins, Ed., vol. 2, pp. 731–915, Academic Press, San Diego, Calif, USA, 1991.
- [10] ATSDR ToxProfile, *Toxicological Profile for Alpha-, Beta-, Gamma-, and Delta-Hexachlorocyclohexane*, Agency for Toxic Substances and Disease Registry, US Department of Health and Human Services, Washington, DC, USA, 2005.
- [11] S. Wang, B. Yang, T. Zhang, G. Yu, S. Deng, and J. Huang, "Catalytic hydrodechlorination of 4-Chlorophenol in an aqueous solution with pd/ni catalyst and formic acid," *Industrial and Engineering Chemistry Research*, vol. 49, no. 10, pp. 4561–4565, 2010.
- [12] E. R. Ritter, J. W. Bozzelli, and A. M. Dean, "Kinetic study on thermal decomposition of chlorobenzene diluted in hydrogen," *Journal of Physical Chemistry*, vol. 94, no. 6, pp. 2493–2504, 1990.
- [13] M. Kosusko, M. E. Mullins, K. Ramanathan, and T. N. Rogers, "Catalytic oxidation of groundwater stripping emissions," *Environmental Progress*, vol. 7, no. 2, pp. 136–142, 1988.
- [14] M. Wirtz, J. Klucik, and M. Rivera, "Ferredoxin-mediated electrocatalytic dehalogenation of haloalkanes by cytochrome

- P450_{cam},” *Journal of the American Chemical Society*, vol. 122, no. 6, pp. 1047–1056, 2000.
- [15] C. Hu, B. Yue, and T. Yamase, “Photoassisted dehalogenation of organo-chlorine compounds by paratungstate A in aqueous solutions,” *Applied Catalysis A: General*, vol. 194–195, pp. 99–107, 2000.
- [16] J.-G. Lin and Y.-S. Ma, “Magnitude of effect of reaction parameters on 2-chlorophenol decomposition by ultrasonic process,” *Journal of Hazardous Materials*, vol. 66, no. 3, pp. 291–305, 1999.
- [17] W. W. Mohn and J. M. Tiedje, “Microbial reductive dehalogenation,” *Microbiological Reviews*, vol. 56, no. 3, pp. 482–507, 1992.
- [18] Y. Yamamoto and S. Tagawa, “Radiolytic and thermal dechlorination of organic chlorides adsorbed on molecular sieve 13X,” *Environmental Science and Technology*, vol. 35, no. 10, pp. 2122–2127, 2001.
- [19] B.-V. Chang, C.-W. Chiang, and S.-Y. Yuan, “Dechlorination of pentachlorophenol in anaerobic sewage sludge,” *Chemosphere*, vol. 36, no. 3, pp. 537–545, 1998.
- [20] C. M. Kao, C. T. Chai, J. K. Liu, T. Y. Yeh, K. F. Chen, and S. C. Chen, “Evaluation of natural and enhanced PCP biodegradation at a former pesticide manufacturing plant,” *Water Research*, vol. 38, no. 3, pp. 663–672, 2004.
- [21] D.-S. Shen, X.-W. Liu, and H.-J. Feng, “Effect of easily degradable substrate on anaerobic degradation of pentachlorophenol in an upflow anaerobic sludge blanket (UASB) reactor,” *Journal of Hazardous Materials*, vol. 119, no. 1–3, pp. 239–243, 2005.
- [22] N. C. Concibido, T. Okuda, Y. Nakano, W. Nishijima, and M. Okada, “Enhancement of the catalytic hydrodechlorination of tetrachloroethylene in methanol at mild conditions by water addition,” *Tetrahedron Letters*, vol. 46, no. 21, pp. 3613–3617, 2005.
- [23] E. N. Balko, E. Przybylski, and F. V. Trentini, “Exhaustive liquid-phase catalytic hydrodehalogenation of chlorobenzenes,” *Applied Catalysis B, Environmental*, vol. 2, no. 1, pp. 1–8, 1993.
- [24] R. A. W. Johnstone, A. H. Wilby, and I. D. Entwistle, “Heterogeneous catalytic transfer hydrogenation and its relation to other methods for reduction of organic compounds,” *Chemical Reviews*, vol. 85, no. 2, pp. 129–170, 1985.
- [25] X. Liu, G. Lu, Y. Guo, Y. Wang, and X. Wang, “Catalytic transfer hydrogenolysis of 2-phenyl-2-propanol over palladium supported on activated carbon,” *Journal of Molecular Catalysis A: Chemical*, vol. 252, no. 1–2, pp. 176–180, 2006.
- [26] F. H. Ribeiro, C. A. Gerken, G. Rupprechter et al., “Structure insensitivity and effect of sulfur in the reaction of hydrodechlorination of 1,1-dichlorotetrafluoroethane (CF₃-CFCl₂) over Pd catalysts,” *Journal of Catalysis*, vol. 176, no. 2, pp. 352–357, 1998.
- [27] C. D. Thompson, R. M. Rioux, N. Chen, and F. H. Ribeiro, “Turnover rate, reaction order, and elementary steps for the hydrodechlorination of chlorofluorocarbon compounds on palladium catalysts,” *The Journal of Physical Chemistry B*, vol. 104, no. 14, pp. 3067–3077, 2000.
- [28] F. J. Urbano and J. M. Marinas, “Hydrogenolysis of organohalogen compounds over palladium supported catalysts,” *Journal of Molecular Catalysis A: Chemical*, vol. 173, no. 1–2, pp. 329–345, 2001.
- [29] T. Naota, H. Takaya, and S.-L. Murahashi, “Ruthenium-catalyzed reactions for organic synthesis,” *Chemical Reviews*, vol. 98, no. 7, pp. 2599–2660, 1998.
- [30] Z. M. De Pedro, J. A. Casas, L. M. Gomez-Sainero, and J. J. Rodriguez, “Hydrodechlorination of dichloromethane with a Pd/AC catalyst: reaction pathway and kinetics,” *Applied Catalysis B: Environmental*, vol. 98, no. 1–2, pp. 79–85, 2010.
- [31] J. Bedia, L. M. Gómez-Sainero, J. M. Grau, M. Busto, M. Martin-Martinez, and J. J. Rodriguez, “Hydrodechlorination of dichloromethane with mono- and bimetallic Pd-Pt on sulfated and tungstated zirconia catalysts,” *Journal of Catalysis*, vol. 294, pp. 207–215, 2012.
- [32] F. Adam, J. N. Appaturi, R. Thankappan, and M. A. M. Nawi, “Silica-tin nanotubes prepared from rice husk ash by sol-gel method: characterization and its photocatalytic activity,” *Applied Surface Science*, vol. 257, no. 3, pp. 811–816, 2010.
- [33] C. Basheer, F. S. J. Hussain, H. K. Lee, and S. Valiyaveetil, “Design of a capillary-microreactor for efficient Suzuki coupling reactions,” *Tetrahedron Letters*, vol. 45, no. 39, pp. 7297–7300, 2004.
- [34] C. Basheer, S. Swaminathan, H. K. Lee, and S. Valiyaveetil, “Development and application of a simple capillary-microreactor for oxidation of glucose with a porous gold catalyst,” *Chemical Communications*, no. 3, pp. 409–410, 2005.
- [35] F. Adam, J. N. Appaturi, Z. Khanam, R. Thankappan, and M. A. M. Nawi, “Utilization of tin and titanium incorporated rice husk silica nanocomposite as photocatalyst and adsorbent for the removal of methylene blue in aqueous medium,” *Applied Surface Science*, vol. 264, pp. 718–726, 2013.